Modeling simple and complex fluids under confinement

Cecilia Bores Quijano
Programa de Doctorado en Física de la Materia Condensada y Nanotecnología. Universidad Autónoma de Madrid

Instituto de Química-Física Rocasolano (CSIC)
Director: Enrique Lomba

Contents

Preface

Most fluids found in nature exhibit a complex behavior departing from the regular laws we can find for gasses and solids. In this work we are specially interested in the features of *self-assembling* fluids, which exhibit the emergence of ordered patterns at certain thermodynamic conditions. We will see along this work how relevant these systems are to industrial and biological processes, and we will explore the origin of their peculiar behavior. To name some examples, understanding self-assembly is decisive for describing colloidal and protein solutions present in food products, and for technological applications such as nano-lithography.

Furthermore, the adsorption and confinement of fluids, particularly at the nanometer scale, have been the focus of great interest over the last decade, since the properties of the original fluid when confined can be modified with a high degree of control by choosing the appropriate adsorbent. The importance and consequences of confinement are astonishing; there are so many applications derived from this process (energy storage, drug delivery, catalysis, new electronic devices, ...) that *nano-science* has been established as a new discipline on itself. For this reason the synthesis, tailoring and characterization of porous media have also greatly progressed in recent years; however, our understanding of the chemical and physical mechanisms of adsorption and confinement and the interplay between adsorbent and adsorbate is far from complete.

The general aim of this work is to enhance our knowledge on the behavior of simple and self-assembling fluids under confinement in a variety of confining topologies. Simple fluids will be considered as a reference and as testing ground for new theoretical approaches, and also in the context of new porous materials for technological applications. Along this thesis we will consider two kinds of porous media: those with *regular pores*, like slit pores (two parallel walls) that show a simple dimensionality reduction, or crystalline nano-structured materials (zeolites, nanostructured carbons); and *disordered porous media*, where the topological disorder conditions the fluid properties in addition to the volume constraints due to the confinement.

Concerning methodology, we will first resort to molecular simulations based on *Monte Carlo* and *Molecular Dynamics* approaches; in addition, we will make use of integral equation theories derived from the *Ornstein-Zernike* relation. One of our aims will be to provide detailed information on the explicit spatial distribution of the fluids inside the porous media. This is a key element for the understanding of adsorption processes, and in particular plays an essential role in the design of new functionalized materials. We will show how new theoretical approaches can complement and extend the capabilities of simulation techniques in this context, with a reduced computational cost.

Summarizing, this thesis pursues three main goals:

- To reveal the effect of the confinement (both regular and disordered) on the behavior of fluids with self-assembly properties.
- To analyze new nano-structured materials for adsorption applications.
- To construct a suitable and efficient theoretical approach, in the framework of integral equation theory, to study adsorption and confinement processes.

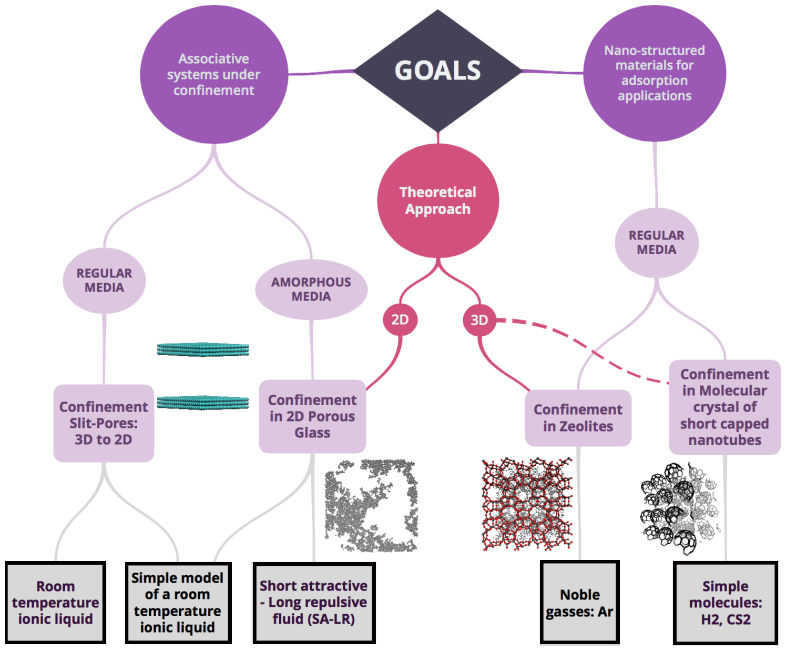

Figure 1: *Diagram showing the systems (bottom) that will be analyzed along this work and their connection with our main goals (top).*

In an attempt to provide a first and clear outline of this thesis to the reader, we present in Figure 1 a diagram summarizing the systems that will be analyzed and their connection with the goals we pursue.

From the organizational point of view, the thesis is divided into five chapters:

- **Chapter 1** will provide a general theoretical background to the reader. It is an introductory section that contains all the relevant physical aspects and approximations included in this thesis: fluids with self-organizing properties, confinement and adsorption processes, and computational methods. At the end of this section we will introduce and describe in detail all the systems that will be analyzed.

- In **Chapter 2** we will describe the methods and theories this thesis is based on, emphasizing the particular approaches we will apply. We have divided this chapter into three parts: first we describe the tools required to analyze and characterize the systems under study: fluids and porous materials, and then we give the details of the methods we have used (molecular simulation and integral equation theory).

- In **Chapter 3** we will focus on self-assembly systems in bulk and under confinement. We introduce a simple mixture model in which short ranged competitive interactions lead to nano-structuring, and to effective potentials with the characteristic short range attractive / long range repulsive (SALR) behavior typical of self-assembly systems. Afterwards, we will see how clustering and nanostructuring are influenced by confinement in regular and disordered porous topology. In the case of regular topologies, we will consider both our simple mixture model and a realistic room temperature ionic liquid model confined in slit pores. This phenomenology is further analyzed using an effective SALR potential model, confined in a disordered matrix by means of simulation and our new theoretical approaches.

- **Chapter 4** will be focused on simple fluids confined in regular crystalline materials. Noble gasses in zeolites will be dealt with in order to test the performance of our theoretical approach in a realistic system. Finally, we will focus on a new material composed of short capped nanotubes, $C_{50}H_{10}$, whose capabilities as molecular carriers and for hydrogen storage will be explored by means of computer simulation.

- Finally, this thesis is closed with a summary of our main findings and conclusions.

I would like to express here my gratitude to all the people and entities who made this adventure possible. First of all, thanks to my family, in particular my parents and Antonio, for their endless support and faith; and my friends who have always cheered me up with their energy.

From an academic point of view, I can not forget my teachers at high school (Don Fer, Magdalena and Rosa) who provided me the tools and interest to study physics; and I owe Maria José López the chance to "become a scientist". I would like to thank Enrique Lomba for trusting me for this project and for his omnipresent guide, support, advises, ... and patience; and also to my group mates: Alberto, Claudio, Eva, Noe and Vicente, for their help and wisdom. I want to thank all the "Rocasolano family" too: Ana, Gloria, Mar, Sagrario, ... for their pleasant company and help.

During these four years, I have enjoyed the opportunity to spend several months abroad. I want to thank Gerhard Kahl, Lev Sarkisov and Marcia Barbosa for letting me feel like one more of their groups, sharing with me their kindness and wisdom. I have met outstanding people in these travels; sadly, I can not name all of them here, but I need to mention Marta, Günter, and Clara (my little Spanish family in Vienna); Andy, Dieter, Emmanuela, Ismene, Jan, Moritz, Silvano (best pizzas ever) and Ulf; Cyntia and Alexandre (amazing trips across Brazil); Elsa and Fernando (Brazilian gastronomy explorers); Alex, Alez, Ares, Nelly, Sofia, ... and all the students in Sanderson building; and Klara (an angel in Hanover's street).

Last, but obviously not least, I want to thank all the economic sources that have make possible this exciting and productive experience: *FIS2013-47350-C5-4-R* and *FIS2010-15502* funded by the Science and Innovation Spanish Ministry and *S2009ESP-1691* funded by Community of Madrid.

Prefacio

La mayor parte de los fluidos que existen en la naturaleza presentan comportamientos que difieren de las leyes regulares que con tanta precisión describen a sólidos y gases. En este trabajo se ha prestado un interés especial en los fluidos complejos con propiedades auto-ensamblantes en los que se observa la emergencia de fases ordenadas en determinadas condiciones termodinámicas. A lo largo de este documento se demostrará la relevancia de estos sistemas en procesos biológicos e industriales y se explorará el origen de este comportamiento tan peculiar. Por nombrar algunos ejemplos, la comprensión de los mecanismos de auto-ensamblaje es decisiva para describir disoluciones de coloides y proteínas que aparecen en productos alimenticios y también para aplicaciones tecnológicas como la nano-litografía.

Además, la adsorción y el confinamiento de fluidos, particularmente en escala nanométrica, han sido de gran interés durante la última década porque las propiedades de los fluidos en condiciones de confinamiento pueden ser modificadas con un alto grado de control simplemente eligiendo el adsorbente adecuado. La importancia y las consecuencias del confinamiento son enormes; debido al gran número de aplicaciones derivadas de este proceso (almacenamiento energético, catálisis, dispositivos electrónicos,...) la nanociencia se ha establecido por si misma como una nueva disciplina. Por esta razón, la síntesis, el diseño y la caracterización de materiales porosos ha experimentado un enorme progreso recientemente; sin embargo, aún queda mucho para que la comprensión de los mecanismos químicos y físicos que permiten que tengan lugar los procesos de adsorción y confinamiento y de

la interacción entre el adsorbente y el adsorbato sea total.

El objetivo general de esta tesis es mejorar el conocimiento del comportamiento de fluidos simples y con propiedades de auto-ensamblaje bajo condiciones de confinamiento en medios porosos con diversas topologías. Se considerarán fluidos simples como referencia para desarrollar nuevas aproximaciones teóricas, y también en el contexto de nuevos materiales porosos con aplicaciones tecnológicas. En esta tesis se van a considerar dos tipos de medios porosos: con poros *regulares*, como confinamiento entre paredes que muestran únicamente una reducción de la dimensionalidad del sistema, o materiales cristalinos nanoestructurados (zeolitas, carbonos nanoestructurados,...); y medios desordenados, en los que el desorden topológico se va a sumar a la restricción del espacio debida al confinamiento a la hora de condicionar las propiedades del fluido.

Con respecto a la metodología, se llevarán a cabo simulaciones moleculares basadas en métodos *Monte Carlo* y de *Dinámica molecular*; además, se aplicarán teorías de ecuaciones integrales derivadas de la relación de *Ornstein-Zernike* al problema del confinamiento. Uno de los objetivos perseguidos consiste en obtener información detallada y explícita a cerca de la distribución espacial del fluido en el interior del medio poroso. Esta idea es un elemento clave para el entendimiento de los procesos de adsorción, y juega un papel esencial particularmente a la hora de diseñar nuevos materiales funcionalizados. Demostraremos cómo nuevas aproximaciones teóricas complementan y extienden las capacidades de las técnicas de simulación en este contexto, introduciendo una reducción del costo computacional.

Esta tesis persigue, en resumen, tres objetivos fundamentales:

- Entender el efecto del confinamiento (tanto en medios porosos regulares como desordenados) sobre el comportamiento de los fluidos con propiedades nano-ensamblantes.
- Analizar nuevos materiales nano-estructurados para aplicaciones de adsorción.

- Construir una aproximación teórica, en el marco de la teoría de las ecuaciones integrales, que eficiente y apropiada para el estudio de procesos de adsorción y confinamiento.

Desde un punto de vista organizativo, este documento se divide en cinco capítulos:

- El **Capítulo 1** tiene como propósito proporcionar al lector una base teórica general, se trata de una sección introductoria que contiene todos los aspectos físico relevantes e introduce las aproximaciones que aparecerán a lo largo de la tesis: fluidos con propiedades auto-ensamblantes, procesos de confinamiento y adsorción y los métodos computacionales empleados. En el último apartado de este capítulo se introducen y se detallan todos los sistemas que se van a analizar en los capítulos posteriores.

- En el **Capítulo 2** se describen los métodos y las teorías en las que se basa esta tesis, enfatizando las aproximaciones particulares que se van a aplicar a los sistemas estudiados. Hemos dividido este capítulo en cuatro secciones: en primer lugar se introducen las bases de la física estadística; después se describen las las herramientas necesarias para analizar y caracterizar los sistemas objeto de estudio (fluidos y materiales porosos), y finalmente se describen los métodos que se usarán a lo largo de esta tesis (simulaciones moleculares y teoría de las ecuaciones integrales).

- El **Capítulo 3** está centrado en sistemas auto-ensamblantes confinados y sin confinar. Introducimos un modelo simple, basado en una mezcla binaria, en el que a partir de interacciones exclusivamente de corto alcance, aparece orden a escala nano-métrica y potenciales efectivos con un comportamiento característico de los sistemas auto-ensamblantes (atractivo a distancias cortas y repulsivo a distancias largas, $SALR$). Posteriormente veremos la influencia que tiene el confinamiento, tanto en poros regulares como desordenados, sobre esta nano-estructuración. En el caso de medios regulares consideraremos

dos sistemas: nuestro modelo de mezcla simple y un modelo realista de líquido iónico a temperatura ambiente. Esta fenomenología será posteriormente analizada usando un modelo descrito mediante un potencial efectivo de tipo SALR, confinado en una matriz desordenada utilizando simulaciones moleculares y una nueva aproximación teórica.

- El **Capítulo 4** se centra en el confinamiento de fluidos simples en materiales porosos con una estructura regular cristalina. Se demostrará la validez de una nueva aproximación teórica en una sistema realista: adsorción de gases nobles en zeolitas. Finalmente, nos centraremos en un nuevo material porosos compuesto por nano-dedales de carbono ($C_{50}H_{10}$) y exploraremos sus capacidades potenciales para almacenamiento de hidrógeno mediante simulación computacional.

- Por último, este documento finaliza con una sección dedicada a resumir y concluir los principales resultados encontrados a lo largo de este trabajo.

Quiero expresar aquí mi gratitud hacia todas las personas y entidades que han hecho posible esta aventura. En primer lugar, gracias a mi famila, en particular a mis padres y Antonio por su ilimitable confianza y apoyo; y a mis amigos ("físicos de Valladolid", "las chicas de Santi" y "los guajes de Guardo") quienes siempre me han animado con su energía.

Desde el punto de vista académico, no puedo olvidarme de mis profesores del instituto (Don Fer, Magdalena y Rosa) quienes me inculcaron el interés y me dieron las primeras herramientas necesarias para estudiar física. Por otro lado, a Maria Jóse López le debo la oportunidad y la inspiración para convertirme en "científico". Quiero agradecer a Enrique Lomba, el director de esta tesis, la confianza que depositó en mi para llevar a cabo este proyecto, y su omnipresente apoyo, guía y paciencia; y también a mis compañeros de grupo: Alberto, Claudio, Eva, Noe y Vicente porque a su lado he crecido un poquito más cada dia, como científico y también

como persona.

Durante estos cuatro años he tenido la oportunidad de pasar varios meses en otros países colaborando con diferentes grupos. Quiero darle las gracias a Gerhard Kahl, Lev Sarkisov y Marcia Barbosa por haber conseguido que me sintiese como un miembro más de sus respectivos grupos, compartiendo conmigo su amabilidad y sabiduría. En estos viajes he conocido gente impresionante; lamentablemente no puedo nombrar a cada uno de ellos, pero siento la necesidad de mencionar a Marta y Clara (mi pequeña España en Viena); Silvano (las mejores pizzas del mundo); Andy, Dieter, Emmanuela, Günter, Ismene, Jan, Moritz and Ulf; Cyntia y Alexandre (viajes increíbles por Brasil); Elsa y Fernando (exploradores de la gastronomía brasileña); Alex, Alez, Ares, Nelly, Sofía... y todos los estudiantes del "Sanderson building"; and Klara (un ángel en Hanover's street).

Y por último, pero no menos importante, quiero agradecer las fuentes de financiación que han hecho posible esta aventura tan apasionante y productiva. *FIS2013-47350-C5-4-R* y *FIS2010-15502* financiado por el ministerio de ciencia e innovación, y *S2009ESP-1691* financiado por la dirección general de investigación de la Comunidad de Madrid.

Chapter 1

Introduction

This section provides the reader an overview of our research motivations and their physical basis. To this aim, we will first describe the fluid state of matter highlighting the case of self-assembling fluids, which exhibit spontaneous pattern formation; then, we will focus on confinement and adsorption processes describing different types of confining media and how to characterize them. Afterwards, we introduce the modeling tools employed in this work, and finally we describe the systems we will investigate. Given the central role of computer modeling in this research, we will stress throughout this introduction the aspects related to the mapping of real systems into simpler models suitable for simulations and theoretical descriptions.

1.1 Fluid state: liquids and dense fluids

Dense fluids

At a given temperature and pressure, substances in nature may appear in different states of matter, characterized by very different macroscopical

properties: *gas, liquid* and *solid* are the most common ones. However, as we vary the temperature and the pressure, the state changes in a way that is characteristic of the substance itself; this transition between states can be represented in a graph called *phase diagram*.

As we can see in Figure 1.1, liquid state constitutes only a small part of the phase diagram of a simple substance, surrounded by solid and vapor states. Furthermore, this state exhibits a behavior characterized by short-range order and high density, typical of solids; and at the same time by the ability to flow and the lack of long-range order, characteristic of gasses. The features of liquids will be presented in some detail in **Section 2.1**. We note here that for temperatures above the critical, the transition between gas and liquid states is blurred. In some instances (e.g. extremely short ranged interactions) the liquid phase itself vanishes completely [Lomba and Almarza, 1994; Hagen et al., 1993]. A few years ago, Brazhkin et al. [2012] proposed the definition of a line (*Frenkel's line*) separating two fluid phases; a solid-like phase and a gas-like one. These two phases can be characterized their different specific heats, a qualitative change in their velocity self-correlation functions, and the disappearance of shear-like modes when going from the solid-like to the gas-like fluid phase. This is an important distinction that extends the simple vapor-liquid classification in the case of fluids lacking a stable liquid phase.

In this thesis we will be dealing with the properties of fluids, either in vapor phase, or in liquid state, or supercritical fluids in the solid-like and gas like region. Fluids are essential to sustain life and are obviously key to many technological applications such as solvents, lubricants or heat transfer media.

Compared to the other states of matter, dense fluids present an intrinsic complexity difficult to cope with by theoretical approaches. The emergence of this state is not trivial and it has been described by Barrat and Hansen [Barrat and Hansen, 2003] as the consequence of a delicate balance between energy and entropy while cooling the system from the vapor state. In

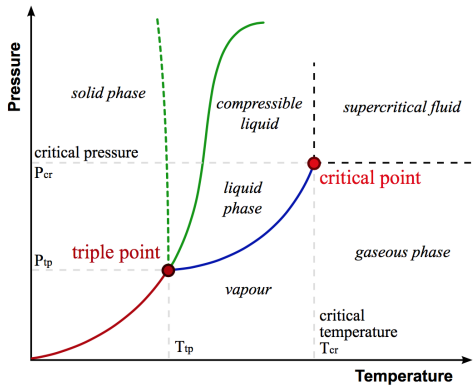

Figure 1.1: *Phase diagram of a simple substance.*

addition, its structure is determined by intrincated excluded-volume effects which depend on the system constituents nature and the interactions among them. This complexity explains the lack of accurate models able to describe systems in the liquid state, comparable with the ideal *crystal lattice* or the ideal *gas model*. Furthermore, in spite of the similarities with other states of matter and numerous attempts in the past (e.g the cell theory for liquids [Diaz Peña, 1979]), it is not effective to study liquid systems as if they were condensed gasses or solids with vacancies: we must understand and treat dense fluids as a *many-body* problem.

Statistical mechanics and Thermodynamics

Thanks to *thermodynamics*, we are able to characterize a system in equilibrium by a small number of *state variables* (temperature, pressure, density,...). Theses quantities are experimentally measurable and they provide useful information about the macroscopic properties of the system.

On the other hand, as we are working on a many-body problem, our system can be microscopically described in terms of its particles *coordinates*

($\mathbf{r} = \mathbf{r_1}, \mathbf{r_2}, ..., \mathbf{r_N}$) and the *momenta* ($\mathbf{p} = \mathbf{p_1}, \mathbf{p_2}, ..., \mathbf{p_N}$), which comprise the system's *phase space*. *Statistical Mechanics* is the tool that allows us to cross over from the microscopic to the macroscopic level. The origin of this branch of physics is closely related with the kinetic theory of gases stablished by Bernouilli in 1738 in his work *Hydrodynamica*: gasses consist of molecules moving in all directions. Maxwell, based on Krönig and Clausius contributions to the field during the XIX century, formulated his distribution of molecular velocities in 1859, which was the first statistical law in physics. Maxwell's work strongly inspired Boltzmann, who was the real developer of Statistical Mechanics and settled the basis of this field in his *Lectures on Gas Theory* in 1896. The term "Statistical Mechanics" was introduced in 1884, when Gibbs first used the name in his works.

The connexion between macroscopic and microscopic scales is done in the canonical ensemble (NVT) by means of the *partition function* Z that is a sum over all the microstates of the system, i.e. $Z = \sum_{allstates} e^{-\mathscr{H}/k_B T}$; where the Hamiltonian function $\mathscr{H}$ is the sum of potential $\mathscr{V}(\mathbf{r})$ and kinetic $\mathscr{K}(\mathbf{p})$ energies, defined as functions of the positions and the momenta respectively: $\mathscr{H}(\mathbf{p}, \mathbf{r}) = \mathscr{K}(\mathbf{p}) + \mathscr{V}(\mathbf{r})$. This function is directly related to the system's Helmholtz energy and hence all relevant thermodynamic quantities can be derived from it. Alternative -but equivalent- formulations can be derived for other ensembles defined in terms of other thermodynamic quantities (NPT, μVT,...).

Modeling dense fluids

While the particle velocities determine $\mathscr{K}(\mathbf{p})$, $\mathscr{V}(\mathbf{r})$ contains all the information concerning the interactions between the constituents particles of the system. In order to model fluids, we need to know the functional form of this interaction and simplify it as much as possible. In principle, the potential energy may be written as a sum of the interactions of single

atoms in an external potential, pairs, triplets... present in the system.

$$\mathscr{V}(\mathbf{r}) = \sum_i v_1(\mathbf{r}_i) + \sum_i \sum_{j>i} v_2(\mathbf{r}_i, \mathbf{r}_j) + ... \tag{1.1}$$

In the absence of external fields, the dominant term is the second one, the *pair potential*, and for many purposes it has been shown [Egelstaff, 1992] that it is a good approximation to truncate the expansion of the potential energy after this term (*pairwise approximation*). If the system is isotropic, homogenous and composed of spherically symmetric particles, $v_2(\mathbf{r}_i, \mathbf{r}_j)$ only depends on the distance between the pair of atoms $r = |\mathbf{r_i} - \mathbf{r_j}|$, thus it can be written as $v_2(r)$.

One of the simplest pair potentials that represents the interaction between two spherical particles is the *hard-sphere* potential. It is highly idealized and considers only the hard repulsion between a pair of particles, i. e. $U(r)$ is infinite for $r \leq \sigma$ and it is 0 for $r > \sigma$. Colloidal systems can actually be designed to behave as hard-sphere fluids [Bartlett et al., 1992; Royall et al., 2013].

A more realistic pair potential for spherical particles, must take into account features such as the repulsion induced by Pauli principle (equal spin electrons of adjacent atoms can not overlap) and the attractions induced by London dispersion forces (even if the atoms are electrically neutral, fluctuations in their electronic clouds appear). All these considerations are effectively taken into account in *Lennard-Jones* (LJ) potential, which in its 12-6 formulation reads:

$$U(r)_{LJ} = 4\epsilon \left[\left(\frac{\sigma}{r}\right)^{12} - \left(\frac{\sigma}{r}\right)^{6} \right], \tag{1.2}$$

where the parameters σ (the collision diameter) and ϵ (well depth) are calculated by fitting macroscopic properties obtained using the suggested potential to experimental results or/and ab initio calculations. The LJ potential successfully describes the interaction between noble gas atoms and

quasispherical molecules such as CH_4 or even SF_6 [Allen and Tildesley, 1987, p. 6].

In the case of mixtures, the total interaction includes contributions between the atoms of different species. Here, *Lorentz-Berthelot* mixing rules (among other possible rules) define the cross terms as:

$$\sigma_{AB} = 1/2[\sigma_{AA} + \sigma_{BB}]$$

$$\epsilon_{AB} = [\epsilon_{AA}\epsilon_{BB}]^{1/2},$$

where σ_{AA}, ϵ_{AA} and σ_{BB}, ϵ_{BB} are the LJ parameter between atoms of the same type.

Molecular fluids can be treated in principle resorting to the *Interaction Site Mode* (ISM), in which the pair energy between two molecules A and B is approximated by: $U^{AB}(\mathbf{r_A}, \mathbf{r_B}, \omega_\mathbf{A}, \omega_\mathbf{B}) = \sum_{\alpha,\beta} u_{AB}^{\alpha\beta}(r_{\alpha\beta})$, where α and β designate the interaction sites in molecules A and B.

Additionally, when dealing with highly polar molecules or ions, the simplest solution is to attach electrostatic charges, q, to the particles and extend the effective pair potential with a *Coulombic term*: $V_{ij}(r) = v_{ij}^{nonCoul}(r) + v_{Coul}(r)$; where $v_{Coul} = q_i q_j / 4\pi\epsilon_0 r$. These interactions are long ranged and we will see that, when performing molecular simulations, will require specific strategies to cope with the effect of periodicity implicit in most simulation approaches. Among these strategies we can mention the Ewald summation [Allen and Tildesley, 1987] or the P3M algorithm [Cerdà et al., 2008].

However, the level of complexity exhibited by some fluids in nature (colloids, protein solutions,...), exceeds by far the modeling possibilities of simple ISM approaches. Here is where the *effective potentials* and its design play a central role. Although the LJ potential can be considered in itself an effective potential, we refer here to those designed to model complex

systems through a coarse-graining procedure.

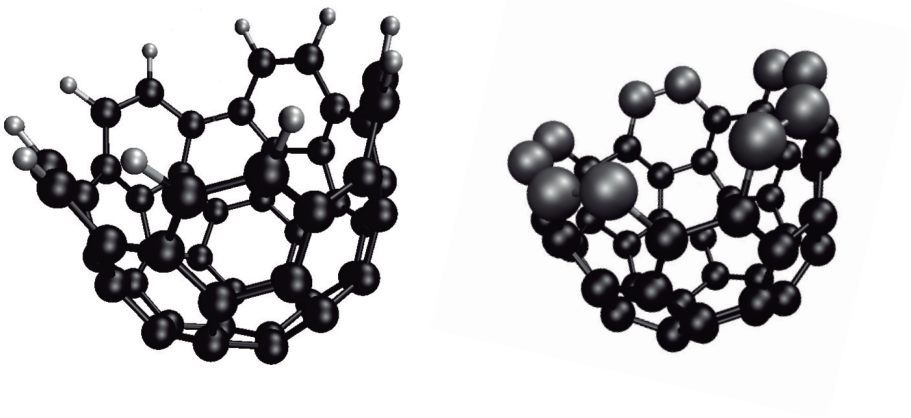

Figure 1.2: *Example of an* united-atoms *model: left figure shows the full chemical structure of the* $C_{50}H_{10}$ *molecule while right figure shows the united-atoms reduction of the system where the carbon atoms of the edge have been grouped with their bonded hydrogens in* sites *placed in the center of mass,* $C_{40}(CH)_{10}$.

Coarse-graining approaches are useful since they link atomistic and mesoscales: they simplify the structure of the fluid, reducing its number of degrees of freedom, while essential information about its behavior is included in the effective potential. One of the most commonly used coarse-graining methods is the so-called *united-atom* model (UAM), which groups several atoms or molecules into a single coarse-grained particle (called *site*). It typically maps CH_n groups onto a single site, but it can be applied to more complex situations [Chennamsetty et al., 2011]. Other coarse-graining techniques integrate out degrees of freedom corresponding to certain components of a mixture. Perhaps one of the simplest examples that illustrates this case is the DLVO theory for colloidal solutions [Derjaguin and Landau, 1941; Verwey and Overbeek, 1948]

The effective potentials and the coarse-graining considerations we have used in this thesis have been thoroughly explained in **Section 1.4** while describing each of the systems under study.

Self-assembling systems

Fluids with *self-assembling* properties are an example of the complex fluids we have introduced above. We aim here at improve our understanding of the origin of the self-assembling behavior, and analyze how it can be modified by confinement.

The understanding of the self-organizing capability of soft and fluid matter is critical for a wide panoply of applications of great relevance nowadays. Self-assembly mechanisms play a crucial role in processes involving protein solutions in food products [Alexander et al., 2002; Mezzenga et al., 2005], therapeutic monoclonal antibodies [Johnston et al., 2012; Yadav et al., 2012; Yearley et al., 2013] or gelation processes [Charbonneau and Reichman, 2007].

The spontaneous emergence of patterns is a consequence of the self-assembly behavior and it appears in a diverse collection of physical, chemical and biological systems [Seul and Andelman, 1995]. In spite of the diverse nature of these systems, the appearance of the emerging microphases is quite similar: in 2-D systems circular droplets, stripes or "bubbles" occur, and in 3-D systems one may find spherical droplets, sheets or tubes. In some cases the patterns appear as transient states due to energy or mass fluctuations that occur in the process of spinodal decomposition, but sometimes these states can be stabilized.

As mentioned before, in the realm of colloidal science, systems with extremely short ranged repulsive interactions are often used as an experimental realization of the hard sphere fluid [Royall et al., 2013], a system notorious for its theoretical interest. The addition of non-adsorbing polymers to the colloidal solution typically activates an attractive inter-particle interaction, due to depletion mechanism. Moreover, changing the concentration and molecular weight of the polymer, the attraction range and strength of the colloid-colloid interaction can be tuned. In this situation, clustering is to be expected due to the presence of the attractive forces [Poon

et al., 1997; Segre et al., 2001], but in principle it would correspond to meta-stable states and/or irreversible processes of kinetic nature. Nevertheless, microphases formed by clusters and percolating structures can be stabilized in protein solutions and colloid-polymer mixtures both in experiment [Stradner et al., 2004] and in theoretical descriptions [Groenewold and Kegel, 2001] due to the presence of additional repulsive interactions stemming from electrostatic forces. An extreme example of the stabilizing role of charges is the nanostructural organization that appears in room temperature ionic liquids (RTIL's) [Canongia Lopes and Pádua, 2006]. We will go back to ionic liquids in **Chapter 3** in order to study the delicate interplay between confinement, packing effects and wetting.

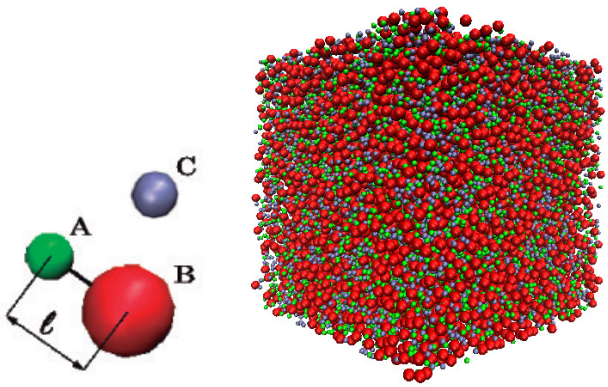

Figure 1.3: *Model (top left), snapshot (bottom left) and effective interactions in the room temperature ionic liquid model we have considered to study the emergence of intermediate range order in systems with only short-range interactions.*

It has been shown, furthermore, that long range repulsive interactions alone can give rise to stable nanostructural order [Camp, 2003], the driving force of attractive interactions to induce spontaneous aggregation being replaced by external forces (e.g. pressure). Beyond this, we will see in

Section 3.1 that intermediate range order appears naturally even when no explicit long range interactions are present. To this aim, we have employed a coarse-grained model of room temperature ionic liquid composed of heteronuclear dimers and monomers (Figure 1.3), that interact via a combination of attractive and repulsive short ranged potentials mimicking the interactions present in the modeled room temperature ionic liquid. We find that intermediate range ordering (or nanostructuring) emerges for certain ranges of density and temperature [Bores et al., 2015b].

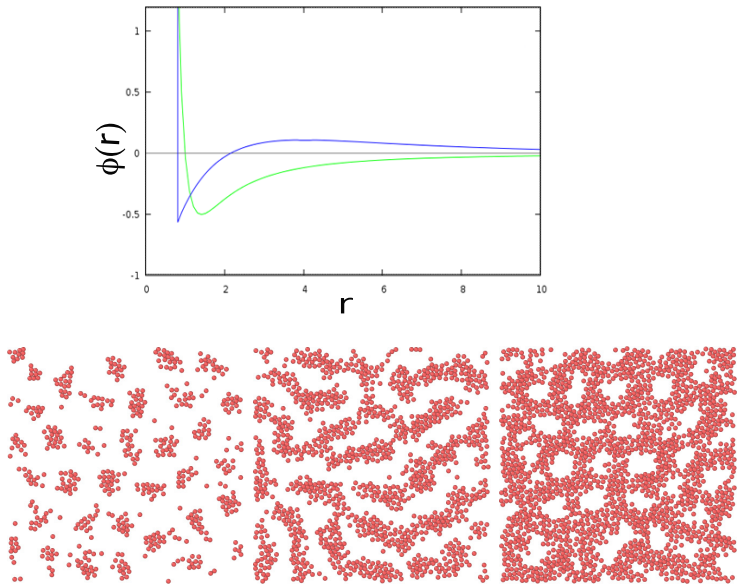

Figure 1.4: *Upper graph: Short attractive - long repulsive potential introduced by [Sear et al., 1999] and parametrized by [Imperio and Reatto, 2004] (blue line) compared with the simple short attractive Lennard Jones potential (green line). Lower figures: Droplets (left), stripes (central) and bubbles (right) patterns may be distinguished.*

Back to electrostatic forces, the colloid-colloid interaction between charged colloidal particles which are screened by ions in the solvent, has been shown

on theoretical grounds to be adequately represented by a Yukawa potential [Verwey and Overbeek, 1948] according to the Derjaguin-Landau-Verwey-Overbeen (DLVO) theory. Following this, numerous works have resorted to potentials with a combination of short range attraction and long range repulsion (SALR) in the form of a double Yukawa [Bomont et al., 2012; Godfrin et al., 2013], or a Lennard-Jones (LJ) plus a Yukawa interaction [Godfrin et al., 2014; Mani et al., 2014; Sciortino et al., 2004] in order to model the spontaneous emergence of microstructured patterns in fluids.

However, already in 1999, Sear et al. [1999] made use of an empirical two exponential form, Equation 1.3, with SALR characteristics in order to explain the experimental appearance of stable microphases of nanoparticles (quantum dots) at the air-water interface.

$$\phi(r) = -\epsilon_a \frac{\sigma^2}{R_a^2} exp(-\frac{r}{Ra}) + \epsilon_r \frac{\sigma^2}{R_r^2} exp(-\frac{r}{Rr}) + u_{sr}(r) \tag{1.3}$$

This potential has been studied in depth in model systems, both in bulk and in confinement [Archer, 2008; Imperio and Reatto, 2004, 2006; Schwanzer and Kahl, 2011; Bores et al., 2015a; Lomba et al., 2014], and as a rough approximation to account for vegetation patterns in ecosystems with limited resources [Meyra et al., 2012]. We note here that the effective potential derived for our simple self-assembly mixture can be fitted to a very similar functional form, which further supports the use of this type of SALR interactions as effective potentials. We will analyze in depth the effects of confinement and disorder in the topology of the confining media on the system modeled with the interaction of Eq. 1.3 (see Figure 1.4) in **Section 3.2**.

1.2 Confinement and Adsorption processes

Fluids are often found in nature under different levels of confinement: water remaining inside the pores of the sponges, sap traveling inside capillary tubes throughout the whole plant, cell components enclosed by the cell membrane... In connection with the latter issue, confinement plays a vital role in biological mechanisms, and it seems to be a cornerstone for life emergence [Kuhn, 2008].

Historically, absorbent materials such as clays, sand, charcoal,... were used for drying, desalinating water, clarifying oil or treating certain deseases [Robens, 1994]. First references of the adsorption phenomenon are very old: they appear even in the Bible (Judg. 6:33-40); however, a systematic investigation in the field did not begin until the 18th century with the work of Fontana [1777] and Scheele [1777]. The number of technological applications of porous materials has greatly increased since then: they are widely used nowadays for drying out, separating gasses, purifying liquids and air, supporting catalytic processes, microfluidics, medicine, ... Additionally, fluid adsorption or inclusion has a relevant role in the design of new porous materials as adsorbents (using templating techniques [Nishihara et al., 2009]) and in the design of nanodevices (self-assembly under confinement).

The synthesis and tailoring [Barton et al., 1999] of porous materials have greatly progressed in recent years due to their commercial interest; however, the understanding of chemical and physical mechanisms underlying adsorption processes is still an open field of research. As atoms located on the surface of a material are not able to fulfill their bonding requirements, they are more reactive than those atoms belonging to the inner part of the material which are fully surrounded. For this reason, the surfaces of solid materials present unique properties different from those in the bulk: they are responsible for the *adsorption* process, which can be defined [Rouquerol et al., 2014a] as the "enrichment of one or more components in an interfacial layer". The porous solid with cavities or channels on which adsorption

takes place is called the *adsorbent*; and the fluid molecules immersed into those pores are the *adsorbate*.

The adsorbed molecules might exhibit unusual properties due to the geometrical constraints of the confinement they are exposed to. The previously described competition between fluid-pore and fluid-fluid interactions leads to shifts in phase coexistence curves and critical points, emergence of new transitions such as *wetting* or *layering*, variation of diffusion and viscosity values... These effects have been observed in many different systems experimentally [Gelb et al., 1999, and references therein] and also by means of computer simulation [Schöll-Paschinger et al., 2001].

Due to the critical influence of pore properties on the technological applications of porous materials, their characterization has been extensively studied [Thommes and Cychosz, 2014]. The structural information of porous materials is quantified by means of the surface area, pore volume, pore size distribution and porosity [Rouquerol et al., 1994]; all these quantities will be analyzed in more detail in **Section 2.2**. Experimental techniques [Thommes and Cychosz, 2014; Myers and Monson, 2014] such as Raman, infrared, NMR spectroscopy or X-ray and neutron scattering provide indirect evidence of the micro-structural properties of the porous media. Computational methods [Sarkisov, 2012; Sarkisov and Harrison, 2011; Gelb and Gubbins, 1998] are a complement to the experimental techniques and furnish an atomistic view of these materials that has to be made compatible with the experimental evidence.

When the pore width is of the order or a few molecular diameters (nanoscale), the dimensionality of the system is modified: the system may be forced to be almost *two-dimensional* when it is confined in a slit pore or *one-dimensional* when it is confined in a cylindrical pore. This process is becoming a very important tool for instance in the fabrication of nanomaterials by means of templates, e.g. supercapacitors or molecular sieves.

In close connection with confinement at the nanoscale, *nanoscience* and

nanotechnology involve studying and working with matter on an ultra-small scale: the scale of nanometers ($1nm = 10^{-9}m$). Richard Feyman introduced the concept behind this science in 1959 in his talk: "There's plenty of room at the bottom", at the California Institute of Technology. He envisioned the possibility of manipulate and control individual atoms and molecules, and this prediction became possible in 1981 by means of the scanning tunneling microscopy. The main interest of matter at nanoscale is that it behaves in a different manner than at larger sizes, and the new properties cannot be extrapolated from those of the bulk because they are a consequence of size confinement, predominance of interfacial phenomena and quantum mechanics [Mansoori, 2005]. Nano science has been quickly evolving since its origin, and nowadays a lot of innovative technologies and applications in other fields such as chemistry, biology, physics,... are rising driven by progress in nanotechnology [NSTC, 2000].

Types of confinement

Depending on the size of the pores, the IUPAC -International Union of Pure and Applied Chemistry- distinguishes between *micropores* (less than 2nm), *mesopores* (between 2nm and 50nm) and *macropores* (more than 50nm). Pores can be classified as *open* (if they are communicated with the external surface of the material) and *closed* (if they are totally isolated) [Rouquerol et al., 1994]. It is important to remark that the existence of inter-connected pores throughout the material allows the fluid to flow or to diffuse across the system; thus, closed pores do not contribute to the adsorption although they determine macroscopic properties of the bulk materials such as density or conductivity. In this work we have used a *percolation* model to elucidate whether the pores spread across the material or not (see **Section 2.2**).

Furthermore, the geometry of the adsorbent is a fundamental feature to

take into account before characterizing or modeling a porous system [Rouquerol et al., 2014b]. There is a distinction between materials presenting pores regularly disposed and those presenting randomly distributed pores: we call them *regular* and *disordered* porous materials respectively. Some examples of disordered and crystalline porous structures are shown in Table 1 of Ref. [Gelb et al., 1999].

Crystalline structures such as those found in zeolites, metal organic framework (MOF) materials or some nano-structured materials can be fully determined by X-ray diffraction. On the other hand, modeling the structural properties and random pore shapes present in disordered porous materials is a more difficult task: their surface roughness and topological disorder lead to a large dependence of the adsorption properties on the particular sample when carrying out computer simulations. It is necessary therefore to work with very large systems or to average over several samples in order to get results independent of the system size.

Along this work we will consider both regular and topological disordered porous media. As regular pores, we will focus on slit-pores in **Section 3.1** in order to analyze the transition from 3D systems to a two dimensional situation (which mimics and interface) and the effect of this transition on the emerging ordered nano-structures both in our simple self-assembling mixture and our realistic model for RTIL. Furthermore, molecular crystals of short-capped nanotubes and zeolites will be considered in **Section 4.1**. On the other hand, a topological disordered porous media (porous glass) will be considered in **Section 3.2** in order to illustrate the effect of the competition between confinement and disorder on the emerging nano-structures of a self-assembling fluid modeled by a SALR potential. Figure 1.5 shows the confining media employed in this work.

On the other hand, depending on the interaction between the matrix and the adsorbate, adsorption may be *specific* or *non-specific* [Kiselev, 1965]. Only a few adsorbents -such as graphitized carbon, silica gels, some zeolites and MOF solids- present non-specific interactions with a high

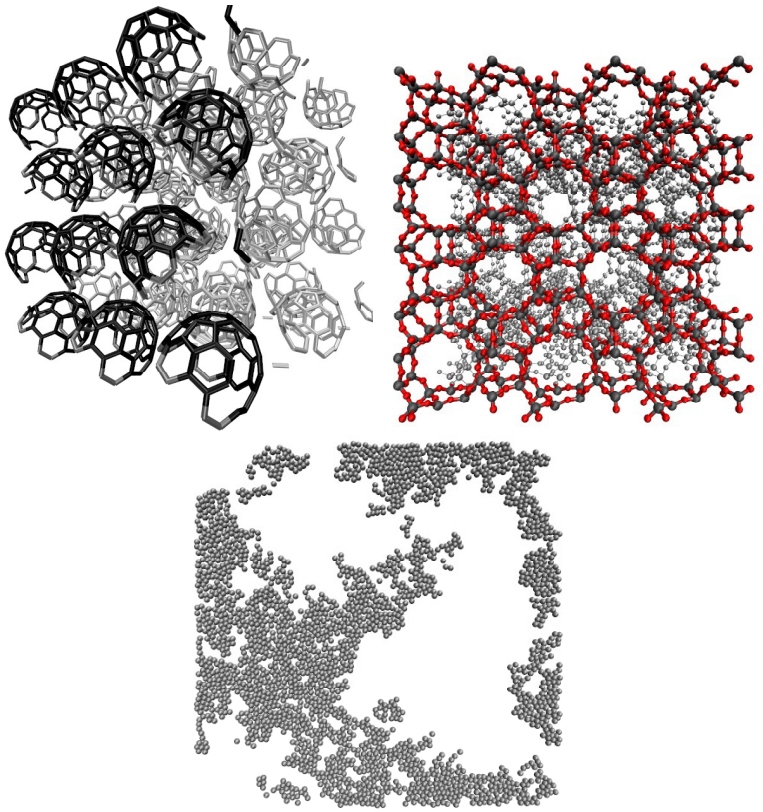

Figure 1.5: *Porous materials considered in this thesis. Crystalline porous media: molecular crystal of short-capped nanotubes (top left) and zeolite MFI (top right), versus a two dimensional model of an amorphous porous glass (bottom).*

number of molecules, i.e. the adsorption energy is little influenced by the adsorbent-adsorbate interplay but it is very similar for different adsorbed molecules. London dispersive forces, short-range repulsions and polarization terms between the adsorbent and the adsorbed molecules are non-specific interactions: in these cases the geometry and orientation of the

adsorbent and of the adsorbate are determining, and the interaction can be basically represented by a simple hard repulsion preventing the overlap between the fluid and the solid; however when specific interactions take place in the system they must be explicitly incorporated into the interatomic potentials. Extreme cases are e.g. the acid sites in zeolites due to the presence of Al cations, in particular when interacting with aromatic molecules. Modeling this type of interactions is a highly non-trivial problem [Martín-Calvo et al., 2015].

Quenched-annealed systems

As we have mentioned when referring to dense fluids, systems that lack long range order but endowed with a certain degree of local order (absent in low density gas phases) pose particular difficulties for theoretical treatments. Such is also the case for the study of adsorption in disordered materials. From a strict statistical mechanical stand point, these systems imply two kinds of averages: first a thermal average on the adsorbed fluid configurations for a given adsorbent microstate, and then an average over disorder, i.e. an average over a significative number of samples of adsorbent configurations. This approach maps the adsorption process onto the problem of a partially quenched (or quenched-annealed) mixture, in which the degrees of freedom of one of the components are frozen. This is an usual approximation for the study of adsorption (or more strictly fluid inclusions). A formal treatment of these problems within the framework of statistical mechanics was introduced by Madden and Glandt [1988] in the context of integral equation theory.

We note also that the idea of considering the adsorbent as a system of frozen particles is also the common approach when performing computer simulations, and it is the approximation we have used in this work. When considering a specific configuration of a disordered crystalline material, the effect of the adsorbent on the adsorbate can be dealt with as that of a external field. This is the standard approach in simulations (average over disorder must be implemented at a later stage) and will be of use in our theoretical treatment as well.

On the other hand, it must be noticed that the influence of the adsorbed fluid on the structure of the adsorbent material cannot be neglected in many porous materials such as in some porous glasses, activated carbons or even some zeolites [Scherer, 1986; Haines and McIntosh, 1947; Koningsveld and Tuinstra, 1989]. The development of flexible models of porous materials (see for instance [Kowalczyk et al., 2008]), able to incorporate the induced deformation, is a current challenge encouraging the development of new

theoretical, experimental and computational methods [Gor and Neimark, 2011].

Templated systems

Templating is a well stablished synthetic approach for the development of new porous materials. The basic idea is the use of a structured material as template in a mixture, which can later be removed, normally by treatment with very reactive solvents, such as hydrogen fluoride in the case of silica templates.

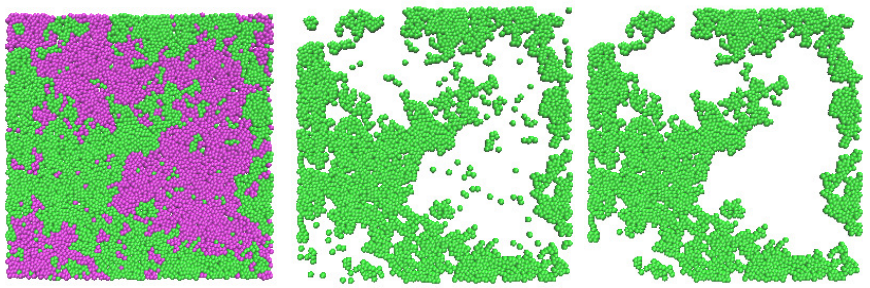

Figure 1.6: *Generation of the two dimensional porous glass model used in 3. Binary mixture of non-additive hard spheres is taken to an state near the spinodal decomposition (left), one of the components is removed (center) and the isolated particles of the matrix are eliminated (right).*

Two different approaches are possible. One typically applied for the design of controlled pore glasses, is based upon the use of a molten binary mixture (e.g. borosilicate) which is brought to conditions close to the spinodal decomposition [Siggia, 1979]. The mixture is then quenched, and the template (the silica) is washed away by means of treatment with acid. This is the typical process of synthesis of Vycor glass [Haller, 1965]. A slightly different approach is used for the synthesis of zeolite templated carbons (ZTC) [Nishihara et al., 2009]. In this case a zeolite is filled with furfuryl alcohol, which is polymerized in the zeolite channels and then carbonized at high temperature. The silica is afterwards washed away by treatment with hydrogen fluoride. In both cases one ends up with systems with high porosity and with a considerable control on the pore size of the resulting

material, though in the second case (ZTC) the pore size distribution is much narrower.

esto tambien lo dejaria para depues de introducir las ecuaciones integrales [Zhang and Van Tassel [1999] generalized the Given and Stell's replica approach to deal with templated systems of the type of Controlled Pore Glasses (CPGs), and Gelb and Gubbins [1998] have explored in detail simulation procedures that attempt to mimic the synthesis process of Vycor glasses.[

We will make use of the templating approach for CPGs to construct bidimensional topologically disordered porous systems (see Figure 1.6) whose effects on self-assembly and nano-structuring will be studied by means of computer simulation and a new theoretical approach in **Section 3.2**.

1.3 Computer modeling

Nowadays, scientist and engineers are able to tune the properties of materials -higher strength, lighter weight, greater chemical reactivity,...- manipulating them at the nanoscale. However, basic difficulties in nano science must be solved to exploit its full potential. Many applications in this field require the knowledge of the correlations between nano structures, and these remain unknown in many relevant cases. In order to improve the technologies and the applications of these innovative materials, it is necessary to know and to understand how do nano structures interact with each others. To this aim, there are sophisticated experimental techniques for manufacturing and analyzing objects in this size range: beams of electrons or ions, scanning tunneling microscopy, lithography or self-assembly. In this connection, a theoretical (or more properly computational) description of the systems at hand will be of invaluable help.

However, multiple problems arise to achieve this desired goal. Most of the equations that describe the laws of nature (from classical mechanics to

fluid dynamics including many other fields of physics) cannot be exactly solved [Thijssen, 1999]: only a few of quite simple systems (such as ideal gas or harmonic crystal) can be completely described by the theory. In our case (molecular systems in the liquid state) we must deal with a many-body problem which is also non-analytically solvable. Furthermore, if we aim to compare our theory to real systems (the number of particles in real samples is around 10^{23}), we need to take into account as many particles as possible, making the issue even harder to manage.

Some of these problems can be coped with by resorting to computational methods. When working at the microscopic level (atomistic description) they describe the atomic correlations using a variety of techniques well suited to the particular problem under study:

- *Ab initio methods:* from simple *Tight Binding* approaches to *Density Functional Theory* or more elaborated *Quantum Chemical* approximations [Fulde, 1995], these techniques aim at describing the atomic systems as a many-electron problem where the nuclei act as fixed external fields (within the Born-Oppenheimer approximation). Of great accuracy, ab initio approaches are limited to a few up to several thousand atoms depending on the level of approximation required. If the nuclei are to be considered as quantum mechanical objects (e.g. in low temperature hydrogen), then approaches as the *Path Integral* formalism [Kleinert, 2006] come to our aid.

- *Effective potentials.* These are the key elements in most applications of Statistical Mechanics for the modeling of realistic systems. Basically they are constructed by fitting more or less simple functional forms (sometimes with a physical background. e.g. in the Lennard-Jones potential), to experimental macroscopic properties, or to the results of ab initio calculations. They might include simple pair terms, or three-body contributions (e.g. Axilrod and Teller [1943] for noble gasses, Stillinger and Weber [1985] for Si, C, etc.), four-body,

or many-body contributions (e.g. embedded atom models in liquid metals cite). The number of fitting parameters is very variable, and it is sometimes connected with the transferability of the potential. It might range from the simple one-parameter hard-sphere models, to the multi-parameter AIREBO potential for hydrocarbons [Stuart et al., 2000], or the neural network many body potentials for semiconductors [Behler and Parrinello, 2007].

Once the interactions, have been defined, we need computational tools that take us from the microscopic properties characterizing atoms to the macroscopic world we are interested on. Here we will have:

- **Computer simulations**

  We will employ *Monte Carlo* (MC) techniques, based on stochastic approaches, and *Molecular Dynamics* (MD), a fully deterministic approach based on the solution of the equations of motion. Other techniques might be of use depending on the nature of the problem, such as brownian dynamics (dynamics with stochastic forces), or Lattice-Boltzmann simulations (for much longer time scales approaching the hydrodynamic regime).

  Advanced techniques of *atomistic computer simulations* are very useful to study how matter interacts at the nanoscale: these are in some cases a complement to the experimental work, but in other cases they are a guide to devise the experiments or even an alternative to them. The origin of computer simulations is correlated with the rise of electronic computing machines rise, emerged for developing nuclear weapons and code breaking during the Second World War.

  In the framework of this thesis, we have employed Monte Carlo and Molecular Dynamics methods, and we describe them in some detail

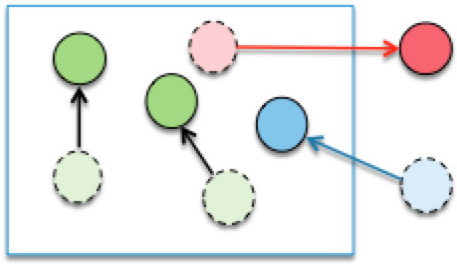

Figure 1.7: *Grand-canonical Monte Carlo scheme. Green circles and arrows represent particles displacements within the system boundaries, blue color represent insertion of a particle into the simulation box and red shows the removal of a random particle.*

in **Section 2.3**. We recall here the idea of a liquid made up of atoms or molecules interacting with each other. We can reproduce their dynamic following two different strategies: solving the equations of motion straightforwardly (Molecular Dynamics), or following a stochastic path devised to generate microscopic configurations with statistical weights defined by a given thermodynamic ensemble (importance sampling Monte Carlo). Both approaches enable us to explore the phase space in order to find all the *microstates* (set of positions and velocities of all the particles in the system) consistent with a given *macrostate* (set of thermodynamic variables that define a system: N,V,T,P,...). This is important because statistical mechanics, in order to calculate thermodynamic quantities from the microscopic information of its particles, requires to average over all these compatible microstates.

The Monte Carlo approach is a useful method for simulating fluids under confinement, specially in the grand-canonical ensemble. *Grand canonical Monte Carlo* (GCMC) implies three different kind of particle movements: displacement, insertion of a new particle and removal of a random particle in the system (see Figure 1.7). However,

when applying a GCMC scheme to confined fluids, we will encounter efficiency issues: most of the displacement and insertion trials will be rejected since they lead to overlaps with the confining medium. The solution is to perform a biased sampling of preferential areas of the simulation box avoiding overlaps with the matrix particles. This strategy is called *cavity bias* and we will describe it in **Section 2.3**. Other complementary biasing alternatives have been proposed [Snurr et al., 1993] but will not be needed for our purposes.

In the framework of Molecular Dynamic simulations, *Targeted Molecular Dynamics* (TMD) is an useful technique for studying molecular inclusions [Schlitter, 1993; Schlitter et al., 2001] to calculate binding Gibbs free energies of complexes. It introduces an external force to the classical molecular dynamic simulation that drives the *guest* particle out of the *host*: the binding Gibbs free energy of the complex is connected to the constant pressure work exerted by the external force. This method will be used in **Section 4.1** of this thesis in order to analyse the stability of Van der Waals complexes formed by short-capped nanotubes and small host molecules, and it is described in detail in **Section 2.3**. These complexes might have applications in the process of encapsulation of chemically or biologically active molecules, as well as for transport or storage of gases.

- **Theoretical approaches**

There is a wide number of theoretical tools at our disposal in this context, ranging from *Perturbation Theory*, *Classical Density Functional Theory*, or *Integral Equation Theory* (IE) [Hansen and McDonald, 1986]. In this work, we will restrict ourselves to the latter, in particular to the family of Ornstein-Zernike approaches.

The target of *Integral Equation Theories* in its Ornstein-Zernike for-

mulation is to predict the structure of the system, via the pair correlation functions (that provide information about the arrangement of particles in a fluid, as we will see in **Section 2.1**), from the knowledge of the pair potential $U_{ij}(r_{ij})$ (that describes the interactions present in the system). Thus, they aim at solving a non-linear equation like: $g(r_{ij}) = F[U(r_{ij})]$, where $g(r_{ij})$ is the pair distribution function. More sophisticated (and computationally expensive) theories can provide information on triplet correlations as well [Barrat et al., 1988; Jorge et al., 2001; Attard, 1991]. This integral equation approach has been widely used since it was proposed at the beginning of the twentieth century, to describe homogeneous monoatomic fluids such as the hard sphere fluids; and it has been extended to more complicated systems such as mixtures, molecular fluids or electrolytes [Hansen and McDonald, 1986]. Moreover, it has been also applied to inhomogeneous fluids, such as those confined in single pores (cylindrical, spherical or rectangular) [Henderson, 1992] and to anisotropic fluids [Lado and Lomba, 1998].

Beyond this, it is also possible to use the integral equation approach to describe confinement in topologically disordered porous media. Madden and Glandt [1988] considered a fluid constrained by an external field, due to the confining matrix particles, that varies according to a certain probability distribution. This system requires two types of statistical averages to be considered: a thermodynamic one over the fluid particle configurations, and another over frozen disorder, including the possible matrix configurations given by a certain probability distribution.

An alternative view of confinement processes in disordered media is to consider the quenched-annealed model: Given and Stell [1992] applied the *replica method*, originally introduced by Edwards for describing spin systems with frozen degrees of freedom [Edwards and Anderson, 1975], to these systems with frozen and disordered con-

fining matrix. This method implements a completely artificial construction, which constitutes an useful mathematical abstraction, to simplify the problem: the former system, consisting of a quenched matrix (M particles) plus an equilibrated fluid (N particles), is represented by an equilibrated mixture of N particles of the fluid plus M particles of the matrix plus $s-1$ non interacting replicas of the N fluid particles in the limit of $s \to 0$. The integral equations derived from this formalism are called *Replica Ornstein Zernike* (ROZ) -see **Section 2.3**- and has been applied to a variety of systems under disordered confinement, such as hard-sphere fluids [Lomba et al., 1993], binary mixtures [Schöll-Paschinger et al., 2001], diatomic molecules [Fernaud et al., 2001], dipolar fluids [Fernaud et al., 2003], associative fluids [Pizio et al., 1998],...

Additionally, and of special relevance to this thesis, Zhang and Van Tassel [1999] generalized the Given and Stell's replica approach to deal with templated systems of the type of Controlled Pore Glasses (CPGs), and Gelb and Gubbins [1998] have explored in detail simulation procedures that attempt to mimic the synthesis process of Vycor glasses.

Why should we pursue a new theoretical approach?

The ROZ approach yields average thermodynamic properties, fluid-fluid and fluid-matrix correlations, but if one is interested in the explicit spatial distribution of the fluid/adsorbate for a given configuration of the matrix an alternative approach is needed. Pair correlation functions cannot provide a precise information of the most likely location of fluid particles in complex confining geometries (such as zeolites or functionalized carbons) since they only furnish average probabilities over a pair of particles, either

fluid-fluid or fluid-matrix. Higher order correlations are lost.

Detailed information on the explicit spatial distribution of the fluid (adsorbate) is of paramount importance in many processes of industrial interest, such as gas storage or catalysis, and also for the understanding of many biological processes such as the catalytic activity of enzymes. The knowledge of this adsorbate distribution within the adsorbent is essential, specially when dealing with functionalized adsorbents [Wood et al., 2012]. Experimental techniques such a FTIR, NMR spectroscopy [Grahn et al., 2008; Fyfe et al., 2005] or neutron scattering [Llewellyn et al., 1993; Floquet et al., 2007] provide very valuable information in this context. Also molecular simulations allow the calculation of density maps, however it might turn into a computationally lengthy process especially when the sampling is poor due to problems of accessibility.

Therefore, the development of reliable and fast tools capable of describing explicitly and accurately the three dimensional structure of a fluid confined in porous materials is of primary interest. In this way, methods based on *Integral Equation theory* are good candidates. As we have mentioned above, ROZ -the method for dealing with fluids confined in disordered porous media in the framework of integral equation theory- does not provide information of the confined fluid at this level.

As an alternative, we may follow the prescription formulated by Beglov and Roux [1995] for describing the solvation of solutes with arbitrary geometry; this approach formulates the inhomogeneous Ornstein-Zernike equations, based on the hypernetted chain approximation (HNC), and provides the solvent structure in the external field induced by the solute. The key element here is to consider the solvent and solute as a mixture, and take the limit of infinite dilution. This methodology has been extended to molecular liquids, both polar and non-polar [Beglov and Roux, 1996; Perkyns et al., 2010; Kovalenko and Hirata, 1998], and also to solvation of small proteins [Yamazaki and Kovalenko, 2011]. In this approximation, since the solute-solvent interaction is considered as a many-body potential,

it turns out that information concerning solvent-solute correlations will be recovered beyond the pair level. This is in close connection with Attard's method [Attard, 1991] to calculate triplet correlations using the inhomogeneous Ornstein-Zernike equation and the source particle approximation [Jorge et al., 2001; Attard, 1991].

In this thesis we will explore the extension of this approach to confined systems. Actually, Beglov and Roux [1995] already applied their integral equation approach to compute the density profile of a monoatomic Lennard-Jones fluid adsorbed in a simplistic model of zeolite. We have further improved their method by including in the equations the fluid-fluid direct correlation function corresponding to the confined case, instead of using the bulk-fluid approximation as it was originally done in [Beglov and Roux, 1995]. Our approach, which combines the Ornstein-Zernike equation explicitly in 2D or 3D with the HNC closure, will be denoted by 3DOZ-HNC or 3DOZ-HNC.

We will describe the key elements of Beglov and Roux [1995] formalism and its extension to confined fluids in **Section 2.3**. Furthermore, we make use of the two and three-dimensional versions of the new approach in **Section 3.2** and **Section 4.2** for the study of the structure of a SALR fluid confined in a 2D porous glass, and for noble gases in zeolites, respectively.

Advances in Computer science

Even making use of the high calculation capabilities of today's computers, the size of the system is limited by the available storage and the execution speed. We spend a time proportional to N^2 when evaluating the forces or potential energies of a system of N particles; thus, only *small* samples ($N \leq 10000$) can be analyzed and then very long and time-consuming simulations are required to obtain statistically accurate results. Further-

more, when dealing with such small systems, there is a non-despicable amount of atoms in the surface of the system that are subject to different conditions (*surface effect*). Trying to bypass this handicap, several techniques have been developed: *potential truncation* diminishes the number of terms involved in the energy and forces calculation (when dealing with short-range interactions), *periodic boundary conditions* makes the system infinitely periodic avoiding surface effects, *neighbor lists and link-cell* approaches scale the size dependence of the calculations to 0(N),... A more detailed description of some of these techniques is presented in **Section 2.3**.

The appearance of parallel computing in 1980s resulted in a huge advance for computing science since it allows many calculations to be carried out simultaneously. Most of the current computer software for soft matter calculations make use of this advantageous technique. Progress in computer science has helped to increase the size and complexity of the systems under study, and also the time scale of the simulations. Some advances in parallel computing with a direct impact in computer simulation concern the use of *GPU*'s (graphics processing units) for molecular modeling since NVIDIA introduced in 2007 the application programming interface CUDA (Computer Unified Device Architecture) to exploit the power of modern GPU's in scientific applications [Stone et al., 2007]. In our particular case, the numerical solution of the OZ integral equations and the Molecular Dynamics of simple self-assembling systems are suitable for GPU processing with speed-ups of one to two orders of magnitude.

1.4 Systems of interest

As we have indicated in the **preface**, the goals of this research are: to analyze the effect of confinement on self-assembly fluids, to study nano-structured materials for adsorption applications, and the development of a new theoretical approach to describe the topology of adsorbates under confinement. In order to achieve these goals, several *porous media* (both regular and disordered) will be used to confine various *fluids* (from simple molecules to complex fluids exhibiting structural order emergence), and the adsorption/confinement process will be studied by means of different *computational methods* (classical simulations and theoretical approaches). Figure 1 reveals the connection between the studied systems and the goals we pursue.

In the current section we will introduce and describe all the systems that will be studied in this thesis. We will divide them into two groups: complex fluids with associative properties under confinement (**Chapter 3**) and simple fluids adsorption in nano-structured materials (**Chapter 4**).

1.4.1 Self-assembly under confinement: regular and topological disordered media

This part of the work is focused on self-assembling fluids that exhibit the emergence of ordered nanostructures at certain thermodynamic conditions. In particular we have studied three systems showing this feature, modeled with different effective potentials: First we have explored the possibility of nano-structuring in a simple model of a binary mixture where only short range interactions appear. From the nanostructured fluid configurations it is possible to extract an effective potential that exhibits the features of a SALR interaction. We have then focused on the effect of regular confinement on structural order, and its role to stabilize the nanostructures. We then turn to a more realistic model of room temperature ionic liquids, where the long-ranged interactions that stabilize the emerged patterns are

represented by electrostatic charges. Finally we have considered the SALR potential [Sear et al., 1999], where the effective interaction is modeled by a simple contribution of competing exponential functions.

1.4.1.1 A nanostructured binary fluid mixture with short-range competing interactions

As we mentioned in **Section 1.1**, the origin of nanoscale pattern formation has been attributed, in most of the cases, to the presence of short-ranged forces that originate the patterns and long-ranged forces that stabilize them. However, in **Section 3.1** we will explore the possibility of pattern formation in a system, consisting of a simple equimolar mixture of diatomic molecules and monomers, in which only short-ranged forces are present, and pattern formation emerges as a collective effect due to competing interactions between different species and/or molecular sites.

Our model system, composed of heteronuclear dimers and monomers combine attractive and repulsive potential so as to mimic the interactions present in room temperature ionic liquids, but without electrostatic forces. It consists in an equimolar fluid mixture of two different species (see Figure 1.3): a two-site dimer, AB, and a monomer, C. The dimers are represented by a two center LJ site-site potential, in which the sites are separated by a distance l. Our monomers also interact via LJ potentials. In all cases, the interactions are cut and shifted at a distance r_c, by which the explicit form of the site-site potentials is:

$$\begin{aligned} u_{ij}(r) =& 4\epsilon \left[\left(\frac{\sigma_{ij}}{r}\right)^{12} - \left(\frac{\sigma_{ij}}{r}\right)^{6} - \left(\frac{\sigma_{ij}}{r_c}\right)^{12} + \left(\frac{\sigma_{ij}}{r_c}\right)^{6} \right] \quad \text{if} \quad r < r_c; \\ u_{ij}(r) =& 0 \qquad \text{otherwise.} \end{aligned} \tag{1.4}$$

Our model is to a certain degree inspired by the simple coarse-grained model for imidazolium based room temperature ionic liquids (RTILs) of

Merlet et al. [2012b]. Thus, we will preserve the attractive/repulsive character of the interactions in the RTIL but avoiding long-ranged interactions like the electrostatic ones. In our model then, C monomers would correspond to anions and AB dimers to the molecular cations; the imidazolium ring that contains the positive charge is represented by site A, and the nonpolar tail by the larger site B. This implies that AA and CC interactions will be repulsive, BB and AC are attractive, finally BC and AB interactions are also repulsive.

We will see in **Section 3.1** to what extent this simple model, with just two sites and purely short ranged interactions can reproduce the presence of nanostructural order as found in RTILs. We will address the emergence of intermediate-range order analyzing the behavior of the partial and concentration-concentration structure factors, and performing a cluster analysis. The results obtained via our molecular dynamics simulations will be compared with those from Reference Interaction Site Model (RISM) equation calculations done by A. Perera [Bores et al., 2015b], which turn out to agree remarkably well.

We will analyze how the intermediate-range order found can be tuned by changing the density of the system, the size of B particles, and introducing electrostatic charges to our model, which get us closer to real ionic liquids. We will see that by using an Inverse Monte Carlo [Almarza and Lomba, 2003] approach, the short range attractive - long range repulsive interaction appears naturally as an effective interaction when one of the components of the mixture is effectively "integrated out". It is somewhat striking to see how the short ranged competitive interactions give rise to a very long ranged effective repulsive potential.

Nanostructuring and regular confinement

We have analyzed the effect of confinement in slit pores of systems which

exhibit nanostructuring. We will consider two systems:

A. Self-assembling simple binary mixture

In our toy model of self-assembling mixture we will analyze the change in the demixing critical temperature from the pure three dimensional limit to the 2D case, and its dependency with pore size. By means of extensive computer simulations we will analyze the changes in the nanostructuring induced by confinement and the stabilization of membrane like entities. We will see how the decrease in the degrees of freedom encourages the formation of finite versus continuum percolating structures.

B. Ionic liquids

Historically, traditional molten salts are the precursor of the room temperature ionic liquids. Currently, after decades of research on the field it has been possible to synthesize organic salts with stable liquid phases at room temperature. Among these, water-stable imidazolium cation are the most used ones. Ionic fluids are defined in the literature as salts showing a melting point below 100^oC, strong ion-ion interactions and, most of them, having organic cations and inorganic anions. Due to the possibility of mixing and changing the nature of the cations and anions, a huge amount of ionic liquids with tuned properties can be prepared. Nevertheless, they present some common properties that are unusual in other molecular liquids and that justify the importance of these unique materials [Wilkes, 2002; Ohno, 2005]. Thanks to their ionic composition, these liquids are non volatile, non flammable and thermally stable; and this together with the wide liquidus range make ionic liquids a great choice in the development of new solvents for synthesis and catalysis [Welton, 1999]. Gas separation technologies, specially for CO_2 capture, is another interesting application where ionic liquids seems to be a promising solution due to their low vapor pressure [Bates et al., 2002].

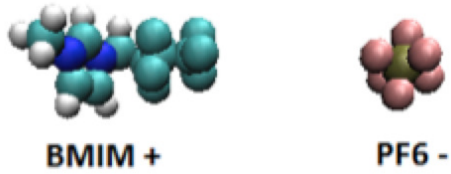

Figure 1.8: Imidazolium based ionic liquid. Left: cation. Right: anion.

In order to perform molecular simulations of ionic liquids, we require to know the particular form and parameters of the interactions between all the particles involved. This information is condensed in the force field model, and the parameters are often obtained from both experimental work and high-level quantum mechanical calculations. The 1-alkyl-3-methylimidazolium cation family (represented in Figure 1.8) are the most extensively studied ionic liquids because they are water stable and easy to prepare. In this case, force field models have greatly evolved since the first model of Hanke et al. [2001] until that of Canongia-Lopes et al. [2004], which we will employ in this thesis. Finally, also coarse grained models of these systems have been developed and successfully tested [Merlet et al., 2012b], and have inspired the simple self-assembly mixture model introduced above. Studies on this field show that structural heterogeneities appear in the special case of liquid imidazolium salts, with the heterogeneous region size depending on the length of the alkyl cation chain (see[Bhargava et al., 2008; Maginn, 2009]).

In addition, these materials are particularly interesting when they come into contact with a solid because their properties change drastically: wetting, immobilization or phase behavior modification are possible phenomena due to the interactions between the solid and the ionic fluid [Sha et al., 2012; Gobel et al., 2012; Singh et al., 2014; Sha et al., 2008].

A large amount of simulation studies on confined ionic liquids have been already performed; most of them are related with ionogels and tend to ana-

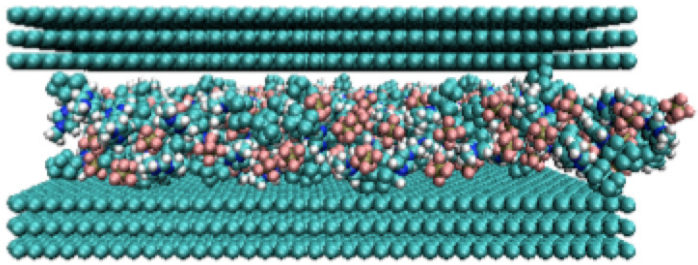

Figure 1.9: Ionic liquid confined in a slit pore whose walls consisting of three graphene layers.

lyze ionic liquids confined in complex geometries that mimic real carbon or silica porous materials [Monk et al., 2011; Rajput et al., 2014; Merlet et al., 2012a] or in nanotubes that mimic biological nano channels [Coasne et al., 2011; Singh et al., 2010]. However, there are only a few comprehensive works about the confinement of ionic liquids in simple slit pores, and most of them are focused on the electrochemical response of the ionic liquids, so the walls are usually charged or polarized trying to reproduce the complex real electrode systems [Pinilla et al., 2007; Reed et al., 2007; Fedorov and Kornyshev, 2008; Feng et al., 2009; Tazi et al., 2010; Vatamanu et al., 2010; Rajput et al., 2012a; Mendez-Morales et al., 2014].

In **Section 3.1.2.2** we will study the structural behavior of imidazolium based room temperature ionic liquids when confined in simple pores consisting in two graphitic parallel walls (see Figure 1.9). These systems correspond to a structured slit pore, and consequently is closely connected with the studies we have carried out for our simple mixture model. We have employed molecular dynamics simulations performed with GROMACS to analyze the structural order of the ionic liquid when confined in a simple slit-like pore, and in this way assess the interplay between microheterogeneity and confinement. In particular, we will explore the possibility of employing small amounts of RTIL as a wetting agent of graphitic walls in order to enhance their capabilities as adsorbent materials.

1.4.1.2 Short-attractive and long-repulsive potential (SALR)

As mentioned, a common approach for reproducing fluids with self-assembling properties is to use short-attractive and long-repulsive potentials (SALR). The origin for the long-range repulsion has been attributed to electrostatic forces (as in the case of ionic liquids in the Section above) which due to screening can be effectively represented by exponential functions as we have already said in **Section 1.1**. Moreover, as we will show with our self-assembling mixture model, these interaction can also naturally result from the effective reduction of one component in nano-structured mixtures.

In **Section 3.2** we will study the behavior or a fluid whose constituent particles will interact via a potential $\phi(r)$ consisting of a repulsive region (with a spatial extent σ) plus a tail that is attractive at short distances and repulsive at larger particle separations. Here, we have chosen a slightly modified version of the standard parameterization for this type of interaction introduced previously by Sear et al. [1999] and further studied by Imperio and Reatto [2007] among others. This potential has the shape shown in Figure 1.4 and the following functional form:

$$\phi(r) = -\epsilon_a \frac{\sigma^2}{R_a^2} \exp\left(-\frac{r}{Ra}\right) + \epsilon_r \frac{\sigma^2}{R_r^2} \exp\left(-\frac{r}{Rr}\right) + u_{sr}(r). \tag{1.5}$$

The strength and the range of the attractive and repulsive interactions of the potential tail are represented by ϵ_a, ϵ_r, σ_a and σ_r respectively; the short range repulsive part of $\phi(r)$ is given by a soft-core repulsion that replaces the hard-core term used in the original potential form Imperio and Reatto [2004] in order to ease the study of dynamic properties by means of molecular dynamics simulations.

$$u_{sr}(r) = (\frac{\sigma + \delta}{r})^n. \tag{1.6}$$

Depending on the density and the temperature this system is able to show a rich structural phase behavior, which is characterized below a certain temperature by the formation of three archetypes of mesophases: clusters (at low densities), stripes (at intermediate densities) and bubbles (at high densities). The phase behavior of this system has been extensively studied during recent years [Schwanzer and Kahl, 2010; Imperio et al., 2006; Imperio and Reatto, 2006; Archer, 2008] and quantitative structural information obtained for our particular model will be presented in **Section 3.2**. Using grand-canonical Monte Carlo simulations and integral equation theory, will study the structural and thermodynamic properties of both the bulk and the confined SALR. Besides, we will study the dynamics of this complex fluid in bulk and under confinement. We will consider a quenched-annealed system where the quenched component is a solid matrix based on a controlled porous glass model and the annealed component is the previously described SALR fluid exhibiting spontaneous aggregation.

In this case, the confinement of the fluid will be done in a controlled pore glass with relatively large but irregular cavities. Topological disorder will affect the structural features of the confined fluid in addition to the volume restrain due to the physical boundaries. Moreover, since matrix-fluid interactions will be defined as plain hard-core repulsions, we can anticipate that any deviations in the behavior of the confined fluid with respect to the properties of the bulk fluid will originate from the effects of randomness in the volume constraints, and the topology of the confining matrix.

Pore glasses are solid amorphous materials, consisting of approximately 96% of silica, that present micro and nano-metric pores. As a consequence of the rigid silica network, these porous materials exhibit a high degree of chemical, thermal and mechanical resistance. Furthermore, characteristic features of the glass such as porosity, pore size, etc can be tuned by the

thermal treatment and/or the original composition of the precursor material. The typical pore size ranges present on these materials lie between 1nm and 1μm.

As an example of a controlled pore size glass, we have borosilicate glasses whose precursors are typically mixtures of $Na_2O - B_2O_3 - SiO_2$. The production of such a porous glass is realized in what is known as the VYCOR process [Haller, 1965; Levitz et al., 1991]: after thermal treatment a glass is formed via spinodal decomposition of the molten mixture into a sodium-rich borate phase and a silica phase; once quenched in a subsequent step the silica phase is removed by treatment with hydrogen fluoride, HF, leaving a highly porous, disordered matrix.

If one aims at a quantitative prediction of such processes, it is indispensable to mimic the underlying theoretical models the features both of the matrix as well as of the adsorbed fluid as faithfully as possible. In our case, we will construct the disordered matrix model from a two-dimensional non-additive hard-sphere fluid (which shows close to its demixing critical point large concentration fluctuations), after a subsequent quenching of the particle positions and removal of one of the components. This process is depicted in Figure 1.6 and described in detail in **Section 3.2**.

Once the porous system is defined, we can compare both thermodynamic, structural and dynamic properties for the SALR fluid in bulk and confined in the pore glass. To this purpose we have employed Monte Carlo simulations in the grand-canonical ensemble; molecular dynamic simulations using the LAMMPS package for studying the dynamics of the system, together with our own MD code; and a new approach based on Integral Equation Theory which will provide detailed average density maps of the adsorbed fluids.

Finally, we have also analyzed the confinement of our simple mixture model in this disordered two-dimensional pore glass in order to compare both models.

1.4.2 Confinement in regular nano-structured materials

In **Chapter 4** we will first focus on the characterization of new nano-structured materials for adsorption applications, and on the development of new theoretical tools for the study of the distribution of adsorbents within complex porous topologies. First we will analyze a recently synthesized carbon based material (short capped nanotube) and study its ability for encapsulation small molecules, such as CS_2 and H_2. Then we will explore the feasibility of storing hydrogen on molecular crystals consisting of these nano-structures; all these results are presented in **Section 4.1**. Lastly, in **Section 4.2** we will study the adsorption of noble gasses in zeolites, systems that have already been largely studied in the last 40 years both by experimental, theoretical and simulation approaches. Our purpose in this thesis is to use these systems as a testing ground in order to assess the performance of our theoretical approach for fluids confined in three dimensional regular pore networks.

1.4.2.1 Encapsulation of small molecules in short-capped nanotubes

Carbon has been used for many different purposes since the antiquity: it was first used in the form of charcoal as a fuel by the Egyptians, in the form of graphite as a pigment, and in the form of diamond as a jewel. However, carbon also presents modern and sophisticated uses [RSC, 2014]: to cut and drill hard materials, protect surfaces, enhance the resistance of materials subject to high stress, ... and many other applications that are closely related with their adsorptive properties (such as purification, catalysis or gas storage).

Because of the varying bonding capabilities of carbon atoms, two crystalline allotropic forms of the carbon arise naturally depending on how the atoms bond to each other: graphite (sp^2 bonds) and diamond (sp^3 bonds). However, carbon exhibiting amorphous structures, without long-range or-

der, also exist (mixed sp^2 and sp^3) [Robertson, 1986]: coal, soot, carbide derived carbons, etc.

In 1985 Kroto et al. [1985] discovered the *fullerenes*: they found experimental evidence of the spontaneous self-assembly of an almost perfect spherical molecule consisting in 60 carbon atoms, which had already been theoretically predicted [Kroto, 2003]. Fullerenes discovery seemed to give rise to a new carbon allotrope, but it has been lately considered to belong to the graphite family with every carbon atom bonded to three neighbors: it can actually be seen as a rounded graphitic (graphene) carbon layer.

After this decisive finding, many carbon structures closely related to the fullerene soon emerged: onions (embeded fullerenes), giant fullerenes (spherical molecules with more than sixty carbon atoms), nanotubes... Carbon *nanotubes*, first synthesized by Iijima [1991], may be described as an elongated giant fullerene or as a curved graphene layer. All these carbon nano-structures are the cause of a science revolution because of their novel properties, far different from those of carbon structures at a larger scales.

Fullerenes have the shape of a natural molecular container due to their large inner cavity: first guests found were metal atoms, $La@C_{60}$ [Chai et al., 1991], but other components such as noble gas atoms, hydrogen molecules, clusters of metal or nonmetal atoms,... [Shinohara, 2014] were soon also encapsulated into the fullerenes. The host molecules modify the fullerene providing these compounds, *endohedral fullerenes*, with unusual properties and motivating many potential applications [Popov et al., 2013]. Nevertheless, the main drawback of endohedral fullerenes is the difficulty to extract the guest molecule: although the synthesis is possible and the component is stable, a lot of energy is needed to recover the adsorbate [Dodziuk, 2011].

Since carbon nanotubes have open edges, they minimize the problem of extracting the adsorbed substances and they are a promising material for adsorption applications. Studies about the hydrogen storage on carbon nanotubes [Dodziuk and Dolgonos, 2002] show that the content of hydrogen

at room temperatures is too low for the real application of these materials. Apart from this, carbon nanotubes exhibit amazing properties that make them popular materials: they are super strong, heat and mechanical resistant, light-weighted and exhibit a variable electronic response depending on their structure.

Actually, only one open edge is enough for extracting the guest molecule. A new carbon based material showing this feature has been recently synthesized by Scott et al. [2011] from corannulene. It is a hemispherical hydrocarbon ($C_{50}H_{10}$) with the shape of an opened fullerene or a short semi-closed nanotube: it has been called in the literature *short capped nanotube*. Furthermore, this novel material has a fixed diameter and chirality, properties that extremely affect the nanotubes behavior, and it can be used for nanotube growing acting as a template.

Fullerenes may form a crystal at certain thermodynamic conditions [Kratschmer et al., 1990] and also nanotubes self-organize into ropes [Thess et al., 1996]. Two types of pores exist in both arrangements [Shinohara, 2014]: the spaces inside the spheres (adsorption in these pores is denoted as *adsorbate@adsorbent*) and the spaces between the spheres (where adsorption is denoted as *adsorbate(adsorbent)*). Similarly, Scott et al. [2011] have also found a stable crystalline structure for short capped nanotubes and CS_2. These crystalline structures may in principle be used for adsorption applications as well as other porous solid materials like zeolites, porous glasses,... and we intend to explore its potential in this connection.

In a work in collaboration with us, Helena Dodziuk and Tatiana Korona carried out several energy and stability calculations, by means of a SAPT (symmetry-adapted perturbation theory) technique [Dodziuk et al., 2012, and references therein], of the $C_{50}H_{10}$ nanotube with a high number of different guest molecules encapsulated into the cage. As a sample, they considered monoatomic molecules (noble gas atoms), linear molecules (H_2, CS_2, CO_2,...), more complex molecules (H_2O, CH_4, ...) and many more. It was found that the complexes were predicted to be stable in all cases at

0K, but at room temperature and using simple minded finite temperature corrections only $CS_2@C_{50}H_{10}$ was stable.

Here, using more elaborate approaches, we will first assess the binding energy and thermal stability of complexes composed of short capped nanotubes with different molecules such as CS_2 or H_2, in order to evaluate its capabilities as encapsulating agents at non-zero temperatures. To that aim, we have resorted to molecular dynamics simulations for the systems in vacuum and in a solvent solution. Simple NVT simulations allow us to study the stability of the complex; and the more sophisticated techniques Targeted Molecular Dynamics (TMD) provides quantitative results for the binding Gibbs free energy.

Two different models will be used to describe the molecules. First, an all-atom approach that considers every atom present in the nano-structure: $CS_2@C_{50}H_{10}$; and secondly a united-atom model that considers the hydrogens on the edge joined to their adjacent carbon atoms defining new $C' = CH$ sites, and also the hydrogen molecule as a single molecular site $H' = H_2$: $H'@C_{40}C'_{10}$. For the interactions of the $H'@C_{40}C'_{10}$ complex we have used a new LJ effective forcefield derived from new ab initio calculations provided by R. Notario at the IQFR-CSIC.

A porous distribution analysis of the molecular crystal of $C_{50}H_{10}$ shows that this material is not amenable to be used as adsorbent of gases such as N_2, but still He or H_2 can be adsorbed. Therefore, Gran Canonical Monte Carlo simulations were carried out for molecular hydrogen adsorbed in the short capped nanotubes crystal described in [Scott et al., 2011] in order to evaluate this material's ability for H_2 storage. Additionally, we will analyze the hydrogen distribution within the molecular crystal, by means of density maps generated using extensive Molecular Dynamics simulations. All the results found for these systems are presented in **Section 4.1**.

1.4.2.2 Nobles gasses adsorbed in zeolites

In **Section 4.2** we will explore the ability of our inhomogeneous integral equation approach to provide a full three dimensional description of simple fluids under conditions of confinement in porous media. Explicitly, we will consider the case of argon adsorbed into zeolites, with a three-dimesional porous structure composed of linear and zig-zag channels of 5-8 Å diameter.

Zeolites are crystalline aluminosilicates with open 3D framework structures built of SiO_4 and AlO_4 linked tetrahedra forming a framework with cavities and channels inside where cations, water and/or small molecules may reside. They were introduced in 1954 as adsorbents for industrial separations and purifications and are used now in a variety of applications such as petrochemical cracking, water softening and purification, in the separation and removal of gases and solvents, agriculture, construction... [Corma, 1997; Smit and Maesen, 2008] thanks to their unique porous properties. More than 150 zeolites have been synthesized and about 40 natural zeolites have been identified during the past 200 years [Baerlocher et al., 2007]; in **Section 4.2** we have studied three pure silica zeolites: MFI, MEL and FAU (see Figure 1.10). The fact that we restrict ourselves to pure silica zeolites is important, since the presence of Al sites induces a charge imbalance that is compensated by OH^- groups, which considerable complicates the physicochemistry of the adsorption processes.

On the other hand, the use of noble gasses as the confined fluid is basically academic and makes possible, thanks to their molecular size and inert behavior, to analyze and characterize the porous structure acting as a reference and a testing ground.

Our system will thus be composed of Ar atoms which interact with each other and with the zeolite oxygen atoms via a LJ potential whose parameters have been taken from García-Pérez et al. [2008]: $\epsilon_{ArAr}/k_B = 124.07$K and $\sigma_{ArAr} = 3.38$Å; and for the zeolite-Ar interaction $\epsilon_{OAr}/k_B = 107.69$K and $\sigma_{OAr} = 3.15$Å, being k_B Boltzmann's constant as usual. The structure

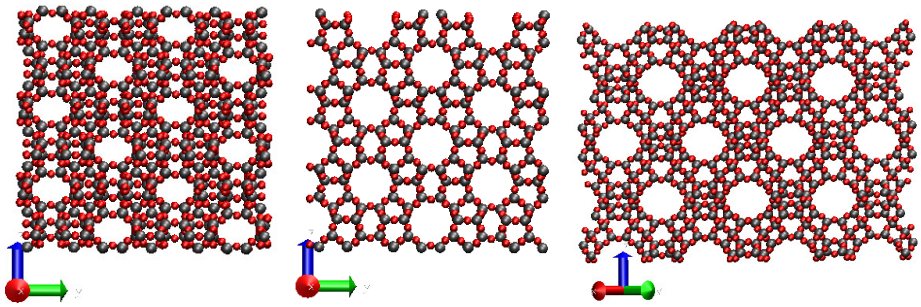

Figure 1.10: *MFI (left), MEL (center) and FAU (right) zeolites are shown. Note that the xy and xz projections of the MEL zeolites are identical, and the xz projection of the MFI zeolite is identical to that of the MEL zeolite. The projection of the FAU zeolite corresponds to the plane 110. Oxygen and silicon atoms are represented by red and grey circles respectively.*

of the three zeolites in question is illustrated in Figure 1.10 and it has been taken from [Terasaki et al., 1996; Olson et al., 1981; Baerlocher et al., 2007]. For our calculations, we have used a super-cell of $2 \times 2 \times 3$ unit cells for the MFI and MEL frameworks and one of $2 \times 2 \times 2$ unit cells for the FAU framework.

As it is customary when modeling adsorption in zeolites, if charges are not taken into account, the interaction between Ar and Si atoms is neglected, being the latter completely embedded within the oxygen tetrahedra. In the case of the faujasite framework, one must take into account that in each unit cell there are eight inaccessible cavities, large enough to host an Ar atom. Obviously, these cavities will not participate in the adsorption process, and this must be borne in mind both when running grand canonical Monte Carlo (GCMC) simulations or when building the matrix-adsorbate potential for the solution of the 3DOZ equation.

For these systems we have first solved the Replica Ornstein-Zernike

equations in the Hypernetted Chain Approximation, in order to obtain a reasonable approximation for the fluid-fluid direct correlation functions [Lomba et al., 2015]. Interestingly, the adsorption isotherms obtained from this crude integral equation approximation reproduce the simulated (and experimental) saturation behavior. From this level of approximation, we solved the 3DOZ-HNC equation obtaining adsorbate density maps and average fluid-zeolite correlations in good agreement with the studies performed by means of GCMC and long MD runs. This study of the 3DOZ performance on a realistic model of adsorbate fluid on a zeolite, closes the results sections of this thesis.

Chapter 2

Theory and Methods

Most of the times we are interested in macroscopic data like energy, temperature, pressure, ... while the information we obtain directly from molecular modeling concerns microscopic data. For this reason, we have to make use of the *Statistical Mechanics*, which connects both worlds. Key elements needed for its application in what follows can be found in standard textbooks [Hansen and McDonald, 1986; Barrat and Hansen, 2003].

On the other hand, although the nature of the systems analyzed along this thesis is diverse, all can be cast into the cathegory of fluids -simple and complex- under confinement. In **Section 2.1** we have described the characteristic features of *fluid systems* and how to analyze them; and in **Section 2.2** we have detailed how to characterize *porous media*.

Finally, **Section 2.3** deals with *computer simulation* techniques and *Integral Equation* theory, and the specific methods we have used to analyze the systems under study.

2.1 Dense fluids

The *ideal crystal lattice* model stresses the most characteristic feature of solids: their structural order. It constitutes a good approximation to describe the solid state at least as a reference state. The *ideal gas model* is the equivalent representation for modeling gasses: it emphasizes the lack of correlations between particle positions and neglects interactions. In one extreme structure plays a central role (solids), in the other (gasses) it is altogether neglected. In order to accurately describe liquid state, the analysis of the structural and the thermal features of the system is an essential point.

The **structure** of dense fluids exhibits a short-range order that distinguishes this state of the matter from the gas -where the particles positions are uncorrelated- and from the solid -where the order extends periodically to macroscopic distances. As a consequence, order in fluids will have to be described in probabilistic terms resorting correlation functions. We will see how these functions are related, how they can be computed by means of theoretical approaches and computer simulation, and very specially how they relate to thermodynamics

Dynamics. Solids are characterized by the presence of periodic long range order in the minimum of their potential energy landscape. Particles vibrate around these periodic minima, with occasional migrations of defects (vacancies or interstitial atoms). Particles in gasses move in a ballistic regime, no oscillations around potential energy minima occur. Liquids again, represent an intermediate situation. The minima of their potential energy lack long range order, but they exhibit an inherent structure in same cases reminiscent of solid phases. Particles spend a considerable amount of time within the "valleys" formed by the potential energy minima (cage effect) but they easily migrate from valley to valley, which gives rise to net particle diffusion. Bellow the glass transition temperature, this diffusive movements disappear, particles are trapped in the potential energy minima, but these lack long range order. This explains why the "glassy state" lies somewhere in between liquids and solids.

Particle time correlations will help us to classify the dynamic behavior, in particular for dense fluids which, as Brazhkin et al. [2012] pointed out, can exhibit solid-like or gas-like dynamics.

In this section we introduce different methods to analyze and characterize both the structure and the dynamics of dense fluids, stressing the peculiarities of the analysis of mixtures and self-organizing systems.

2.1.1 Structure

In this section we introduce the quantities that provide us a better understanding of the atomic structure of the fluids. As mentioned, these quantities are of statistical nature, and will provide a probabilistic view of the problem at hand.

2.1.1.1 Pair distribution function

The *particle distribution function* $g^{(n)}(\mathbf{r}^n)$ is one of the most simple examples of these microscopic quantities, and it provides a picture of the relative spatial average arrangement of the particles in the system.

This function is related with the equilibrium *n-particle density* $\rho^{(n)}(\mathbf{r}^n)$, that is defined as the probability of finding n particles in the volume elements $d\mathbf{r}_1, ..., d\mathbf{r}_n$ and all the possible permutations. Actually, considering interacting particles, there would always be some correlation between their positions: *n-particle distribution function* $g^{(n)}$ is defined as a static correlation function of the *n-particle density*:

$$g^{(n)}(\mathbf{r}^n) = \frac{\rho^{(n)}(\mathbf{r}^n)}{\prod_{i=1}^{n} \rho^{(1)}(\mathbf{r}_i)},$$

where the denominator represents the n-particle density for independent particles. This quantity provides a measure of the deviation from the randomness: if particles are statistically independent (uncorrelated particles) -e.g. they are separated enough so they do not feel each other- $g \equiv 1$.

The second-order correlation function (usually called *pair distribution function*, *PDF*) is the most representative one: it gives the probability that, given a fixed particle in $\mathbf{r}_i$, there be another particle in $\mathbf{r}_j$, scaled with that of an ideal gas:

$$g^{(2)}(\mathbf{r}_i, \mathbf{r}_j) = \frac{N(N-1)}{\rho^2} \frac{\int exp[-\beta U_N(\mathbf{r}^N)] d\mathbf{r}^{(N-2)}}{Z_N}. \tag{2.1}$$

In the particular case of isotropic and homogeneous systems it is a function only of the separation $r_{ij} = |\mathbf{r}_i - \mathbf{r}_j|$ and we should notice that $4\pi\rho g(r) r^2 dr$ is the number of particles located in a spherical shell of width dr around the particle fixed in the position r. For a system of N particles, Eq. 2.1 transforms into [Hansen and McDonald, 1986, p. 39]:

$$\rho g^{(2)}(r) = \frac{1}{N} \langle \sum \sum_{i \neq j}^{N} \delta(r - r_{ij}) \rangle, \tag{2.2}$$

where $< ... >$ denotes an ensemble average. This equation serves as a basis to implement the estimation of pair distribution functions in computer simulation. Once properly discretized, Eq. 2.2 reads:

$$\rho g^{(2)}(r) = \frac{1}{N} \frac{1}{4\pi r^2 \Delta r} \times \left\langle \sum_{i}^{N} \sum_{j}^{N} H(r_{ij} - r + \Delta r/2) H(r - r_{ij} + \Delta r/2)(1 - \delta_{ij}) \right\rangle, \tag{2.3}$$

where ¡...¿ denotes an average over particle configurations. The product of the *Heaviside step* functions will contribute to the PDF value only if both of them are one, and this occurs for $r + \Delta r/2 > r_{ij} > r - \Delta r/2$.

- **Total correlation function and OZ integral equation theory**

  When calculating the structure factor (see Section below) one must eliminate the forward scattering, and the remaining part contains the Fourier Transform of the function:

$$h^{(2)}(\mathbf{r}_{12}) = g^{(2)}(\mathbf{r}_{12}) - 1 \tag{2.4}$$

  which vanishes for large separations and accounts for the particle correlations. Therefore it is called *total correlation function.*

  As we will see in **Section 2.3**, the Integral Equations theory of fluids connects the correlation functions between the particles with the interatomic potential that describes the system. In this thesis, we have worked in the framework of the Ornstein-Zernike theory, and in this approach the total correlation function is calculated as the sum of two different contributions: the direct part, given by the *direct correlation function* between particles 1 and 2 ($c(r_{12})$ which is closely connected with the interaction potential) and the indirect part, that represents correlations mediated by one or more particles in the fluid (see Figure 2.1), namely:

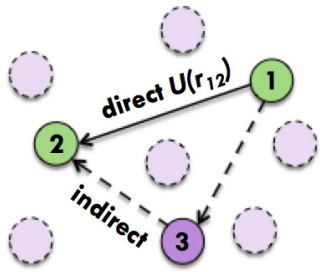

Figure 2.1: *Diagram showing the influence of particle 1 on particle 2. Solid arrow represents the direct correlation, given by the interacting pair potential $U(r_{12})$; dotted arrows represent the indirect correlation mediated by the rest of the particles.*

$$h(\mathbf{r}_{12}) = c(\mathbf{r}_{12}) + \int c^{(2)}(\mathbf{r}_{13})\rho^{(1)}(\mathbf{r}_3)h^{(2)}(\mathbf{r}_{32})d\mathbf{r}_3 \qquad (2.5)$$

The functions $h(r)$ and $c(r)$ can be further related performing a diagrammatic expansion in terms of the one particle density and Mayer bonds ($f(r) = \exp(-\beta U(r)) - 1$) which after grouping and renormalization [Hansen and McDonald, 1986] gives:

$$h(r) = \exp(-\beta U(r) + h(r) - c(r) + b(r)) - 1 \qquad (2.6)$$

where U(r) is the pair interaction and b(r) is the so-called *bridge function*, making a reference to its first diagram which recalls the shape of the Wheatstone bridge. Different approximations (*closures*) can be formulated depending on how $b(r)$ is approximated. The most straightforward one is the Hypernetted Chain approximation (HNC), with reduces to $b(r) = 0$. The well known Percus-Yevick relation can be simply derived from the HNC by linearization of the exponential (by which $b(r) \neq 0$). Many other alternatives can be defined if $b(r)$ is taken from a well defined reference system, e.g. hard sphere fluid (Reference HNC) [Lado et al., 1983], or using parametric closures and imposing thermodynamic consistency conditions (e.g. HMSA [Zerah and Hansen, 1986]).

2.1.1.2 Structure Factor

Experimentally, it is possible to determine the pair distribution function directly from imaging techniques [Kepler and Fraden, 1994; Crocker and Grieg, 1996]; however, the most common way is to calculate it from the *structure factor*, $S(\mathbf{k})$, which is determined via radiation diffraction experiments [Barrat and Hansen, 2003]. The choice of the radiation source is determined by the resolution of the particular measure: X-ray and thermal neutron are fit for molecular scale studies because their wavelength is of the order of angstroms. Thus, the structure factor is defined in terms of scattered intensity from the liquid as: $S(k) = I(k)/Nf^2$, where $k = 4\pi sin\theta/\lambda$,

I(k) is the intensity, θ the reflection angle and λ the wavelength of the scattered radiation, N is the total number of atoms and f is the atomic scattering factor in the case of X ray scattering, or the scattering length for neutron diffraction.

From a theoretical point of view, $S(\mathbf{k})$ can be defined as the autocorrelation function of the one-particle density Fourier transform $\rho_{\mathbf{k}}$: $S(\mathbf{k}) = \frac{1}{N} < \rho_{\mathbf{k}}\rho_{-\mathbf{k}} >$, where we have simply assumed all the scattering lengths equal to one. This expression would be useful to analyze correlations in Fourier space, e.g. divergences for finite k associated with periodic order, but when comparing with experiment, then the scattering lengths or form factors must be explicitly taken into account. Expanding the last expression, the structure factor ends up being the Fourier transform of the radial distribution function [Hansen, 1986, p. 98], which once forward scattering is removed leaves for the atomic structure factor of a homogeneous and isotropic system:

$$S(\mathbf{k}) = 1 + \rho \int \exp(-i\mathbf{k}\cdot\mathbf{r})h(\mathbf{r})d\mathbf{r}.$$

In the case of a monoatomic fluid we can integrate over the angles by which [Fischer et al., 2006]:

$$S(k) = 1 + 4\pi\rho \int_0^\infty h(r)r^2 \frac{\sin(kr)}{kr} dr. \tag{2.7}$$

The discrete integration *rectangular* method is used to calculate numerically the last expression [Evrard and Pusztai, 2005]:

$$S(k) = 1 + \frac{4\pi\rho}{k} \sum_{i=0}^{i_{max}} h_i \int_{r_i}^{r_i+1} r\sin(kr)dr, \tag{2.8}$$

where h_i is considered to be constant on each range $\Delta r = [r_1, r_{i+1}]$ and the integrals may be computed analytically.

Alternatively, along a computer simulation, the structure factor can be calculated by direct evaluation using the definition of the density self-correlation, i.e.

$$\begin{aligned} S(\mathbf{k}) =& \langle (\sum_i e^{-i\mathbf{k}\mathbf{r}_i})(\sum_i e^{i\mathbf{k}\mathbf{r}_i})^* \rangle = \\ &= 1 + \langle \frac{1}{N} | \sum_i e^{-i\mathbf{k}\mathbf{r}_i}) |^2 \rangle. \end{aligned} \tag{2.9}$$

Notice that in our simulations we will use a periodic box of sides (L_x,L_y,L_z), which must be consistent with the $\mathbf{k}$ vectors that must reflect the periodicity of the sample. This implies that the allowed values of $\mathbf{k}$ are ($\frac{2\pi n_x}{L_x}, \frac{2\pi n_y}{L_y}, \frac{2\pi n_z}{L_z}$), with n_x, n_y and n_z integers. These formulas are needed whenever the range of the computed $h(r)$ is short, and the numerical evaluation of Eq. 2.8 introduces artificial ripples in the short range of $S(k)$, and of course in the presence of inhomogeneities or anisotropy.

- **Structure Factor for mixtures**

  The definition of the $S(k)$ introduced above is easily extended to the case of multicomponent systems. In these situations we can calculate the partial contribution of each component to the total structure factor, by summing over only the number of particles of every specie. Thus, if we consider a homogeneous system consisting of N_ν particles of species ν (with $\nu = 1$ to n), in such a way that the total number of particles is $N = \sum_\nu N_\nu$ and the concentration of the specie ν is $x_\nu = N_\nu/N$, the related partial structure factor $S_{\nu\mu}(\mathbf{k})$ is given by:

$$S_{\nu\mu}(\mathbf{k}) = x_\nu \delta_{\nu\mu} + x_\nu x_\mu \rho \int exp(-i\mathbf{k}\cdot\mathbf{r}) h_{\nu\mu}(\mathbf{r}) \mathbf{r}$$

  The total structure factor is defined as a linear combination of these partial contributions: $S(\mathbf{k}) = \sum_{i=1}^{N_\mu} \sum_{j=1}^{N_\nu} S_{ij}(k)$. It tends to one as

k tends to ∞ while each partial structure factor tends to its corresponding species mole fraction.

In the case of binary mixtures ($\nu = 1$ or 2), the approach introduced by Bathia and Thornton [1970] is specially important: They have defined a set of linear combinations of the partial structure factors, $S_{\nu\mu}(\mathbf{k})$, which are related with the fluctuations in number density and concentration of the system:

$$S_{NN}(\mathbf{k}) = \frac{1}{N} < \rho_k^N \rho_{-k}^N >$$
$$S_{NC}(\mathbf{k}) = \frac{1}{N} < \rho_k^N \rho_{-k}^C >$$
$$S_{CC}(\mathbf{k}) = \frac{1}{N} < \rho_k^C \rho_{-k}^C >$$

The last of these quantities is called *concentration-concentration structure factor* and it is expressed, for a binary mixture, in terms of the $S_{\nu\mu}(\mathbf{k})$ as follows:

$$S_{CC}(\mathbf{k}) = x_2^2 S_{11}(k) + x_1^2 S_{22}(k) - 2x_1 x_2 S_{12}(k) \tag{2.10}$$

It describes the chemical order in the fluid and fluctuates around $x_1 x_2$. Furthermore, its low k limit is related with the demixing phase transition (which will be introduced below, in Section 2.1.2) in such a way that for an ideal mixture $S_{CC}(0) = x_1 x_2$, but for real mixtures, when approaching the critical point (temperature, concentration, and total density) the fluctuations of the concentration become macroscopic in range, and $S_{CC}(\mathbf{k})$ diverges as $k \to 0$. Large values or divergences for $k \neq 0$ indicate the presence of compositional quasiperiodic or periodic spatial patterns.

2.1.1.3 Clustering analysis

In computer experiments, it is sometimes desirable to identify the presence of clusters and their size distribution. Clusters are more or less long lived aggregates of particles. Particles are considered to belong to a given cluster when their separation is below a given threshold (distance criterion) or their interaction energy is lower than certain value (energy criterion) or both. Since $g(r)$ and $S(k)$ show the correlations between the particles of the system, these quantities should allow us to identify the presence of aggregated states -where the particles are not homogeneously distributed but they are forming certain patterns.

In a $g(r)$ graph the presence of clusters in fluid systems appears as a long-range extended correlation: i.e., beside the peaks at short distances, related with the correlation between individual components, there should be also broad peaks at higher separations due to the particle aggregates. The distance between these peaks yields a rough estimation of the distance between clusters and the peak widths are connected to their size. According to the definition of the wave vector, long-range correlations between the atoms with features observable at r_{cl} will affect the low k region of the structure factor with new features emerging at $k_{cl} = 2\pi/r_{cl}$. Thus, the existence of particle aggregation is typically associated with a pre-peak at low k region in $S(k)$, whose position informs us about the inter cluster separation.

In spite of the usefulness of the correlation functions in order to detect the presence of particle aggregation in a system, other quantities beyond pair correlations are needed to fully describe the structure and the evolution of the clusters in the system. To this aim, we will perform a *geometric cluster analysis* and calculate the *cluster size distribution.*

The definition of a *cluster* C is somewhat arbitrary; here we will define it as a set of particles topologically connected, i.e. the distance from a neighbor within the cluster is less than a critical distance r_{cl}, called *link distance.* This condition may be mathematically expressed: if $i \in C$ and

$r_{ij} \leq r_{cl}$ then $j \in C$, where r_{ij} is the distance between particles i and j. This last definition was used in [Stoddard, 1978] and is equivalent to that introduced by Stillinger [1963]. Again the choice of the distance r_{cl} is not unique, in [Stillinger, 1963] the author selects half the distance at which the inter-particle potential vanishes. However one does not always know the shape of the effective potential of a fluid, in these cases it is appropriated to choose r_{cl} as the distance at which the first minima of the radial distribution function occurs.

In the case of periodic systems (e.g. simulations with PBC), we have performed clustering analysis based on the algorithm given in [Bunz, 1986], that allows us to count the number of atoms belonging to the same cluster, i.e. the *cluster size* (s). We may represent the results obtained from the former analysis as a histogram of cluster sizes, $n(s)$. However, this quantity is biased towards smaller cluster sizes and it is not an appropriate function to describe the state of the major part of the particles in the system: If half the system particles, N_p, are forming a huge cluster and the rest are isolated monomers, $n(s)$ will exhibit two peaks weighted with the number of cluster of each size, thus the peak at size one will be $N_p/2$, much bigger than that at size $N_p/2$ that will be 1.

For this reason we will use the normalized function that was proposed by Stauffer [1979] and used in [Chen et al., 1994; Godfrin et al., 2013, 2014], $N(s)$, which we will call *Normalized cluster size distribution*:

$$N(s) = (\frac{s}{N_p})n(s). \tag{2.11}$$

This function represents the average fraction of particles contained in clusters of size s, and it thus provides a balanced information on the clustering distribution.

2.1.2 Thermodynamics and phase transitions

An isolated system in stable thermodynamic equilibrium is characterized by a maximum in the entropy: $dS = 0$ and $d^2S < 0$; and it can be described with a set of thermodynamic quantities such as the internal energy U, the volume V, ... In principle, the thermodynamic formalism we will be dealing with is designed to describe systems in equilibrium.

A stable and homogeneous system always satisfies the stability criteria, whose physical meaning is contained in *Le Chatelier principle* (or *Equilibrium Law*): whenever a spontaneous process disturbs a system in equilibrium, the system will adjust itself in such a way that the effect of the change will seek the equilibrium restoration [Callen, 1981]. The stability criteria equations are:

$$\left(\frac{\partial T}{\partial S}\right)_V = \frac{T}{c_V} > 0 \ ; \ -\left(\frac{\partial P}{\partial V}\right)_T = \frac{1}{V\chi_T} > 0, \tag{2.12}$$

where c_V is the *specific heat* at constant volume and χ_T the *isothermal compressibility* (these quantities are named *response functions* because they measure the response of the system to certain stimulus) [Stanley, 1971]. If we take into account that for an equilibrium system (or a quasi-static process) $dQ = TdS$ -being dQ the heat exchanged in the process-, then the first stability criterion states that a heat supply in a system leads to a temperature increase. The second criterion (r.h.s. of Eq. 2.12) means that at constant temperature, applying pressure on a system must decrease its volume.

However, when the stability criteria are not fulfilled, the system looses its homogeneity and it separates into two or more parts through a *phase transition*. During a fluid liquefaction, near the *critical* point, small pressure variations lead to a large rise in the molar volume, $V_m = V/N$. This behavior causes a divergence of isothermal compressibility: $\kappa_T = -1/V(\partial V/\partial P)_T = \infty$.

On the other hand, when multicomponent systems, such as binary mixtures, do not satisfy the stability criterion, they separate into phases with different composition. This *phase separation*, also called demixing transition, is characterized with large concentration fluctuations. There are different *order parameters*, i.e. quantities that are zero in the stable homogenous phase, and change when a given symmetry of the system is broken. These quantities characterize every phase separation: L-V transition is linked with the density difference $\rho_l - \rho_v$, and demixing transition in a symmetric binary mixture with $x = 1/2 - x_A$, being x_A the mole fraction of one of the components. If we represent the phase diagram in terms of the temperature as a function of the density (for LV transition) or the concentration (for demixing transition in mixtures), we may represent all the points corresponding to equilibrium states between both phases with a line called *binodal* or *coexistence* curve, which delimits the region where a stable system may start to phase separate (indicated by $\partial G/\partial \phi = 0$, where G is Gibbs energy and ϕ the order parameter). Inside this region there might be metastable states until one reaches the limit of stability (set of points where $d^2G/d\phi^2 = 0$) called *spinodal* curve. All the states between both lines are metastable, and within spinodal curve only unstable points may be found. Spinodal decomposition is clearly a non-equilibrium process through which a thermodynamic unstable state decomposes into two stable phases.

Thermodynamics and structure

Thermodynamic variables, together with the equation of state, define the state of the system; they remain invariant in time, if the system is in equilibrium, and in space, if the system is homogeneous. Once the system structure is known, one may determine several thermodynamic properties, such as the pressure, chemical potential or the isothermal compressibility, through the relatively simple equations we present here below for the

isothermal compressibility.

Pressure and radial distribution function are connected through the virial equation expressed for simple fluids interacting via pair potentials as follows [Hansen and McDonald, 1986, p. 35]:

$$\beta P = \rho - \frac{2\pi}{3}\beta\rho^2 \int_0^\infty \mathbf{r}\nabla U(r) g(r) r^2 dr. \tag{2.13}$$

The excess internal energy is related whit the structure in a pairwise interacting system by means of:

$$\beta U^{ex} = 2\pi\rho \int_0^\infty U(r) g(r) r^2 dr. \tag{2.14}$$

As to the chemical potential, it can be determined by means of Kirkwood's charging procedure, namely:

$$\mu^{ex} = \rho \int_0^1 \frac{\partial U(\mathbf{r}_{12};\lambda)}{\partial\lambda} g(\mathbf{r}_{12};\lambda) d\lambda d\mathbf{r}_1 d\mathbf{r}_2, \tag{2.15}$$

where $U(\mathbf{r}_{12};\lambda)$ is the interaction potential between a probe particle and bulk fluid whose interaction potential is $U(\mathbf{r_{12}})$. $U(\mathbf{r}_{12};\lambda = 0) = 0$ and $U(\mathbf{r}_{12};\lambda = 1) = U(\mathbf{r_{12}})$. In principle the parametric dependence on λ can be linear.

In order to integrate Eq. 2.15 we must know the dependence of $g(\mathbf{r}_{12};\lambda)$ on $U(\mathbf{r}_{12};\lambda)$, or perform a full thermodynamic integration, e.g. performing a series of simulations for systems with different values of λ [1]. From a theoretical point of view one can make use of an approximation such as the

[1] In practice in simulation one usually applies Widom's insertion method [Frenkel and Smit, 2002].

HNC (Eq. 2.6 with $b(r) = 0$) and perform the integration analytically to obtain:

$$\beta\mu^{ex} = -\rho \int c(r) d\mathbf{r} + \frac{1}{2}\rho \int h(r) \left(h(r) - c(r)\right) d\mathbf{r}. \tag{2.16}$$

On the other hand, the isothermal compressibility χ_T is related to fluctuations in an open system. Thus, the *compressibility equation* connects this quantity with the correlation functions in the grand canonical ensemble :

$$\begin{aligned} \frac{\rho\chi_T}{\beta} = \frac{< N^2 > - < N >^2}{< N >} &= 1 + \rho \int [g(\mathbf{r}) - 1] d\mathbf{r} \\ &= \left[1 - \rho \int c(\mathbf{r}) d\mathbf{r}\right]^{-1}. \end{aligned} \tag{2.17}$$

We can derive, from this equation and the structure factor definition (Eq. 2.7), the limit of the structure factor at $k = 0$:

$$S(0) = \frac{\rho\chi_T}{\beta}. \tag{2.18}$$

The behavior of the structure factor at low k provides important information. Actually, taking into account Eq. 2.12, it will describe how close we are to a spinodal decomposition. If the system is close to a phase transition, certain domains arise where quantities such as density strongly differ from the average values. These long ranged fluctuations lead to large isothermal compressibility values also reflected in increasing values of $S(k)$ at $k = 0$, which when dealing with light scattering is the visible range is known as critical opalescense.

In the case of mixtures the isothermal compressibility may be expressed in terms of the partial structure factors through this relation:

$$\rho k_B T \chi_T = \frac{|\mathbf{S}(0)|}{\sum_{ab} (x_a x_b)^{1/2} |\mathbf{S}(0)|_{ab}}, \tag{2.19}$$

where the components of the matrix $\mathbf{S}(0)$ are the partial structure factors at $k = 0$; $|\mathbf{S}(0)|$ is the matrix determinant and $|\mathbf{S}(0)|_{ab}$ are the cofactors of each element $S_{ab}(0)$.

The expressions for pressure, internal energy and chemical potential can easily be extended to mixtures [Anta, 1997].

2.1.3 Dynamics

Studying the motion of the fluid constituents over the time provides information on dynamic and transport properties. Three different regimes exist in the dynamics of a fluid depending on the value of the time of the measurement and the sampling distance, compared to the *mean collision time* τ and the *mean free path* l respectively: short times and distances represent the *free-particle* regime (particles move almost independently of each other), times and lengths comparable to τ and l constitute the *kinetic* regime (provides information at a molecular level) and large times and lengths are related to macroscopic processes such as transport or flow and correspond to the *hydrodynamic* regime.

Dynamical properties of fluids are described by means of the time-correlation functions, which show how positions or velocities of the particles in the system are affected by one another after a period of time Δt [Hansen, 1986, C. 7]. Some important time-dependent functions, that help us to analyze the dynamic of fluids are described in the following sections. The discretization and adaptation of these quantities, in order to calculate them in the context of computer simulation, have been done using the algorithms given by Rapaport [Rapaport, 2004].

2.1.3.1 Mean square displacement

The *mean square displacement*, *MSD(t)*), [Balucani and Zoppi, 1994, p. 20] is the squared average displacement of a particle from a given origin to a time t, i.e.

$$MSD(t) =< [\mathbf{r}_i(0) - \mathbf{r}_i(t)]^2 > . \tag{2.20}$$

In the case of liquids, the shape of this function shows different behavior depending on the time scale we are considering: for very short times the MSD increases quadratically with time as it corresponds to a free particle; and for large times, (typical of the diffusive regime) it has a linear shape. The slope of $MSD(t)$ for long times is connected to the *diffusion coefficient*, D, by:

$$\lim_{t\to\infty} \frac{d}{dt} MSD(t) = 2dD, \tag{2.21}$$

where d is the dimension of the system, and thus $MSD(t) = 2dDt$ for $t \to \infty$, which is known as *Einstein relation.*

2.1.3.2 Velocity autocorrelation function

The *velocity autocorrelation function* [Egelstaff, 1992, C. 12], $\tilde{Z}(t)$, correlates the velocity of certain atom i at a time $t = 0$ with its velocity at a later time t:

$$\tilde{Z}(t) = \frac{1}{d} < \mathbf{v}(0)\mathbf{v}(t) > . \tag{2.22}$$

The value of $\tilde{Z}(t)$ at $t = 0$ is $\tilde{Z}(0) = k_B T/m$ due to the energy equipartition theorem. $\tilde{Z}(t)$ for very long times tends to 0 since final and initial velocities are completely uncorrelated.

Since $\mathbf{r}(t) - \mathbf{r}(0) = \int_0^t \mathbf{v}(t')dt'$, $\tilde{Z}(t)$ and $MSD(t)$ are closely connected, and their relation, for very long times, becomes:

$$MSD(t) = 2\int_0^t d\tau < \mathbf{v}_i(0)\mathbf{v}_i(\tau) > . \tag{2.23}$$

This leads another definition of the *diffusion coefficient*: $D = \int_0^\infty \tilde{Z}(s)ds$ where s is the time interval. In other words, D is the area under the $\tilde{Z}(t)$ curve.

Another relevant function for studying fluids dynamics is the Fourier transform of $\tilde{Z}(t)$:

$$Z(\omega) = \frac{1}{2\pi d}\int_{-\infty}^{+\infty} < \mathbf{v}(0)\mathbf{v}(t) > e^{(-i\omega t)}dt, \tag{2.24}$$

which means that $D = Z(0)$. This quantity is known as the frequency spectrum of the system, and its structure reflects translational movements, rotations and very specially intramolecular vibrations. It can be compared with infrared and Raman spectra -but these have selection rules (by which some vibrations are absent)- and very specially with the spectra obtained from inelastic neutron scattering experiments (INS).

2.1.3.3 Dynamic structure factor

The *Van Hove distribution function* $G(\mathbf{r}, \tau)$, which is a generalization of the pair distribution function described in the Section 2.1.1.1, gives the probability of finding an atom at position r_2 and time t_2 if there was an atom at r_1 and t_1. It may be expressed as the time correlation of the

particle density function $\rho(\mathbf{r},\tau) = \sum_i \delta[\mathbf{r} - \mathbf{r}_i(\tau)]$:

$$\begin{aligned} G(\mathbf{r},\tau) =& \frac{1}{\rho} < \rho(\mathbf{r}' + \mathbf{r},\tau)\rho(\mathbf{r}',0) >= \\ & \frac{1}{N}\left\langle \sum_i \sum_j \delta(\mathbf{r} + \mathbf{r_j}(\mathbf{0}) - \mathbf{r_i}(\tau)) \right\rangle \end{aligned} \tag{2.25}$$

It is often more convenient to consider the density-density autocorrelation function of the Fourier component ρ_k, i. e. the *intermediate scattering function*, and its spectrum, the *dynamic structure factor*:

$$F(\mathbf{k},t) = \int G(\mathbf{r},t)\exp(-i\mathbf{kr})d\mathbf{r} \tag{2.26}$$

$$S(\mathbf{k},\omega) = \frac{1}{2\pi}\int F(\mathbf{k},t)\exp(-i\omega t)d\mathbf{r} \tag{2.27}$$

The dynamic structure factor is closely connected with the experimental measurements of the inelastic scattering of slow neutrons or scattering of electromagnetic radiation [Egelstaff, 1992, p. 178], and it informs us about single-particle and collective dynamics of the fluid through its limiting behavior as $k \to \infty$ and $k \to 0$ respectively.

Now, these expressions can be split into "self" and "distinct" components with:

$$\begin{aligned} G_s(\mathbf{r},t) &= \frac{1}{N}\langle \sum_i \delta(\mathbf{r} + \mathbf{r}_i(0) - \mathbf{r}_i(t))\rangle \\ G_d(\mathbf{r},t) &= \frac{1}{N}\langle \sum_{i\neq j} \delta(\mathbf{r} + \mathbf{r}_j(0) - \mathbf{r}_i(t))\rangle \end{aligned} \tag{2.28}$$

and hence:

$$G_s(\mathbf{r},t) + G_d(\mathbf{r},t) = G(\mathbf{r},t) \tag{2.29}$$

with similar definitions for $F_s(\mathbf{k}, t)$, $F_d(\mathbf{k}, t)$ and $S_s(\mathbf{k}, t)$, $S_d(\mathbf{k}, t)$.

2.2 Porous Materials

The features of the particular porous material are crucial for adsorption and confinement processes, for this reason we need a comprehensive knowledge of the adsorbent system's nature before analyzing the arrangement, movement and behavior of the fluid adsorbed in it. Characterization of such materials has been therefore highly developed during the last years with two main aims: to optimize their adsorption qualities, and to improve certain features of the adsorbed substances. While from the experimental point of view there are numerous techniques, in the case of model systems we would like to mention Poreblazer [Sarkisov and Harrison, 2011] as an useful software that provides porous media structural characterization, pore size among other properties. This software performs a geometric characterization of the material model based on connectivity analysis and various volume and suface stochastic integration methods. We will deal with porous materials characterization in **Section 2.2.1**.

In addition, the knowledge of the confined fluid structure is an essential feature to understand adsorption mechanism and then to improve it. Experimental techniques such as Raman, Infrared or Nuclear magnetic resonance spectroscopies, and X-ray and neutron diffraction provide indirect information to elucidate adsorbate structure; moreover, simulation and theory provide direct information about this issue. We will see how to describe the fluid into the confining medium in **Section 2.2.2**

2.2.1 Characterization of Porous Solids

Properties such as the adsorbent geometry, the size and the shape of the pores, the area of the pore walls, the surface chemical structure and the

interaction with the adsorbate are features that greatly determine the effects of confinement and adsorption processes. This analysis is particularly relevant for disordered (non-crystalline) porous materials, since contrary to what happens in e.g. zeolites, here the specific positions of the constituents particles are unknown.

- **Pore Size**

  Most of the times the best approach is to classify porous solids depending on the pore size rather than on the chemical nature of the material. Certain amorphous porous solids, which exhibit random surface topology, are characterized by a fixed porosity or pore size. For instance, porous glasses are manufactured in a controlled way and it is possible to select a specific value of the pore size by fixing some parameters during the production process. In these cases, it is necessary to reproduce this property when modeling the porous materials.

  Pore size is generally determined by the pore width that is taken as the distance between opposite walls. In the case the pore presents a non uniform shape, pore size is determined by the smallest dimension of the cavity that is the limiting distance for adsorption. From the experimental point of view, pore sizes as estimated by analyzing the volumetric adsorption isotherms of probe molecules (He, H_2,...).

- **Accessible volume and Porosity**

  The *accessible volume* is defined as the volume that the matrix particles leave for the fluid to move in and that percolates throughout the sample. This means that a fluid particle can in principle diffuse through the sample and reach any point within the accessible volume. We hence discard all isolated cavities. This quantity is calculated

experimentally by performing volumetric adsorption experiments using normally N_2 and He as probe molecules, applying the T-method [Rouquerol et al., 2014b]; however, in the case of computer simulation, where we fully know the atomistic geometry of the system, a Delaunay tessellation allows us to assess the value of this quantity and also to characterized the pores. Delaunay tessellation consists in a triangulation study, purely geometric, that decomposes the system in different non-overlapping regions completely filling the volume and taking as vertices (*Delaunay-vertices* or *D-vertices*) the center of mass of our matrix particles (represented by black points in upper left panel of Figure 2.2).

This decomposition is based on the Voronoi decomposition as it has been described in [Delaunay, 1934] for a d-dimensional space. To decompose a two-dimensional system, we generate all the possible circles (*D-circles*) containing non D-vertex inside and three lying on its perimeter; afterwards, we construct lines (*D-edges*) connecting the three D-vertices of every circle perimeter, that form triangles (*D-triangles*) inscribed in the D-circles and wholly filling the system area (green lines in upper right panel of Figure 2.2).

Taking into account the matrix and fluid particle diameters, we classify D-edges in crossable or non-crossable depending on the feasibility of a fluid particle to cross the D-edge. We show this classification in Figure 2.2, and how it enables us to classify the space into available or non-available (red lines in lower left panel of Figure 2.2) if any D-edge defining a D-triangle is crossable (green lines in lower left panel of Figure 2.2) or all of them are non-crossable respectively.

This analysis, complemented by a percolation study based on the analysis of the available pore length, will define accesible pores (green in lower right panel of Figure 2.2), and non accessible pores when they are isolated areas completely surrounded by non-crossable D-edges

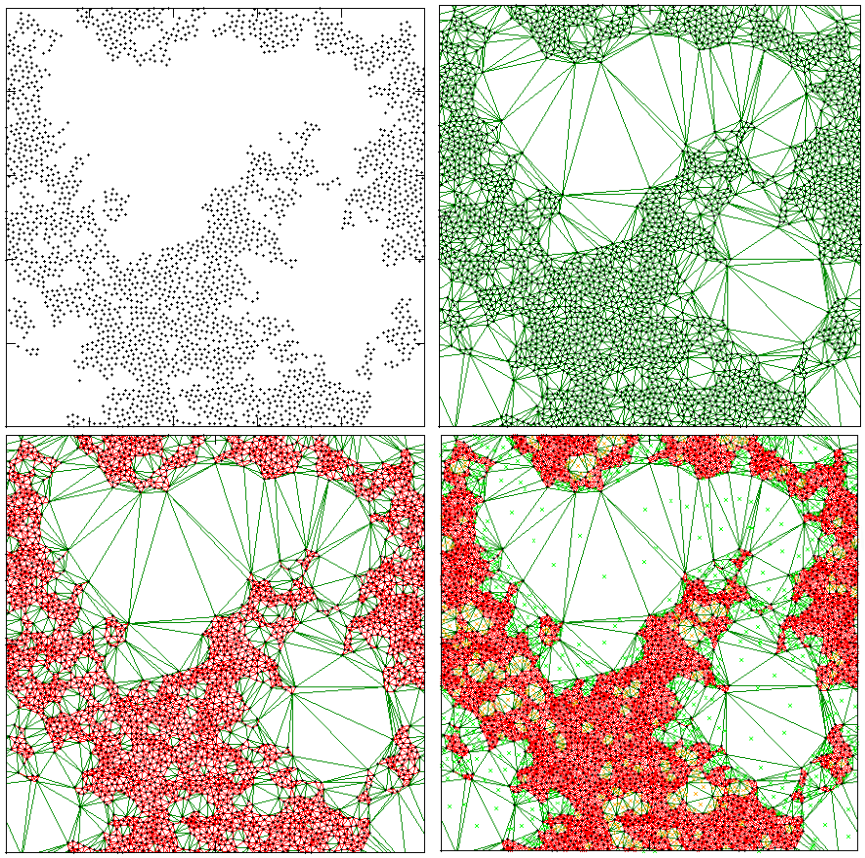

Figure 2.2: *Delaunay decomposition of a two-dimensional system. Upper left: D-vertices are the centers of mass of the matrix particles represented by black points. Upper right: D-edges (green lines) decompose the area of the system in D-triangles. Lower left: Classification of D-edges in crossable (green) and non crossable (red). Lower right*: Classification of D-triangles in non-accesible (red), available (green), and non-available (orange).

(orange in lower right panel of Figure 2.2). Finally, by summing over the area enclosed in all the accessible D-triangles we may calculate

the *accessible volume* and consequently the *porosity* (ϵ) as the ratio of the total accessible pore volume V_p to the total volume of the adsorbent V: $\epsilon = \frac{V_p}{V}$.

From the experimental point of view, theories such as the Brunauer-Emmett-Teller (BET) and Broekhoff-de Boer (BdB) methods provide information about the surface area and the pore size distribution (PSD) respectively; furthermore, hysteresis phenomena are related with the porous network topology. In order to compare with the experimental results obtained from the methods listed above, one can define quantities such as the BET area, the accessible volume, the geometric pore size distribution, etc, which have been analyzed from a computational point of view by Sarkisov and Harrison [2011]. They describe in their article computational methods for calculating the accessible surface area and the pore size distribution, by means of Monte Carlo methods of different nature.

2.2.2 Adsorption Features

We have considered all along this thesis rigid adsorbent systems during the adsorption process: this means that we have ignored the effect of the adsorbate presence over the adsorbent structure. Using this approach, the interaction adsorbent-adsorbent is only required to build the solid matrix exhibiting the desired features (pore size, porosity,...) and, during the adsorption process, we will omit these interactions.

Thus, we simulate the movement of the adsorbed particles -constrained into the rigid matrix- interacting with another adsorbed particles (through the same potential they exhibit in bulk conditions) and with the matrix. The interactions between the matrix and the adsorbent molecules modify the bulk behavior of the fluid and determine the adsorption features: adsorption isotherms and density profiles will be used to quantify these adsorption features.

- **Adsorption isotherm**
  The amount of gas adsorbed is a function of the pressure, the temperature and the interactions between matrix and adsorbent. If we represent this quantity for a given matrix-adsorbent system at a fixed temperature, the shape of the graph provides representative information about the system [Rouquerol et al., 2014b]. Experimentally these isotherms represent amount adsorbed vs. adsorbate pressure. Here we will normally use adsorbate chemical potential instead, since this is the key input in the GCMC simulations and we will not make comparisons with experiment. In any case, μ and P are connected by means of the adsorbate equation of state, which in many cases reduces to the simple law of the ideal gases.

- **Density maps and profiles**

  A graphical representation of the fluid density distribution inside the porous material is a useful tool that allows us to discover preferred adsorption sites and to understand the structural behavior of the confined fluid. Being an inhomogeneous system we can compute $\rho(x, y, z)$, taking as origin a given site of the porous matrix. This can be represented graphically either in 3D resorting to visualization tools [Humphrey et al., 1996] or across a given section of the adsorbent material. When projected on a given axis it will give the density profile, which provides a more quantitative picture of the average fluid density distribution.

  A practical implementation of the calculation of $\rho(x, y, z)$ implies the discretization of the sample space in a regular grid, where $\rho(x_0, y_0, z_0)$ is defined by counting the average number of particles in a parallelogram defined by $(x_0 \pm \Delta x, y_0 \pm \Delta y, z_0 \pm \Delta z)$. This technique implies considerable sampling difficulties as we will see in the next chapters,

since sampling bins are small and the number of adsorbate particles is typically low. Additionally, some regions of the porous system might be difficult to access, by which MD procedures will stumble with kinetic bottlenecks. This might be bypassed by means of smart byassing techniques or, as we will see, resorting to theoretical approaches.

2.3 Molecular Simulations and Integral Equation Theory

2.3.1 Molecular Dynamics

The core of a MD program [Hansen, 1991] consists in the solution of the equations of motion:

$$\frac{d}{dt}(\partial\mathscr{L}/\partial\dot{q}_i) = \partial\mathscr{L}/\partial q_i, \tag{2.30}$$

where $\mathscr{L}$ is the Lagrangian function defined as $\mathscr{L} = \mathscr{K} - \mathscr{V}$, $\mathscr{K}$ and $\mathscr{V}$ the kinetic and potential energies of the system, and q_i the generalized coordinates. For spherical particles the generalized coordinates are their centres of mass, $\mathbf{r}$, and the equations of motion in a conservative system become:

$$m_i\ddot{\mathbf{r}}_i = \mathbf{F}_i = -\partial\mathscr{V}/\partial\mathbf{r}_i, \tag{2.31}$$

and if V is pairwise additive $\mathbf{F}_i(\mathbf{r}_i) = \sum_{j\neq i} F(|\mathbf{r}_i - \mathbf{r}_j|)\hat{\mathbf{r}}_{ij}$, i.e. the force on the atom i and it is related to the gradient of the intermolecular potential. The main computational effort in the MD scheme is the calculation of the force on each atom, specially when long-range interactions are involved.

In order to integrate Eq. 2.31, *Verlet-like* algorithms use information of the coordinates at current and previous times, and are based on their Taylor expansions:

$$\begin{aligned}\mathbf{r}_i(t+\delta t) &= \mathbf{r}_i(t) + \delta t\dot{\mathbf{r}}_i(t) + \frac{1}{2}\delta t^2\ddot{\mathbf{r}}_i(t)\\ \mathbf{r}_i(t-\delta t) &= \mathbf{r}_i(t) - \delta t\dot{\mathbf{r}}_i(t) + \frac{1}{2}\delta t^2\ddot{\mathbf{r}}_i(t).\end{aligned} \tag{2.32}$$

Adding these equations we may predict the position of the particle i at $t+\delta t$ from its value at $t-\delta t$, and the velocities are computed from the positions:

$$\begin{aligned}\mathbf{r}_i(t+\delta t) &= 2\mathbf{r}_i(t) - \mathbf{r}_i(t+\delta t) + \delta t^2\mathbf{F}_i(t)/m_i\\ \mathbf{v}_i(t+\delta t) &= \frac{\mathbf{v}_i(t) - \mathbf{v}_i(t+\delta t)}{2\delta t}.\end{aligned} \tag{2.33}$$

The error of the position estimation is of order δt^4; the velocities however, are correct to the order δt^2. Some variants of Verlet algorithm have been developed to solve this problem, such as *Leap-frog* and *velocity-Verlet* schemes [Frenkel and Smit, 2002].

After a certain number of time step integrations N_t starting from an energetically reasonable configuration, the algorithm produces a phase space trajectory. Finally, once the system has reached thermal equilibrium, time averages may be performed over this MD trajectory to calculate the desired properties:

$$\bar{A} = \lim_{T\to\infty}\frac{1}{T}\int_0^T A(t)dt \simeq \frac{1}{N_t}\sum_{n=1}^{N_t} A(n\delta t), \tag{2.34}$$

where N_t is the number of integration timesteps and δt the time step. As this method describes the real time evolution of the system, it is particularly convenient to study dynamical features. It provides direct information on transport phenomena and can be adapted to describe non-equilibrium

behavior [Rapaport, 2004]. As formulated in Eq. 2.30 - 2.33, these equations preserve the number of particles, the volume and the total energy (conservative system), hence they correspond to the NVE (microcanonical) ensemble. The equations can be generalized to other ensembles more appropriate to mimic experimental conditions, such as the canonical ensemble (NVT) or the isobaric-isothermal ensembles (NPT). This can be achieved by introducing thermodynamic constraints: in the first case the system is considered to be surrounded by a heat bath (thermostate) and in the later by a pressure reservoir [Rapaport, 2004; Frenkel and Smit, 2002].

We have made use of computer packages developed by various organizations that have invested a considerable effort to produce fast and flexible multipurpose codes. LAMMPS [Plimpton, 1995] or GROMACS [Berendsen et al., 1995; Lindahl et al., 2001] are two examples of codes widely used in this thesis. Additionally, we have developed our own code particularly adapted to 2D problems and SALR potentials, both in bulk and under confinement.

2.3.1.1 Targeted Molecular Dynamics

In order to deal with molecular systems and/or various thermodynamic ensembles, molecular dynamics software implements fancy techniques and approaches such as *rigid body constraints*, *pressure and temperature* thermostats, external fields, walls, etc. and we select the most suitable method depending on the complexity of the system and the physical feature we are focused on.

Here we will pay special attention to *targeted molecular dynamics*, which is especially useful for studying molecular aggregates: it provides pathways of configurational transitions and estimations of ligand Gibbs energy. We will make use of this approach in order to study the encapsulation of small molecules in $C_{50}H_{10}$, and we will briefly summarize here the key elements of this technique as implemented in the LAMMPS package [Schlitter, 1993;

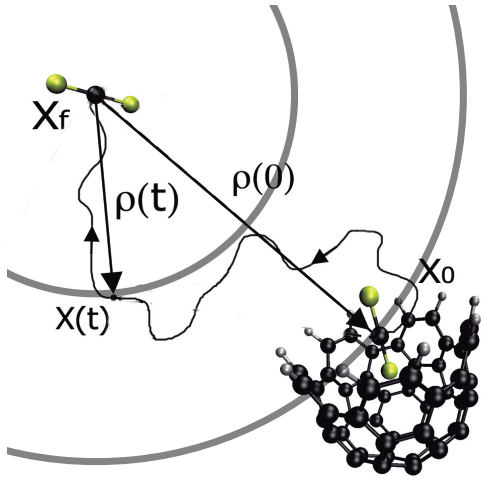

Figure 2.3: *Two-dimensional projection of the trajectory generated by TMD in a solvation example. Starting with the guest molecule into the host (x_0) and continuously diminishing the distance ρ, the trajectory ends in a position far away from the host molecule (X_f).*

Schlitter et al., 2001].

This method generates an artificial trajectory by introducing an additional force that decreases a root mean square distance between a starting and a final configuration of the complex; this process is represented in Figure 2.3.

TMD defines a weighted configurational distance: $\rho = [\sum_j \mu_j^2(\mathbf{r}_j - \mathbf{s}_j)2]^{1/2}$, where the $\mu_j = (m_j/m_{total})^{1/2}$ is the factor that introduces the mass-weighting and $\mathbf{r}_j$ and $\mathbf{s}_j$ are the coordinates of the initial and target configurations. Afterwards, in order to solve the equations of motion, following the ideas of the SHAKE and RATTLE algorithms to fix bonds and/or angles in molecular simulations [Allen and Tildesley, 1987], a con-

straint is introduced as:

$$\sigma(\rho, \rho_0) = [\sum_j \mu_j^2 (\mathbf{r}_j - \mathbf{r}_{fin,j})^2]^{1/2} - \rho_0 = 0$$

This constraint enters the Lagrange equations, by which the leapfrog algorithm is modified as follows,

$$\begin{aligned} \mathbf{r}_i(t+\delta t) &= \mathbf{r}_i(t) + \Delta t[\mathbf{v}_i(t - \Delta t/2) + \Delta t \mathbf{F}_i(t)/m_i + \Delta t 2\lambda \mu_i^2 (\mathbf{r}_i(t) - \mathbf{r}_{fin}/m)] \\ &= \mathbf{r}_i^u(t+\Delta t) + \delta \mathbf{r}(t); \qquad \delta \mathbf{r} = \gamma(\mathbf{r}_i(t) - \mathbf{r}_{fin}), \end{aligned}$$

that will we solved together with the constraint equation:

$$\Phi(r') = (\mathbf{r} - \mathbf{r}_{fin})^2 - \rho_0'^2 = 0; \qquad \mu r = r'.$$

During the simulation, this method will explore the configurational space of $3N-1$ coordinates and drive the system to the desired final configuration. Finally, the work exerted by the external artificial force is connected with the binding Gibbs free energy: $dG =< f^c >_{constr} d\rho$. In vacuum at 0K this is precisely the binding energy.

2.3.2 Monte Carlo simulation

Monte Carlo (MC) methods were introduced by von Neumann, Ulam, and Metropolis in 1949 [Metropolis and Ulam, 1949] to study the diffusion of neutrons, and constitutes an alternative to Molecular Dynamics for studying fluids [Murthy, 2003], [Landau and Binder, 2009]. This method is connected with the Monte Carlo approach for the evaluation of multidimensional integrals, which is useful for complex boundary conditions. As simple (but inefficient) example is the "hit and miss" calculation of π by Monte Carlo integration [Allen and Tildesley, 1987]. In the evaluation of the multidimensional integrals of statistical mechanics, such as the configurational integral or the ensemble averages of physical quantities, we will see

that particularly efficient Monte Carlo approaches can be developed. For example, in the canonical ensemble:

$$< A >_{NVT} = \frac{\int d\mathbf{r} A e^{-\beta U}}{\int d\mathbf{r} e^{-\beta U}} \approx \frac{\sum_{\tau=1}^{\tau_{max}} A e^{(-\beta U(\tau))}}{\sum_{\tau=1}^{\tau_{max}} e^{(-\beta U(\tau))}}, \tag{2.35}$$

being τ_{max} the number of trials. If we sample randomly the whole phase space, most of the computing effort is spent on points that hardly contribute to the average since their Boltzmann weight is negligible. *Importance sampling* is a technique that allows to guide the sampling so as to be concentrated in the regions of space with significant contribution to the configurational integral.

Thus, the generation of the Monte Carlo trajectory is based in the construction of statistically independent configurations (phase space points) X, which are accepted or rejected with a probability $\exp[-\beta U(X)]$, i.e. within a Boltzmann distribution. To that aim, the *Metropolis* method -making use of the importance sampling technique- generates the sought configurations through a so-called *Markov chain*, in which the probability distribution of a new configuration is independent of the previous one: "The past has no influence in the future once the present is specified" [Murthy, 2004, p. 35]. In the case of a monoatomic fluid, the configurations generation scheme is as follows [Frenkel and Smit, 2002]:

1. Select a particle at random.
2. Calculate the energy $U_{old}(\mathbf{r}^N)$ of the "old" configuration.
3. Give the particle a random displacement $\mathbf{r}' = \mathbf{r} + \delta r$.
4. Calculate the energy $U_{new}(\mathbf{r}'^N)$ of the "new" configuration.
5. Generate a random number n_{random}.
6. Accept the proposed move if $n_{random} < \exp(-\Delta U / k_B T)$ and reject it otherwise.

For systems consisting in more complex molecules the proposed movements will include center of mass translations, rotations of the molecules, and even changes in the internal degrees of freedom (bonds and lengths) in non-rigid molecules.

2.3.2.1 Grand-canonical Monte Carlo

The former scheme corresponds to the canonical ensemble (NVT), which was the first formulated in MC simulations. Nevertheless, it is also possible to simulate other ensembles such as the microcanonical, isobaric or isothermal, Gibbs,... when required by the problem or the system we are focused on. For instance, in adsorption studies the natural ensemble to use is the grand-canonical ensemble, μVT, in which the controlled thermodynamic variables are the adsorbate chemical potential, the sample volume and the temperature.

The most immediate method for simulating adsorbed fluids would be to mimic the real adsorption experiment where the adsorbent is in contact with a gas reservoir by means of MD simulations; however, it would take too long until the adsorbate diffuses inside the adsorbent and the equilibrium is reached, if reached at all (depending on the temperature and the chemical potential of the reservoir). *Gran-canonical Monte Carlo* (GCMC) provides an advantageous alternative to mimic the experimental procedure of adsorption since it allows to fix the temperature and the chemical potential while the number of molecules fluctuates until equilibrium is achieved. In this ensemble, our sample is in "virtual" contact with a particle reservoir with which it exchanges particles and heat (i.e. the temperature is the same both in the reservoir and in the sample). Additionally the volume of the sample (adsorbent and adsorbate) is kept constant.

For sampling all the possible configurations in this ensemble, we must try to insert and remove particles, in addition to the particle displacement trials of the canonical MC method. These "new" trial moves that allow to

change the system configuration from N to $N+1$ particles or from N to $N-1$ particles, will be accepted with a probability:

$$\begin{aligned} P(N \to N+1) &= min[1, \frac{V}{\Lambda^3(N+1)} e^{\beta(\mu - U(N+1) + U(N))}] \\ P(N \to N-1) &= min[1, \frac{\Lambda^3 N}{V} e^{-\beta(\mu + U(N-1) - U(N))}] \end{aligned} \tag{2.36}$$

When we are dealing with adsorption problems in systems with frozen adsorbent particles, the GCMC method can be optimized introducing a *cavity bias* that avoids insertion moves leading to overlaps with matrix particles. To this purpose, we scan the system at the beginning of the simulation and build a grid where the cells are classified as available to the fluid if no matrix particle is located on the cells. Then, insertion trials along the simulation will we performed only in available cells. Obviously, V in Eqs. 2.36 will now correspond to the volume of the available cells, not the sample volume.

2.3.2.2 Semigrand ensemble MC

As mentioned before, we will also be interested in a determination of the phase equilibrium in binary mixtures, which is determined by the conditions: $\mu_A^I = \mu_A^{II}$, $\mu_B^I = \mu_B^{II}$, $p^I = p^{II}$ where I and II denote the two coexisting phases. This equilibrium will be of use for the construction of models of controlled pore glasses. Now, the calculation of chemical potentials is not straightforward with the MC algorithms we have presented so far. There is however an alternative particularly suitable for the case of symmetric binary mixtures, which will be the situation we are interested on, namely the Semigrand ensemble Monte Carlo.

The semigrand ensemble MC simulation method has been widely used in the past in symmetric mixtures of non-additive hard spheres [Lomba et al., 1995; Gozdz, 2003]. We set the system's volume, the temperature, the difference between the chemical potentials of the two components and

the total number of particles (V,T,$\Delta\mu = \mu_B - \mu_A$,$N = N_A + N_B$); thus, the number of molecules of each species fluctuates, while the total density remains constant. The equilibrium of such a system is achieved by combining the common Monte Carlo translations (and rotations when dealing with non-linear molecules) with particle identity changes.

The probability of an identity change is given by: $P = min[1, Q_{\alpha\to\beta}]$, where

$$Q_{A\to B} = \frac{N_A}{N_B + 1}$$
$$Q_{B\to A} = \frac{N_B}{N_A + 1}$$

When we approach the critical point, we need to cope with the critical slowing down: correlations become long-ranged and larger samples are needed. In the case of symmetric non-additive hard sphere mixtures, we can take advantage of the symmetry of this particular system and complement single particles moves with cluster moves following the Swendsen and Wang [1987] strategy. Thus, identity samplings are performed through an efficient cluster algorithm that involves identity changes in whole clusters instead of individual changes [Almarza et al., 2015]. In this way is possible to reach thermodynamic states quite close to the consolute point (the critical point in a demixing transition) with large samples, so that extrapolation to the thermodynamic limit is feasible.

2.3.2.3 Inverse MC

This method tries to solve one of the key problems when dealing with many-particle systems: to determine the Hamiltonian of a given system from information on its microscopic structure. Henderson [1974]'s theorem states that if the system's potential energy is pairwise additive, given a

pair distribution function, $g(r)$, the corresponding pair potential that reproduces the $g(r)$, is unique.

Here we present the procedure developed by Almarza and Lomba [2003], based on Wang-Landau's sampling approach [Wang and Landau, 2001]: this is a simulation-based iterative procedure that pursues to minimize the difference between the test pair distribution function and the input reference, by iteratively improving the trial interaction potential.

This method starts from an initial guess of the effective interaction $v(r_i)$ and a particle configuration (for example a fcc lattice structure). The program tries, for each stage, N trial particles displacements, ruled by the potential $v^{old}(r)$ previous to the modification, and computes a instantaneous RDF ($g_{inst}(r)$). Afterwards, the effective potential is modified from the current values $v^{old}(r)$ to the new estimated $v^{new}(r)$:

$$\beta v_i^{new} = \beta v_i^{old} + \lambda_l \frac{g_{inst(r_i)} - g_i}{\Delta g_i} < \Delta g_i >,$$

$$\text{where} \qquad < \Delta g_i >= \frac{1}{m} \sum_{i=0}^{m-1} \Delta g_i.$$

Finally, after every n_c stages, we check the convergence of the method by comparing the original radial distribution function with that we are generating during the iterations:

$$\frac{1}{m} \sum_{i=0}^{m-1} \left(\frac{g_l(r_i) - g_i}{\Delta g_i} \right)^2 \leq \eta, \tag{2.37}$$

where η is the convergence parameter.

2.3.3 Integral Equation theory

Integral Equation theory is an alternative (in some cases a complement) to full scale molecular simulations in systems ranging from simple atomic

fluids to moderately complex molecular fluids. The idea is to establish a connection between the interaction potential, $U(r_1, ..., r_N)$, and the structure of the fluid defined in terms of distribution functions $g^n(r_1, ...r_n)$.

At this point various approaches exist, e.g. Yvon-Born-Green hierarchy and Orstein-Zernike family of integral equations among others. We will only consider in this work the Orstein-Zernike (OZ) equation, which was already formulated in Eqs. 2.4 and 2.5 for pairwise additive systems.

For a simple fluid these equations can be solved iteratively, first transforming Eq. 2.4 to Fourier space :

$$\tilde{h}(k) = \tilde{c}(k) + \rho\tilde{h}(k)\tilde{c}(k). \tag{2.38}$$

Then one defines the indirect correlation function: $\gamma(r) = h(r) - c(r)$, which by definition is continuous for all systems. With this, Eq. 2.38 now reads:

$$\tilde{\gamma}(k) = \rho[\tilde{\gamma}(k) + \tilde{c}(k)]\tilde{c}(k) = \frac{\rho\tilde{c}^2(k)}{1 - \rho\tilde{c}(k)}. \tag{2.39}$$

This equation can be Fourier inverted to obtain $\gamma(r)$, which is then inserted into Eq. 2.5, rewritten as:

$$c(r) = \exp(-\beta U(r) + \gamma(r) + b(r)) - 1 - \gamma(r), \tag{2.40}$$

which can be Fourier transformed to get a new $\tilde{c}(k)$, and thus the equation solved iteratively. There are many sophisticated numerical procedures to speed up convergence [Ishizuka and Yoshida, 2012; Kelley and Montgomery Pettitt, 2004], but for the purposes of this work a simple Broyles mixing iterates approach [Broyles, 1960] will suffice. Namely, once a new $\gamma_{new}(r)$ is obtained by inversion of Eq. 2.39, our new estimate will be given by:

$$\gamma^{i+1}(r) = \alpha\gamma^i_{new}(r) + (1 - \alpha)\gamma^i_{old}(r), \tag{2.41}$$

where typically $\alpha \approx 0.5$ works in most instances, and for stubborn cases $\alpha = 0.95 \approx 0.99$. This new $\gamma^{i+1}(r)$ can then be inserted in Eq. 2.40 to yield another estimate $c^{i+1}(r)$, and to proceed with the iterations.

As mentioned, it is not possible to consider all the terms in $b(r_{12})$ in Eq. 2.40, and they have to be approximated. In the case of *hypernetted-chain* (HNC) approach we find $b_{HNC}(r_{12}) = 0$, leading to:

$$h_{HNC}(r_{12}) = exp[-\beta U(r_{12}) + h(r_{12}) - c(r_{12})] - 1, \tag{2.42}$$

which once linearized gives the PY approximation:

$$h_{PY}(r_{12}) = exp[-\beta U(r_{12})](1 + h(r_{12}) - c(r_{12})) - 1. \tag{2.43}$$

The extension of the OZ to mixtures, by means of matrices, is straightforward. In Fourier space, Eq. 2.38 now reads,

$$\tilde{\mathbf{H}}(k) = \tilde{\mathbf{C}}(k) + \tilde{\mathbf{H}}(k)\boldsymbol{\rho}\tilde{\mathbf{C}}(k).$$

Here $\tilde{\mathbf{H}}(k)$ and $\tilde{\mathbf{C}}(k)$ are the matrices of elements $\tilde{h}^{\alpha\beta}(k)$ and $\tilde{c}^{\alpha\beta}(k)$ respectively, where α and β are the components of the mixture, and $[\rho]_{\alpha\beta} = \rho_\alpha \delta_{\alpha\beta}$. Additionally, molecular fluids can be treated using molecular distribution functions which are expanded into spherical harmonic series (linear fluids) or rotational invariants (non-linear fluids) [Gray et al., 2011], or alternatively using a site-site approach such as the Reference Interaction Site Model (RISM) [Hansen and McDonald, 1986]

2.3.3.1 Replica Ornstein-Zernike Integral Equations (ROZ)

This approach was developed for disordered confining media where both components of the system (fluid and matrix) are not in equilibrium, since one of them (the matrix) has frozen degrees of freedom. It reduces the problem of a partly-quenched system to a completely equilibrated mixture formed by the matrix plus s identical replicas of fluid that do not interact with each other. The origin of this transformation of the system is

not physical but purely mathematical, and it is based on the definition of logarithm as [Edwards and Anderson, 1975]:

$$\log x = \lim_{s\to 0} \frac{d}{ds} x^s. \tag{2.44}$$

The free energy of the fluid particles (denoted by the subscript 1) confined in a disordered quenched matrix (denoted by the subscript 0), averaged over all the possible matrix configurations, is:

$$-\beta \bar{F}_1 = \frac{1}{N_0! Z_0} \int d\{\mathbf{q}^{N_0}\} exp[-\beta_0 H_{00}(\mathbf{q}^{N_0})] log Z_1(\mathbf{q}^{N_0}), \tag{2.45}$$

where $Z_1(\mathbf{q}^{N_0})$ is the partition function of the fluid. At this point, using Eq. 2.44 the following expression for the free energy can be obtained:

$$\begin{aligned} -\beta \bar{F}_1 &= \frac{1}{Z_0} \lim_{s\to 0} \frac{d}{ds} \frac{1}{N_0!(N_1!)^s} \int d\{\mathbf{q}^{N_0}\} (d\{\mathbf{r}^{N_1}\})^s exp[-\beta H^{rep}] \\ &= \frac{1}{Z_0} \lim_{s\to 0} \frac{d}{ds} Z^{rep}(s), \end{aligned}$$

where βH^{rep} describes the Hamiltonian of the equilibrated mixture of the matrix particles plus the s fluid replicas. This is called the *replicated system*, and $Z^{rep}(s)$ is its partition function.

From this, Given and Stell [1992] formulated the Replica Ornstein-Zernike equations for a thermally equilibrated fluid adsorbed in a matrix formed by a quenched simple fluid, which reads:

$$\begin{aligned} h_{00} &= c_{00} + \rho_0 c_{00} \otimes h_{00} \\ h_{01} &= c_{01} + \rho_0 c_{00} \otimes h_{01} + \rho_1 c_{01} \otimes h_{11} - \rho_1 c_{01} \otimes h_{12} \\ h_{11} &= c_{11} + \rho_0 c_{01} \otimes h_{01} + \rho_1 c_{11} \otimes h_{11} - \rho_1 c_{12} \otimes h_{12} \\ h_{12} &= c_{12} + \rho_0 c_{01} \otimes h_{01} + \rho_1 c_{11} \otimes h_{12} + \rho_1 c_{12} \otimes h_{11} - 2\rho_1 c_{12} \otimes h_{12} \end{aligned} \tag{2.46}$$

with the corresponding closures in r-space. The closure for c_{12} (replica-replica) has $U_{12} = 0$, and the matrix equation is fully decoupled as it should be for a frozen system. Subscripts 0 and 1 denote respectively the matrix and the fluid, and 2 the replicas of fluid particles.

Later on, Zhang and Tassel [2000] expanded the ROZ equations for a templated matrix from those of a two component matrix system simply dismissing the interactions between the template and the adsorbed fluid after quenching. In [Lomba and Weis, 2010; Lomba et al., 2014] one may find the explicit procedure to build and solve the ROZ equations for templated matrices. First, the ROZ equations are written in matrix form in Fourier space in terms of density scaled [2] Fourier transformed functions as:

$$\begin{aligned}
\mathbf{H}^{00} &= \mathbf{C}^{00} + \mathbf{C}^{00}\mathbf{H}^{00} \\
\mathbf{H}^{01} &= \mathbf{C}^{01} + \mathbf{C}^{00}\mathbf{H}^{01} + \mathbf{C}^{01}\mathbf{H}^{11} - \mathbf{C}^{01}\mathbf{H}^{12} \\
\mathbf{H}^{11} &= \mathbf{C}^{11} + \mathbf{C}^{01}\mathbf{H}^{01} + \mathbf{C}^{11}\mathbf{H}^{11} - \mathbf{C}^{12}\mathbf{H}^{12} \\
\mathbf{H}^{12} &= \mathbf{C}^{12} + \mathbf{C}^{01}\mathbf{H}^{01} + \mathbf{C}^{11}\mathbf{H}^{12} + \mathbf{C}^{12}\mathbf{H}^{11} - 2\mathbf{C}^{12}\mathbf{H}^{12}.
\end{aligned} \tag{2.47}$$

Now, each of the matrix functions $\mathbf{F}_{ij}$ (where $\mathbf{F}$ stands for either $\mathbf{H}$ or $\mathbf{C}$) can be explicitly expressed in terms of the density scaled Fourier transforms of the total correlation function, $\widetilde{h}_{\alpha\nu}$, or the direct correlation function, $\widetilde{c}_{\alpha\nu}$, according to:

$$\mathbf{F}^{00} = \begin{bmatrix} \tilde{f}_{0_\alpha 0_\alpha} & \tilde{f}_{0_\alpha 0_\beta} \\ \tilde{f}_{0_\beta 0_\alpha} & \tilde{f}_{0_\alpha 0_\beta} \end{bmatrix}, \qquad \mathbf{F}^{01} = \begin{bmatrix} \tilde{f}_{0_\alpha 1} \\ \tilde{f}_{0_\beta 1} \end{bmatrix}, \qquad \mathbf{F}^{11} = \tilde{f}_{11}, \qquad \mathbf{F}^{12} = \tilde{f}^{r}_{11} \tag{2.48}$$

where the superscript r specifies correlations between the replicas of the annealed fluid.

[2] By density scaled we mean that the forward Fourier transform of a function $f_{\alpha\beta}$ is multiplied by a factor $(\rho_\alpha \rho_\beta)^{1/2}$, and the corresponding reverse transform by a factor $(\rho_\alpha \rho_\beta)^{-1/2}$.

These equations in Fourier space are complemented by the corresponding closures in r-space, which in the HNC approximation read:

$$\begin{aligned}
h_{0_i0_j}(r) &= exp(-\beta u_{0_i0_j}(r) + h_{0_i0_j}(r) - c_{0_i0_j}(r)) - 1 \\
h_{11}(r) &= exp(-\beta u_{11}(r) + h_{11}(r) - c_{11}(r)) - 1 \\
h_{0_\alpha 1}(r) &= exp(-\beta u_{0_\alpha 1}(r) + h_{0_\alpha 1}(r) - c_{0_\alpha 1}(r)) - 1 \\
h_{0_\beta 1}(r) &= exp(h_{0_\beta 1}(r) - c_{0_\beta 1}(r)) - 1 \\
h^r_{11}(r) &= exp(h^r_{11}(r) - c^r_{11}(r)) - 1
\end{aligned} \tag{2.49}$$

Equations for the matrix-matrix interactions ($\mathbf{H}^{00}$ and $h_{0_i0_j}(r)$ in Eq. 2.47 and 2.49) can be solved independently, and the equations for the rest of correlations (matrix-fluid and fluid-fluid) can be cast into a more compact matrix form for computational convenience, and solved iteratively:

$$\begin{bmatrix} \mathbf{C}^{01} \\ \mathbf{C}^{11} \\ \mathbf{C}^{12} \end{bmatrix} = \begin{bmatrix} \mathbf{I} - \mathbf{C}^{00} & -\mathbf{C}^{01} & \mathbf{C}^{01} \\ -\mathbf{C}^{10} & \mathbf{I} - \mathbf{C}^{11} & \mathbf{C}^{12} \\ -\mathbf{C}^{10} & -\mathbf{C}^{12} & \mathbf{I} - \mathbf{C}^{11} + 2\mathbf{C}^{12} \end{bmatrix} \begin{bmatrix} \mathbf{H}^{01} \\ \mathbf{H}^{11} \\ \mathbf{H}^{12} \end{bmatrix} \tag{2.50}$$

Last equation can be efficiently inverted for the components of the total correlation function in terms of the direct correlation function using a LU decomposition based algorithm [Anderson et al., 1999]. Iterations can be performed between real and Fourier space following a mixing iterates procedure as indicated in Eq. 2.41, or accelerated using Ng's procedure [Ng, 1974].

Finally, once the correlation functions are determined, we can calculate thermodynamic properties for the adsorbed fluid such as the excess internal energy per particle using the expressions found in **Section 2.1**, and for the adsorbed fluid excess chemical potential:

$$\begin{aligned}
\beta\mu_\alpha = &- \rho_0 \tilde{c}_{0\alpha}(0) + \frac{1}{2}\rho_0 \int d\mathbf{r} h_{0\alpha}(r)\gamma_{0\alpha}(r) + \\
&+ \frac{1}{2}\rho_1 \int d\mathbf{r} \left(h_{11}(r)\gamma_{11}(r) - h_{12}(r)\gamma_{12}(r) \right).
\end{aligned} \tag{2.51}$$

2.3.3.2 3DOZ-HNC approach

When dealing with adsorption, in ordered and disordered porous materials, the adsorbate molecules will be in the presence of a highly inhomogeneous field. If we decide to make use of an Ornstein-Zernike approach to treat this problem, Eq. 2.5 has to be generalized to something like:

$$h(\mathbf{r}_1, \mathbf{r}_2) = \int c(\mathbf{r}_1, \mathbf{r}_3)\rho(\mathbf{r}_3)h(\mathbf{r}_3, \mathbf{r}_2)d\mathbf{r}_3, \tag{2.52}$$

where now, in three dimensions, h and c will be six-dimensional functions, and $\rho(\mathbf{r}_3) = \rho(x, y, z)$. Clearly, this approach is unfeasible with the current computational facilities.

There is however an alternative that was first exploited by Beglov and Roux [1995] for the study of solvation of large molecules, in order to provide a full three dimensional description of the solvent structure around the solvate. If we follow Percus source particle approach [Percus, 1964] and consider the solute particle (in our case the adsorbent) as a source of an external potential, then the one particle density of the solvent (adsorbate) can be expressed as: $\rho_1(x, y, z) = \bar{\rho}g_{01}(x, y, z)$, where in Beglov-Roux approach $\bar{\rho}$ is the solvent's bulk density, and $g_{01}(x, y, z)$ is the solute-solvent pair distribution function. In our case $\bar{\rho}$ is a density related parameter that will have to be defined self-consistently later on, and $g_{01}(x, y, z)$ the adsorbent-adsorbate pair distribution function. Now if we make use of the HNC approximation, the singlet fluid density is given by:

$$\rho_1(x, y, z) = \bar{\rho}_1 \exp(-\beta U(x, y, z) + h_{01}(x, y, z) - c_{01}(x, y, z)). \tag{2.53}$$

We can now consider the inhomogeneous OZ equation for a mixture of solvent-solute particles:

$$\begin{aligned} h_{01}(\mathbf{r}_1, \mathbf{r}_2) - c_{01}(\mathbf{r}_1, \mathbf{r}_2) = &\int h_{00}(\mathbf{r}_1, \mathbf{r}_3)\rho_0(\mathbf{r}_3)c_{01}(\mathbf{r}_3, \mathbf{r}_2)d\mathbf{r}_3 \\ &+ \int h_{01}(\mathbf{r}_1, \mathbf{r}_3)\rho_1(\mathbf{r}_3)c_{11}(\mathbf{r}_3, \mathbf{r}_2)d\mathbf{r}_3 \end{aligned} \tag{2.54}$$

If $\mathbf{r}_1$ (coordinate of the solute) is taken as origin and $\rho_0 \to 0$ (infinite dilution limit):

$$h_{01}(\mathbf{r}_1, \mathbf{r}_2) - c_{01}(\mathbf{r}_1, \mathbf{r}_2) = \int h_{01}(\mathbf{r}_1, \mathbf{r}_3)\rho_1(\mathbf{r}_3)c_{11}(\mathbf{r}_3, \mathbf{r}_2)d\mathbf{r}_3, \tag{2.55}$$

and we approximate: $\rho_1(\mathbf{r}_3)h_{01}(\mathbf{r}_3) \approx \bar{\rho}_1(g_{01}(\mathbf{r}_3) - 1)$, by which:

$$\rho_1(\mathbf{r}) = \bar{\rho}_1 \exp\left[-\beta U_{01}(\mathbf{r}) + \int c_{11}(\mathbf{r}, \mathbf{r}')(\rho_1(\mathbf{r}') - \bar{\rho}_1)d\mathbf{r}'\right]. \tag{2.56}$$

Additionally, following Beglov and Roux we now assume that $c_{11}(\mathbf{r}', \mathbf{r}) = c_{11}(|\mathbf{r}' - \mathbf{r}|)$, i.e. the inhomogeneous fluid-fluid correlation can be approximated by that of an isotropic and homogeneous fluid. In the case of solvation problems, the natural approximation is to replace the solvent-solvent direct correlation function by that of the bulk fluid (without solute), i.e. $c_{11}(\mathbf{r}', \mathbf{r}) = c_{11}^{bulk}(|\mathbf{r}' - \mathbf{r}|)$. This approximation has been successfully applied to study the physics of solvation of complex molecules, including proteins [Beglov and Roux, 1996; Beglov et al., 1997; Cortis et al., 1997; Kovalenko and Hirata, 1998, 1999; Du et al., 2000].

Beglov and Roux [1996] actually made use of this crude approach to calculate the density profile of a simplistic model of zeolite as confining media for a simple fluid with relative success. The shortcomings of this approximation are rather obvious, since the direct correlations of a confined fluid are well different from those of the bulk, as we will demonstrate later on.

As an alternative, we propose the use of the fluid-fluid correlations approximated by the ROZ-HNC, by which $c_{11}(\mathbf{r} - \mathbf{r}')$ in Eq. 2.56 is given by:

$$c_{11}(x - x', y - y', z - z') = c_{11}^{ROZ-HNC}(\sqrt{(x - x')^2 + (y - y')^2 + (z - z')^2}), \tag{2.57}$$

and $c_{11}^{ROZ-HNC}(r)$ is computed from Eqs. 2.46 and 2.49. Once $c_{11}(x,y,z)$ is known, Eq. 2.56 can be solved iteratively using a mixing iterates approach Eq. 2.40 [Beglov and Roux, 1995]. The use of acceleration procedures is rather limited by the available RAM storage, particularly in the three dimensional case. For numerical convenience, Eq. 2.56 can be conveniently rewritten as:

$$\begin{aligned} h_1(x,y,z) = & \exp[-U_{01}(\mathbf{x},\mathbf{y},\mathbf{z})/k_BT + \\ & + \bar{\rho}_1 \int dx'dy'dz' c_{11}(\rho_1(x-x',y-y',z-z')h(x',y',z')] - 1, \end{aligned} \tag{2.58}$$

$\rho_1(x,y,z) = \bar{\rho}_1(h(x,y,z)+1)$ and $U_{01}(x,y,z) = \sum_{i=1}^{N_0} u_{01}(x-x_{0i}, y-y_{0i}, z-z_{0i})$, where N_0 is the number of matrix particles. This latter equation can easily be extended to multicomponent matrices.

Note that the convolution in Eq. 2.58 can easily be evaluated in Fourier space, and the computation of the numerical Fourier transform is straightforward using efficient library routines such as those of the FFTW3 library (see Appendix A). For the particular nature of our problem, and taken into account that we will analyze fluid density distributions for a given configuration of matrix particles that is assumed to have periodic boundary conditions, the Fourier transforms can be carried out without zero padding. Note that our calculations will be compared to simulation results obtained using precisely the same periodic boundary conditions. This periodic nature of the problem must be very specially borne in mind when approximating the inhomogeneous direct correlation function in Eq. 2.57 using the averaged ROZ fluid-fluid correlations.

Additionally, Eq. 2.58 can be linearized to yield a Percus-Yevick (PY)

like approximation of the form:

$$h(x,y,z) = \exp(-U_{01}(x,y,z)/k_BT) \left[1 + \bar{\rho}_1 \int dx'dy'dz' c_{11}(x-x', y-y', z-z') h(x',y',z')\right] - 1 \tag{2.59}$$

Even if the main result of Eq. 2.58 (in combination with a sum rule specified below, Eq. 2.62) is the fluid spatial density distribution, $\rho_1(x,y,z)$, this quantity can also give information on the average matrix-fluid correlations. In fact, these can be obtained by means of the average:

$$g_{01}(r) = \frac{1}{\bar{\rho}_1 N_0} \sum_{i=1}^{N_0} \int \rho_1(\mathbf{r}' - \mathbf{r}_{0_i}) \delta(\mathbf{r} - \mathbf{r}' + \mathbf{r}_0) d\mathbf{r}', \tag{2.60}$$

where the integration over the Dirac's $\delta(\mathbf{r} - \mathbf{r}' + \mathbf{r}_0)$ can be discretized as:

$$\begin{aligned} g_{01}(r) = & \frac{1}{\bar{\rho}_1 N_0} \sum_{m=1}^{N_0} \sum_{i,j,k} \rho_1(x'_i, y'_j, z'_k) H(r + \Delta r - r'_m) \times \\ & \times H(r'_m - r + \Delta r) \frac{\Delta x \Delta y \Delta z}{\Delta V_{shell}} \end{aligned} \tag{2.61}$$

In the last equation, $r'_m = \sqrt{(x'_i - x_m)^2 + (y'_j - y_m)^2 + (z'_k - z_m)^2}$, $H(x)$ is a step function, and the space is discretized according to $x'_i = i\Delta x$, $y'_j = j\Delta y$ and $z'_k = k\Delta z$. ΔV_{shell} defines the volume of the spherical shell (circular in two dimensional problems) determined by the discretized Dirac δ, i.e., here $\Delta V_{shell} = 4\pi r^2 \Delta r$. For practical purposes, we have chosen our grid in r such that $\Delta r = \Delta x$. The summation in 2.60 and 2.61 runs over the number of matrix particles, e.g., over the unit cell in a periodic system.

Now, in Eq. 2.58, the value of the effective density $\bar{\rho}_1$ is not straightforwardly defined for our problem. In solvation problems [Beglov and Roux, 1995; Kovalenko and Hirata, 1998; Yamazaki and Kovalenko, 2011; Beglov et al., 1997], the density in question can accurately be approximated by the bulk density, but this is certainly not the case in situations of strong confinement. On the other hand, we know that the density distribution must satisfy the sum rule:

$$\rho_1' = \frac{\bar{\rho}_1}{L_x L_y L_z} \int dxdydz(h(x,y,z)+1) \tag{2.62}$$

where L_x, L_y, L_z are the dimensions of the periodic cell. Once the fluid inhomogeneous density, $\rho_1(x,y,z)$, is known, the effective homogeneous density $\bar{\rho}_1$ can be evaluated iteratively solving Eqs. 2.58 and 2.62 self-consistently, taking into account that ρ_1' must converge towards $\rho_1 = N_1/V$, i.e. the net number of fluid particles divided by the total volume of the fluid plus matrix particles.

The reduction of the above equations to the two dimensional case is straightforward, and we will denote it in what follows by 2DOZ-HNC or 2DOZ-PY depending on the choice approximation, i.e. Eq. 2.58 or Eq. 2.59. In three dimensions, the evaluation of the adsorbent-adsorbate potential $U_{01}(x,y,z)$ and the integration in Eq. 2.61 over an $N \times N \times N$ grid (with $N \geq 256$) are extremely time consuming tasks which can be accelerated resorting to the use of GPU computing. For short range potentials using a cell method (or a neighbor list) in order to avoid the computation of inter particle distances for non-interacting pairs also considerably accelarates the evaluation of $U_{01}(x,y,z)$.

Chapter 3

Associative systems under confinement

3.1 The origin of effective SALR interactions: a simple model

The aim of this Section is to explore the possibility of pattern formation, typical of SALR interactions, in a system consisting of a simple equimolar mixture of diatomic molecules and monomers, in which only short-ranged forces are present. This somehow contrasts with the common assumption that long range repulsive interactions alone stabilize pattern formation vs-simple phase separation. We will see how a suitable combination of short range potentials leads to the desired stabilization of nano-heterogeneous structures. We have here addressed the emergence of intermediate-range order analyzing the behavior of the partial and concentration-concentration structure factors, and performing cluster analysis. Our simulation results have been compared with Reference Interaction Site Model (RISM) equation calculations carried out by A. Perera [Bores et al., 2015b], which will be shown to agree remarkably well. Furthermore, we have extracted effective site-site potentials from the pair correlation functions using an inverse Monte Carlo approach (see **Section 2.3**). We will see that these potentials,

despite the fact that all interactions at play are short ranged, exhibit the features characteristic of a SALR potential.

Additionally, we have also analyzed the effect of charges on our model, which in fact by the addition of electrostatic site-site interactions becomes a coarse-grained representation of a room temperature ionic liquid. In addition, we have studied too the effect of confinement on the self-organizing behavior of this system, and on a realistic model of imidazolium based ionic liquid. In this Section, the confinement of self-assembling fluids has been carried out in narrow regular pores, in particular slit pores of a few molecular diameters width, that constrain the volume of the system decreasing its dimensionality.

Description of the Model

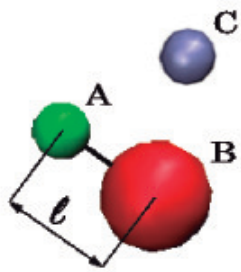

Figure 3.1: *System components: monomers (C) and dimers (A-B).*

The system studied in this Section consists in an equimolar fluid mixture of two different species, a two-site dimer AB and a monomer C (see Figure 3.1). The dimers are represented by a two center LJ site-site potential, in which the sites are separated by a distance l, and our monomers also interact via LJ potentials. In all cases, the interactions are cut and shifted at a distance r_c, by which the explicit form of the site-site potentials is:

$$
\begin{aligned}
&u_{ij}(r) = 4\epsilon\big[(\frac{\sigma_{ij}}{r})^{12} - (\frac{\sigma_{ij}}{r})^{6} - (\frac{\sigma_{ij}}{r_c})^{12} + (\frac{\sigma_{ij}}{r_c})^{6}\big]; \quad \text{if } r < r_c \\
&u_{ij}(r) = 0 \quad otherwise
\end{aligned}
\tag{3.1}
$$

Our model is to a certain degree inspired by the simple coarse-grained model for imidazolium-based room temperature ionic liquids (RTILs) of Merlet et al. [2012b]. To that aim, we will preserve the attractive/repulsive character of the interactions in the RTIL whilst droping the Coulomb interactions. Table 3.1 outlines the parameters and the character of the LJ interactions between the particles of the fluid. Since the size of the non-polar tail is essential to determine the nanostructural ordering [Canongia Lopes and Pádua, 2006] we have considered various sizes for σ_{BB} (always with $\sigma_{BB} > \sigma_{AA}$). For the attractive interactions, we have truncated and shifted the LJ potential at $r_c = 3\sigma_{BB}$. For the repulsive interactions, we have simply used $r_c = 2^{1/6}\sigma_{ij}$, thus defining purely repulsive soft spheres following the prescription of Weeks, Chandler, and Andersen (WCA) [Weeks et al., 1971].

Table 3.1: Lennard-Jones potential parameters of our self-assembling mixture model

i	j	Interaction	ϵ(kJ/mol)	σ_{ij}(Å)	r_c(Å)
A	A	Repulsive	2.092	4.0	$2^{1/6} \cdot \sigma_{AA}$
A	B	Repulsive	2.092	$(\sigma_{AA} + \sigma_{BB})/2$	$2^{1/6} \cdot \sigma_{AB}$
A	C	Attractive	2.092	4.0	$3 \cdot \sigma_{BB}$
B	B	Attractive	2.092	σ_{BB}	$3 \cdot \sigma_{BB}$
B	C	Repulsive	2.092	$(\sigma_{BB} + \sigma_{CC})/2$	$2^{1/6} \cdot \sigma_{BC}$
C	C	Repulsive	2.092	4.0	$2^{1/6} \cdot \sigma_{CC}$

Moreover, in order to analyze the effect of charges on the intermediate range order, we have considered explicitly the same model with a positive

charge $+q$ on the A sites and a corresponding negative charge $-q$ on the monomers. The value of q is varied between 0 and $0.25e$, where e is the elementary electron charge. Again these values are of the same order as those considered in the model of Merlet et al. [2012b]. Eight different systems have been analyzed showing different charges, B particles diameters and densities. We present them in Table 3.2.

Table 3.2: Potential parameters and thermodynamic state variables for the systems under study

	$\|q\|(e)$	σ_B(Å)	ρ(Å^{-3})	T(K)	P(atm)
System 1	0	8.0	0.001	226.4	27.05
System 2	0	8.0	0.00125	226.5	39.5
System 3	0	8.0	0.0015	226.5	59.4
System 4	0	9.0	0.001	226.5	30.4
System 5	0	9.0	0.00125	226.4	53.2
System 6	0	9.0	0.0015	226.4	96.7
System 7	0.1	8.0	0.0015	226.4	39.4
System 8	0.25	8.0	0.00195	226.3	0.61

We have also confined our mixture confined into a slit pore generated by two rigid and flat walls interacting with the fluid atoms via a pure repulsive soft interaction. For the fluid particles interactions we have preserved the LJ parameters of System 3 (see Table 3.1). Preliminary calculations for $x_{AB} = x_C = 1/2$ indicate the disappearing of the droplet phase as a consequence of the reduced dimensionality, we have therefore investigated phases with larger monomer concentrations up to $x_{AB} = 1/4$ and $x_C = 3/4$.

In order to deal with equivalent and comparable systems when going from 3D to 2D, in confined systems, we have redefined the densities so as to keep constant the packing fractions [Hansen and McDonald, 1986, p. 95]

defined as:

$$\begin{aligned} \eta_{3D} &= \pi/6[\rho_{AB}(\sigma_A^3 + \sigma_B^3) + \rho_C(\sigma_C^3)] \\ \eta_{2D} &= \pi/4[\rho_{AB}(\sigma_A^2 + \sigma_B^2) + \rho_C(\sigma_C^2)] \end{aligned} \tag{3.2}$$

for three and two dimensional systems respectively. For the system 3 fluid with $x_{AB} = x_C = 1/2$ the packing fraction is $\eta = 0.25133$, thus the new densities for the fluid with $x_{AB} = 1/4$ and $x_C = 3/4$ are $\rho_f = 0.02\text{Å}^{-3}$ and $\sigma_f = 0.04\text{Å}^{-2}$ for three and two dimensions respectively. More dimers-monomers concentrations have been considered in order to analyze the emerging patterns, and as mentioned the equivalent densities have been calculated preserving the packing fraction.

We have confined the fluid in a slit-like pore modeled by two flat walls applying a perpendicular force on the particles of the fluid [Magda et al., 1985]. The interactions between the walls and the fluid particles is purely soft repulsive and consists in a 12/6 Lennard Jones potential ($\epsilon_{wall} = 1.0 Kcal/mol$ and $\sigma_{wall} = 1\text{Å}$) which has been truncated and shifted at $r_c = 2^{1/6}\sigma_{wall}$, keeping only the repulsive region of the potential [Weeks et al., 1971]. We have considered different pore widths -defined as the distance between the walls- being the width of the thiner pore equal to the biggest particle diameter, i.e. 8Å. For the side of the simulation box we have considered $L_x = L_y = 151.43\text{Å}$ and the Z-dimension defined by the separation between the walls: $w = 8\text{Å}$, $w = 24\text{Å}$ and $w = 40\text{Å}$. Thus, the number of particles of the confined fluid is determined by the width of the pore $N = N_{AB} + N_C = \rho/w l_x l_y$: $N = 1251$, 3777 and 7500 for $w = 8\text{Å}$, 24Å and 40Å respectively.

Simulations details

We have performed extensive molecular dynamics simulations, using the LAMMPS package, in the canonical and isothermal-isobaric ensembles with a Nose-Hoover thermostat. Our samples contained 16384 particles, but samples up to 65536 particles were investigated and no significant size dependence was found. Initial themalization runs at a temperature of 226K were $2x10^6$ step long (with a timestep of 1 fs) followed by production runs of $5x10^6$ step long, and averages were carried out every 5000 steps.

The confined model described above has been studied in terms of Molecular Dynamics simulations using LAMMPS package [Brown et al., 2011; Plimpton and Thompson, 2012; Plimpton, 1995] in the canonical ensemble using a Nose-Hoover thermostat [Frenkel and Smit, 2002]. The system was thermalized during 10^6 steps at $T = 113.22K$ with a time step of $1fs$ and afterwards we have performed simulations of $5x10^6$ steps long recording 500 configurations to analyze every 10000 steps.

Thermodynamic equilibrium

One of the problems one can encounter when performing simulations in the canonical ensemble in this type of system is the occurrence of phase transitions, either vapor-liquid equilibria or demixing. In order to guarantee that the states under consideration correspond to thermodynamic equilibrium conditions, and consequently any potential intermediate range order is not the result of a spinodal decomposition, we have run additional isothermal-isobaric simulations and analyzed the volume fluctuation of the samples. In this way one can avoid those states that lie inside the liquid-vapor spinodal.

Moreover, one can compute the partial structure factors defined as:

$$S_{ij}(k) = x_i\delta_{ij} + x_i x_j \rho \int (g_{ij}(r) - 1) e^{-\mathbf{qr}} d\mathbf{r}, \tag{3.3}$$

where ρ is the total number density. Here sites A and B are considered as different particles and g_{ij} is the atom-atom pair distribution function. Our samples are large enough to allow for an accurate integration of the pair distribution functions, and the results are consistent with direct k-sampling. Notice that as far as Equation (3.3) is concerned, $x_A = x_B = x_C = 1/3$, hence in the large k limit all structure factors will tend to 1/3. Furthermore, we have also calculated the Bathia and Thornton concentration-concentration structure factors, introduced in Eq. 2.10 of **Section 2.1**, where now one has to consider explicitly the structure factors corresponding to the molecular species AB, and as a consequence $x_{AB} = x_C = 1/2$. We can simply approximate $g_{AB-AB} = g_{B-B}$ and $g_{C-AB} = g_{C-B}$, as if the scattering length or form factor of A sites was negligible compared to that of B sites. This is in principle not unreasonable given the much larger size of B sites, but in a realistic situation one should take explicitly into account the true scattering lengths or form factors of sites A and B. Now one has to correct for the different values of the molar fraction when AB is considered as a single species and Eq. (3.3) is used in the concentration-concentration structure factor Eq. (2.10). In this way, $lim_{k\to\infty} S_{cc}(k) = x_C x_{AB} = 1/4$. With all this in mind, the presence of a divergence when $k \to 0$ in $S_{cc}(k)$ is a signal of a demixing transition, so this quantity will be essential to assess the stability of the thermodynamic states chosen for our simulations.

Finally, back to the vapor-liquid transition, one can analyze the corresponding k-dependent linear response susceptibility $\rho k_B T \chi_T$ (previously defined in Eq. 2.19 of **Section 2.1**) in density fluctuations, namely [Hansen and McDonald, 1986], whose $k = 0$ limit is precisely the isothermal compressibility. The presence of a divergence -or a substantial increase in $x_T(0)$- is an indication of the vicinity of a vapor-liquid transition. A careful monitoring of this quantity together with the use of NPT simulations provides a reliable assessment of the stability of the state points under consideration

during the simulation runs.

In the case of the System 8, when increasing the charge from $0.10e$ to $0.25e$ the conditions of temperature and density corresponding to system 3, 6 and 7 lie in the two-phase region. Consequently we resorted to an isothermal-isobaric simulation at low positive pressure to achieve thermodynamic equilibrium conditions in our system with $q = 0.25e$. The final value of total particle density achieved in this way is indicated in Table 3.2.

Inverse Monte Carlo method

With the pair correlation functions produced along the simulations runs and the corresponding statistical uncertainties calculated using block averages, we have used the IMC procedure proposed by Almarza and Lomba [2003] (see **Section 2.3**) in order to produce single component site-site effective potentials able to reproduce the microscopic structure exhibited by our mixture model. As it has been explained in the Methods chapter, the procedure starts from a simple approximation $\beta u_{in}^{eff}(r) = -\log g(r)$ and proceeds to modify the pair potential along the simulation run in such a way that the calculated $g^{eff}(r)$ matches the input $g(r)$. In our case, we have used a total of 4000 particles. The procedure of inversion was carried out in 20 stages. In the last stages, the effective potentials hardly varied, and the convergence between input and calculated $g(r)$'s was achieved successfully in all the cases.

In this way, one can use as input of the IMC procedure either $g_{AA}(r)$, $g_{BB}(r)$ or $g_{CC}(r)$ and obtain a corresponding set of $u_{AA}^{eff}(r)$, $u_{BB}^{eff}(r)$ and $u_{CC}^{eff}(r)$, which will obviously be different, but in the case of emergence of intermediate range order should exhibit some common features.

3.1.1 Bulk system

3.1.1.1 Pair structure

Here, we have analyzed the effect of the molecular geometry on the nanostructure formation changing the diameter of σ_{BB}. We have first considered, $\sigma_{BB} = 8$Å, 9Å, 10Å and 12Å. Some snapshots of configurations for varying σ_{BB} are depicted in Figure 3.2. We have found that for $\sigma_{BB} > 9$Å clustering or microheterogeneity of C particles can only be appreciated when the packing of the B-sites is so high that it resembles that of a solid. In fact in this case, the height of the first peak of $S_{BB}(k)$ exceeds 2.7, which according to the Hansen-Verlet rule [Hansen and Verlet, 1969] indicates that freezing conditions have been reached. Moreover, the prepeak in the structure factor characteristic of the presence of IRO is absent from $S_{BB}(k)$. The clustering of C particles results from a mere steric effect, since these are restricted to occupy the holes between the large B particles. These effects can be appreciated in the snapshots of Figure 3.2, where the dense packing of B-sites is readily apparent. The color coding here, and in the rest of the Chapter is red for B sites, green for A sites and blue for C monomers.

For the reasons mentioned above, we will concentrate on the results for $\sigma_{BB} = 8$Å and 9 Å. Already in the corresponding snapshot of Figure 3.2, one can appreciate the formation of a bicontinuous network of percolating clusters, connecting both AB dimers and C monomers. By bicontinuous network, we mean that the clusters formed by B-sites and C particles will be seen to both span practically the whole sample, forming two continuous interpenetrated percolating microphases. This can be analyzed from a more quantitative perspective by first taking a look at the corresponding pair distribution functions and partial structure factors, which are depicted in Figures 3.3 and 3.4, respectively, for Systems 1–6. Focusing first on the g_{AA} pair distribution function, one first appreciates the large exclusion hole after the first layer, which is a simple consequence of the large size of B-sites. Obviously, the exclusion hole grows with the size of the B-sites, as can be seen when comparing figures on the left and right columns. Correlations

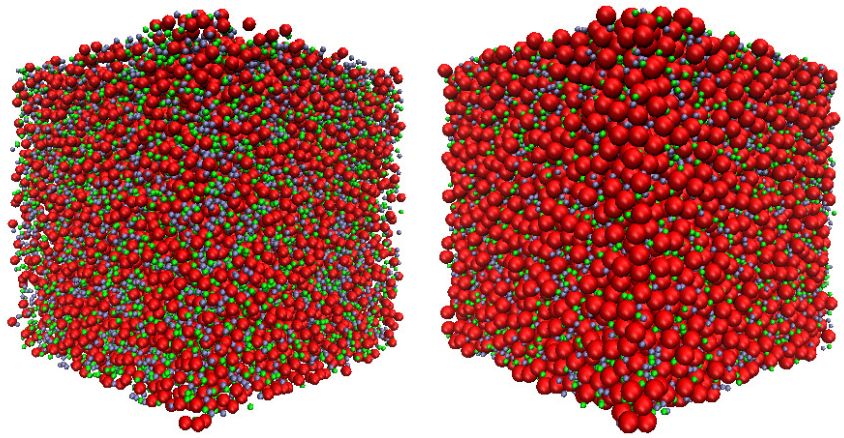

Figure 3.2: *Snapshots of configurations for total particle density* $\rho = 0.00125 \AA^{-3}$ *and temperature* $T = 226.45K$ *for two B-site diameters. As the size of B-sites grows, C monomers cluster in the cavities formed by the B-sites due to excluded volume effects. All other diameters and total density are kept fixed,* $\sigma_{AA} = \sigma_{CC} = 4.0 \AA$. *(a)* $\sigma_{BB} = 8 \AA$. *(b)* $\sigma_{BB} = 12 \AA$. *B sites are depicted in red, A sites in green and C monomers in blue.*

between A-sites extend up to five σ_{AA}, and the width of the g_{CC} correlation is $\approx 2\sigma_{CC}$. These features hint at the presence of some degree of IRO. B-B correlations (graphs in the middle row) behave like those of a dense fluid, and no apparent sign of clustering or IRO is evident. In contrast, the wide first peak of g_{CC} is characteristic of clusters of particles confined in cavities, in this case formed by B-sites. This effect, as mentioned before, is maximized for the largest σ_{BB}. We will see later that these clusters of partly occluded C-particles are connected, forming a three dimensional percolating structure.

If we take now a look at the partial structure factors, we immediately appreciate a feature characteristic of the emergence of IRO, namely, the presence of a prepeak at 0.25 Å^{-1}. This corresponds to correlations in the

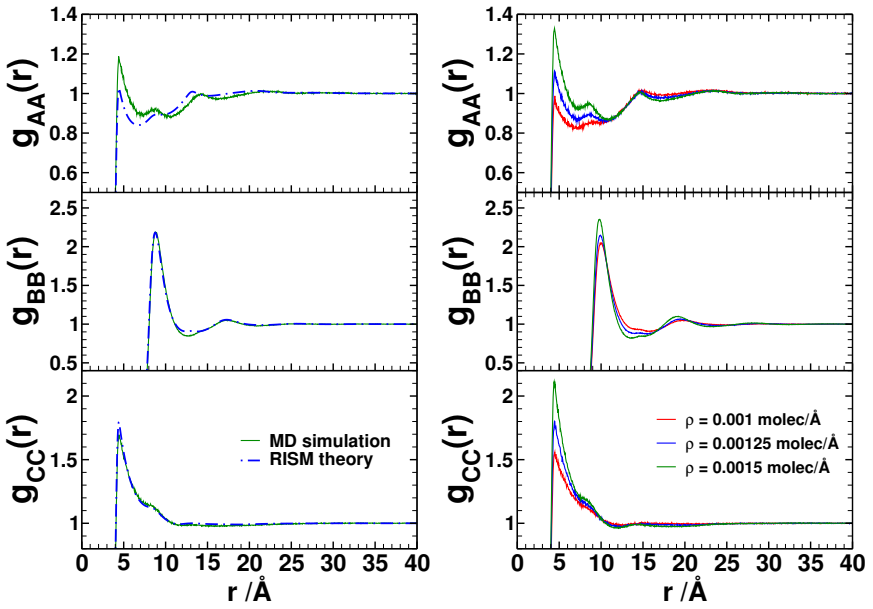

Figure 3.3: *The figures show the radial distribution functions for A, B, and C particles, respectively. Left column corresponds to* $\sigma_{BB} = 8$ *Å for system 3 (theory vs. simulation) and right column presents the simulations results for systems 4-6 for* $\sigma_{BB} = 9$*Å. Total density is indicated in the legend. Simulation results are represented by solid lines and dashed-dotted curves correspond to integral equation calculations.*

range of 25Å, the distance at which any sign of structure of the pair distribution function dies out. Interestingly, the prepeak is almost absent in S_{AA}, except for a small maximum visible for the $\sigma_{BB} = 9$Å and the highest density. This quantity shows otherwise very little structure for $k > 0.5$ Å^{-1}. As seen in the g_{AA}'s, the most relevant feature in the AA correlations is the exclusion hole due to the presence of the B-sites. In contrast, S_{BB} does exhibit a prepeak, even when no evidence of IRO was visible in g_{BB}. This prepeak is more apparent in the monomer structure factor S_{CC}. When the density is lowered, the prepeak in the B-site structure factor

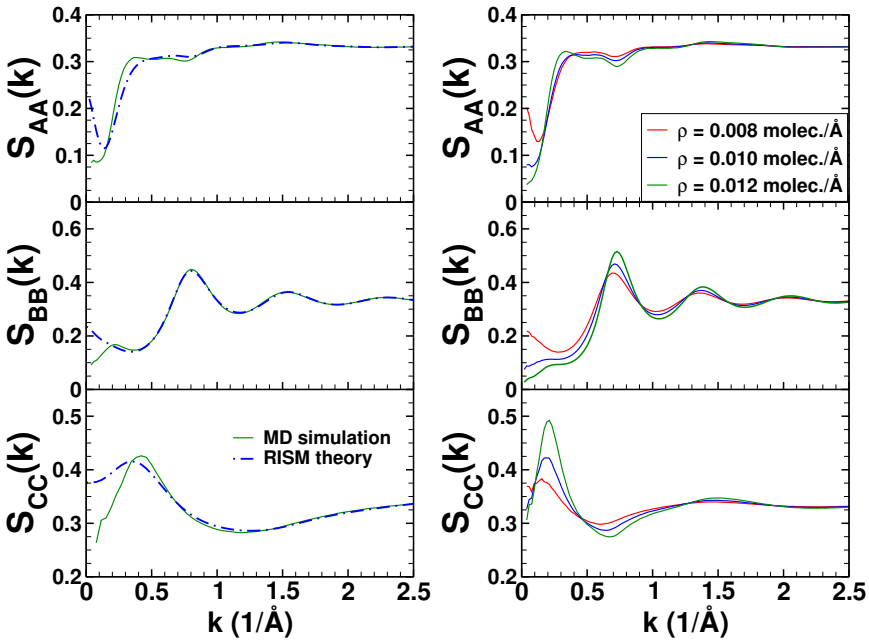

Figure 3.4: *The figures show the structure factors for A, B, and C particles, respectively. Left column corresponds to $\sigma_{BB} = 8$Å for system 3 (theory vs. simulation) and right column presents the simulations results for systems 4-6 for $\sigma_{BB} = 9$Å. Total density is indicated in the legend. Simulation results are represented by solid lines and dashed-dotted curves correspond to integral equation calculations.*

shifts to lower k-values and vanishes at $\rho = 0.001\text{Å}^{-3}$. In the case of S_{CC}, the position of the prepeak is preserved, but its magnitude decreases. In Figure 3.5, the corresponding concentration-concentration structure factor is displayed. The prepeak at $k_0 \approx 0.25\text{Å}^{-1}$ is preserved, although its magnitude decreases when the total density is lowered. In contrast, no increase when $k \to 0$ is visible. This implies that we are encountering concentration fluctuations inducing spatial inhomogeneities, but no demixing transition. In Figure 3.6 we have plotted the k-dependent susceptibility corresponding

to density fluctuations. The prepeak is visible except for the lowest density, which implies that density inhomogeneities with a spatial pattern are also correlated with the corresponding concentration inhomogeneities. But now, the $k \to 0$ behavior is different. As density is decreased, the susceptibility (i.e., the isothermal compressibility) grows, an indication of the vicinity of a vapor-liquid transition. This means, that lowering the density from the value of $\rho = 0.001$ Å^{-1} at the same temperature could move the system across the spinodal curve into the two-phase region and induce vaporization. Our analysis indicates that the thermodynamic conditions we have simulated can be considered equilibrium states. Moreover, we have confirmed that the results do not have a significant sample size dependence, by which metastability can also be ruled out.

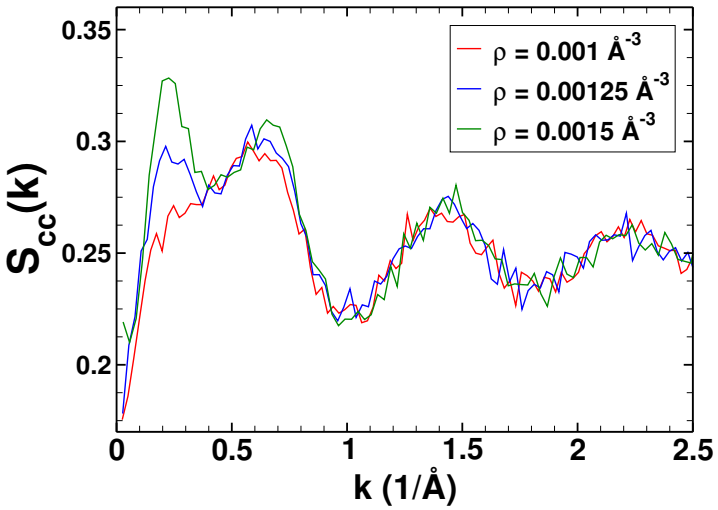

Figure 3.5: *Concentration-concentration structure factor for the systems 1-3.*

The site-site correlation functions and structure factors obtained from the RISM theory in the HNC approximation (see [Bores et al., 2015b] for further information) are represented in dashed lines in Figs. 3.3 and 3.4. It

is seen that the agreement is excellent in most cases, particularly in what concerns the BB and CC correlations. The AA correlations are systematically underestimated near contact and overestimated at larger distances. The most significant differences are seen for the structure factors in Fig. 3. Integral equations in the HNC approximation tend to exaggerate concentration fluctuations and often tend to interpret small aggregate formations as the onset of demixing or a vapor/liquid transition [Perera and Kezic, 2013; Perera and Mazighi, 2015]. We observe here a similar trend for the low density case $\rho = 0.001\text{Å}^{-3}$, for which fluctuations compete the most with aggregate formation. The prediction of aggregation, through the pre-peak is in very good agreement with simulations for the highest density $\rho = 0.0015\text{Å}^{-3}$, precisely when the denser packing tends to favor aggregation. This is also in line with previous observations of similar type of behavior for model ionic liquids. These features are a direct consequence of the fact that the HNC closure approximation misses high order correlations. We observe that in all cases, the $k = 0$ behavior of the RISM structure factor always overestimates the concentration fluctuations.

3.1.1.2 Effective pair potentials

In Figure 3.7, we present the effective potentials obtained from the site-site pair distribution functions. By construction, using these effective potentials in a simulation for a single component system will lead to a pair distribution function coincident with the original site-site correlation of the mixture. This is one of the possible alternatives to reduce the behavior of a complex system to a simpler one component system. Other alternatives, such as the force-matching approach[Izvekov et al., 2004], will lead to quantitatively different results, but certainly retaining the essential features of the effective potentials found here. Among these features, we see that in all cases, the effective potential has a short range (extremely short in the case of AA potentials) attractive well and this is followed by a long range repulsive region, which extends to 20-30Å. The repulsive region of U_{eff}^{CC} is much less visible and is illustrated in the inset. The repulsive range is more

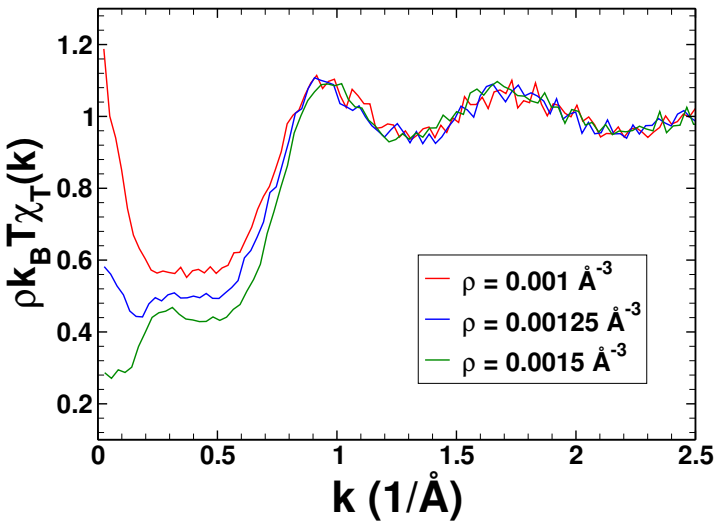

Figure 3.6: *Isothermal compressibility as a function of k for systems 1-3.*

influenced by the change in the total density. The attractive part of AA and CC effective interactions is due to depletion forces (in this case, the plain site-site interactions are repulsive). In the case of AA interactions, most of the attractive wells are masked by the excluded volume effect of the B sites in the AB molecules (the large repulsive potential between 5-15 Å corresponds to the exclusion hole in g_{AA}). Note that even if in g_{BB} long range correlations due to nanostructure organization are not clearly visible, there are long range repulsions in the BB effective potential, which are reflected in the prepeak in S_{BB} as an indication of IRO. The long range repulsion vanishes for $\rho = 0.001\text{Å}^{-3}$, which we have seen is a state approaching the gas-liquid transition.

Figure 3.7 shows the effective pair potentials as obtained by the RISM integral equation approach. The comparison with the simulations is overall quite good in all cases. However, it is seen that the repulsive shoulder

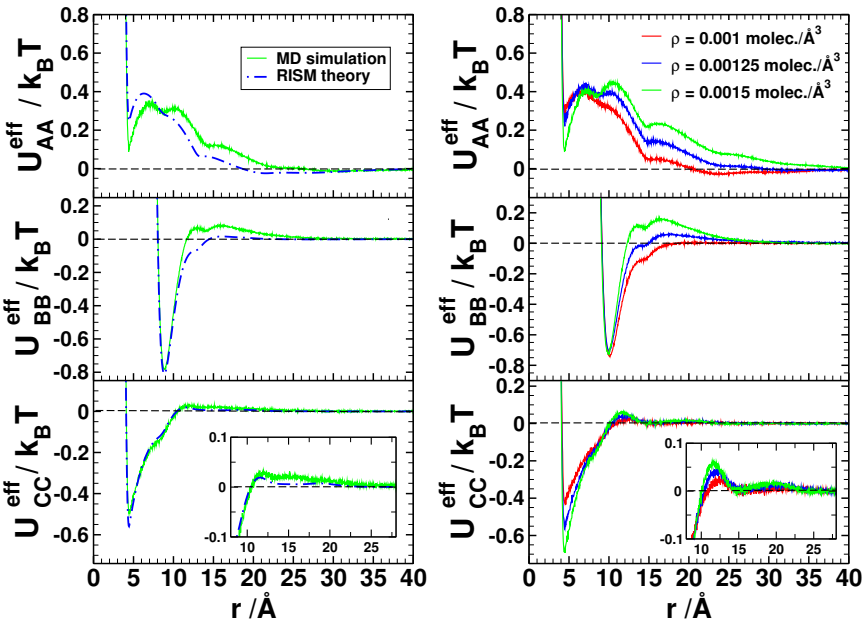

Figure 3.7: *Effective potentials for A, B, and C particles, respectively. Left column corresponds to $\sigma_{BB} = 8$Åfor system 3 (theory vs. simulation) and right column presents the simulations results for systems 4-6 for $\sigma_{BB} = 9$Å. Total density is indicated in the legend. Simulation results are represented by solid lines and dashed-dotted curves correspond to integral equation calculations.*

-which is the signature of the clustering ability- is always systematically underestimated by the theory. This is a direct consequence of the weaker tendency of the integral equation theory to predict clustering.

Taken into account that B-sites are much larger than A-sites, we can think of our model as a system of B particles in a "sea" of C monomers, just like colloids in solution. Following the work of Mani et al. [2014], we

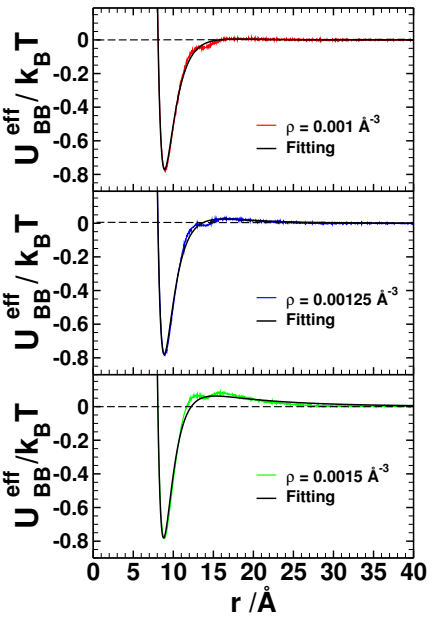

Figure 3.8: *B-B effective interaction for systems 1-3, fitted to a generalized LJ+Yukawa interaction.*

can use a functional form of the type:

$$U(r)/K_BT = 4a_0\big[\big(\frac{\sigma_{BB}}{r}\big)^{12} - \big(\frac{\sigma_{BB}}{r}\big)^{a_1}\big] + \frac{a_2 a_3}{r} e^{-\frac{r}{a_3}} \qquad (3.4)$$

to represent the BB effective interactions. Note that given the large size of the B-sites, we have retained the repulsive part of the bare LJ interaction in order to account for the short range repulsive component of the effective potential. One can see that the fits of the effective interactions $U_{BB}^{eff}/(k_BT)$ to Equation (3.4) represented in Figure 3.8 are fairly accurate except for the minor inflection of the curve around 13Å. The parameters of the fit are collected in Table 3.3. Notice that the exponent of the attractive LJ component, a_1, deviates substantially from the standard value of 6, being its range shorter as density increases. The range parameter a_3

grows considerably with the density, reflecting the increase of intermediate range ordering as the total density is increased. We observe that a single component representation of our system can be well performed by a standard SALR potential in which the long range repulsion has the form of a Yukawa interaction, even when the original bare interactions in the mixture are relatively short ranged LJ potentials.

Table 3.3: Parameters of SALR effective interaction Charbonneau and Reichman [2007] between B sites fitted to the data extracted from the IMC procedure. Note that the potential is scaled with k_BT, by which a_0 is dimensionless.

	a_0(Å)	a_1(Å)	a_2(Å)	a_3(Å)
System 1	1.788	8.185	3.749	4.297
System 2	2.066	8.667	0.843	7.282
System 3	3.578	9.927	0.231	14.816

3.1.1.3 Cluster analysis

In order to go beyond the mere qualitative information provided by simulation snapshots and the two-body level of pair distribution functions, we present now a cluster analysis of the simulation samples. We will use various values or r_{cl} in the range 10-12Å for B-sites and C monomers and 6-8 Å for A-sites. This choice is determined by the attractive range of the corresponding effective potentials depicted in Figure 3.8. The effects of the particular choice of r_{cl} on the cluster distribution will be analyzed. Specifically, we have calculated the normalized cluster size distribution, $N(s) = n(s)(s/N)$, as proposed by Stauffer [1979] and described in Section 2.1.

Of all the systems analyzed, in Figure 3.9, we have chosen to plot the results of system 6, which exhibits a significant prepeak in its partial struc-

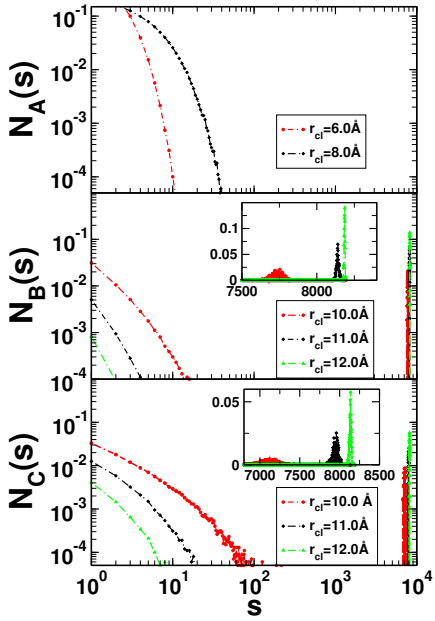

Figure 3.9: *Normalized cluster distribution function for A and B sites and C monomers of system 3.*

ture factors. We observe that the normalized cluster size distributions of both A and B-sites and C monomers present the same qualitative features: first, one finds a maximum for isolated particles which decays monotonously to zero at a value of cluster size, s, that strongly depends on r_{cl}. This is a typical behavior of a non-associating fluid, in which instantaneous clusters are created and destroyed as particles explore their configurational space. If stable finite clusters were formed, the cluster size distribution should exhibit the corresponding maxima for the preferred sizes. On the other end of the s-axis, interestingly, one finds large clusters that span all the simulation cell. Here, N(s) shows little dependence on r_{cl}, particularly for the B-sites and C monomers. Finally, the cluster size distribution of A and B sites is qualitatively very similar, which is understandable taking into account that both sites are linked into single molecular units. We will see in the next

section that this symmetry is broken by the presence of charges and a new symmetry between A-sites and C particles emerges.

Thus, from our analysis, a more clear picture shows up, in which we have a large portion of the sample linked into microsegregated clusters forming bicontinuous structures, with a remnant of disconnected particles that form short lived structures up to tens or hundreds of particles depending on the choice of r_{cl}, as one would expect in a non-associating fluid.

3.1.1.4 The effect of charges

Our previous results have shown that microheterogeneity or stable intermediate range order can be induced by competing short range interactions in a simple mixture model of dimers and monomers. As we have already said before, our model was somehow inspired by a coarse grained representation of ionic liquids, which are in reality characterized by the presence of Coulombic interactions, absent from our model. An immediate question that deserves to be answered is then how the presence of charges affects the stability of the aforementioned bicontinuous structures. To that aim, we have carried out the corresponding analysis on systems 7 and 8 that, as mentioned, correspond to system 3 with charges $+q$ added to sites A and $-q$ to the C monomers. For $q = 0.1e$, standard canonical molecular dynamics simulations were run. Recall that in the case of $q = 0.25e$, density had to be increased in order to move out of the vapor-liquid coexistence region. This was simply achieved by means of an isothermal-isobaric simulation run at the same T as the original system and a pressure of 0.61 MPa, leading to a total $\rho = 0.00195\text{Å}^{-3}$.

In the snapshots of Figure 3.10, one can readily see that the charges enhance the formation of microstructural order, and particularly for the highest charge, one see very well defined stripes of C particles, stripes that now appear to be finite. A more clear picture emerges when taking a look at the partial structure factors, presented in left panels of Figure 3.11. Now,

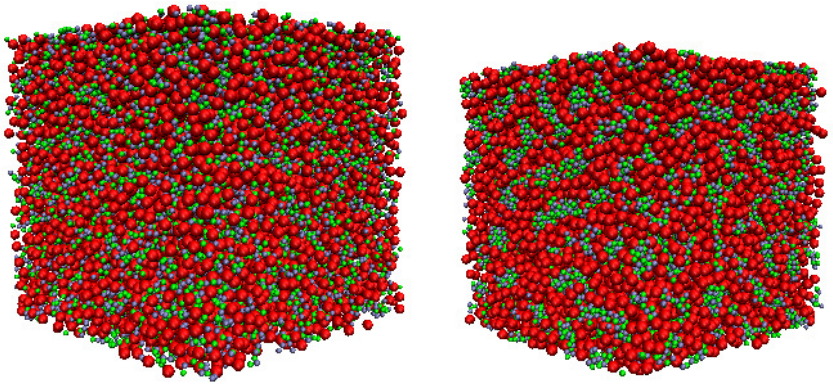

Figure 3.10: *Snapshots of the equimolar mixture of AB dimers and C monomers with embedded charges (indicated on the figures). Left:* q_A = *0.10e;* q_C = *-0.10e. Right:* q_A =*0.25e;* q_C =*-0.25e.*

the prepeak is perfectly defined even for the S_{AA} structure factor for the lowest charge, in contrast with the uncharged system S_{AA}. The extremely large values of $S_{\alpha\beta}(k_0)$ for $k_0 \approx 0.25$ Å^{-1} resemble Bragg peaks and indicate the presence of quasiperiodic order in the microstructural domains. Moreover, if now one looks at the cluster size distributions plotted on the right panels of Figure 3.11, together with the percolating clusters, one finds now a maximum centered at $s \approx 20$ for $q = 0.25e$ for C and A-sites, which indicates the presence of finite clusters of monomers and A-sites. This maximum is preserved in the results obtained for other charges up to $q = 0.2e$ (not shown for the sake of clarity), to disappear for weaker Coulombic interactions. It is obvious that the net effect of charges on the microstructuring of our model mixture is to enhance the formation of nanostructures, also giving rise to the formation of finite size clusters for sufficiently high charges. In contrast, B-sites form a percolating bicontinuous structure coexisting with some disconnected B-sites or short lived aggregates. A-sites and C monomer form aggregates embedded in the percolating network of B-sites. All this suggests that the network of B-sites forms cavities, with the A-sites pointing inside the cavity. This in turn is filled by C monomers.

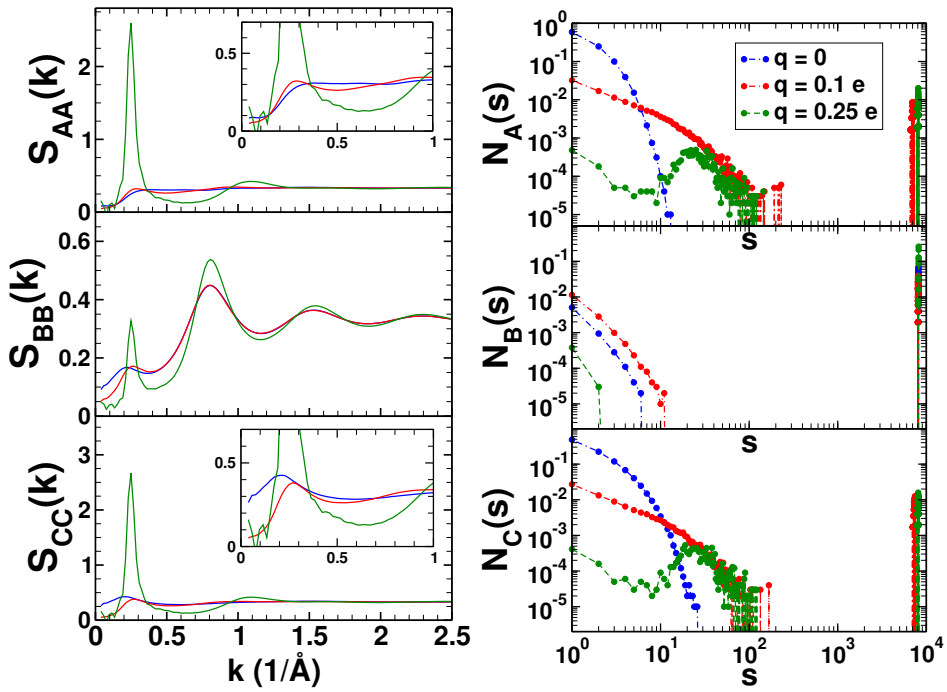

Figure 3.11: *Left: Charge dependence of the partial structure factors for A (top), B (middle), and C (bottom) particles. Right: Charge dependence of the cluster size distribution. Charge magnitudes are specified in the legend.*

This configuration is favored both by steric effects and by the net attraction between the positively charge A sites and negatively charged C monomers.

On the other hand, despite the fact that A-sites form part of the AB dimers and C monomers are independent particles, due to the symmetry of the electrostatic interactions and the symmetry in shape and density - $\sigma_{AA} = \sigma_{CC}$, $\rho_A = \rho_C$- as the charges increase, AA and CC correlations become extremely similar- compare S_{AA} and S_{CC} in Figure 3.11 -as one would encounter in a simple fully symmetric electrolyte.

The next question is how this is all reflected on the effective potentials. These are plotted in Figure 3.12. In all cases, one observes the characteristic SALR structure, obviously being the CC and AA effective interactions those that are most affected by the introduction of charges. In spite of the fact that these two effective interactions result from the coarse graining of many body effects, the dominant role of electrostatic interactions already reflected in the partial structure factors leads to surprisingly similar effective potentials when charges are present. On the other hand, the changes in U_{BB}^{eff} are just quantitative. The attractive part is hardly influenced by the charges, since it results mostly from the depletion interactions and the bare attractive u_{BB}. The long range repulsion is enhanced, and as the charge reaches $q = 0.25e$, oscillations appear. These oscillations recall the Friedel oscillations characteristic of effective cation-cation potentials in liquid metals[Cusack, 1987]. In the latter instance, the oscillations result from the quantum nature of the electrons. Here, they result from the interplay of the Coulombic interactions and depletion forces. Thus, for sufficiently large charges, the long range attractive interaction between C and A sites propagates through the AB bonds and induces the attraction well around 30Å as a result of a many body effect.

3.1.2 Confinement in slit pores

We will now see how confinement in a regular geometry (slit pore) modifies clustering effects and pattern formation. As mentioned we will focuse on two closely related systems, first our simple mixture model which has been analyzed in the preceding paragraphs in bulk, and then a realistic representation of a RTIL confined between graphene layers. In this latter instance we will pay special attention to the phenomenon of wall wetting by the RTIL at low pore fillings. This is an important technological issue, since given the large ability of RTIL's as universal solvents (in particular also for CO_2 absortion), one could potentially enhance the adsorption of carbonaceous porous materials if an appropriate RTIL wets their inner porous surface before pore filling conditions.

3.1.2.1 The simple mixture model

As mentioned, we will keep a constant packing fraction $\eta = 0.2513$ (see Eq. 3.2) in order to make comparisons between systems under equivalent thermodynamic conditions. Different aspects of confinement effects will be addressed, namely:

A. Critical density and corresponding states

First of all we have examined how does the confinement modify the critical behavior of this fluid, in particular concerning demixing. We have performed molecular dynamics simulations for the fluid in different confinement situations: bulk, several pore widths ($W = 40$Å, $W = 24$Å, $W = 8$Å) and the purely two-dimensional case. We have explored a large number of temperatures and inspected the corresponding concentration-concentration structure factors and isothermal compressibility in search for an approaching divergence as $k \to 0$.

We can infer from Figures 3.13, 3.14, 3.15, 3.16, 3.17 that a phase transition occurs for all the cases at different temperatures. Furthermore, looking at the isothermal compressibility (right column in Figure 3.18) we see that no liquid-vapour transition happens since it shows no divergence at low ks. Instead of that, we have found a divergence in the concentration-concentration structure factor (left column in Figure 3.18) revealing a demixing transition.

We have associated the temperature immediately above to that showing a divergence in the S_{cc} graph, Figure 3.18, with a rough estimation of the critical temperature of the fluid for each confinement situation. Arbitrarily we have considered $S_{cc}(k \to 0)$ as diverging when its slope at $k \to 0$ is beyond 10. The concrete values of $S(k \to 0)$ for the minimum k that

can be evaluated ($2\pi/L$, with L the largest side of the simulation box) are obviously constrained by the sample size, and a true divergence would only occur in the thermodynamic limit, $N \to \infty$. We have plotted the difference $T_c(bulk) - T_c(W)$ versus $1/W$ (see Figure 3.19) and we have found a good agreement with Kelvin's scaling law [Almarza et al., 2009; Davis, 1996]: $T_c(bulk) - T_c(W) \propto 1/W$. Note that this decrease in the critical temperature is a straightforward consequence of the decrease in the number of neighbors that surround each particle, and the subsequent decrease of the intensity of the interactions. The extreme situation is clearly the 2D limit.

When analyzing pattern formation, we should not compare systems at the same temperature because they correspond to thermodynamic states considerably different with respect to the critical point, i.e. its location in the phase diagram would be different. The estimation of the critical temperatures for every confinement condition makes possible the comparison between states in different confinement situations resorting to *corresponding states* principle. We define a reduced temperature with respect to our estimate of the critical temperature, $T_r = T/T_c$, and then comparisons will be carried out for $T_r = 1.1667$, which is slightly above the demixing critical temperature. In this way we will be able to see how confinement affects pattern formation for different states in "equivalent" thermodynamic states, that are stable.

B. Structural order induced by confinement

First of all we have analyzed the averaged order induced across the slit pore. To this aim, we have calculated the density profiles for every type of particle in a plane perpendicular to the pore walls, and the orientational profile for dimers. In Figure 3.20 we show the number density profile of the fluid confined into the slit pore for different walls separations. The most remarkable feature one appreciates is the inhomogeneous structure that emerges when the fluid is confined. For the thiner pore all A, B and C par-

ticles show a similar symmetric distribution around the center of the pore (left panel in Figure 3.20). However, as we increase the distance between the walls (central and right panel in Figure 3.20), the particles exhibit a preference for specific location into the pore: B particles are mostly located in the center of the pores while A and C particles stay near the walls, specially for larger pore widths. Since the walls are purely repulsive, this is basically a larger depletion effect, by which volume occupancy is optimized if C particles are microseggregated from B particles. Since C and A particles attract each other, the latter necessarily point in the direction of C particles that stay close to the walls.

As we have seen in Figure 3.20, each type of particle (A, B and C) prefers different average location inside the pore. That suggests that the dimers will also present preferential orientations in consequence of the inhomogeneous distribution of particles. Figure 3.21 illustrates the orientation of the dimers into the slit-pore. Here we represent the normalized angular distribution of the $\cos\alpha$, being α the angle formed by the AB dimer axis and the vector perpendicular to the pore walls. Given the symmetric nature of the walls, $f(\cos(\alpha))$ is symmetric with respect to $\cos(\alpha) = 0$. One can observe that for the thinnest pore ($w = 8$Å) the dimmers have no room to lie perpendicular to the pore, and most of them are parallel ($\cos(\alpha) = 0$); however, in the case of the widest pore ($w = 40$Å), the graph reveals a preferred distribution of the dimers perpendicular to the pore walls ($\cos(\alpha) = \pm 1$), which agrees with the higher concentration of B particles in the center of the pore shown in Figure 3.20.

The last two Figures reveal the existence of an inhomogeneous layered structure of the fluid confined inside the pore. For a clearer illustration of this feature, we have split the system in slides of width 8Å (see Figure 3.20), and represented the snapshots corresponding to these layers in the lower graphs of Figures 3.22, 3.23 and 3.24. Upper graphs of the last figures shows two projections of the confined fluid configurations: a cut perpendicular to the walls (left) and other parallel (right).

Apart of the emergence of layering across the pore, induced by the confinement, in this Section we have explored the presence of intermediate-range order on the unbounded plane parallel to the pore walls. To this aim, we have studied the correlations of the fluid into the pore by means of two dimensional structure factors and performed a clustering analysis. We note that the use of a two dimensional approximation for the structure factor is somewhat crude for the largest pore widths, but a complete analysis of the inhomogeneous structure factor following the steps of Nygard et al. [2012] is too complex, and in our opinion it would not add further information concerning the emergence of IRO as compared with the simple 2D approximation. In the case of $W = 40$Å the 2D analysis leads to meaningless results and are therefore not presented. In this case the system is expected to approach bulk behavior as far as pattern formation in the direction parallel to the planes is concerned.

Figures 3.25 and 3.26 compares the pair distribution function and the structure factors of the fluid confined in the pores: $w = 8$Å and $w = 24$Å, and the purely three and two dimensional system. In all the cases we observe the presence of a prepeak for all species indicating the emergence of IRO. The purely 2D system is clearly closer to demixing. Note that despite our attempt to study an equivalent 2D system, there are considerable differences between the smallest pore width, $w = 8$Å, and the 2D. Even if for $w = 8$Å the B sites are restricted in a 2D space, the dimers have a certain degree of rotational freedom, by which they can pack better than the purely 2D dimers. The same can be said for the C monomers. This is clearly appreciated in the peaks of the g_{AA} and g_{CC} distribution functions (and to a lower extent also in g_{BB}) which are shifted to larger r-values, in the 2D case, as if the particle size, was larger. As a result one observes in the low-k behavior of $S_{BB}(k)$ a tendency to diverge, i.e. the 2D system is closer to demixing.

Finally, we have carried out an analysis of the clustering similar to that performed for the bulk mixture (see further explanation in **Section 2.1**). The link distance we have selected to define the clusters (maximum distance

between a pair of particles that belong to the same cluster) corresponds to the first minimum in the radial distribution functions (left graph in Figures 3.25 and 3.25). The results obtained, shown in Figures 3.27, completely agree with the behavior found by means of the radial distribution function and the structure factor. As one could qualitatively appreciate in the snapshots of Figures 3.17 - 3.13, the cluster size distribution (Figure 3.27) clearly indicates that confinement enhances the formation of finite size clusters, very well defined in the case of $w = 8$Å, and not so well in the 2D case (here only B particles show a maximum in N(s)). This difference is likely due to the aforementioned inexact mapping of the 2D system conditions due to the different packing constraints.

C. Composition dependency of the structural patterns

As in other fluids with self-assembly features, we would expect a structural phase diagram rich in different nano-structures such as micelles, lamellas,... as a function of density. In this case, as we are dealing with a mixture, we have analyzed the ordered patterns that appear for different concentrations of monomers and dimers. We have analyzed this issue on the purely two dimensional fluid, again keeping a fixed packing fraction for every case so as to assess the effects of composition on their own. As before, $\eta_{2D} = 0.2513$.

Here we have performed simulations at a temperature slightly below T_c, ($T_r = 0.83$), so that the structures are more stable. As a consequence, one can first observe in Fig. 3.28, that for all compositions the system seggregates in a monomer fluid and a lamellar phase formed by layers of AB dimers oriented AB-BA, with C monomers interspersed between the A sites. After 7.5 ns lamellar domains coallesce into a single region in all cases but for $x_C = 11/12$. In this latter case one observes smaller domains separated by a sea of C-monomers. After sufficiently long simulation times, 15 ns, this domains also merge into a single region, which is the energeti-

cally most favorable structure. The low temperature and small number of dimers in this system makes the process extremely long.

Now in Fig. 3.29 we can take a look at the structure of the lamellar phase. One sees immediately the characteristic trigonal order of a 2D solid phase. In the case of the B sites this ordering is limited by the fact that they form a bilayer but for A sites and C monomers, one interestingly sees that each C monomer has the characteristic six neighbors of the trigonal phase, alternatively between A sites and C monomers. Despite this solid-like ordering, this lamellar structures are flexible, and for high monomer concentrations reorganize themselves constantly at the boundaries.

In summary, we can say that the most favorable structural patterns for all concentrations are seggregated lamellar regions which even though exhibit solid-like order, are flexible dynamic entities. At higher temperatures, as we have seen, the lamellar regions break into finite domains, that give rise to the maxima found in the cluster size distribution of Fig. 3.27.

3.1.2.2 Room temperature Ionic liquids

The aim of this Section is to understand the effect of neutral confinement over the structure of ionic liquids, exploring in which conditions the liquid wets the surface. This is an important feature for studying ionogels, i.e. ionic liquids which are confined in porous matrices improving the adsorption and storage capacity of the confining medium.

In particular, we have performed molecular dynamic simulations (using GROMACS [Berendsen et al., 1995; Lindahl et al., 2001]) of a room temperature ionic liquid with cations based on imidazolium organic salts, more specifically 1-butyl-3-methylimidazolium hexa-fluoro-phosphate ($[BMIM^+][PF_6]^-$), confined into slit pores made up of graphitic walls, see Figure **??**. Different pore sizes and fluid densities inside the pore have been considered in order to build a picture that illustrates the behavior of ionic liquid at different confinement levels, in particular the wetting properties

Table 3.4: Lennard-Jones parameters for the $[BMIM]^+$ cation [Canongia-Lopes et al., 2004]

	σ_{ij} (Å)	ϵ_{ij} (kcal/mol)
$C-C$	0.276	0.350
$H-H$	0.126	0.242
$N-N$	0.713	0.325

Table 3.6: Lennard-Jones parameters for the graphitic walls.

	σ_{ij} (Å)	ϵ_{ij} (kcal/mol)
$C-C$	0.0998	0.335

We have used the model of Canongia-Lopes et al. [2004] for simulating the $[BMIM^+][PF_6^-]$ ionic liquid. This model is based on the Jorgensen et al. [1996] OPLS-AA (optimized potentials for liquid simulations in an all-atom representation) force field, which includes intramolecular interactions such as bond stretching, angle bending, dihedral torsion, as well as van der Waals and Coulombic interactions. Thus, its functional form is the following:

$$
\begin{aligned}
E = & \sum_i K_{b,i}[r_i - r_{0,i}]^2 + \sum_i K_{b,i}[\theta_i - \theta 0, i]^2 \\
& + \sum_i \left[\frac{1}{2} V_{1,i}(1 + cos(\phi_i)) + \frac{1}{2} V_{2,i}(1 + cos(2\phi_i)) \right. \\
& \left. \frac{1}{2} V_{3,i}(1 + cos(3\phi_i)) + \frac{1}{2} V_{4,i}(1 + cos(4\phi_i)) \right] \\
& + \sum_i \sum_{j<i} \left\{ \frac{1}{4\pi\epsilon_0} \frac{q_i q_j e^2}{r_{ij}} + 4\epsilon ij \left[\left(\frac{\sigma_{ij}}{r_{ij}} \right)^{12} - \left(\frac{\sigma_{ij}}{r_{ij}} \right)^{6} \right] \right\},
\end{aligned}
\tag{3.5}
$$

where K is the force constant, r_0 and θ_0 the nominal values, q the partial atomic charges fixed on each atom center and distributed among the sites of the $[BMIM]^+$ and $[PF_6]^-$ as shown in [Canongia-Lopes et al., 2004], and σ_{ij} and ϵ_{ij} the LJ radii and potential well depths respectively. Lennard-Jones parameters for each type of atom are collected in Tables 3.4 and **??**, and the interactions between atoms of different type were parametrized using Lorentz-Berthelot mixing rules.

The walls of the slit pore we are considering in this work consist of three uncharged and completely rigid graphene layers separated by a distance 0.335 nm. They are made up of Lennard-Jones particles with $\epsilon = 0.0998$ KJ/mol and $\sigma = 0.335$ nm (see Table 3.6). The potential energy landscape inside the slit-pore, due to the graphitic walls, is represented in Figure **??** and shows two attractive wells near the walls and a flat region in the center

of the pore where the force is zero. The separation between the walls (Δ) gives us the pore width, and here we have considered: 7nm, 6nm, 5nm, 4nm, 3nm and 2.1nm; and the pore volume to calculate the fluid density is defined as $V = X \times Y \times (\Delta - 0.34nm)$, where X and Y are the size of the simulation box in those directions.

Computationally, we have employed the particle-mesh Ewald [Darden et al., 1993] method to handle long-range Coulomb interactions with a cut-off of 1.5nm and used a cut off for the Lenard-Jones interactions of 1.2nm. The temperature coupling was performed by means of the Nose-Hoover thermostat [Nosé, 1984; Hoover, 1985] and the pressure coupling by means of the Parrinello-Rahman algorithm [Parrinello and Rahman, 1980, 1981].

First of all, we have checked the consistency of the model both in bulk and confined. We have simulated the bulk system consisting of 128 $[BMIM]^+$ cations plus 128 $[PF_6]^-$ anions for testing the reliability of the model. After a simulation 5ns long we found that at room temperature the system density is $\rho = 1.350 g/cm^3$, which agrees with the simulated and experimental values from the literature ($\rho = 1.363 g/cm^3$, [Bhargava and Balasubramanian, 2007; Canongia-Lopes et al., 2004; Chun et al., 2001]).

Afterwards, the RTIL at the bulk density was confined into the slit pore, and the structural order emerged has been studied as a function of the pore width. Due to the high viscosity of ILs, we have to chose a high value of the temperature, $T = 550K$, in order to avoid that the system gets stuck into a local minimum. Even at this high temperature, the system's dynamic is very slow and long simulations (up to 10ns) are required to get reliable and symmetric density profiles. Figure 3.32 shows the density profile for the ionic liquid confined into slit-pores of different sizes illustrating anion and cation profiles; we have split the data into two graphs for clarity (left panel corresponds to bigger pores and right panel to smaller pores).

We have found peaks revealing an ordered structure induced by the presence of the walls, even in central areas of the pore for the largest widths.

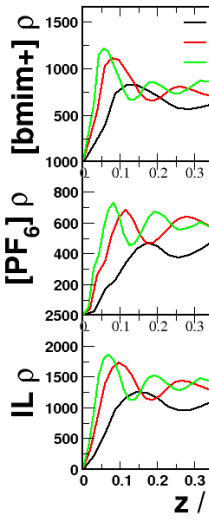

Figure 3.32 *and the total at T=550K a*

As one can appreciate in Figure 3.32, the number of layers depends on the pore size and in central regions of the larger pores, the ions show a more relaxed structure and density values converge towards these of the bulk system, $\rho_{bulk,T=550K}$ =1.156g/cm^3). This layered order found for the IL near the walls agrees with the literature [Singh et al., 2011a; Maolin et al., 2008] for this particular ionic liquid as well as for other systems [Rajput et al., 2012b; Singh et al., 2011b]. This feature has been also seen for confined molten salts systems in the 90s [Bratko et al., 1990].

The main goal of this study is to analyze the structure of the confined ionic liquid inside the pore, specially near the walls. We have already seen that when the density of the fluid is that of the bulk at the same temperature, it exhibits ordered layers next to the walls. Now, we will analyze how is the structure of the IL for a lower density. To this aim, we have performed MD simulations 12 ns long at $T = 550$ K for different pore loadings, and we have calculated the density profiles averaging over the resulting trajectories. Figures **??**, 3.34, **??**, 3.36, **??**, 3.38 show the profiles we have obtained, and complement then with snapshots of the corresponding systems.

We may see that for highest loadings (near the bulk density) the structure is similar for all the pore widths: a layered structure near the walls. However, when the liquid density decreases two different behaviors emerge depending on the pore size and the liquid density inside the pores. We designate them as *wetting*, when the mass density profile shows maxima near the walls; and *aggregation*, when there is empty space near the walls and the IL remains at the center of the pore. The transition between both behaviors is progressive, for the widest pores the ionic liquid takes the shape of a percolating sheet in the center of the pore, and as the pore width decreases the clusters start to stick to the walls avoiding the percolation and taking the shape of a pile between the walls.

Although the minima of the confining potential energy appear only next to the walls, the symmetry of the system and the strong electrostatic interactions between the ions, makes that at certain densities the IL molecules

prefer to stay in the center of the pore, separated from the walls. Somehow, this recalls the non-wetting behavior of water in graphitic walls, in which despite a LJ-like attraction between oxygen and carbon atoms, electrostatic interactions drive water molecules away from the wall. Here the situation is somewhere in between and wetting exhibits a density dependence, given the much larger attraction between the non-polar tails of the ions and the graphene walls.

Finally, in Figure **??** we present a diagram summarizing all the information about ILs structural behavior previously commented on. We may see that, depending on the IL loading and on the dimension of the pores, they behave in a different way. For high loadings ILs show layering order next to the walls for any pore size. However, when the amount of IL is not enough to completely fill the pore, they adopt two different configurations: for small pores, ILs are affected by the walls attraction and they thus form clusters that are fixed to the walls, keeping the layering order as we can see in the density profiles (wetting states); however, for larger pores, the ILs stay forming an infinite sheet in the middle of the pore (due to the symmetry of the system and the strong interactions between the ions), where the force is zero, and only the molecules closer to the walls notice the attraction.

From a practical point of view is clear, that with this type of RTIL it would not be possible to coat the walls of a porous carbon material with a layer of ions, so as to enhance the adsorption potential of the material. It remains open, the question of how one can actually modify the diagram of Fig. **??**, by tuning parameters such as the temperature and very specially the length of the non-polar tail of the cations.

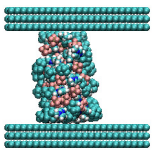

Figure 3.36:
correspond to
20%, 40%, 6

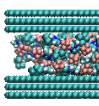

Figure 3.38:
correspond to
20%, 40% an

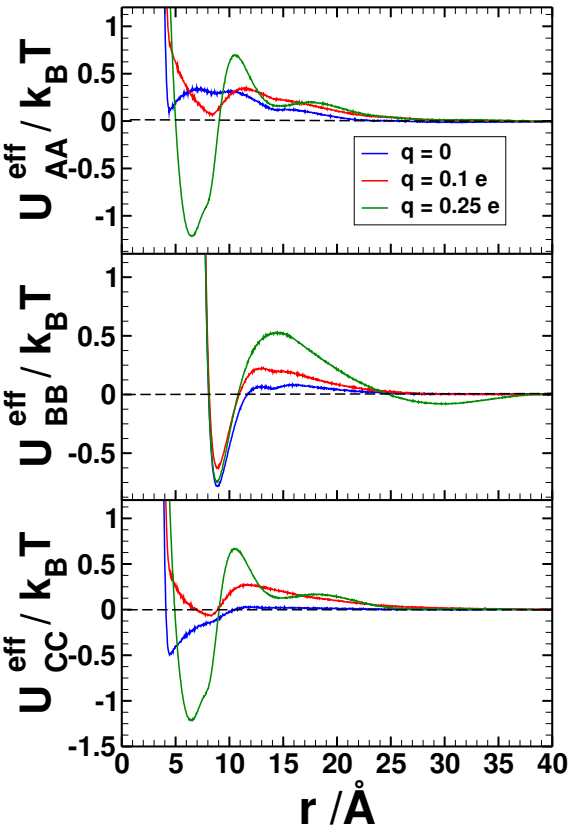

Figure 3.12: *Charge dependency of the effective potentials for A (top), B (middle) and C (bottom) particles. Charge magnitudes are specified in the legend. Values of r_{cl} correspond to the inflexion points of the effective potentials in their first minimum, i.e., $r_{cl}(A\text{–}A) = 6$ Å, $r_{cl}(B\text{–}B) = 11$Å, and $r_{cl}(C\text{–}C) = 10$Å.*

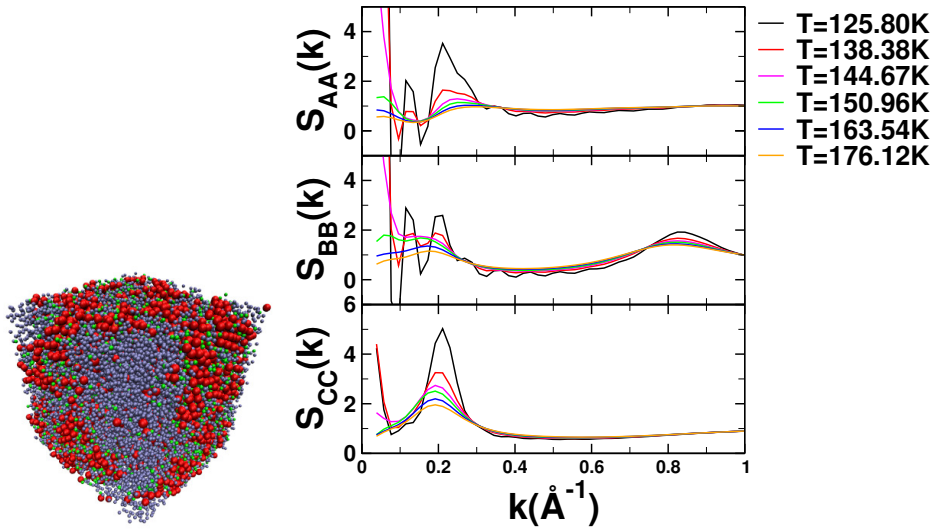

Figure 3.13: *Snapshot of the system at a temperature slightly below the critical value (left) and partial structure factors (right) of the bulk fluid* $\rho = 0.02\AA^{-}3$ *and* $x_{AB} = 1/3x_C$ *for different temperatures.*

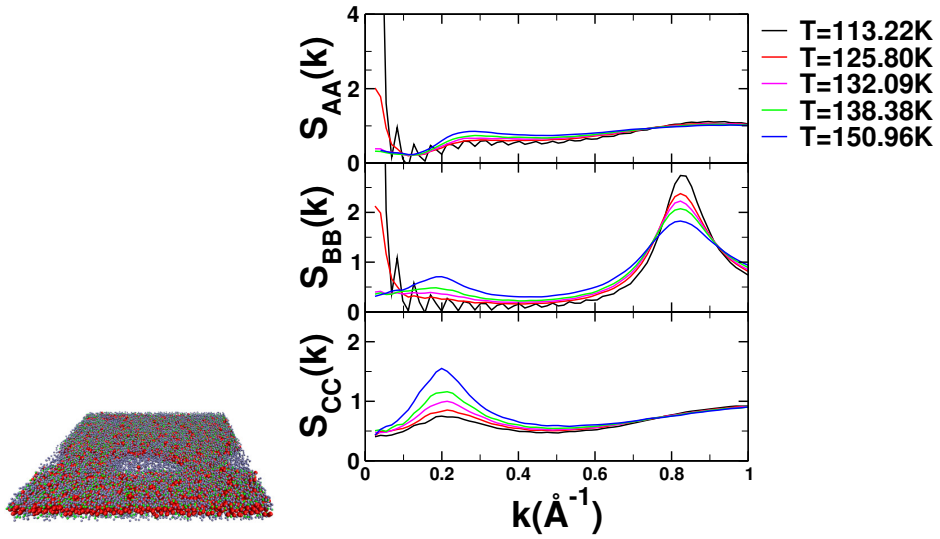

Figure 3.14: *Same as 3.13 for the fluid confined in a pore of* $W = 40\mathring{A}$.

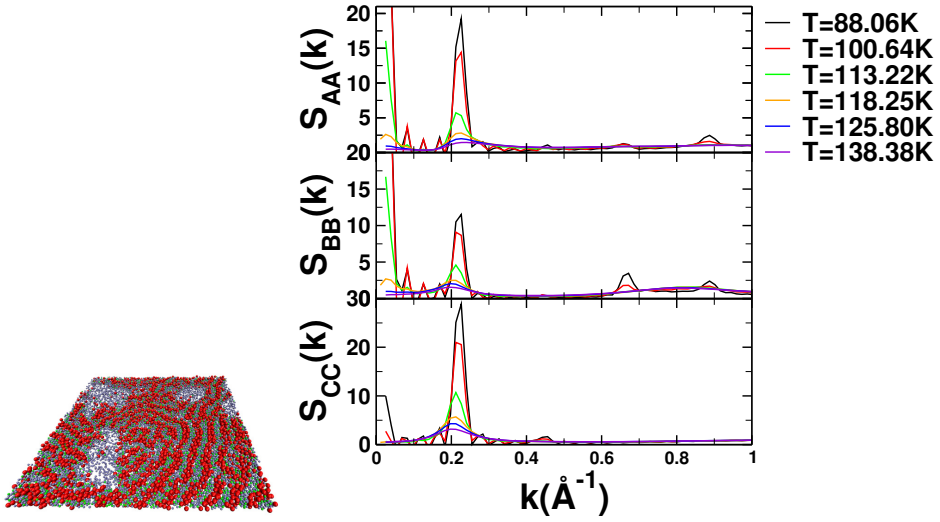

Figure 3.15: *Same as 3.13 for the fluid confined in a pore of* $W = 24\mathring{A}$.

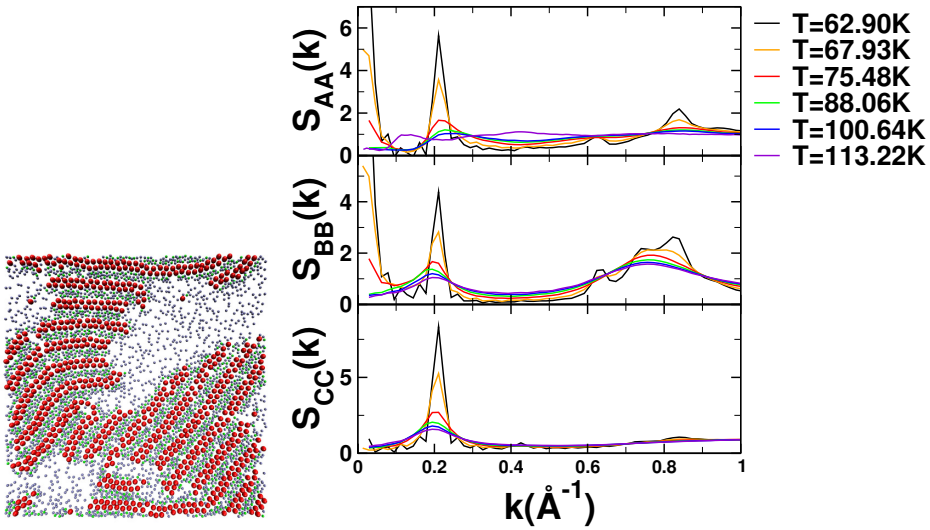

Figure 3.16: *Same as 3.13 for the fluid confined in a pore of* $W = 8\mathring{A}$.

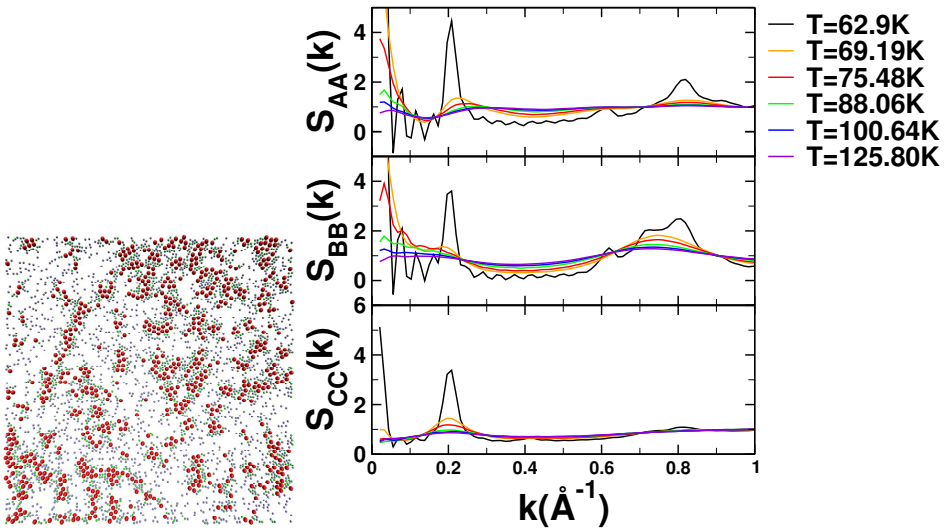

Figure 3.17: *Same as 3.13 for the purely 2D system.*

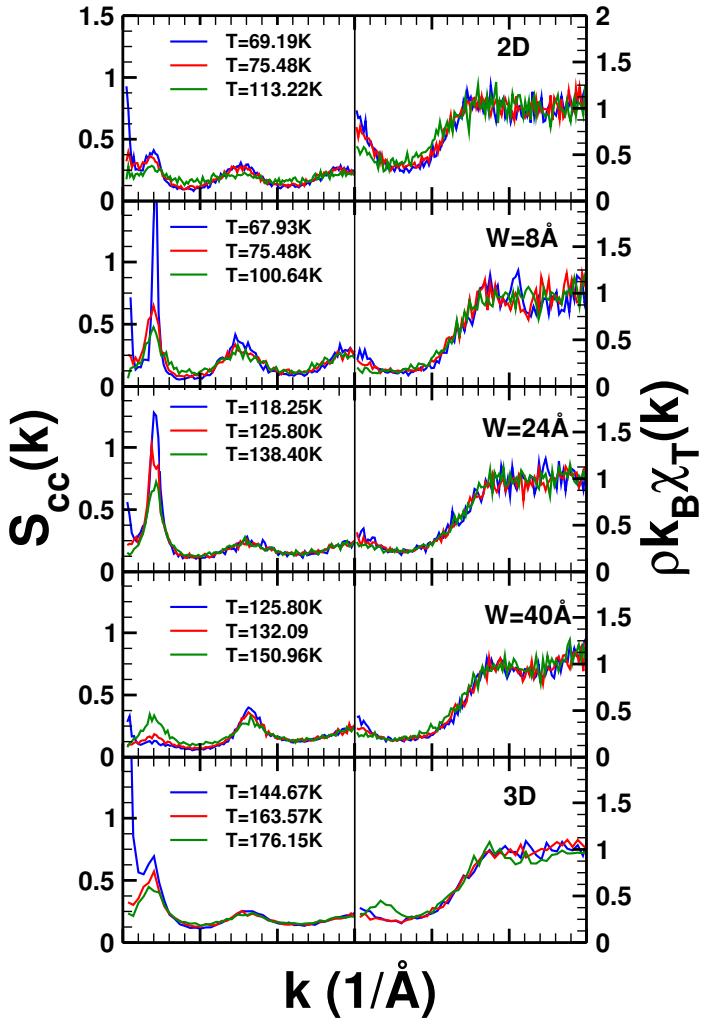

Figure 3.18: *Concentration-concentration structure factors (left) and Isothermal compressibility (right) for the fluid at* $\rho = 0.02\AA^{-}3$, $x_{AB} = 1/3x_C$ *and confined in different pore widths (from down to up: purely 3D,* $W = 40\AA$, $W = 24\AA$, $W = 8\AA$ *and purely 2D). Different temperatures are indicated in the key.*

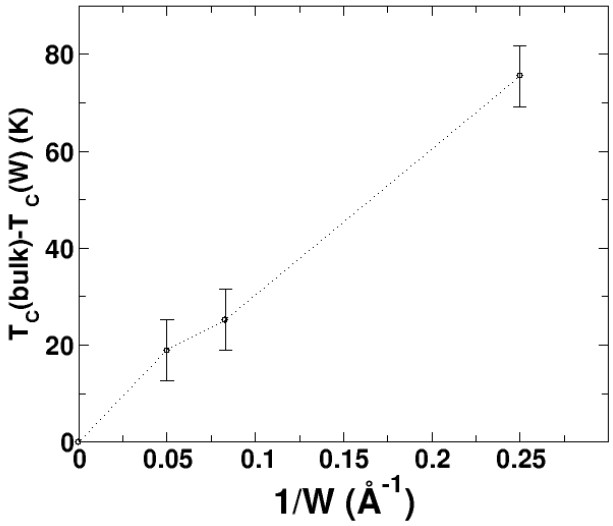

Figure 3.19: *Kelvin-like behavior of the critical temperature when decreasing the confining pore width:* $T_c(bulk) - T_c(W) \propto 1/W$.

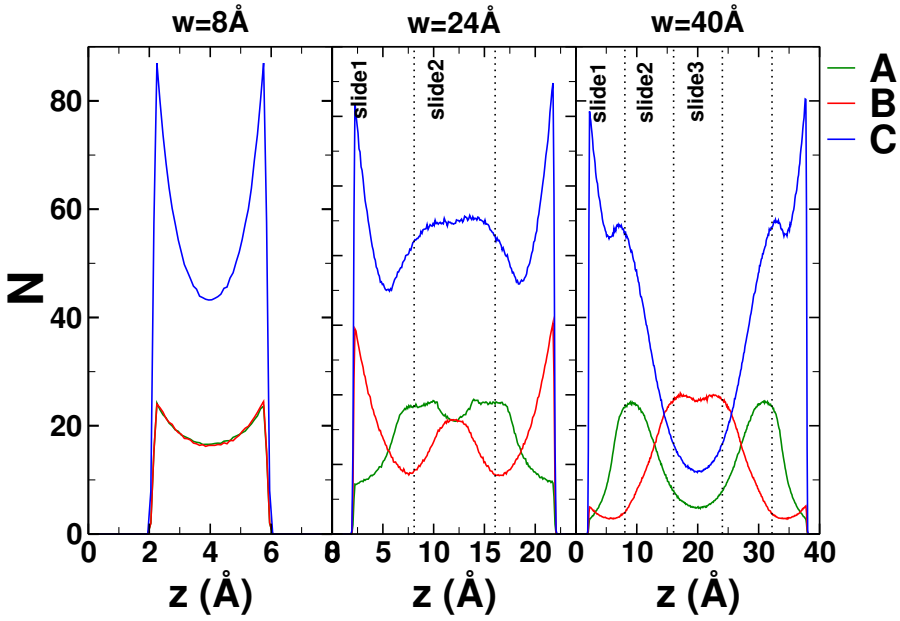

Figure 3.20: *Number density profiles of the binary mixture of dimers and monomers ($x_{AB} = 1/4$ and $x_C = 3/4$) confined in slit-pores of different widths: $w = 8Å$ (left panel), $w = 24Å$ (central panel) and $w = 40Å$ (right panel). Profiles for different particle specie are represented with different colors indicated in the legend. Dotted lines divide regions $8Å$ wide.*

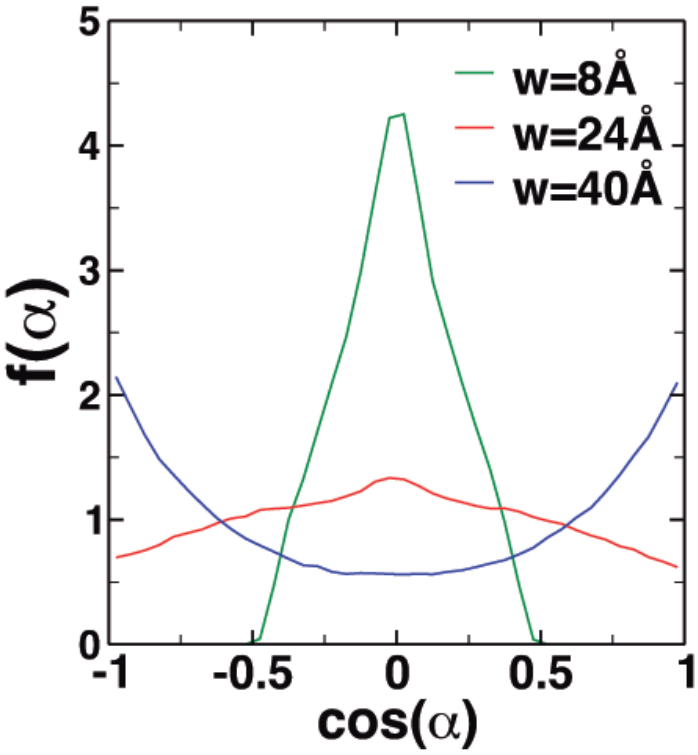

Figure 3.21: *Angular distribution of the AB dimers with respect to a vector perpendicular to the pore walls. It corresponds to the system confined in the three pore widths we have considered:* $w = 8\AA$, $w = 24\AA$ *and* $w = 40\AA$*; at a temperature above the critical one:* $T_r = T/T_c = 1.1667$.

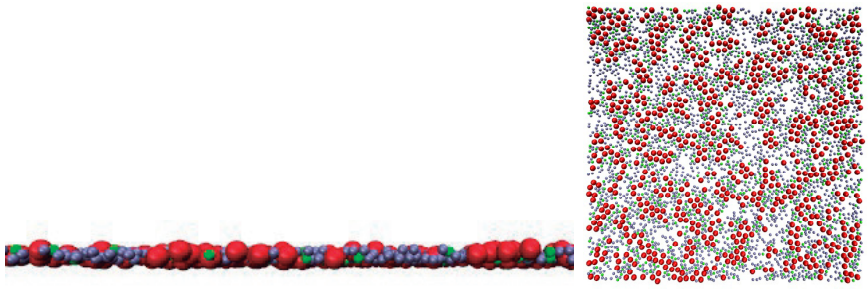

Figure 3.22: *Snapshots of the fluid confined in a pore* $8\mathring{A}$ *wide. Two views have been displayed for a better comprehension of the system: right figure corresponds to a plane perpendicular to the pore walls and the left one to a parallel plane.*

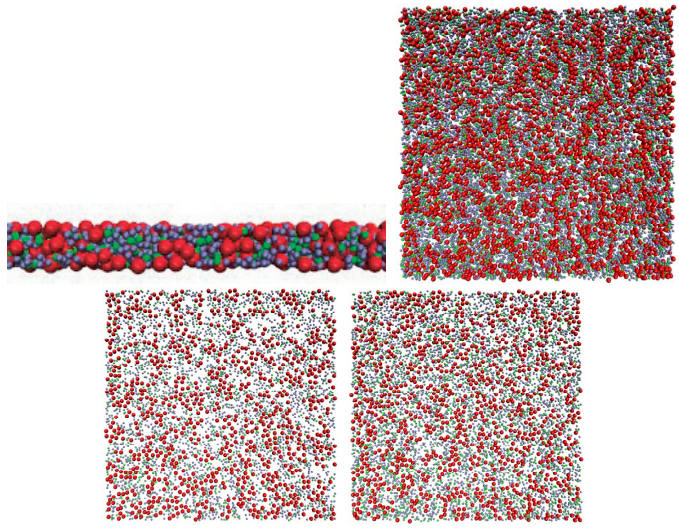

Figure 3.23: *Snapshots of the fluid confined in a pore* $24\mathring{A}$ *wide. We have split the configuration into three slides* $8\mathring{A}$ *wide, and we show here only two of them (the other one are omitted due to the symmetry across the pore): region near the walls (left), and the center of the pore (right).*

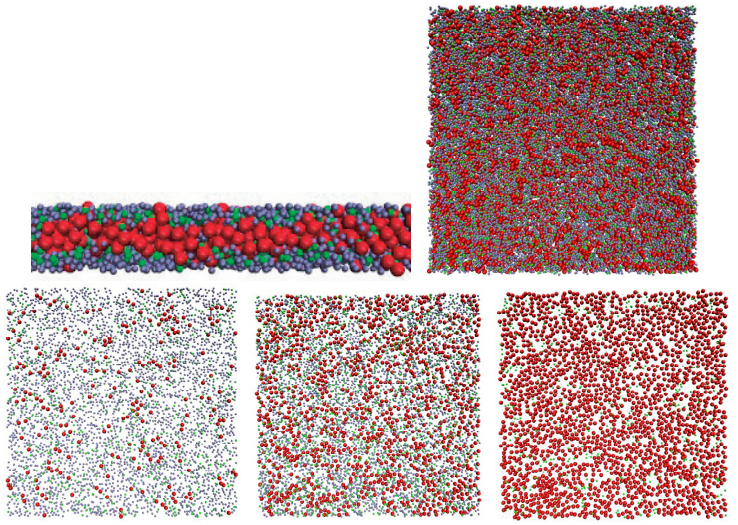

Figure 3.24: *Snapshots of the fluid confined in a pore* $40\mathring{A}$ *wide. The configuration has been split into five slides* $8\mathring{A}$ *wide, and we show here only three of them (the others two are omitted due to the symmetry across the pore): region near the walls (left), intermediate region (central) and the center of the pore (right).*

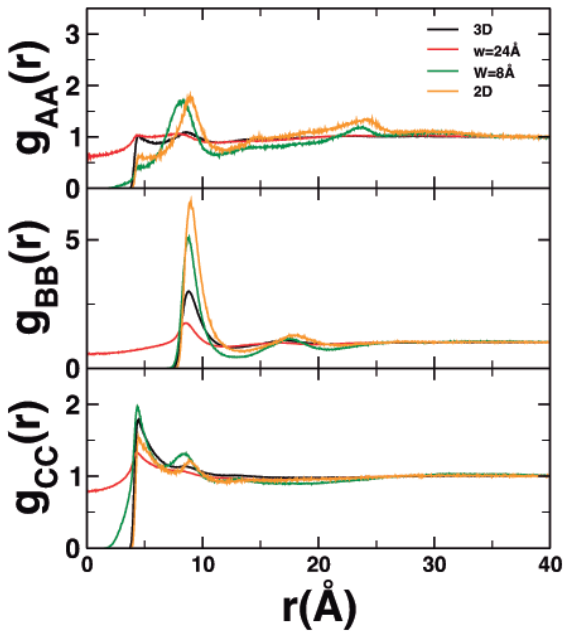

Figure 3.25: *Radial distribution function (left) and structure factor (right) for equivalent systems under different confinement conditions (different colors).*

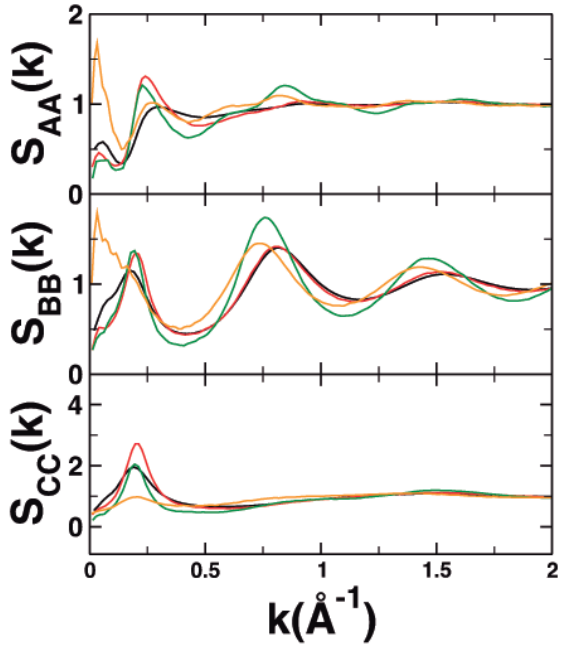

Figure 3.26: *Radial distribution function (left) and structure factor (right) for equivalent systems under different confinement conditions (different colors).*

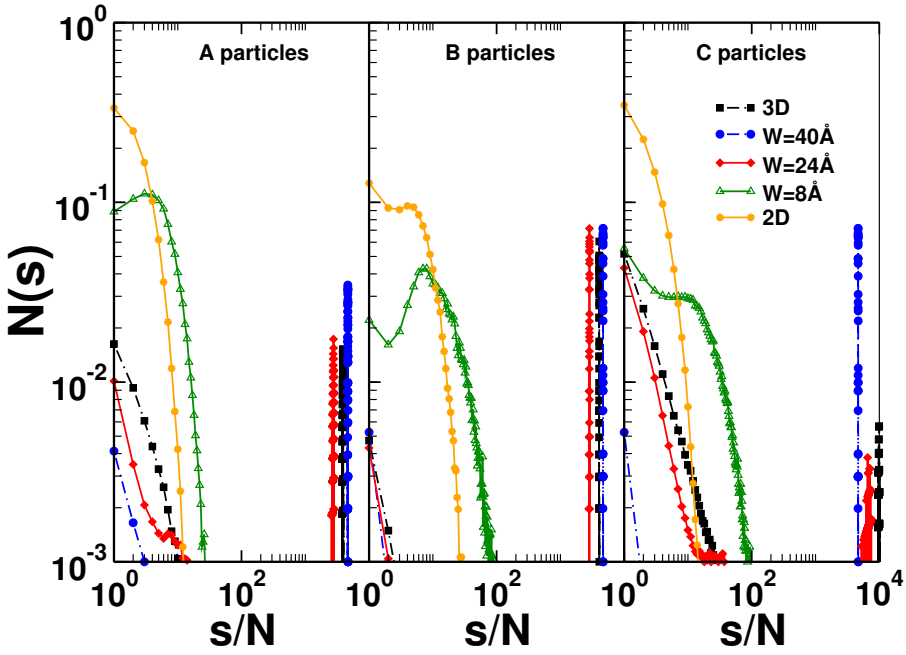

Figure 3.27: *Radial distribution function (left) and structure factors (right) for equivalent systems under different confinement conditions (different colors).*

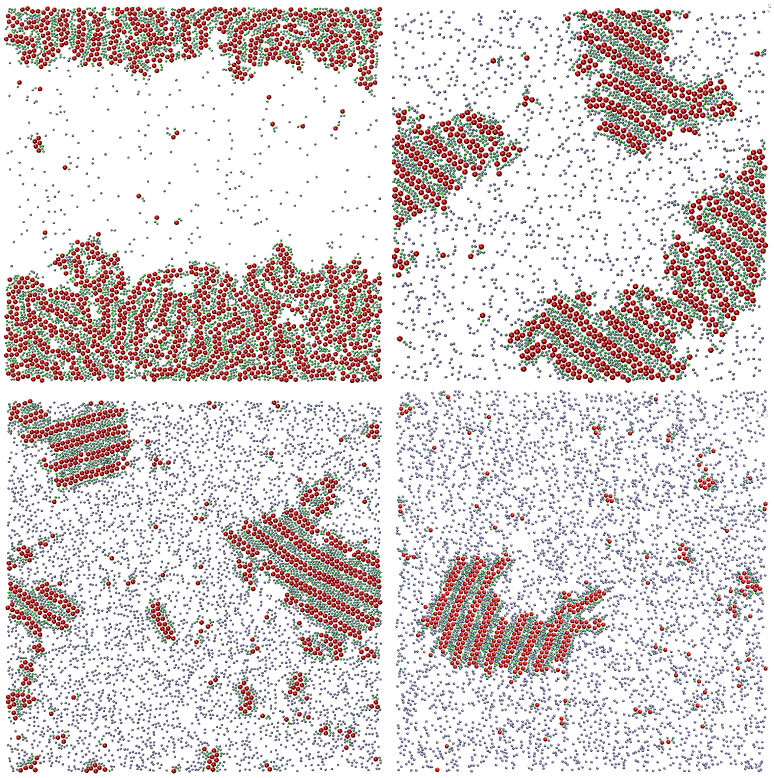

Figure 3.28: *Snapshots of the two-dimensional binary mixture at different monomer concentrations at* $T_r = 0.833$. *From left to right:* $x_C = 1/2$, $x_C = 3/4$, $x_C = 7/8$ *and* $x_C = 11/12$

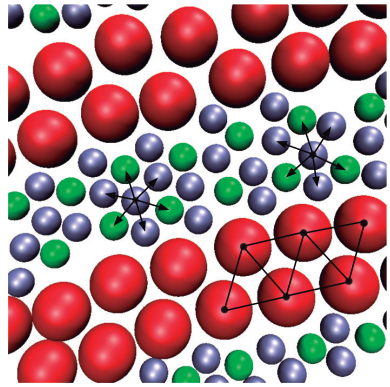

Figure 3.29: *Zoom showing quantitatively the hexagonal order emerged between the system particles within the lamellar pattern.*

3.2 Topological disorder: confinement and self-assembly

In this section we will study the influence of confinement realized via a disordered, porous matrix on the properties of a fluid with competing interactions. Being more specific, we have analyzed the structural and dynamic behavior of a system composed of a two-dimensional SALR fluid confined into a controlled pore size glass, where the typical pore size ranges are between $1nm$ and $1\mu m$. Since matrix-fluid interactions will be modeled by plain hard-core repulsions, we can anticipate that any deviations in the behavior of the confined fluid with respect to the properties of the bulk fluid will originate from the effects of randomness and the topology of the confining matrix. Here, using both GCMC simulations and a two-dimensional OZ approach, we have studied the structural and thermodynamical properties of both bulk and confined SALR fluid. Additional MD simulations in the canonical ensemble will be run to obtain accurate density profiles and analyze the dynamic properties of the confined fluid.

The system under study will be described in the first part of this section where we analyze the features of matrix and adsorbent fluid separately. Following sections present the results we have obtained for the confined self-assembling fluid concerning its thermodynamic, structure and dynamical properties.

3.2.1 Devising the model

This is a quenched-annealed system where the quenched component is a solid matrix based on a controlled porous glass (CPG) obtained by means of a templating process. The annealed component is a SALR fluid exhibiting spontaneous aggregation. In the next we describe the essential characteristics of the fluid and the process of generation of the confining medium: the porous matrix.

- **Self-assembling Fluid**

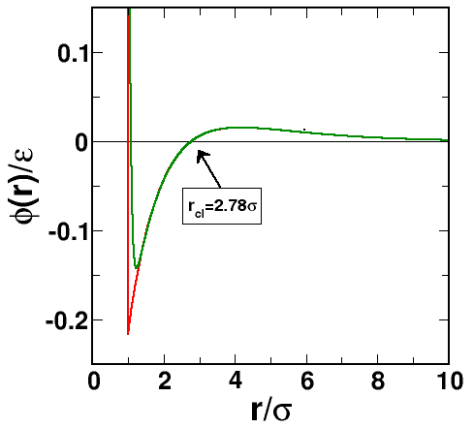

Figure 3.40: *Interaction potential $\Phi(r)$ as a function of the distance r. The red line shows the original SALR potential as used in [Imperio and Reatto, 2004, 2006] with the parameters specified in the text; the green line denotes the softened version of the SALR potential used in this contribution and as specified in equation 3.6. The distance r_{cl} highlighted in the figure corresponds to $\Phi(r_{cl}) = 0$ and defines our reference distance to consider two particles linked in a cluster.*

The particles of the fluid considered in this section interact via a potential, $\phi(r)$, which consists of a short range repulsive region (with a spatial extent σ) plus a tail that is attractive at short distances and repulsive at larger particle separations. Here, we have chosen a slightly modified version of the parameterization for this type of interaction introduced previously by Sear et al. [1999] and analyzed in detail in several works by Imperio and Reatto [2004, 2006, 2007]; Imperio et al. [2006]; Schwanzer and Kahl [2011]. This potential has the shape shown in Figure 3.40 and the following functional form:

$$\begin{aligned}\phi(r) &= u^{at} + u^{rep} + u_{sr} \\ &= -\epsilon_a \frac{\sigma^2}{R_a^2} \exp(-\frac{r}{R_a}) + \epsilon_r \frac{\sigma^2}{R_r^2} \exp(-\frac{r}{R_r}) + (\frac{\sigma+\delta}{r})^n \end{aligned} \tag{3.6}$$

The strength and the range of the attractive and repulsive interactions of the potential tail are represented by ϵ_a, ϵ_r, σ_a and σ_r respectively; the short range repulsive part of $\phi(r)$ is given by the term $u_{sr}(r)$, where $n = 20$ and $\delta = -0.01\sigma$. For computational convenience all interactions are cut and shifted at $R_c = 10\sigma$.

In our case, we have chosen the following potential parameters: $R_a = \sigma$, $R_a = 2\sigma$, $\epsilon = \epsilon_a = \epsilon_r$, that have been used and tested in previous studies of SALR fluids. The cutoff radius is chosen large enough to preserve the clustering behavior; since the cutoff is located in the repulsive tail of the interaction, increasing the cutoff value would only imply larger inter-cluster separations. Decreasing the repulsive range would lead to a collapse of the clusters giving rise to a vapour-liquid transition. In fact, very recently Godfrin et al. [2014] have suggested using a reference fluid in which the repulsive part of the SALR interaction is removed in order to map the clustering region onto the vapor-liquid spinodal of the reference fluid. As mentioned before, the long-range repulsion stabilizes the clusters, therefore this corresponding states phase behavior helps to define the limits of stability of cluster regions, but obviously does not provide information on the different types of cluster topologies present.

As usual, we have introduced the dimensionless temperature, $T^* = k_B T/\epsilon$. The potential $\phi(r)$ is drawn as a function of the distance r in Figure 3.40 for this particular set of parameters.

- **Porous Glass Matrix**

  For our theoretical investigations we create a matrix by a process that mimics the experimental preparation of a realistic controlled pore glass.

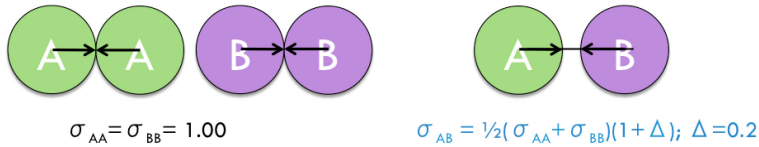

Figure 3.41: *Illustration of the non-additive binary mixture, which acts as the solid matrix precursor.*

In an effort to capture the main features of the CPG fabrication in our model of the matrix, we have reproduced the method used by Gelb and Gubbins [1998]. This is a realistic method that mimics the processes by which Vycor and controlled-pore glasses are produced by making use of spinodal decomposition [Siggia, 1979], quenching and removal of one of the components.

Instead of the Lennard-Jones mixture used in [Gelb and Gubbins, 1998], we have used in our investigation one of the simplest possible systems that shows spinodal decomposition: a binary mixture of (positively) non-additive hard disks [Dijkstra, 1998]. In this system the diameters of both species (labeled 'A' and 'B') are equal ($\sigma_{AA} = \sigma_{BB} = \sigma$), and will be used henceforward as the unit length, while the cross interaction diameter is set to: $\sigma_{AB} = \frac{1}{2}(1 + \Delta)\sigma$ with $\Delta > 0$, demixing will be driven by entalpic and entropic effects (at constant pressure volume effects). This means, for a given pressure the system will try to maximize the entropy (disorder) and minimize the occupied volume. Figure 3.41 illustrates this system.

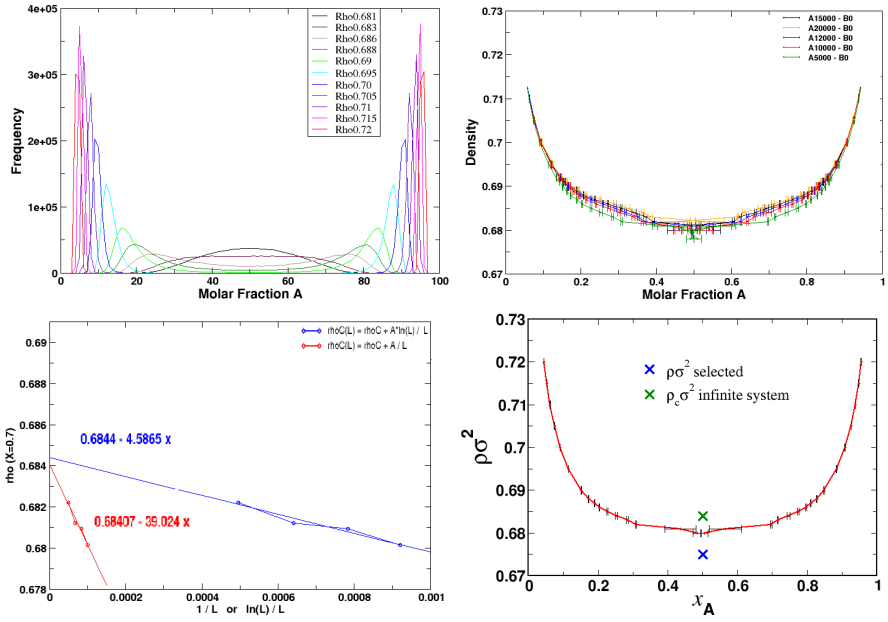

Figure 3.42: *Critical density value determination.*

For this binary mixture we have performed semi-grand canonical Monte Carlo simulations, imposing the difference in chemical potential $\Delta\mu = \mu_A - \mu_B$ between species A and B, the area $A = L^2$ with L being the edge length of the square simulation box, the temperature T and keeping the total number of particles $N = N_A + N_B$ fixed; $x_A = N_A/N$ is the concentration of particles of species A. The total number density $\rho = N/A$ is thus fixed. In addition to the conventional Monte Carlo moves, particles can also exchange their identity in suitable Monte Carlo moves [Lomba et al., 1995]. After 5×10^5 Monte Carlo sweeps for equilibration, our simulations were typically extended over 10^6 Monte Carlo sweeps.

Thus, setting the parameters to the values described in the para-

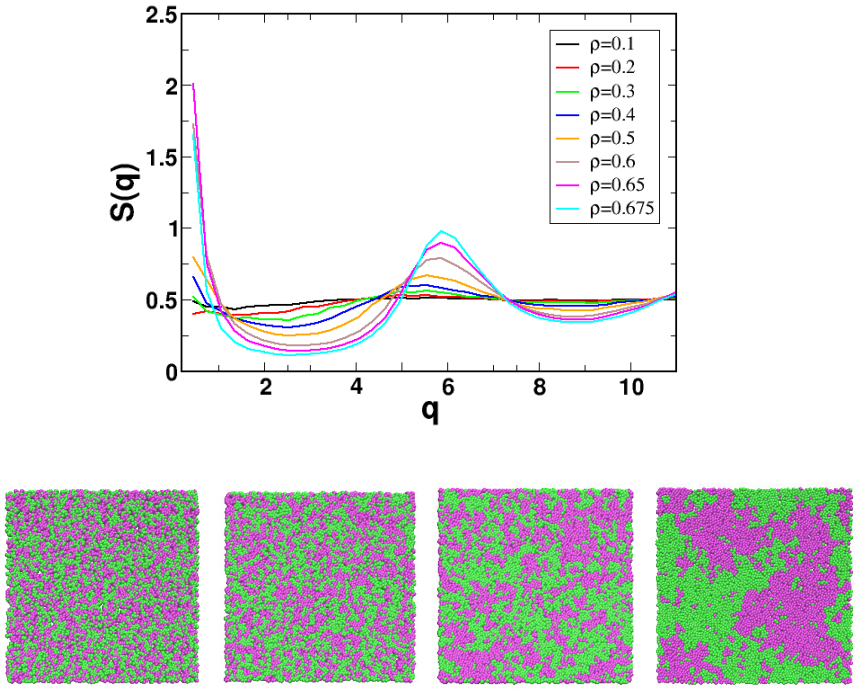

Figure 3.43: *Structure factor of the A-particles at different densities (upper graph), and typical snapshots of our two-dimensional binary mixture of non-additive hard spheres (lower pictures) as we increase the density of the system to the critical value where the demixing transition occurs. The respective values for the overall number density are:* $\rho\sigma^2 = 0.4, 0.5, 0.6$ *and* 0.675*, from left to right.*

graph above, the system undergoes above a certain critical density, ρ_c, a demixing transition. Analyzing the molar fraction histograms for the binary mixture for different densities and system sizes, the concentrations at coexistence, $x_A(\rho)$ and the phase diagram of the system can be evaluated. In an effort to locate the critical density

ρ_c at which demixing transition occurs, we have considered different system sizes with N varying between 5000 and 20000 particles, see Figure 3.42.

Using the scaling laws given in [Ferreira and Prodanescu, 2005], the value of the critical density for an infinite system size is estimated to be $\rho_c = 0.684$. As we approach the density of the system to the critical value, the system demixes (see Figure 3.43), and for density values close to the critical density the system exhibits strong spatial fluctuations in x_A (and conversely in x_B), a fact that will be of relevance when creating a matrix of desired density, ρ_m and porosity.

So, for a given system size, we choose a total density sufficiently close to the spinodal decomposition (say $\rho\sigma^2 = 0.675$) where concentration fluctuations approach the range of the simulation box. The corresponding partial structure factors $S(k)$ for the A-particles at different densities are depicted in upper graph of Figure 3.43. It shows that a divergence appears at low k-values when we approach the critical density, a feature characteristic for a system close to spinodal decomposition that is a direct result of the presence of concentration fluctuations (or clustering) with length scales comparable to the simulation box size. Moreover, the low-k behavior of $S_{AA}(k)$ corresponds to that of a porous material and can be related to the surface of the pore network and its structure: this is a much used approach in the analysis of small angle diffraction data in porous materials [Sink'o et al., 2008].

Now we quench the system (freeze the particle positions) and from these particle configurations we construct our matrix: one of the two particle species will play the role of matrix particles (A particles) while the other specie acts as a template (B particles) and is to be removed thereby creating the pores of our matrix. In addition, those A particles that remain disconnected after the removal of the B particles are also removed. Connectivity of the matrix is analyzed by

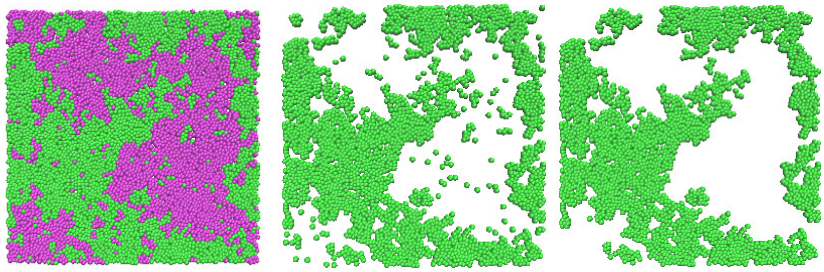

Figure 3.44: *Visualization of the matrix creation process.*

identifying clusters of matrix particles, and two particles are considered to be linked in a cluster if their separation is smaller than two particle diameters. All disconnected clusters formed by less than ten particles are removed. This procedure attempts to roughly mimic the template and some loose matrix particles being washed away from the porous matrix. This process is schematically displayed in Figure 3.44.

We have analyzed and characterized the porous structure on a quantitative level by means of a Delaunay decomposition (see Section 2.2) of the simulation cell. Starting from the positions of the matrix particles centers (top-left panel of Figure 3.45) Delaunay triangles are constructed following the rules well defined in [Delaunay, 1934; Torquato, 2001] (see top-right panel of Figure 3.45). The edges of these triangles are now classified either as 'crossable' edges (i.e. they are sufficiently long to let particles of diameter σ pass) or as 'non-crossable' edges (i.e they are shorter than σ); these edges are respectively colored in green or red in the bottom-left panel of Figure 3.45. We have discarded, for obvious reasons, those Delaunay triangles with only non-crossable edges (marked with a red cross in bottom-right panel of Figure 3.45) and finally retained only accessible Delaunay triangles with crossable faces and that can be reached by the fluid particles by diffusion and inclusion (those marked with green and orange crosses in bottom-right panel of Figure 3.45).

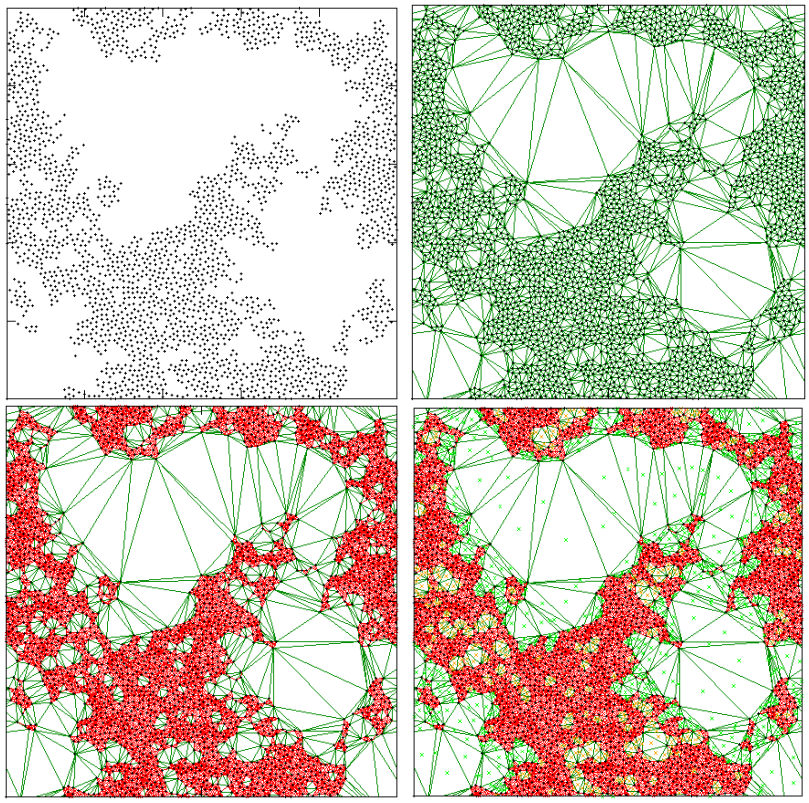

Figure 3.45: *Quantitative analysis of a representative matrix configuration based on a Delaunay decomposition. See text for a full explanation of the method.*

The total area covered by accessible Delaunay triangles in relation to the total surface of the simulation cell yields the porosity parameter p (defined as the ratio of area available for the insertion of a test fluid particle in an empty matrix configuration with respect to the total matrix sample area), with $0 \leq p \leq 1$. In this way we can generate many equivalent disordered matrix configurations and perform its analysis in terms of a Delaunay decomposition. We obtained

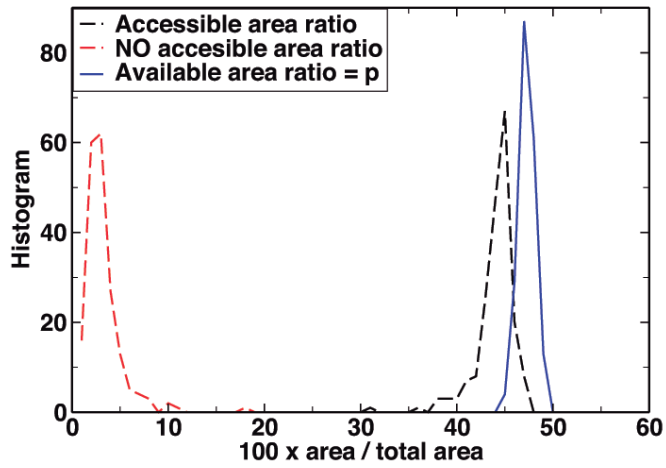

Figure 3.46: *Ratio of different areas with respect to total sample area found for 100 independent configurations of porous glasses. Porosity p (available area/total area) displays a narrow distribution around* $p \approx 47\%$ *which agrees with the experimental porosity of these materials.*

a narrow probability distribution of the porosity value (displayed in Figure 3.46) of all the generated matrices, centered around $p \approx 47\%$. The value obtained if the accessible area is used instead porosity is somewhat lowe, $\approx 45\%$, but comparable to the value of p. We note in passing that the composition of the original sample prior to quenching and removal of B particles is not equimolar. This explains why the portion of solid material in the matrix is above 50%, and is simply due to the fact that in the semi-grand canonical ensemble the composition fluctuates. Interestingly, we find for these model porous glasses porosities that lies within the experimental range [Gelb and Gubbins, 1998].

- **Matrix-fluid interactions**

The interaction between matrix (denoted by the subscript 1) and fluid particles (denoted by the subscript 0) used in this Section is a simple short range repulsion. However, we have slightly modified the plain hard-core repulsions in order to avoid the divergence and be able to perform MD simulations, as we did with the short-range repulsion between fluid particles (last term in Equation 3.6):

$$u_{01}(r) = (\frac{\sigma + \delta}{r})^n \tag{3.7}$$

taking $n = 20$ and $\delta = -0.01\sigma$.

Simulations have been realized in a square simulation box of area $A = L^2$ using periodic boundary conditions. In the case of the bulk fluid we have used $L = 64\sigma$ and for the confined system $L = 86\sigma$. When comparing values of the densities of the bulk and of the confined fluid (ρ_0), in the latter case we refer to the *effective* density of the adsorbed fluid, evaluated as the number of fluid particles per area of the accesible matrix sample. Densities reported correspond to averages along the simulation runs and have standard deviations that vary typically in the range of $1 - 3\%$.

An explicit description of the structure of a fluid inclusion in a particular matrix configuration can be achieved by means of an approximation to the full twodimensional solution on the Ornstein-Zernike (OZ) equation following the prescription of Beglov and Roux [1995]. A key element in this description is the approximation of the fluid-fluid direct correlation function, for which in [Beglov and Roux, 1995] that of the bulk fluid was used. As we mentioned in **Section 2.3**, this is inappropriate under conditions of close confinement, and in the present instance, the fluid-fluid correlation will be approximated by that of a confined fluid in a disordered matrix, which is in turn averaged (via the ROZ-formalism) over disorder. The matrix is here manufactured by means of a templating procedure, which means that the problem can also be theoretically modeled with the Zhang and Tassel [2000] ROZ formulation.

3.2.2 Thermodynamics

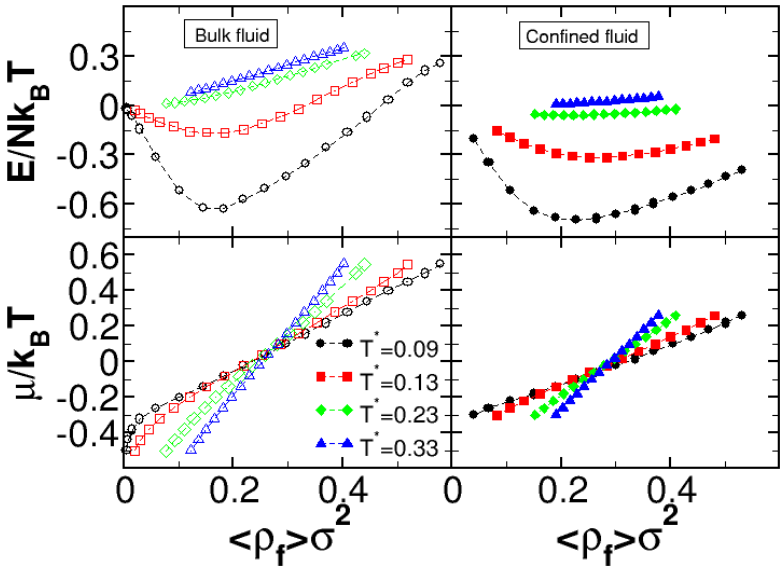

Figure 3.47: *Upper graphs: temperature scaled internal energy E/Nk_BT. Lower graphs: chemical potential μ/k_BT. These quantities are represented versus the fluid density $<\rho_1>\sigma^2$ and correspond to the SALR fluid in the bulk (left panel) and adsorbed into the matrix (right panel) at different temperatures indicated in the legend. Lines are drawn as a guide to the eye.*

The adsorption isotherms [1] (chemical potential, μ/k_BT versus average fluid density $<\rho_1>$) and the fluid potential energy E/Nk_BT for the bulk and in confinement are shown and compared in Figure 3.47. These quantities are represented versus the average fluid density $<\rho_1>\sigma^2$ for several temperatures from $T^*=0.09$ to $T^*=0.33$, corresponding to state points

[1] Strictly speaking the adsorption isotherm represents the quantity of adsorbate -e.g. in $mmols/g$ of adsorbate- versus the adsorbate pressure. This quantity can be directly connected with μ/k_BT using an equation of state.

where cluster formation is observed. We first observe that the fluid density and the chemical potential exhibits a rather linear dependence. The slope of the curves is somewhat smaller for the confined fluid, i.e. at the same chemical potential the density of the confined fluid is higher than in the bulk. This is the result of the missing long range repulsions between the matrix particles and the fluid ones, and the fact that the matrix particles are clustered together by construction, minimizing the fluid-matrix repulsive energy. For this reason, the work needed to insert a particle in the matrix cavities with fluid is lower than in the bulk.

Effects of clustering are visible in the energy at low temperature: the energy curves exhibit a minimum and then bend upwards as the density is increased ($\rho_1\sigma^2 \gtrsim 0.15$ in the bulk and $\rho_1\sigma^2 \gtrsim 0.23$ under confinement) due to the effect of increasingly dominant inter-cluster repulsions. The presence of the matrix shifts the effect of long-ranged interparticle repulsion to a higher fluid density value and the potential energy remains negative over all the density range considered. These features are most likely due to the effect of the limited spatial separation forced upon the fluid particles as a consequence of the presence of matrix. One might expect on this basis that the cluster phase will be stable even up to higher densities in the confined system. This will become evident in the next subsection when plotting the structural phase diagram.

As a first test of our theoretical approach, we have checked the performance of the ROZ-HNC equation for the matrix density $\rho_0\sigma^2 = 0.314$. This corresponds to the highest density for which the HNC equation can be solved for the non-additive hard disk fluid which is the precursor of our templated matrix. The HNC matrix-matrix correlations enter the solution of the ROZ-HNC equations, and therefore, in all theoretical calculations in this work, we will approximate the confined fluid-fluid correlations by those of the ROZ-HNC solved for a matrix of $\rho_0\sigma^2 = 0.314$, even when the case of study has a somewhat larger matrix density and hence a different topology.

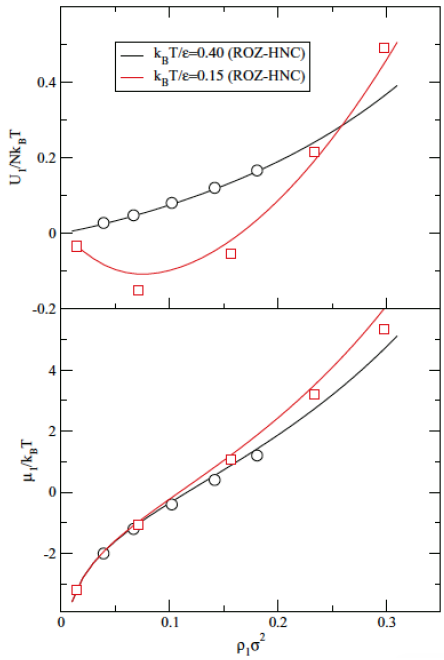

Figure 3.48: *Average fluid excess internal energy and chemical potential for a matrix density* $\rho_1\sigma^2 = 0.314$ *at various temperatures.*

In Figure 3.48, we plot the adsorption isotherms (lower curve) and the excess potential energy obtained from the ROZ equations for the SALR fluid inserted into the matrix solved following the procedure introduced in [Lomba and Weis, 2010] and with the same discretization conditions (see details in Section 2). These graphs correspond to a relatively high temperature ($k_BT/\epsilon = 0.4$) and a much lower one ($k_BT/\epsilon = 0.15$), for which clustering effects can be appreciated. Actually, the low density non-monotonous behavior of the internal energy reflects the competition between attractive forces (dominant at low densities) and repulsive forces that start to shape the system's behavior for densities above $\rho_1\sigma^2 \approx 0.06$. The simulation results correspond to averages over ten matrix configurations. We see that the

ROZ-HNC results for this situation perform rather well, with minor deviations, for the internal energy in the region where clustering effects start to dominate. This of course can be understood taking into account the limited performance of the HNC in the strong association regime [Hoye et al., 1993].

3.2.3 Structure

We have studied the characteristic mesophases that occur in the SALR fluid in bulk and we have investigated to what extent they appear in the confined geometry. To this aim we have calculated correlation functions, 2D density maps and cluster distributions. All these results are described in the following items:

3.2.3.1 Correlation functions and pattern formation

We have first performed a qualitative visual inspection of characteristic snapshots for thermodynamic states exhibiting characteristic clustering patterns, followed by a more quantitative analysis in terms of *structure factors*, $S(k)$, and *pair distribution functions*, $g(r)$. These results are collected in Figure 3.49 for the bulk and in Figure 3.50 for the confined fluid.

We start our discussion with the bulk case: in the left column of Figure 3.49 one can see in representative snapshots of the system (taken at a sufficiently low temperature $T^* = 0.09$) that particles self-assemble into the characteristic mesophases corresponding to each density ($< \rho_1 > \sigma^2 = 0.144$ shows droplets, $< \rho_1 > \sigma^2 = 0.2955$ shows stripes and $< \rho_1 > \sigma^2 = 0.4454$ shows bubbles). On the other hand, in the left column of Figure 3.50 we have presented the corresponding snapshots for the confined system at fluid densities similar to those of the bulk case. From a simple visual inspection one can already infer that our particular type of confinement tends to favor the formation of droplets over the percolating structures; only for higher fluid densities signatures of stripe formation within the pores are observed.

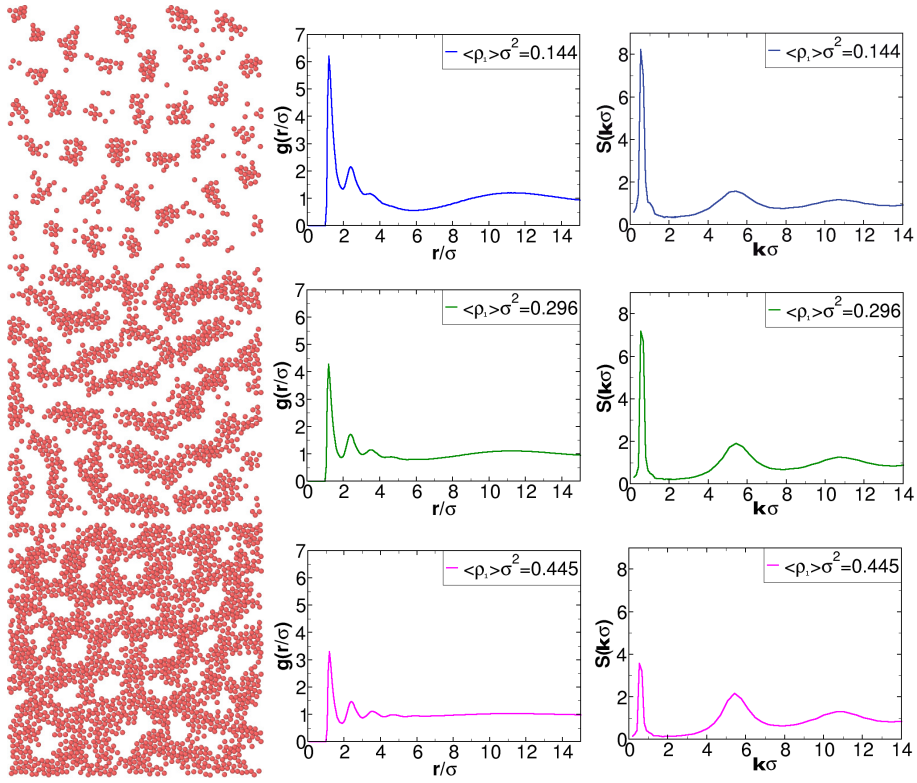

Figure 3.49: *Left panels: typical snapshots obtained by means of GCMC simulations of the system studied in this section: a two-dimensional system where particles interact via the potential described in Equation* (3.6)*. The temperature was set to* $T* = 0.09$*; snapshots were taken at different densities (from top to bottom* $< \rho_1 > \sigma^2 = 0.144$*,* $< \rho_1 > \sigma^2 = 0.2955$ *and* $< \rho_1 > \sigma^2 = 0.4454$*). Central panels: pair distribution functions* $g(r)$ *as function of* r*. Right panels: static structure factors* $S(k)$ *as function of* k*.*

Our qualitative observations are also reflected in the corresponding pair distribution functions and the structure factors, collected in the second and

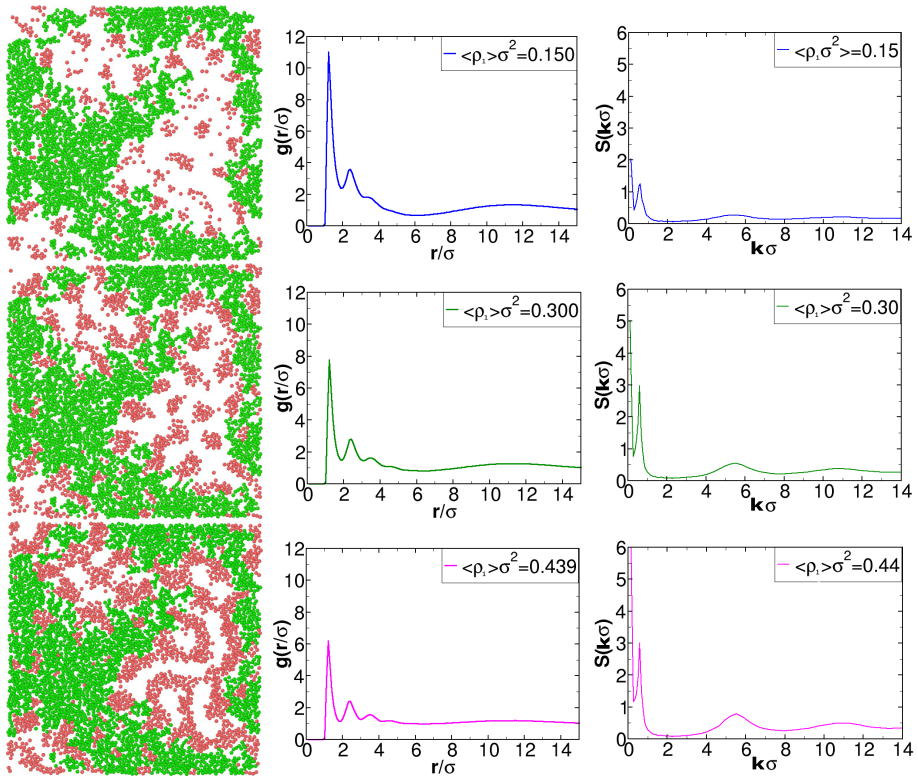

Figure 3.50: *The same as Figure 3.49 for the fluid confined in the porous matrix. average fluid densities are indicated in the graph legends.*

third columns of Figures 3.49 and 3.50. These graphs show the distinct signature of clustering or intermediate range order, namely the presence of a large prepeak in $S(k)$ and a wide maximum in $g(r)$ at intermediate distances corresponding to the inter-cluster separation [Schwanzer and Kahl, 2010; Imperio and Reatto, 2006, 2007; Archer, 2008].

The structure factor $S(k)$ shown in the last column of Figures 3.49 and 3.50 for bulk and confined SALR fluid respectively, provides evidence for

the occurrence of a mesophase at an intermediate range via a prepeak at low q-values. In the confined case we observe a marked growth in $S(k)$ as $k \to 0$, a characteristic feature of the presence of a porous structure with long-ranged correlations induced by the matrix. By construction these correlations have in our case the same range as the spatial extent of the simulation box, since they result from the proximity of the spinodal decomposition of the non-additive hard disk mixture (the precursor matrix). In fact if one calculates the structure factor of the matrix particles one finds the corresponding $k \to 0$ divergence (see Figure 3.43) but the prepeak is obviously missing.

As we mentioned, we observe both in the bulk and in the confined case a prepeak in $S(k)$ at $q \approx 0.5\sigma^{-1}$ that is the signature of intermediate range order. The position of this prepeak corresponds in real space to correlations at distances $r \approx 11\sigma$. It is also worth mentioning that in the bulk bubble phase $S(k)$ a prepeak also occurs, reflecting correlations between bubbles. This feature does not have a correspondence in the $g(r)$ graph as we will see in the paragraph below.

In the pair distribution function we can observe two different modulations: a short-ranged one that reflects the local structure of the fluid, with a periodicity of approximately σ, and a long-ranged modulation due to the pattern structure.

This mesophase structure is more pronounced in droplets, whose $g(r)$ exhibits a small minimum around $r \approx 6\sigma$ corresponding to the average diameter of the clusters. The maximum around $r \approx 11\sigma$ indicates the average distance between neighboring clusters and is in agreement with the position of the prepeak in $S(k)$ as we have indicated in the paragraph above. At very low densities and temperatures, the size of the clusters is essentially determined by the position of the maxima in $\phi(r)$, where $d\phi(r)/dr = 0$; in our case this distance is $r \approx 4.16\sigma$. This quantity defines approximately the average size of a cluster for low densities, which in turn conditions the inter-cluster separation in combination with the range of the repulsive tail.

In our case, modifying R_c from 7.5σ to 30σ changes the average interparticle separation from 9.3σ to 11.6σ. Larger densities increase the average cluster size but hardly influence the inter-cluster separation.

In the stripe phase the maximum in $g(r)$ is still clearly visible, reflecting the average distance between stripes. In the presence of the matrix, the essential features can be observed but now the stripe phase no longer occurs as a percolating mesophase. In the snapshots of Figure 3.50 one can identify the emergence of a stripe phase in the largest portion of the pore whose growth is limited by the confinement. As a consequence of the presence of stripes, the long range maximum in $g(r)$ is found again, similar to the stripe phase of the unconfined system at $< \rho_1 > \sigma^2 = 0.296$, shown in the central panel of Figure 3.49.

In what follows we present the correlation functions resulting from solving ROZ-HNC equation, and they are compared with those extracted from the simulation. Figure 3.51 shows the fluid-fluid structure factor, $S_{11}(k)$, which is defined as:

$$S_{11}(k) = 1 + \rho_1 \widetilde{h}_{11}(0), \tag{3.8}$$

where $\widetilde{h}_{11}(0)$ is the Fourier transform of the fluid-fluid total correlation function. The fluid-fluid correlation function in last equation must be replaced (in the ROZ formalism) by its connected counterpart, $h_{11}(r) - h^r_{11}(r)$, when the average over disorder is performed [Fernaud et al., 2003].

The simulation results presented in Figure 3.51 (and below in Figures 3.53 and 3.54) correspond to a molecular dynamics (MD) run for a single matrix configuration and in which the initial fluid configuration is generated in a GCMC run. MD results correspond to averages carried out for 1–2$\times 10^6$ configurations, using samples with 441 and 2399 fluid and matrix particles, respectively, and an integration time step of 0.0025 in reduced time units. The matrix density in this case is $\rho_0\sigma^2 = 0.324$, slightly above the one used in the solution of the ROZ-HNC equations. The presence of

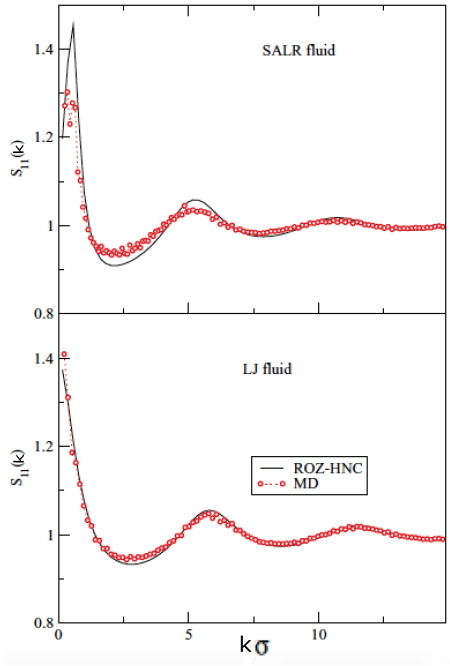

Figure 3.51: *Fluid-fluid structure factor as calculated from the ROZ-HNC equation (curves) and from MD (symbols) for the adsorbed SALR fluid (upper graph) and the LJ system (lower graph) for* $\rho_1\sigma^2 = 0.0596$ *and* $\rho_0\sigma^2 = 0.324$*. Note the marked pre-peak at* $k = 0.578\sigma^{-1}$ *for the SALR fluid. The LJ fluid* $S_{11}(k)$ *grows as* $k \to 0$*, which indicates the vicinity of the condensation transition.*

intermediate range order [Godfrin et al., 2013], is indicated by the marked pre-peak in the fluid-fluid structure factor at $k = 0.578\sigma^{-1}$, that reflects density correlations for distances around 11σ. For comparison in the lower graph, we present results obtained using the same matrix and initial fluid configuration but with the particles of the fluid interacting via LJ potential. We observe in the latter case that the structure factor lacks any signature of intermediate range order, but it clearly shows signs of an approaching

divergence at $k \to 0$, i.e., the vicinity of the condensation transition.

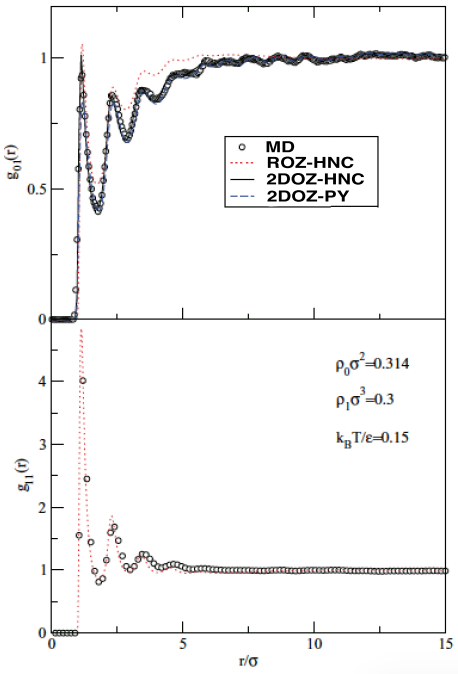

(a) $\rho_1\sigma^2 = 0.3$; $\rho_0\sigma^2 = 0.314$; $k_BT/\epsilon = 0.15$

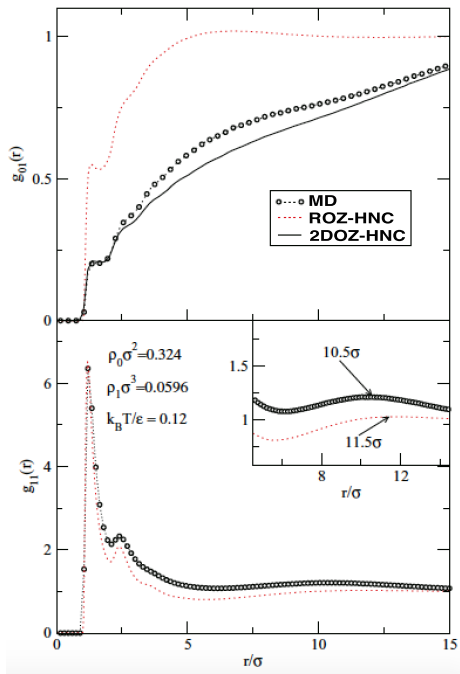

(b) $\rho_1\sigma^2 = 0.0596$; $\rho_0\sigma^2 = 0.324$; $k_BT/\epsilon = 0.12$

Figure 3.52: *Average matrix-fluid (upper graphs) and fluid-fluid (lower graphs) correlations for a SALR fluid inclusion as estimated from MD simulations run from a given GCMC configuration with a fixed matrix configuration (circles), by means of PY-2D (blue dotted line), 2DOZ-HNC equations (black solid line) and ROZ-HNC equations (red dotted line). Note that the ROZ equations provide the average of the correlations over matrix disorder. For the lower fluid density clustering effects are more apparent, as can be inferred by the long range of the fluid-fluid correlations, $g_{11}(r)$, which exhibit a wide maximum -see the inset- around* 10.5σ *(*11.5σ *for the theory).*

Figures 3.52b and 3.52a shows the fluid-fluid correlations (lower graphs) and the fluid-matrix correlations (upper graphs) for high ($\rho_1\sigma = 0.3$) and low ($\rho_1\sigma = 0.0596$) fluid density respectively. We can see that the performance of the ROZ-HNC equation for the calculation of the fluid-fluid correlations is relatively good for the high density case and acceptable for the low density. Differences can be in part attributed to the fact that we are comparing the ROZ results obtained for a matrix density $\rho_0\sigma^2 = 0.314$ with those of the simulation sample for which $\rho_0\sigma^2 = 0.324$, with the additional modification induced in the matrix topology by the removal of disconnected matrix particles. Notice that both theory and simulation reproduce the presence of a wide maximum at approximately 10.5σ, in approximate correspondence with the location of the pre-peak in $S_{11}(k)$. The position of the wide maximum in the ROZ-HNC results is somewhat shifted to higher distances (11.5σ), as a result of the failure of the HNC closure to correctly reproduce the phase of the oscillations in the correlation functions. The comparison of the ROZ-HNC data with simulation results considerably worsens for the fluid-matrix correlations, particularly at low density where clustering is more evident. Obviously, this discrepancy results from the poor description of matrix-matrix correlations when using $\rho_0\sigma^2 = 0.314$ ROZ results to model those of $\rho_0\sigma^2 = 0.324$, which is particularly crucial for the $g_{01}(r)$ correlations at low fluid densities. For higher fluid densities, the packing effects of the fluid dominate and this explains why the ROZ performance for $\rho_1\sigma^2 = 0.3$ is far better than for $\rho_1\sigma^2 = 0.0596$, as far as matrix-fluid correlations are concerned.

Nonetheless, we will only need the fluid-fluid correlations $g_{11}(r)$ -more precisely $c_{11}(r)$- to solve the 2DOZ-HNC equation (Eq. 2.58, and those are reasonably approximated by the ROZ-HNC. The solution of the 2DOZ-HNC is done using a discretized two-dimensional grid of $N_x \times N_y$ points (in this case $N_x = N_y = 512$) with a grid spacing that is given by $\delta x = L_x/N_x$ and $\delta y = L_y/N_y$, where L_x and L_y represent the size of the simulation box corresponding to the matrix configuration whose fluid density distribution will be calculated using Eq. 2.58. Here, we will consider $L_x = L_y = 86.066\sigma$ for low fluid density calculations, $\rho_1\sigma^2 = 0.0596$ (with $\rho_0\sigma^2 = 0.324$) and

$L_x = L_y = 39.84\sigma$, for the moderately high fluid density, $\rho_1\sigma^2 = 0.3$ (with $\rho_0\sigma^2 = 0.314$). The first results that come out from the solution of the 2DOZ-HNC equation are the matrix-fluid correlations calculated via Eq. 2.60 that are depicted in the upper graphs of Figures 3.52b and 3.52a. It is evident that the full 2D approach considerably improves upon the ROZ-HNC approximation for the average $g_{01}(r)$ distributions for a specific matrix configuration, in particular at low densities. For the highest density, we include in the figures results from the PY-2D approximation (see Eq. 2.59), which in this particular instance is more or less of the same quality as the HNC.

3.2.3.2 Two-dimensional density maps

We compare the 2DOZ-HNC density maps with those obtained from Molecular Dynamic simulations in order to test the theoretical approach. Finally, for the sake of comparison, we have also considered the inclusion of a two-dimensional LJ fluid which interacts with matrix particles via a LJ potential as well.

In Figures 3.53a and 3.53b we present the explicit 2D fluid density distributions $\rho_1(x, y)$, for $\rho_1\sigma^2 = 0.3$ ($\rho_0\sigma^2 = 0.314$), and $\rho_1\sigma^2 = 0.0596$ ($\rho_0\sigma^2 = 0.324$) for our SALR fluid at temperatures where clustering becomes apparent (particularly at low density). One can immediately appreciate that, in spite the relatively small difference in the matrix density ρ_0, the matrix porosity is appreciably larger [2] for $\rho_0\sigma^2 = 0.324$ (see Figure 3.53b), and therefore matrix-matrix correlations (and hence matrix-fluid correlations as well) are quite different in both instances as we have seen. This effect will be less appreciable in the fluid-fluid correlations, which are mostly conditioned by the effective density of the adsorbed fluid.

In the case of the higher fluid density, in Figure 3.53a one readily observes that the 2DOZ-HNC equation actually reproduces quite well the

[2] We have in fact $p \approx 21.9\%$ for $\rho_0\sigma^2 = 0.314$ and $p \approx 22.6\%$ for $\rho_0\sigma^2 = 0.324$

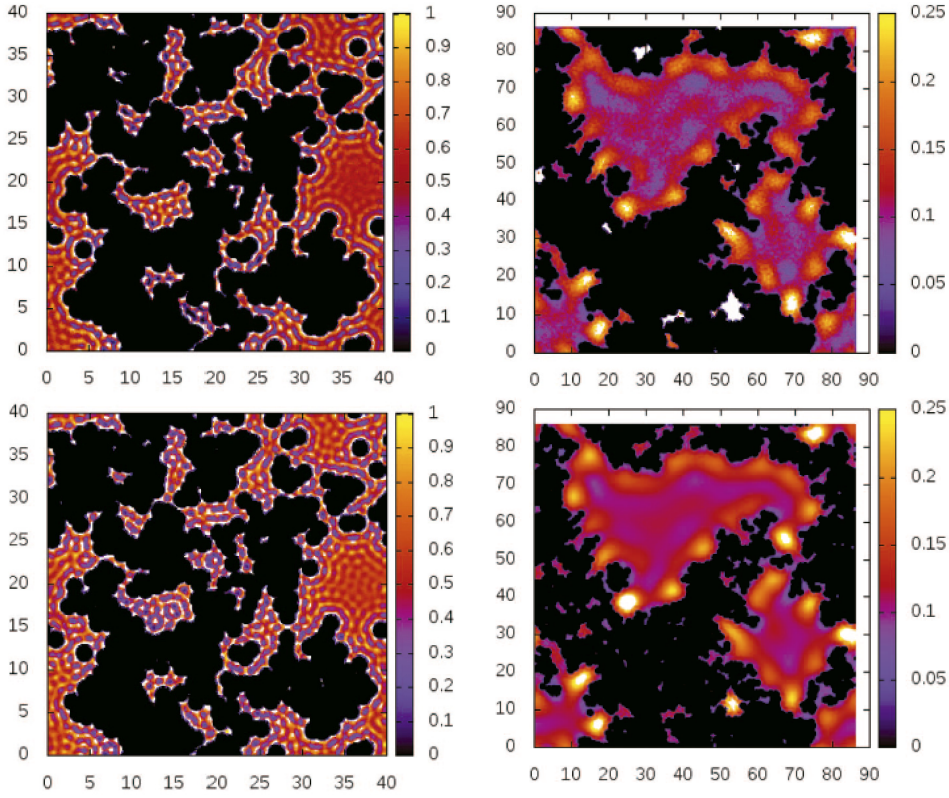

(a) $\rho_1\sigma^2 = 0.3$; $\rho_0\sigma^2 = 0.314$; $k_BT/\epsilon = 0.15$

(b) $\rho_1\sigma^2 = 0.0596$; $\rho_0\sigma^2 = 0.324$; $k_BT/\epsilon = 0.12$

Figure 3.53: *Fluid density distribution $\rho_1(x, y)$ of the SALR fluid from MD (up) and in the 2DOZ-HNC approximation (down). Regions for which $\rho_1(x, y) > 0.25$ are plotted in white.*

simulated density distribution, and interestingly the maxima and minima of $\rho_1(x, y)$ are seen to display the features of a partly ordered system (approaching the local structure of a triangular lattice). Note that in this figure the black region represents the area of the system in which the fluid density vanishes. In this case, this is precisely the area inaccessible to

the centers of adsorbate atoms, i.e., the exclusion surface of the matrix as defined by the positions of its constituent atoms and their corresponding individuals exclusion surfaces. This exclusion surface per matrix particle is given for our matrix-fluid interaction by $\approx \xi\pi\sigma^2$, with a parameter ξ that accounts for the potential softness set to $\xi = 0.98$ for the SALR potential, and $\xi = 0.8$ for the LJ matrix-fluid interaction. In the case of the MD picture, the black region also includes those isolated matrix cavities that were empty from fluid particles in the starting configuration of the MD run. These empty cavities will be thus indistinguishable from the area of the sample excluded by the matrix in these spatial fluid density maps.

It can be appreciated that in the 2DOZ-HNC picture there is a substantially larger number of small disconnected pores partly filled with fluid inclusions as compared with the MD results. In this latter instance, most of the disconnected pores happen to be empty for our particular initial fluid configuration. As mentioned, this results from the fact that our simulation corresponds to a MD run started from a single GCMC configuration of the fluid particles. A better agreement in this respect would be reached at a much higher computational cost calculating the fluid density $\rho_1(x, y)$ as the average from a series of MD runs started from different GCMC configurations of the fluids sampling the same chemical potential. In this case, the average population of the disconnected pores would be determined by the equilibrium grand canonical partition function and we would not have to rely on a single initial fluid configuration which might well be away from the equilibrium average. Notice that for large pores, the subsequent MD sampling would essentially converge toward the GCMC result. An alternative approach, would be the use of configurations in which fluid particles are not allowed to populate disconnected cavities in the matrix, and modify consequently the matrix-adsorbate interaction in the 2DOZ-HNC approach to include an artificial hard core potential that forces $\rho_1(x, y) \to 0$ inside these isolated cavities (e.g., retaining the template matrix particles that occupy these cavities in the original non-additive hard disk mixture). For simplicity, we have retained the original control pore glass like configuration and used our initial test GCMC results as input to generate the MD

trajectories, since in fact we are mostly interested in the fluid behavior inside the medium-large cavities of the matrix, where there is room enough for pattern formation to take place.

On the other hand, the reason for using MD generated configurations and not the output of the GCMC directly, is simply related to computational efficiency in the calculation of the simulated $\rho_1(x, y)$. In order to obtain a smooth density distribution, one needs to perform an intensive sampling of the configurational space with a large number of averages of spatially contiguous particle configurations, which is much simpler to attain using MD.

In Figure 3.53b, we observe a density distribution $\rho_1(x, y)$ characteristic of the presence of clustering. One sees immediately that there are spatially separated regions of substantially higher fluid density, which tend to concentrate in pockets and bays of the porous structure, despite the fact that the matrix fluid interaction is purely repulsive. This is due to the fact that, once particles aggregate in clusters as a consequence of the short range attractive part of the potential, the long-range repulsion between the clusters pushes them apart to places where at least some of them are "sheltered" by matrix particles. The intercluster separation lies in the range $10\sigma \sim 11\sigma$, in agreement with the position of the $S_{11}(q)$ pre-peak and the wide maximum of $g_{11}(r)$. The theoretical results are in excellent agreement with the simulated density distribution. Moreover, we have seen that as the simulation proceeds the results tend to approach the theoretical prediction, since the reorganization of the clusters is a relatively slow process, particularly when they get trapped in narrow pockets. This is one of the reasons why the MD simulations have to be exceptionally long to yield a reliable $\rho_1(x, y)$. As an illustration, the fluid density inside the cavity at $(x, y) \approx (12\sigma, 55\sigma)$ in upper panel of Figure 3.53b was found to remain well above $\rho_1(x, y)\sigma^2 > 0.3$ for close to $1{\times}10^6$ MD steps, to slowly decrease and reach ≈ 0.17 after another $2{\times}10^6$ steps, much closer to the predicted 2DOZ-HNC estimate seen in lower panel of Figure 3.53b.

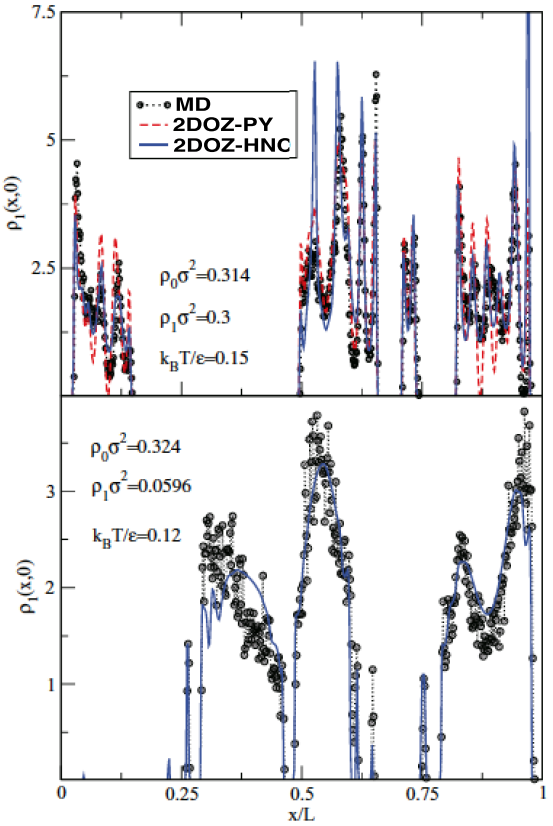

Figure 3.54: *Illustration of the density profile* $\rho_1(x,0)$ *of the SALR fluid along the x-axis taking as origin a given matrix particle. The upper figure corresponds to the density map of Figure 3.53a and the lower one to the map of Figure 3.53b. Distances are scaled with the side of the simulation box since each figure corresponds to samples of different size, and the reference matrix particle is also a different one.*

In order to appreciate the performance of the integral equations more quantitatively, in Figure 3.54 we plot the density profiles along the x-axis using as reference a given matrix particle. We observe that the 2DOZ-PY

approximation underestimates the value of the density minima, and the 2DOZ-HNC slightly overestimates the maxima, which are characteristic features of the YP and HNC correlation functions. Note that the theoretical profile exhibits some spikes corresponding to fluid particle inclusions in the aforementioned isolated cavities. These spikes are either absent in the MD results or have a much lower intensity, as a result of a much lower (or zero) initial density of fluid particles in the cavity in the starting MD configuration. This is again explained in the preceding paragraph as a result of the use of a single GCMC configuration as starting point for our MD calculations. Aside from this detail, the agreement between the theory and the simulation is remarkable.

Finally, for the sake of comparison we have run a long MD simulation (2×10^6 independent configurations in a run of 10×10^6 time steps) from the same starting fluid and matrix configuration as before ($\rho_0\sigma^2 = 0.324$), but where now fluid-fluid and matrix-fluid interactions correspond to a truncated and shifted LJ potential. The temperature of the run was set to $k_BT/\epsilon = 0.55$ and the fluid density as before $\rho_1\sigma^2 = 0.0596$. These conditions are quite close to the gas-liquid transition as can be inferred from the large $S_{11}(0)$ values in Figure 3.51. We have solved the ROZ-HNC equations for this system and obtained the density distribution using the 2DOZ-HNC equation. In Figure 3.55a, we show the fluid-matrix and fluid-fluid correlations. As in the case of the low density SALR fluid, again here the fluid-matrix correlation ROZ-HNC predictions are rather poor, due to the inaccurate representation of the matrix-matrix correlations for this matrix configuration. Also, fluid-fluid correlations do not show any trace of intermediate long range ordering or clustering (the high values of the first peak of $g_{11}(r)$ are just an indication of confinement and the fluid-fluid correlation dies out rapidly). This is in clear contrast with the long range features found in Figure 3.52. Again, the 2DOZ-HNC fluid-matrix correlation agrees quite well with the MD results.

Now, the fluid density distribution for the same density as that of Figure 3.53 can be seen for the LJ system in Figure 3.55b, and again we appreci-

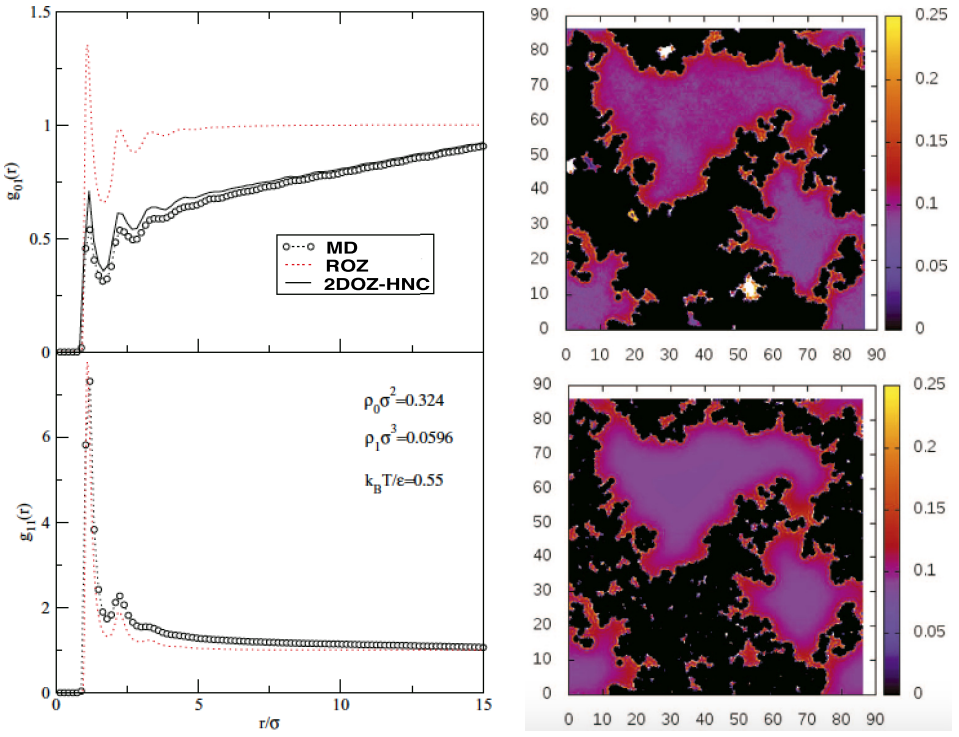

(a) *Radial distribution function*

(b) *2D density maps*

Figure 3.55: *(a) Same as Figure 3.52 for a LJ fluid in a LJ matrix. Note the higher intensity of the first peaks as a consequence of the LJ attraction, the pronounced spatial structure of $g_{01}(r)$ and the lack of maximum at 10σ in $g_{11}(r)$ due to the absence of clustering. (b) Fluid density distribution $\rho_1(x, y)$ for $\rho_1\sigma^2 = 0.0596$ and $k_BT/\epsilon = 0.55$ ($\rho_0\sigma^2 = 0.324$) from MD (up) and in the 2DOZ-HNC approximation (down) for a LJ fluid inclusion in a matrix formed by LJ particles.*

ate a remarkable agreement between theory and simulation. In this case, the simulation had to be particularly long for the density distribution to be smooth enough. The only salient feature appreciated in Figure 3.55b

is the fact that the fluid density is enhanced near the pore walls, due to the attractive nature of the matrix particles. During the simulation run one can see the formation of short lived aggregates as a consequence of the vicinity of the liquid-gas transition, but in contrast to the SALR fluid, they have no preferred positions within the pore space, and the local density enhancements average out.

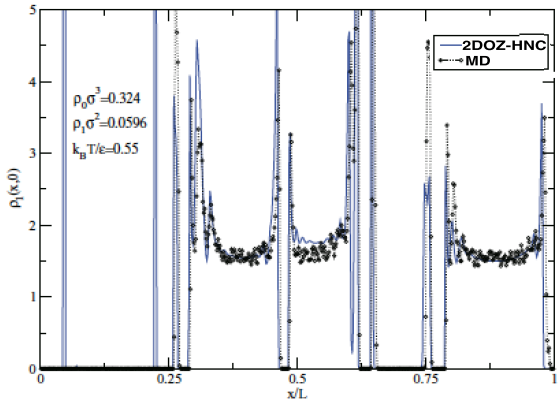

Figure 3.56: *Illustration of the LJ fluid density profile $\rho_1(x,0)$ along the x-axis taking as origin a given matrix particle. The fluid-matrix attraction is reflected in the large values of the density profile in the immediate vicinity of the matrix particles.*

Again, in Figure 3.56 we can have a more quantitative appreciation of the quality of the results in the density profile along the x-axis. The attractive nature of the pore particles is evidenced by the large values of $\rho_1(x,0)$ near the matrix particle boundaries, in contrast to the situation in Figure 3.54, where the repulsive nature of matrix-particle interaction used for the SALR fluid simulations is evident.

3.2.3.3 Clustering

We have simulated a large number of states at different temperatures and chemical potential; by identifying the different types of mesophase structures we have constructed a *structural phase diagram*. The simulations are based on GCMC runs extending over $6\text{x}10^6$ steps ($2\text{x}10^6$ for the confined fluid) of which $5\text{x}10^3$ independent configurations were used in the cluster analysis.

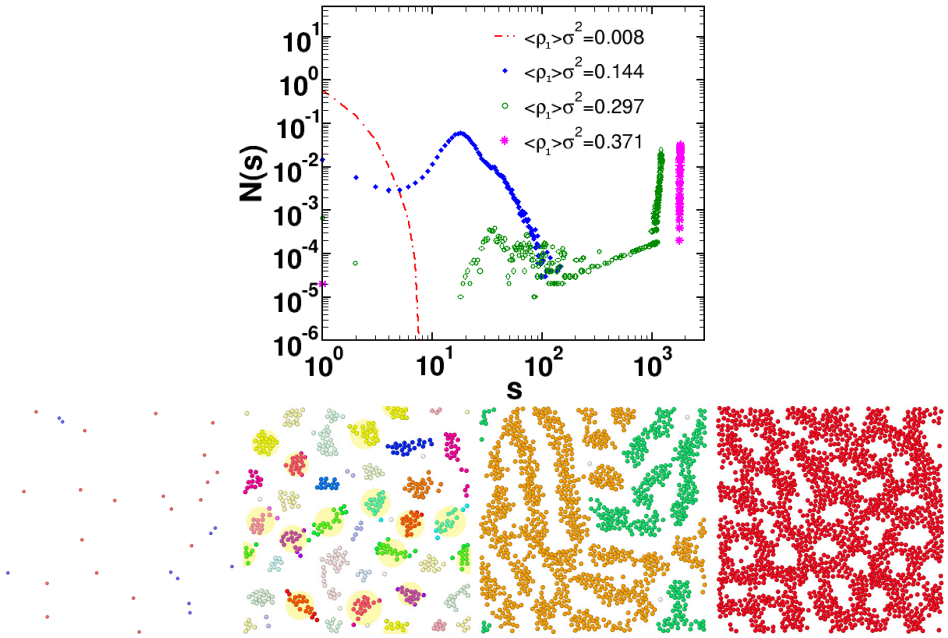

Figure 3.57: *The upper panel shows the normalized cluster distribution $N(s)$ (see text) for various fluid densities of the SALR fluid as labeled. Representative snapshots of the corresponding mesophases are illustrated in the bottom panels (with increasing density from left to right). Different colors of the particles provide an approximate measure of how many particles are involved in separated regions of the respective mesophases.*

We have performed a geometric cluster analysis of these configurations [Godfrin et al., 2013] using as link distance the r-value which corresponds to the point where $\phi(r_{cl}) = 0$, i.e. the link distance, $r_{cl} = 2.78\sigma$ (see equation(3.6) and Figure 3.40). For smaller distances the potential of two interacting particles is negative and particles are thus considered to belong to the same cluster. We have calculated the normalized cluster size distribution, $N(s)$, proposed by Stauffer [1979] (See **Section 2.1**).

Function $N(s)$ allows us to distinguish the different types of possible mesophase structures for the bulk SALR fluid and has been plotted in Figure 3.57. For each type of mesophase a characteristic snapshot is shown on the lower part of this figure. Analysis of $N(s)$ leads to the definition of four distinctively different morphologies: (i) the dispersed fluid mainly consisting of monomers, for which the cluster size distribution has a maximum for $s = 1$ and then decreases monotonically (red line in Figure 3.57); (ii) the clustered fluid, consisting of finite size clusters where the cluster size distribution has a maximum for $s > 1$ and then decreases monotonically (blue line in Figure 3.57); (iii) and (iv) two different percolating states, where $N(s)$ exhibits maxima at cluster size close to the system size. In the case of random percolated states or bubbles all the particles belong to the same cluster (pink line in Figure 3.57) thus $N(s)$ has a single maximum; finally, in the case of cluster percolated states or stripes, $N(s)$ has secondary maxima at given large s-values resulting from the presence of disconnected stripes in the sample (green line in Figure 3.57).

Based on this analysis, we have mapped out the different regions in the phase diagram where different mesophase structures can be identified. In Figure 3.58 the emerging structural phase diagram for the bulk (upper graph) and confined (lower graph) fluid are displayed. Comparing both graphs, we observe that the cluster percolated states dominate the structural phase diagram of the confined fluid. These states correspond essentially to stripe phases in which the stripes are prevented from organizing themselves in a lamellar phase due to the effect of the matrix disorder, despite the relatively large size of the pores of our particular matrix. In a

lamellar phase such as the one depicted in the lower panel of Figure 3.58 one can see that the stripes percolate, which is not the situation in a prototype stripe phase such as the one illustrated in the lower left panel of Figure 3.50. In the case of the confined fluid, the cluster percolated phases are mostly composed of finite size stripes.

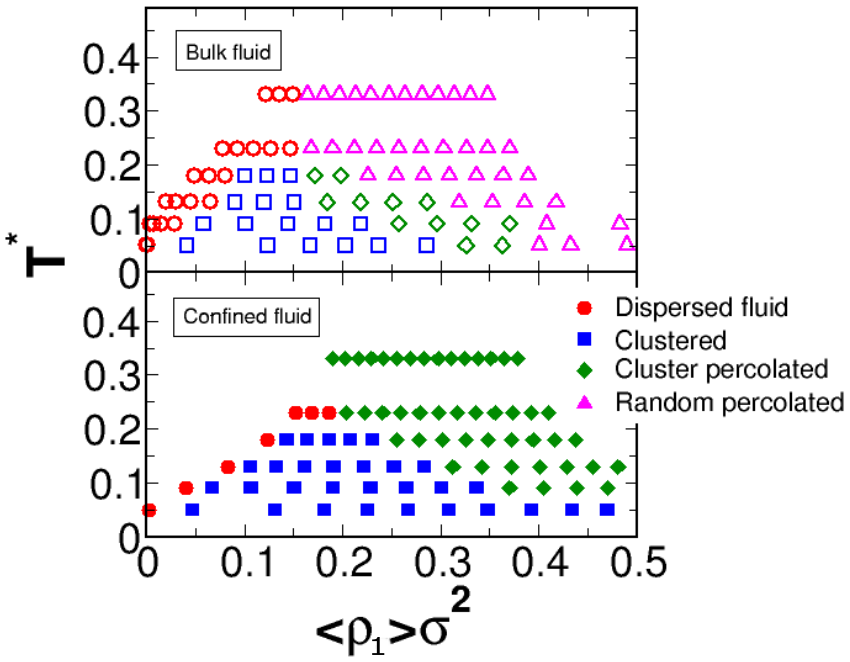

Figure 3.58: *Structural phase diagram of the bulk SALR fluid (upper graph) in the* $(T^*, < \rho_1 > \sigma^2)$ *plane. The lower graph correspond to the phase diagram for the confined fluid. Different mesophases are indicated on the figure by different symbols and colors as labeled (full symbols-bulk fluid, open symbols-confined fluid).*

Interestingly, the cluster fluid phase is nonetheless supported by the presence of the matrix, a fact that already became apparent when com-

paring the internal energies of both systems in Figure 3.47. On the other hand, we note that when the density increases, from a visual inspection the distinction between a confined stripe phase (a cluster percolated state) and the bubble phase (random percolated state) becomes somewhat blurred due to confinement. Some structures could be thought of either as bubbles or short stripes. The presence of a maximum in the the cluster size distribution for finite s however tells us that these cluster percolated phases are more properly interpreted as short stripe phases. This is the reason random percolated states are missing from the structural phase diagram of the confined fluid in Figure 3.58. For fluid densities higher than those depicted in Figure 3.58, one will certainly find random percolated states, even in the confined case for matrices with sufficiently high porosities.

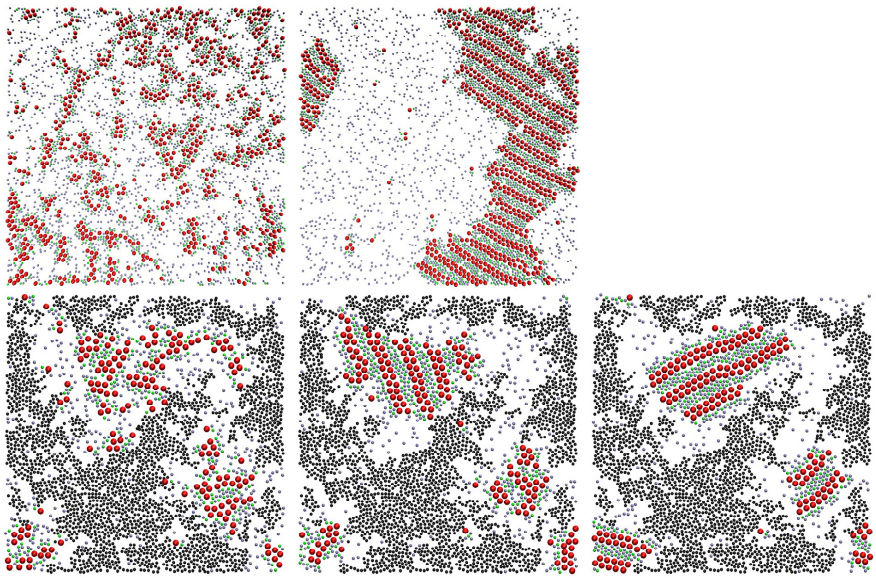

Figure 3.59: *Snapshots of the two-dimensional system (up), and two-dimensional system confined in a porous glass matrix (down) for several temperatures around the critical value: T=0.30 (left), T=0.25 (center) and T=0.20 right).*

3.2.4 The simple mixture model under disordered confinement

In addition, we have studied the effect of disordered confinement on the patterns emerged in the self-assembing mixture model introduced in the Section 3.1. We may appreciate in Figure 3.59 that topologically disordered confinement does no affect the stability of the lamellar phase in this fluid model, contrary to the case of SALR fluid where this kind of confinement hinders the formation of stripes favoring the droplets. Upper and lower rows in Figure 3.59 represent snapshots of the bulk and confined system respectively at the same state (same temperature and pressure), and we see from a simple visual inspection that the structure does not vary because of the confinement. We conclude from these results that droplets do not emerge from this model because of the small size and rigidity of the "non-polar" tail (A-sites) of the dimers, that leads to very stable stripes characterized by the hexagonal order seen in Figure 3.29.

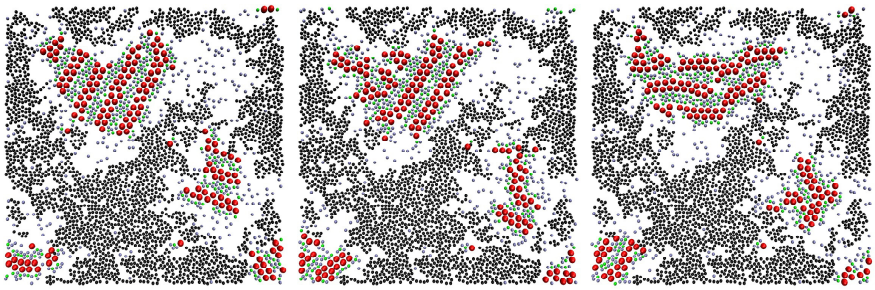

Figure 3.60: *This picture shows the configuration of the emerged pattern, at a temperature below the critical value:* $T_r = 0.833K$*, for the system confined in a matrix based on a realistic porous glass. The frames correspond to three consecutive states picked separated by a time interval of 0.04 ns. We may notice how the fluid evolves between the matrix fixed particles, but it keeps a flexible lamellar structure.*

The lamellar domains become obviously more stable as the temperature is lowered, and the only noticeable effect of the confinement in a disordered

medium is that now the domain size is limited by the size of the cavities, by which finite size clusters are absolutely favoured with respect to unbounded ones. This feature was already observed in 3.2.3.3 for the SALR model and raises naturally from the joint effect of a limited pore size and a disordered topology that hinders the formation of percolating clusters.

Finally, as we already found in Section 3.1, the finite lamellar domains are dynamic and flexible entities, that change shape and exchange constituent particles with the surrounding monomer phase. This is illustrated in the sequence of consecutive snapshots of Figure 3.60, even at a rather low T. This is very clear for the smaller domains but even larger ones are seen to change their shape, even when the internal hexagonal order is preserved.

3.2.5 Dynamics

Dynamical features of the self assembly fluid of particles interacting by means of competing interactions (SALR potential) have been analyzed in terms of time-correlation functions. Since this system does no exhibit a vapour-liquid transition in the regions we have studied, we will attempt to characterize its dynamics behavior in terms of the Frenkel line.

According to [Brazhkin et al., 2012], Frenkel's line signals an important qualitative change in the fluid dynamics: the transition between the solid-like dynamics characterized by oscillatory motion around equilibrium positions at potential energy minima versus a gas-like dynamics characterized by a diffusive dynamics dominated by particle jumps between the potential energy minima. We have analyzed the transition between both dynamical states by means of the analysis of the normalized VACF, defined as $< v(0)v(\tau) > /v^2(0)$, and of the second derivative of the self-intermediate scattering function $F_s(k,t)$. In the case of a solid-like fluid behavior, VACF shows oscillatory behavior at short times (cage effect) and the second derivative of the self scattering function exhibits a maximum also at short times corresponding to these oscillations around the minimum. On

the other hand, gas like dynamics is characterized by a monotonic decay of the VACF and the shift of the maximum in $F_s(k,t)$ second derivative to larger time scales due to the ballistic like jumps.

The close relation between the velocity self correlation function an the self intermediate scattering function is clearly seen in the relation [Balucani and Zoppi, 1994]:

$$\lim_{k\to 0}\left\{-\frac{1}{k^2}\frac{d^2F_s(k,t)}{dt^2}\right\} = \frac{1}{3} < \mathbf{v}_i(0)\mathbf{v}_i(t) >= \tilde{Z}(t), \tag{3.9}$$

which clearly shows that minima in $\tilde{Z}(t)$ will be correlated with maxima in $d^2F_S(k,t)/dt^2$ for small k-values.

Here we have performed extensive Molecular Dynamics simulations in the NVT ensemble using our own code. For the bulk case, we have started from a square lattice configuration of 500 particles whose size is defined by the density; we have averaged over 2×10^6 steps, after equilibrating the system for 7×10^4 steps. In the case of the confined fluid, we have performed the MD simulation taking the final configuration of the GCMC simulations described in the Section above, for the large matrix as the initial state for the run. The averages have been performed in this case over 5×10^6 after 5×10^4 equilibration steps with a time step of 0.001 in reduced time units, being $F_s(k,t)$ an adimensional quantity. Configurations have been recorded every 20 time steps to perform the analysis of the dynamic properties.

Figures 3.61 and 3.62 show the normalized VACF and the $d^2F_s(k,\tau)/d\tau^2$ respectively for the bulk SALR fluid at different densities and temperatures. We denote by τ the time in reduced time units.

In Figure 3.61 we represent VACF in bulk for a series of densities and temperatures ranging form the dense fluid, to the cluster phase and the gas monomer phase. We observe at $< \rho_1 > \sigma^2 = 0.8$ the behavior characteristic of a dense fluid for all temperatures, with the characteristic cage effect at

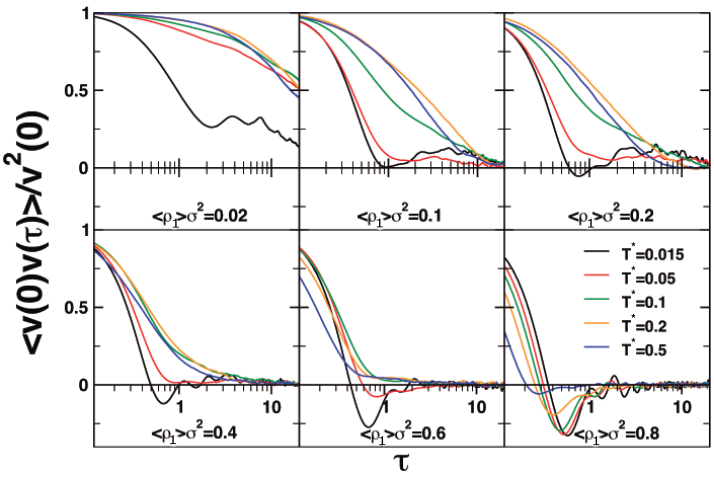

Figure 3.61: *Normalized velocity autocorrelation function of SALR fluid in bulk for different densities and temperatures specified in the graph.*

short times. It is clearly appreciated that as the temperature increases the position of the minimum decreases, i.e. the particles experience the cage effect collisions with their neighbors for shorter times, as their average kinetic energy increases. Now when density decreases we can see that the transition from gas-like dynamics (no VACF minimum) to solid-like dynamics as the temperature is lowered. What is remarkable is that this crossover occurs still for densities clearly on the low dense gas regime ($< \rho_1 > \sigma^2 \leq 0.2$). Even at very low density one can appreciate the presence of a minimum for the lowest $T^* = 0.015$. This is clearly connected with the fact that the system is on the cluster phase, so particle velocities experience a cage-like effect due to their neighboring particles in the cluster. Still the net behavior the VACF retains its gas-like slow decay, since clusters also experience gas-like collective motion. We find now that in this system, which lacks a liquid phase due to the clustering and long-range repulsion, the Frenkel line separating gas-like from solid-like behavior extends down to very low temperatures. One might estimate that for $< \rho_1 > \sigma^2 = 0.02$ $T^*_{Frenkel} \approx 0.02$,

for $< \rho_1 > \sigma^2 = 0.1$ $T^*_{Frenkel} \approx 0.05$, increasing up to $T^*_{Frenkel} \approx 0.1$ for $< \rho_1 > \sigma^2 = 0.6$.

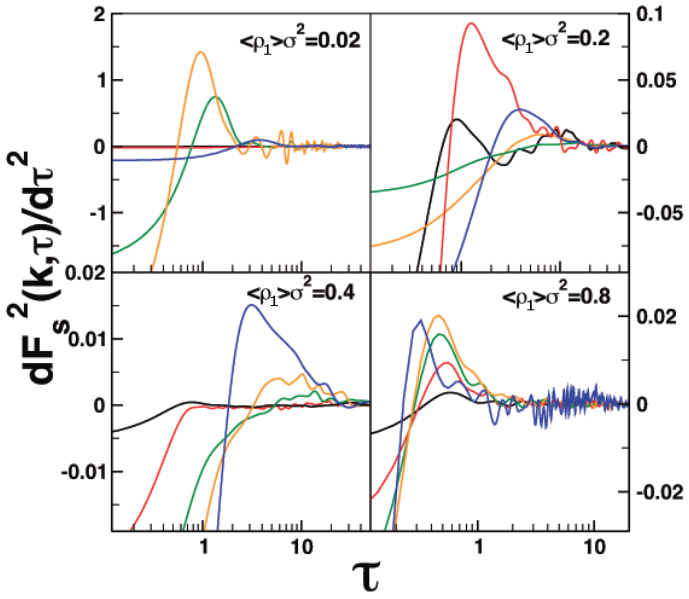

Figure 3.62: *Second derivative of the self-intermediate scattering function of SALR fluid in bulk for different densities and temperatures specified in the graph, for k=0.1568Å*$^{-}$*1.*

In general, one observes various features in Fig. 3.61. For high density, above $< \rho_1 > \sigma^2 = 0.2$ one observes a regular dependence of the VACF on the temperature, as T increases the correlations decay more rapidly due to the higher rate of collisions. As density is lowered there are competing effects (kinetic energy vs. aggregation) which lead to a non-monotonous behavior, but the general trend is that at low temperatures the decay of the correlations is much faster, due to the formation of clusters. This implies that collisions occur at shorter times at low temperatures due the vicinity of particles in the same cluster. At intermediate temperatures, aggregates

are not completely formed and we observe that correlations decay faster for $T^* = 0.5$ than for $T^* = 0.2$, as it occurred for the highest density; now the fact is that the kinetics dominates, since we are outside the cluster phase.

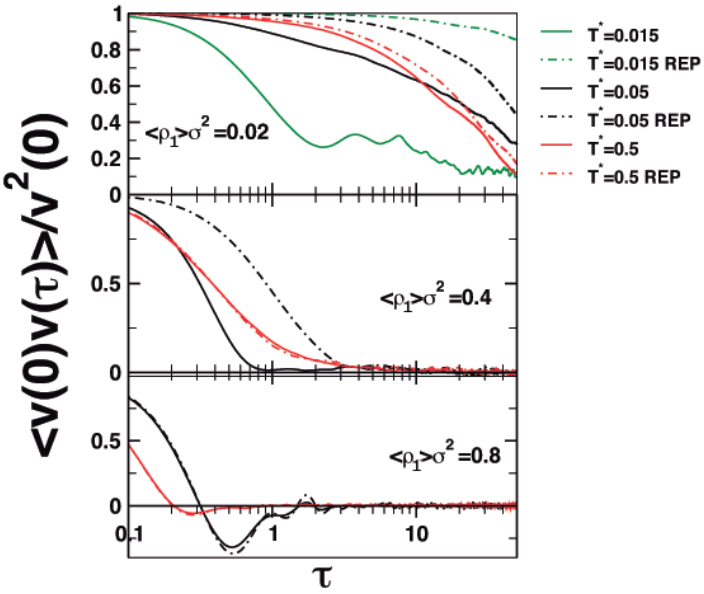

Figure 3.63: *Normalized VACF of a fluid of spherical particles interacting via repulsive soft potential(dotted lines) compared with that of the IR-fluid (solid lines) showing clustering emergence for certain values of density and temperature. Different temperatures and densities have been plotted and are specified on the graph.*

Another feature that is worth mentioning is that the VACF at low temperature for $< \rho_f > \sigma^2 = 0.2$, even though displaying well defined short τ minima, are always positive. We have interpreted these minima as a result of a cage effect within the clusters. Now, the fact that $< v(\tau)v(0) >$ stays positive is an indicative that there is a substantial amount of diffusion of the clusters. It is the change of the relative particle velocities with respect to

the clusters center of mass which gives rise to the oscillation. Whereas the clusters as a whole exhibit a low density gas-like dynamics, this is superimposed on the individual particle dynamics within the aggregates, exhibiting "solid-like" dynamics (cage effects).

These features can be to some extent confirmed in Fig. 3.62 where the behavior of $d^2F_S(k,\tau)/d\tau^2$ is presented. The short time maxima of the function $\tau \lesssim 1$ correspond to the minima in the VACF, i.e. the cage effect that reflects oscillation around the potential energy minima indicating solid like behavior. As T increases, these maxima disappear (except for $< \rho_1 > \sigma^2 = 0.8$ which retains solid-like behavior) and are shifted to much higher τ. Now these maxima represent gas-like dynamics, i.e. transitions from the oscillatory to the ballistic regime [De Lorenzi-Venneri et al., 2008]. Note that this information must be complemented with the study of the VACF, since the statistics for $d^2F(k,\tau)/d\tau^2$ is somewhat poor, particularly at low densities and temperatures.

Now, in Fig. 3.63, we further analyze the effects of clustering by comparing the VACF's of the SALR fluid with those of a system interacting solely through the short range repulsive component of the SALR potential, $U^{ref}(r)$ in Eq. 3.6. Whereas in the dense fluid regime the dynamics of both systems is identical, clear differences emerge already at moderate densities (for low temperature, where clustering takes place at all T's studied). One immediately sees that the correlations die out more rapidly in the cluster phase, even when the densities are identical, due to collisions with close neighbors, that are not present in the purely repulsive fluid gas phase. At very low temperatures we see even a cage-like effect as shown in Fig. 3.62 as well.

Finally, in Fig. 3.64 we perform a comparison for the VACF for the SALR fluid in bulk and under confinement. In the latter instance, densities are obviously calculated in terms of the accessible volume. The only appreciable effect is that at low densities, as temperature is lowered correlations decay somewhat faster in bulk than in confinement. This effect is relatively

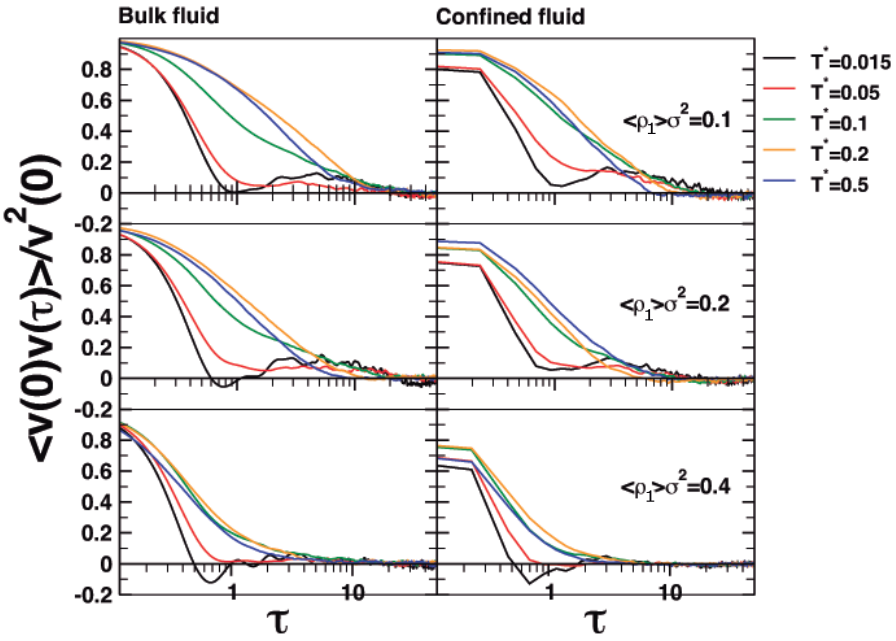

Figure 3.64: *Effect of the confinement on the normalized velocity autocorrelation function. Left column corresponds to bulk fluid and right column to fluid confined in a disordered media. Different temperatures and densities have been plotted and are specified on the graph.*

weak, and it is probably due to the fact that the confining medium is rigid and purely repulsive, by which collisions with the matrix have a lower impact on the velocity self correlation as compared with collisions with other clusters occurring in the bulk, which in a certain sense can be thought as "more inelastic".

Chapter 4

Nano-structured materials for adsorption applications

4.1 Short Capped Nanotubes

In this Section we have explored the ability of a crystal formed by short-capped nanotubes for adsorption applications. We have first studied the encapsulation of small molecules (CS_2 and H_2) in a single short capped nanotube by means of molecular dynamics simulations, in particular using Targeted Molecular Dynamics to assess the binding Gibbs energy. Then, we have investigated the feasibility of a molecular crystal made up of short-capped nanotubes to store hydrogen. To this aim we have studied the adsorption of hydrogen molecules into the crystal via grand-canonical MC, and the arrangement of the confined H_2 into the pores sing density maps obtained from NVT Molecular Dynamics.

For this purpose, we have employed two different models: an all-atom approach to study the complex $CS_2@C_{50}H_{10}$, and a united-atom approach for $H_2@C_{50}H_{10}$. In the first instance the nanocage $C_{50}H_{10}$ model is non rigid (we use a bond order C-C and C-H interaction) and in the case of $H_2@C_{50}H_{10}$, our cage will be rigid, in order to ease the computational cost

of the GCMC simulations.

4.1.1 Encapsulation of small molecules: $CS_2@C_{50}H_{10}$

The aim of this section is in the first instance to compare SAPT(DFT) finite temperature predictions, obtained by Dodziuk et al. [2012] with those of Targeted Molecular Dynamics results for the $CS_2@C_{50}H_{10}$ complex, in vacuum, and then analyze the effect of the presence of an ?? solvent on the stability of the complex.

The interaction energy of the $X@C_{50}H_{10}$ complexes is defined as:

$$E_{int} = E_{A@B} - [E_A + E_B],$$

and using SAPT it was found that these quantity turns out to be negative for all the considered guest molecules (see Table 1 in [Dodziuk et al., 2012]), being lowest for $CS_2@C_{50}H_{10}$. Consequently, at 0K the complex formation is favored in all cases. Using simple approximations, such as ideal gas assumption, separation of rotation from vibrations, the rigid-rotor approximation and the harmonic approximation for vibrations, it is found that also the Gibbs energy for the complex $CS_2@C_{50}H_{10}$ is lowest and negative at room temperature (-1.5kcal/mol) being that of $H_2@C_{50}H_{10}$ and all other complexes positive or barely negative (i.e. the complexes are unstable). In an attempt to go beyond the simple finite approach, here we will assess the binding energy and thermal stability of the $CS_2@C_{50}H_{10}$ resorting to molecular dynamics simulations using effective interactions for the system in vacuum, and in solution using chloroform as solvent. Simple NVT simulations allow us to study the stability of the complex; and a more sophisticated technique, Targeted Molecular Dynamics (TMD),s provides quantitative results for the binding Gibbs free energy. The aim of this study is ultimately, to evaluate the capability of $C_{50}H_{10}$ molecules as

encapsulating agents.

In our model of the complex $CS_2@C_{50}H_{10}$ (see Figure 4.1) both in vacuum and in chloroform solution, all the interactions between pairs of atoms have been considered:

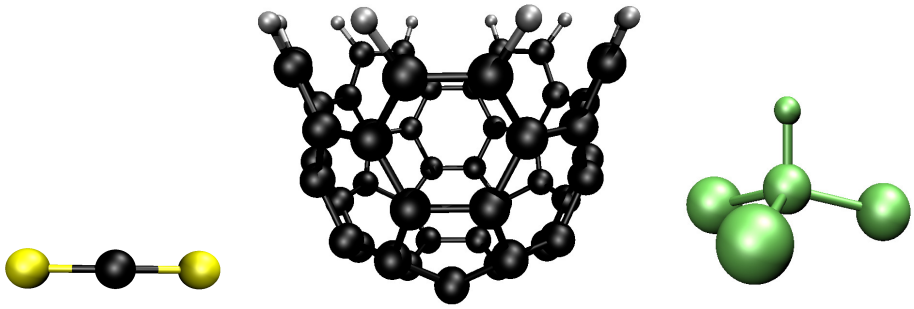

Figure 4.1: *In the left figure we show CS_2 molecule, which has the role of the guest molecule in our system; in the middle $C_{50}H_{10}$ capped nanotube, which is the host molecule; and in the right figure $CHCl_3$ molecule, which acts as the solvent.*

Carbon and hydrogen atoms belonging to the nanocage interact via the AIREBO (Adaptative Intermolecular Reactive Empirical Bond Order) potential of Stuart et al. [2000], which is implemented in LAMMPS. This potential has been proved to effectively work in hydrocarbon molecules as well as single and multi walled nanotubes. It consists of three terms:

$$E = \frac{1}{2}\sum_{i}\sum_{j\neq i}[E_{ij}^{REBO} + E_{ij}^{LJ} + \sum_{k\neq i,j}\sum_{l\neq i,j,k} E_{kijl}^{TORSION}]$$

The first term, named REBO potential, is the dissociable hydrocarbon potential developed by Brenner et al. [2002]. Although this potential was originally developed for simulating the chemical vapor deposition of

diamond, it has been later extended to model many different materials including fullerenes [Brenner et al., 1991], carbon nanotubes [Harrison et al., 1997], ... However, the force field of Brenner does not consider neither dispersion and nonbonded repulsion interactions, thus it is not appropriate when important intermolecular interactions are present. The second term of AIREBO potential solves the problem indicated above. It is a Lennard-Jones 12-6 potential that models the intermolecular interactions of the system including dispersion and short-range repulsion effects. Besides, the last term includes the torsional interactions necessary to represent large hydrocarbon molecules, whose properties are far away from those of the bulk and of the small molecular fragments.

On the other hand, CS_2 is a flexible molecule and its significant quadrupole moment must be explicitly considered; thus, we have used a 3-centre Lennard-Jones plus Coulomb potential to describe it. Lennard-Jones parameters were taken from the work of Tildesley and Madden [1981], and the partial charges for CS_2 and $C_{50}H_{10}$ were obtained from the Natural Bond Orbital analysis, as implemented in MOLPRO [Reed et al., 1985; Mata and Werner, 2007] from the PBE [Perdew et al., 1996] one-electron densities.

Additionally, the intermolecular interactions between the CS_2 and the nanotube were also modeled in terms of a Lennard-Jones plus Coulombic potential: the parameters for the interactions of CS_2 molecule with the nanotube carbon atoms were taken from [Kholmurodov et al., 2010] and with the nanotube hydrogen atoms from [Phillips and Hammerbacher, 1984].

Finally, the potential model for chloroform follows the work of Benjamin [1995] and the nanotube-chloroform cross interactions were defined in terms of the Lorentz-Berthelot rules.

In all the cases both AIREBO, Lennard-Jones and Coulombic interactions have been cut at a distance of 11.0 Å, and all the angles and bonds are flexible with harmonic intramolecular interactions defined in [Kholmurodov et al., 2010; Benjamin, 1995]

We have analyzed the thermodynamic features in order to estimate the binding energy and the stability of the complex, and also the frequency spectra. To this aim, simulations have been performed using LAMMPS in the canonical ensemble at different temperatures. A time-step of 1 fs has been used during the simulations (although a smaller value was proved, we found no substantial difference in the results).

Both the system in vacuum and in chloroform solution have been simulated. Simulation runs of the $CS_2@C_{50}H_{10}$ complex in vacuum were performed during 1ns, fixing the temperature at different values with temperature rescaling [Allen and Tildesley, 1987]. As the system in vacuum possesses only a small number of atoms, the use of the thermostat is inefficient and deviations of the temperature are sometimes larger than 20% even with rescaling. The systems in solution (see Figure 4.6) have been generated by introducing 2048 molecules of $CHCl_3$ in a cubic box of 64.86Å side (the resulting density corresponds to the experimental density at room temperature, $1.48 g/cm^3$), and removing 16 molecules to insert $CS_2@C_{50}H_{10}$ complex, and finally equilibrating the system for 10 ps in a microcanonical run using temperature rescaling every 500 time-steps. Subsequently, during production runs of 1ns length, the temperature was fixed using a Hoover thermostat [Allen and Tildesley, 1987]. These simulations provide information on the thermal stability of the complex as we will see in next section.

4.1.1.1 Complex stability and binding energy

First of all, using the effective potential model for the $CS_2@C_{50}H_{10}$ complex described above, we have computed the potential energy profile of the complex along the main symmetry axis of the $C_{50}H_{10}$ molecule calculating the internal energy of the $CS_2@C_{50}H_{10}$ complex for different position of the CS_2 molecule in its lowest energy orientational configuration (see Figure 4.2), i.e. lying on the symmetry axis. In Figure 4.3 we have plotted the

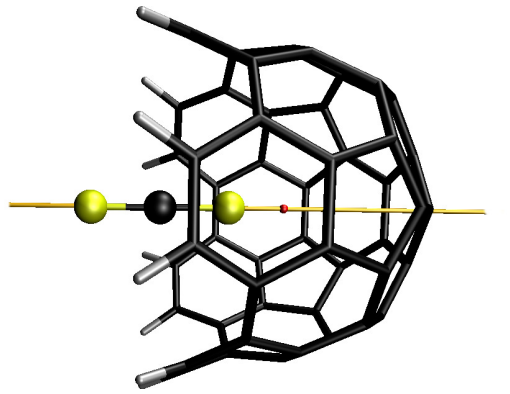

Figure 4.2: *Diagram showing the calculation of the potential energy profile. CS_2 molecule is moved along the symmetry axis of the nanotube, represented here with the yellow line. We have plotted the potential energy of system versus the separation between the CS_2 carbon atom and the nanocage center of mass, represented here with a red point.*

values of the binding energy with respect to the separation between the centers of mass of the $C_{50}H_{10}$ and the CS_2 molecules.

We have obtained an energy minimum of -12.70 kcal/mol at about 3Å separation between the guest and the host centers of mass. This value indicates the CS_2 molecules should have a definite tendency to remain inside the nanocage. Furthermore, we have also used our empirical potential model to minimize the corresponding potential energy for both the complex system and the two separate components, the geometry corresponding to the minimum potential energy is shown in Figure 4.4, and we have found that the binding energy of the system under study obtained through both methods is almost identical:

$$E_{Binding} = E_{CS_2@C_{50}H_{10}} - [E_{CS_2} + E_{C_{50}H_{10}}] = -12.74 \text{ kcal/mol} \quad (4.1)$$

This minimum is also in a very good agreement with the SAPT(DFT)

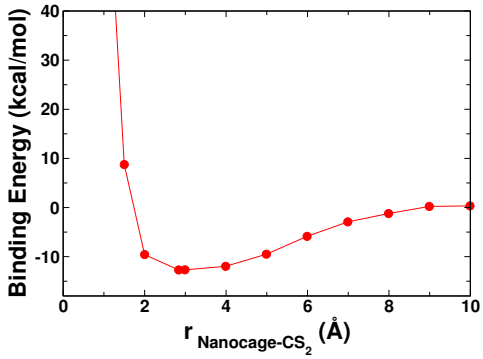

Figure 4.3: *Binding energy of the CS_2 molecule at 0K (lying inside the nanotube along its principal symmetry axis) as a function of the separation between the centers of mass of the guest molecule and the nanotube determined from the effective potentials used in MD calculation.*

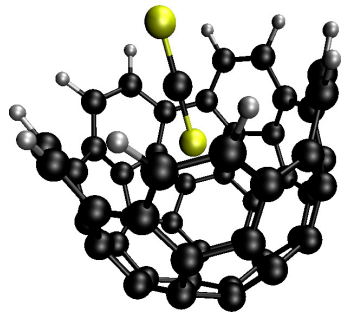

Figure 4.4: *Geometry corresponding to the potential energy minimum of the $CS_2@C_{10}H_{50}$ complex. The separation between the centers of mass of both molecules is about 3Å, which agrees with the potential energy profile.*

results from [Dodziuk et al., 2012] work: $E_{Binding} = -12.36$ kcal/mol, which is a good indication of the quality of the effective interaction model.

Left panel in Figure 4.5 illustrates the thermal stability of the complex

in vacuum. The guest molecule remains in the cage at 300K at a distance of 3.5Å of the center of mass of the nanocage, but it leaves the cage for higher temperatures as estimated from SAPT(DFT) calculations. This occurs in spite of the relatively high dissociation energy, as the result of the thermal fluctuations modifying the structure of both the guest molecule, (rotations and vibrations) and the host (vibrations of the nanotube edge).

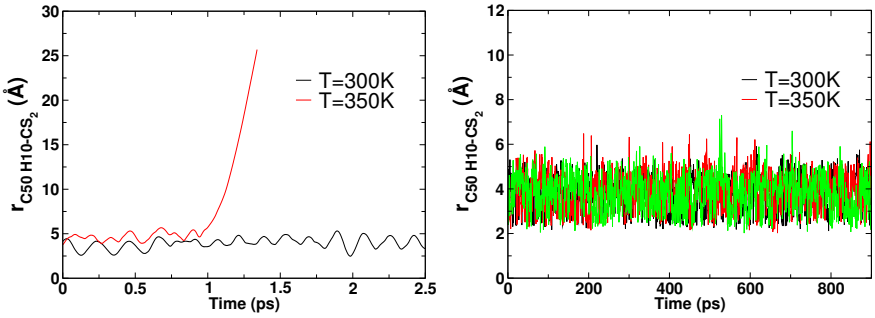

Figure 4.5: *Guest and host centers of mass separation is represented with respect to the time of the simulation for the system in vacuum (left) and in a chloroform solution (right).*

When the solvent is added, see Figure 4.6, although the equilibrium distance between the centers of mass of CS_2 and $C_{50}H_{10}$ increases, the guest molecule remains inside the cage for higher temperatures -see right panel of Figure 4.5-. Being CS_2 fully soluble in $CHCl_3$, this means that, although the chloroform molecules exert an attractive force over the guest, the net effect of the solvent is the stabilization of the complex.

4.1.1.2 Targeted molecular dynamics

In addition to straightforward NVT-MD, we have used Targeted Molecular Dynamics (TMD) (see **Section 2.3**), to evaluate the ligand Gibbs free energy (Δ G), by connecting this quantity with the work required to remove

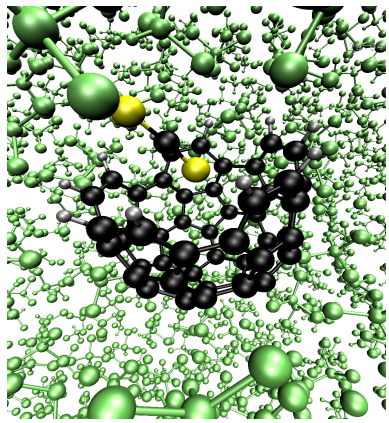

Figure 4.6: *$CS_2@C_{10}H_{50}$ complex immersed into a chloroform solution.*

the CS_2 molecule from the nanocage. We have used a distance type reaction coordinate, ρ that measures the root mean square displacement of the CS_2 molecule from the equilibrium position inside the host towards a target configuration where the CS_2 is beyond the cutoff of the $C_{50}H_{10} - CS_2$ interaction. The Molecular Dynamics is driven until the guest is well off the host. TMD simulations have been run for the complex $CS_2@C_{50}H_{10}$ in vacuum and in the presence of chloroform as solvent for 1ns and for different temperature values.

The results obtained from the TMD simulations are displayed in Figure 4.7. For the system in vacuum (left panel) we can observe that the work needed to pull the CS_2 molecule out of the host, when the temperature approaches at 0K, agrees with the binding energy value previously presented, -12.7 kcal/mol. When the temperature increases to 298K, the entropic effects gain importance and diminish the Gibbs free energy value $\Delta G = -2.5$ kcal/mol but still above the SAPT estimate with finite temperature corrections which is -1.5 kcal/mol. This relatively low value of the Gibbs free energy explains why the CS_2 molecule leaves the host when

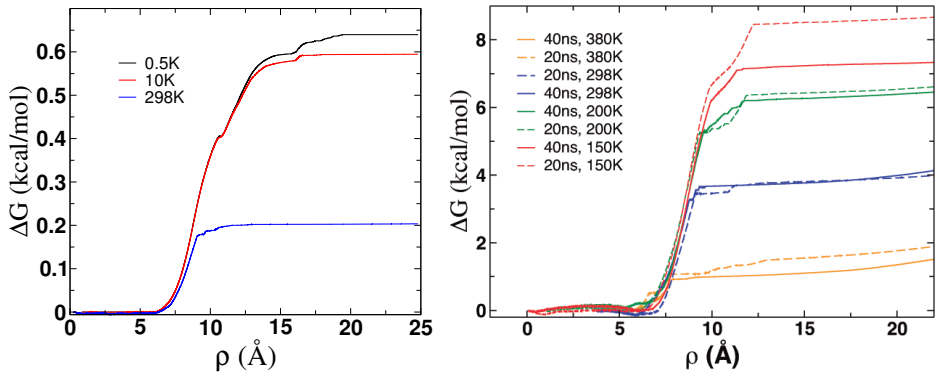

Figure 4.7: *Temperature dependence of the work required to remove the CS_2 molecule from the nano cage at different temperatures in vacuum (left) and in $CHCl_3$ solution (right). Furthermore, right panel also shows the Gibbs energy dependence with the simulation length.*

running Molecular Dynamics simulation at T higher than 300K in vacuum. On the other hand, when the solvent is present (right panel) its stabilizing effect is again noticeable in the binding Gibbs free energy value: at 298K $\Delta G = -10 kcal/mol$, which is substantially larger than the value for the system in vacuum.

TMD results vary considerably with the length of the simulation, since increasing the run length implies exploring a larger portion of the configurational space, thus increasing the chance of finding the absolute minimum free energy path to exit the nano cage (in right panel of Figure 4.7 we show the dependence of the results with the length of the simulation for various temperatures). As a guide to estimate the appropriate length of the simulation in the presence of solvent we have run TMD simulation for a free CS_2 molecule in $CHCl_3$, and chosen the simulation length for which the work required to move the CS_2 molecule tends to vanish (see Figure 4.8). In any case, it is absolutely clear that the nanocage can act as encapsulating agent of a non-polar molecular such as CS_2 in the presence of a practically

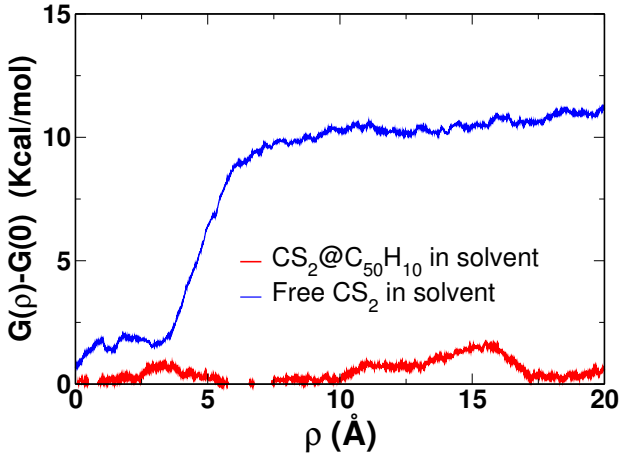

Figure 4.8: *Left: The work required to move a free CS_2 molecule in the presence of solvent (blue line) and to extract this molecule from the nano cage (red line).*

non-polar solvent; this is clearly shown in Figure 4.9.

4.1.1.3 Frequency spectra

In order to study the intramolecular dynamics of the $CS_2@C_{50}H_{10}$ complex, we have run simulations with a time step of in the range of 0.5 fs. Figure 4.10 shows the frequency spectrum (Fourier transform of the velocities autocorrelation function) of the free CS_2 and of the $CS_2@C_{50}H_{10}$ complex. We may appreciate that, together with the typical bands corresponding to the CS_2 molecule vibrations (bending and stretching), a new peak rises in the low infrared region when the complex is conformed. This feature is more evident for sulphur atoms (lower graph in Figure 4.10) and therefore it is not expected to occur in the empty nanocage. We lack experimental information in this respect, but given the relatively good agreement of the result for plain CS_2 with the experiment [Zhu et al., 1988] we have reason to believe that this feature is to be expected as a sign of the complex

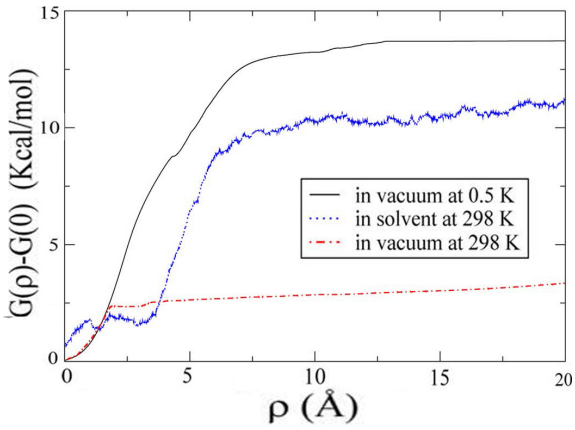

Figure 4.9: *Temperature dependence of the work required to remove the CS_2 molecule from the $CS_2@C_{50}H_{10}$ complex, in vacuum at 0.5 and 298 K and in the presence $CHCl_3$ at 298 K, in terms of the ρ reaction coordinate.*

formation and can be used as a measure of the strength of the interaction.

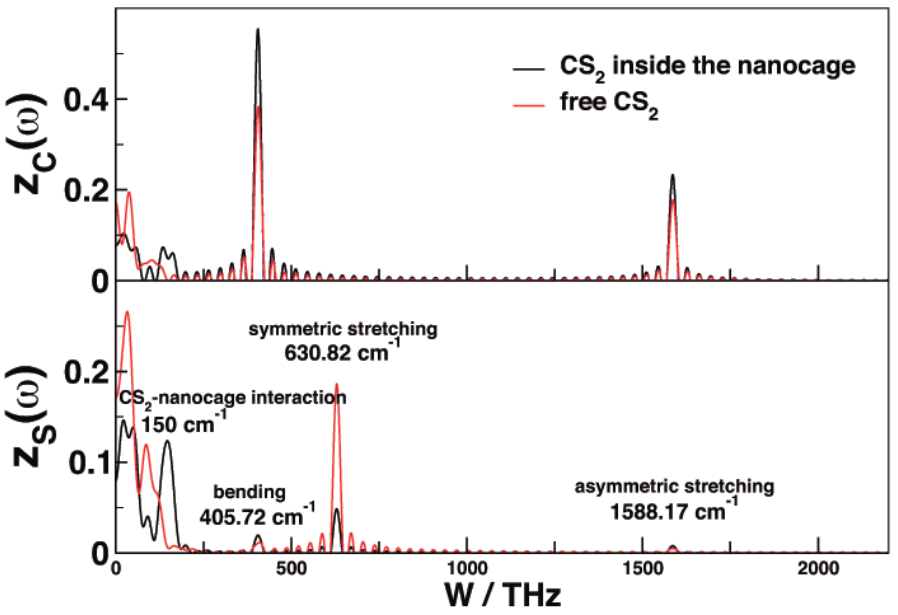

Figure 4.10: *Fourier transform of the velocity autocorrelation function $Z(\omega)$ shows that the CS_2 bound with the nanotube gives rise to a band in the low infrared.*

4.1.2 Encapsulation and adsorption of hydrogen: $H_2@C_{50}H_{10}$

In this Section we have studied, by means of grand canonical MC and MD simulations, the adsorption of hydrogen molecules in a crystal of short-capped nanotubes [Scott et al., 2011], modeled by a united atom approach. First of all, we have analyzed the interaction between a single short-capped nanotube and a hydrogen molecule, both in vacuum and in the presence of more hydrogen molecules acting as solvent. Again, the effect of the solvent on the stability of the complex has been studied using targeted molecular dynamics to calculate Gibbs free energies. Finally, we have explored the possibility of adsorption of molecular hydrogen in a molecular crystalline porous material made of these nano-structures.

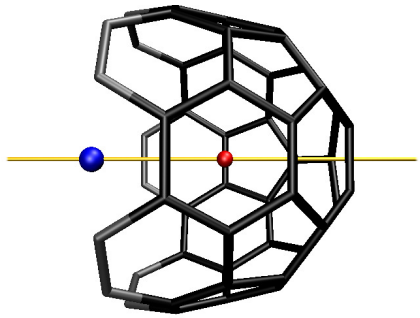

Figure 4.11: *Short-capped nanotube modeled using a united atoms approach. It consists of 40 carbon atoms (black) plus 10T CHs (grey). Molecular hydrogen is also considered as a spherical single particle (blue). Red point indicates the center of mass and yellow line the axis of symmetry of the carbon structure.*

The model we have used for describing short-capped nanotubes is based on a united atom approach: the structure, originally consisting of 50 carbon plus 10 hydrogen atoms ($C_{50}H_{10}$), has been reduced to 40 carbon atoms plus 10 CH sites conforming the open edge of the nanostructure ($C_{40}(CH)_{10}$). The hydrogen molecule has been also described as a single site (see Figure 4.11) following [Levesque et al., 2002]. Now our nanocage $C_{50}H_{10}$ will be considered as a rigid unit, which we believe to be a reasonable approximation, particularly for the low temperature calculations. The use of a rigid model will considerably lighten the computational burden when performing GCMC calculations on the molecular crystal of $C_{50}H_{10}$.

We have thus only taken into account the interactions of the hydrogen molecules, with each other and with the nanotubes. The interatomic potential we have used in this work is based on simple Lennard-Jones interactions that have been tuned in order to reproduce *ab-initio* energy data for the $H_2@C_{50}H_{10}$ complex. In the beginning, we have considered Lennard-Jones interactions between H_2 molecules and H_2-carbon atoms given by

Table 4.1: Effective potentials for the hydrogen-nanotube interaction. (a) [Levesque et al., 2002] and (b) [Zhao et al., 2005].

	σ_{ij}(Å)	$\epsilon_{ij}(kcal/mol)$	ϵ_{ij}^{f}(kcal/mol)
$H_2 - H_2$	2.958 (a)	0.07293 (a)	0.07293
$H_2 - C$	3.18 (a)	0.06369 (a)	($\times$1.5) 0.095535
$H_2 - CH$	3.3265 (a) (b)	0.08555 (a) (b)	($\times$1.8) 0.15399

Levesque et al. [2002]. We have calculated the H_2-CH sites interactions through Lorentz-Berthelot mixing rules, using the Lennard Jones parameters given in [Levesque et al., 2002] (for H_2-H_2) and in [Zhao et al., 2005] (for CH-CH). All these parameters have been summarized in Table 4.1.

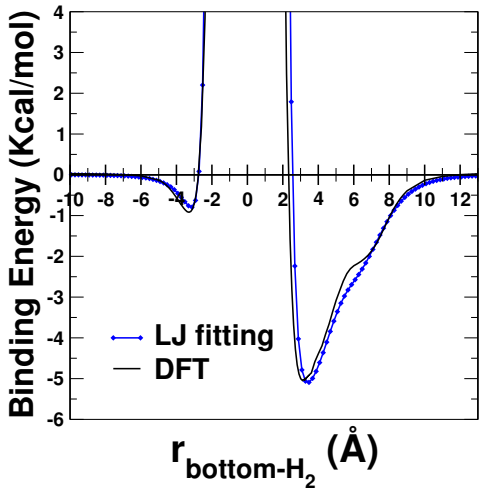

Figure 4.12: *Interaction potential between the H_2 molecule and the nano cage, both structures have been modeled through an all atom approach.*

The *ab-initio* data were obtained from DFT calculations using the

PBE (Perdew-Burke-Ernzerhof) exchange-correlation functional using basis PBE/PBE/6-3/G(d) and complemented by the Grimme's approach (GD3BJ) to account for the effect of dispersion forces (all this implemented in Gaussian09). The effective potential has been tuned to fit these calculations adjusting the strength of the H_2-C and H_2-CH original interactions (see last column in Table 4.1). Figure 4.12 shows the data obtained from DFT and the fitted Lennard-Jones parameters we have employed in this work. It can be seen that a good agreement has been reached between both potentials reproducing both the minimum and the shoulder for larger distances. The DFT calculations were carried at the IQFR by Prof. R. Notario.

On the other hand, $C_{50}H_{10}$ molecules have been shown to form molecular crystals [Scott et al., 2011]: a matrix of open structures that in principle seems to be a promising material to adsorb small molecules. We have characterized this porous material using the tool Poreblazer 3.0.2 [Sarkisov and Harrison, 2011], which gave a system density of 1.309 g/cm^3 and a maximum pore diameter of 3.91Å. The material is inappropriate for the adsorption of even small molecules such as N_2. However, it has a volume available for He of 0.301 cm^3/g, and one can expect hence that H_2 can be adsorbed in a stable fashion.

Hence, we have first analyzed the stability of $H_2@C_{50}H_{10}$ complexes as done before for CS_2, and considered the effect of the presence of an external bath of H_2. Afterwards, with the aim of studying the confinement of hydrogen into the molecular crystal, we have used grand-canonical Monte Carlo simulations to determine the adsorption isotherms of H_2 at various temperatures.

4.1.2.1 Solvation and Binding energy

First of all, we have studied the interaction between a single hydrogen molecule and a short-capped nanotube both in vacuum and in the presence of a H_2 bath. Figure 4.12 shows the interaction energy profile along the

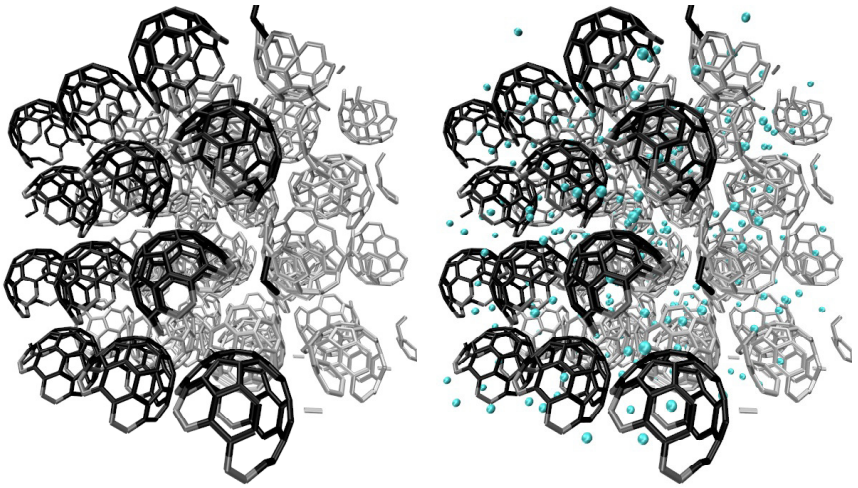

Figure 4.13: *Molecular crystal formed of short-capped nanotubes that results in an ordered porous media.... Only one plane of nanotubes have been colored to provide a clearer scheme of the structural order of the crystal. Left figure shows the empty crystal while the right one corresponds to 22 hydrogen molecules adsorbed per unit cell.*

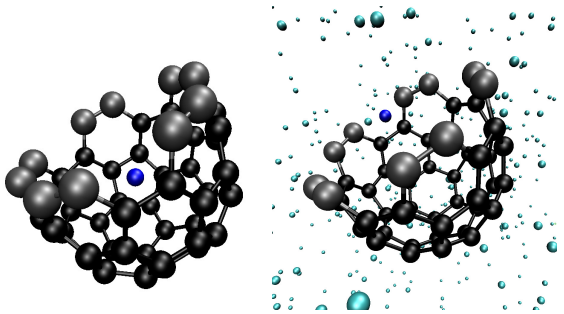

Figure 4.14: *Snapshots of the $C_{40}(CH)_{10}$-H_2 system both in vacuum (left) and in the presence of a H_2 bath (right).*

symmetry axis of the nanotube. One may appreciate that the value on the minimum is of ≈ -5kcal/mol, meaning that this complex is considerably

less stable than $CS_2@C_{50}H_{10}$. The value obtained here is lower than that given in Table 1 of [Dodziuk et al., 2012]. The reason for this discrepancy might be connected with the fact that the treatment of dispersion forces in SAPT(DFT) is essentially different from Grimme's approach implemented in Gaussian09. We believe that the latter is likely to provide better results.

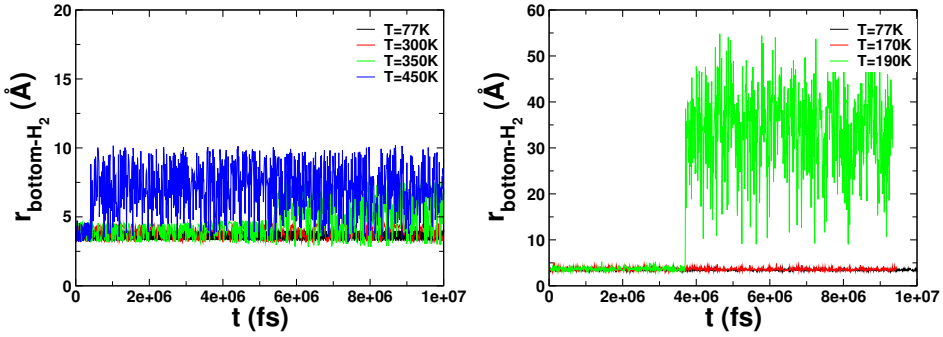

Figure 4.15: *Separation between the bottom of the nanotube and the adsorbed H_2 molecule in vacuum (left) and in the presence of more H_2 molecules acting as solvent (right). It shows that, in the vacuum case, the stability of the H_2-nanotube bond agrees with the minimum in the binding energy. 4.12*

Figure 4.14 shows a snapshot of the system in vacuum (left) and surrounded by hydrogen molecules (right) at a density of $\rho_{H_2} = 0.00763$ molec/Å^{-3} and an average pressure $P = 73.32$atm.

Figure 4.15 corresponds to MD long simulation runs in the NVT ensemble illustrating the change in the position of the H_2 molecule inside the nanotube with respect to its equilibrium position at 0K. They show how the hydrogen molecule remains oscillating around the distance corresponding to minimum of energy (see Figure 4.12) until the kinetic energy is enough to expel the hydrogen molecule from the host nanocage. In the case of the system in vacuum, only at high temperatures (beyond T=300K) the H_2 molecules transition from vibrating around the minimum of energy at

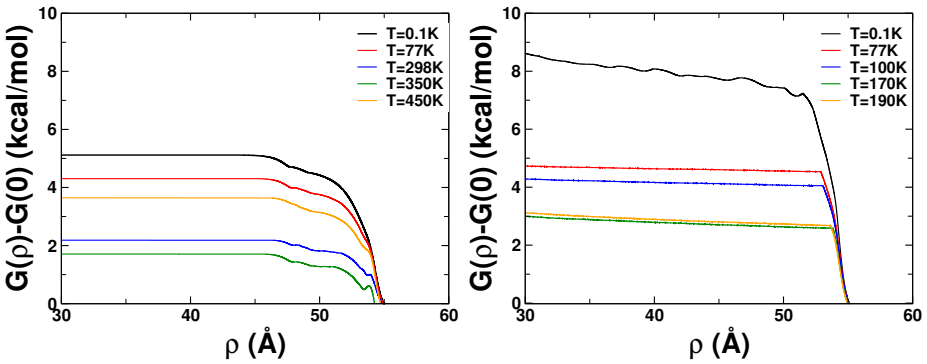

Figure 4.16: *Temperature dependence of the work required to remove the H_2 molecule from the nano cage at different temperatures in vacuum (left) and in a H_2 bath (right).*

$r \approx 3.5$Å to an oscillation around $r \approx 6$Å corresponding to the position of the shoulder in the binding energy (Figure 4.12) at the mouth of the nanotube. We have found that the complex is stable for temperatures higher than 180K, in contrast with the result of Dodziuk et al. [2012], which agrees the deeper energy well we have obtained here. However, when the system is surrounded by hydrogen molecules, the complex becomes unstable for much lower temperatures, between 170K and 190K. This is in marked contrast with the situation for $CS_2@C_{50}H_{10}$ in $CHCl_3$, due to the fact that the host molecule is now surrounded by identical molecules but also at a lower density. In the case of CS_2, the surrounding medium is liquid $CHCl_3$, by which there is an extra penalty to open room for a new molecule in the liquid. Such penalty is inexistent when the surrounding medium is gas, like in the case of H_2.

Once again, the effect of the H_2 bath on the Gibbs energy and the stability of the complex $H_2@C_{50}H_{10}$ has been analyzed by using Targeted Molecular Dynamics. We may see interestingly that whereas at low T the external H_2 atmosphere stabilizes the complex (e.g. at 0.1K the Gibbs binding energy is approximately 88 kcal/mol vs. 5 kcal/mol in vacuum).

Already at 77K this stabilizing effect is gone. For higher temperatures the binding energy is lower in the presence of an H_2 atmosphere.

4.1.2.2 Isotherm

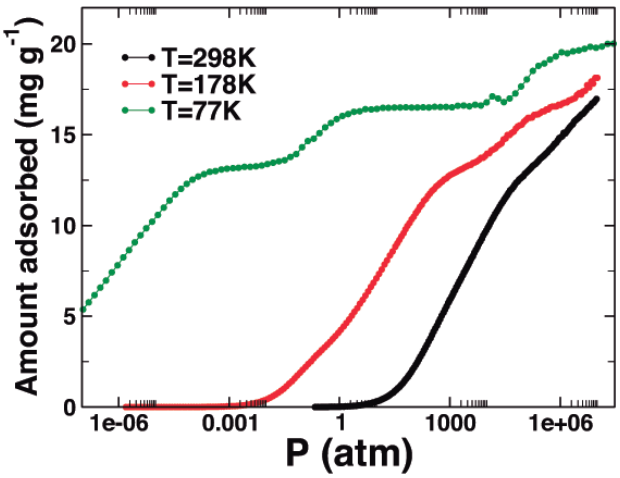

Figure 4.17: *Adsorption isotherms of H_2 molecules in the $C_{50}H_{10}$ molecular crystal, obtained from GCMC simulations at different temperatures.*

In Figure 4.17 we present the adsorption isotherms for hydrogen adsorbed in the crystal of short-capped nanotubes for different temperatures. The calculations have obtained from a big number of grand canonical Monte Carlo simulations. These simulations were 1.5×10^7 steps long, of which the first 5×10^6 steps were used for equilibration. Each step implies a displacement attempt of all the sample particles, one deletion and one insertion attempt. Pressures have been roughly estimated using the ideal gas equation of state, which is reasonable taking into account that the vapor-liquid critical Tc=33K. Use of more sophisticated EOS such as Peng-Robinson equation would quantitatively only modify the pressure axis.

Particularly at 77K we have a type I-VI adsorption isotherm [Rouquerol et al., 2014b], characteristic of a stepped adsorption. The presence of steps evidences the preferential adsorption of the H_2 molecules in the inner part of the cages, the mouth and the interstitial space within the molecular crystal (in this order). As T increases, the molecules tend to spend more time in the mouth of the nanocages (as we have seen in our MD analysis before) and the first step is somewhat blurred as well, but some remnant can still be appreciated in the change of slope of the isotherm. The maximum load values obtained (equivalent to 22 H_2 molecules per unit cell) clearly indicate that this material would certainly be a poor adsorbent for H_2, and the T dependence of the isotherm shows the low thermal stability of the adsorbed phase.

4.1.2.3 3D density maps and profiles

MD simulations in the NVT ensemble have been performed using LAMMPS package. The runs start from an initial configuration generated by a GCMC simulation at $T = 298$ K and the chemical potential needed to achieve the desired loading, 22 H_2 molecules per unit cell close to saturation. The performed simulations are long enough (5×10^5 steps for equilibrating the system plus 10^7 steps for recording configurations) to generate smooth and reliable density maps. Figure 4.18 shows the density maps for the molecular hydrogen adsorbed into the nano cages crystal complemented by representative snapshots of the corresponding system.

One may appreciate that the most intense areas (meaning that the probability of finding a molecule is higher) correspond to: the space inside the nanocages, where the minimum of the energy takes place; the mouth of the nano cage, where the binding energy exhibits a shoulder; and certain positions around the nano cages showing hexagonal order in the X plane (see central pictures in Figure 4.18).

Note that despite the high T, the loading is high, so as to achieve suf-

ficiently good statistics in a reasonable simulation time.

In summary, even if the stability of the $H_2@C_{50}H_{10}$ is acceptable, the molecular crystal is inadequate as a storage material, due to its low porosity and low thermal stability of the complex. An obvious possible improvement can be the design of longer nanocages tuning the synthesis os [Scott et al., 2011]. So as to stabilize the complex, and further on generate a disorder porous aggregate of cages, that increases the interstitial space as well.

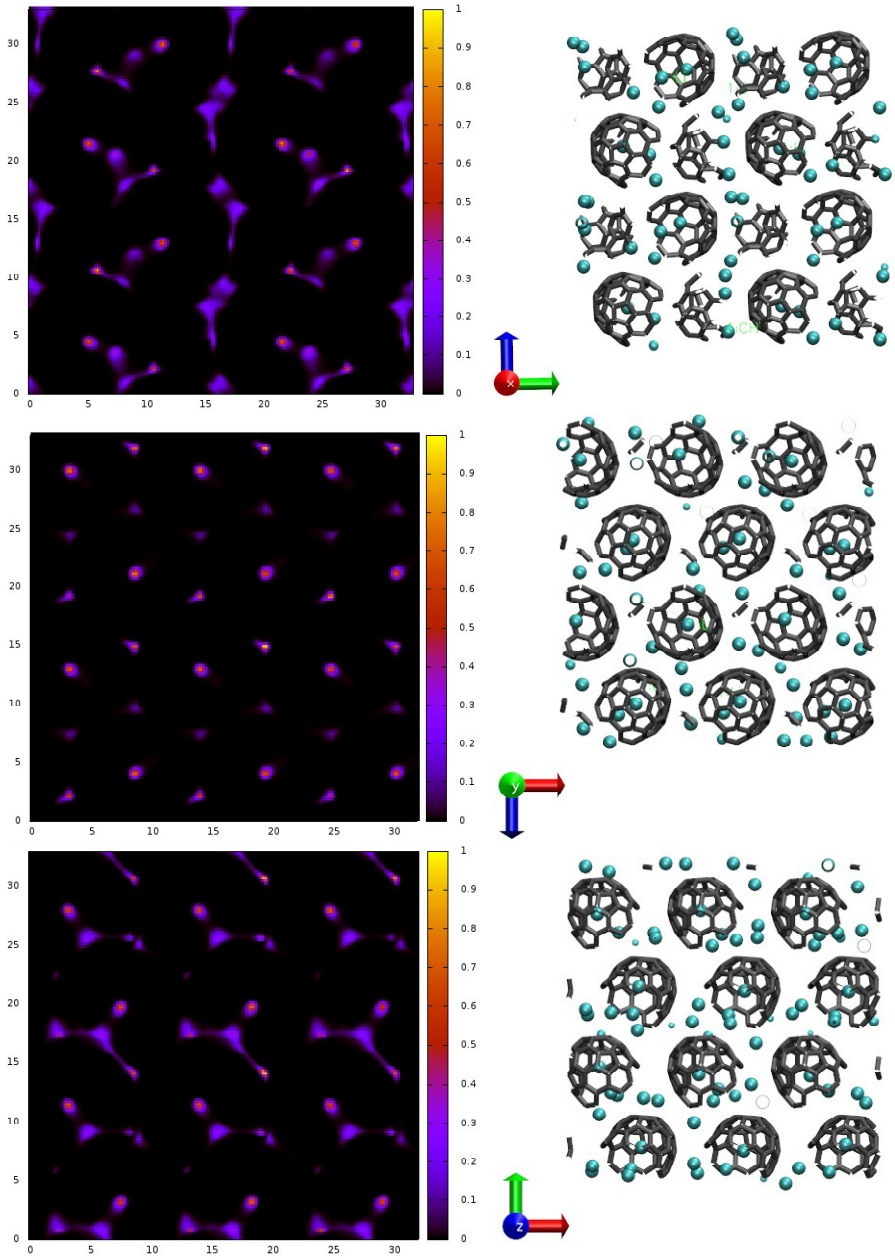

Figure 4.18: *Density maps and representative snapshots for the X (up), Y (center) and Z (bottom) planes of the molecular crystal. Averages have been taken over 500000 configurations of 22 hydrogen molecules per unit cell at 298 K.*

4.2 Simple fluids in zeolites

The aim of this Section is to explore the capabilities of the inhomogenous integral equation described in **Section 2.3** and applied in **Section 3.2** to the case of three dimensional porous systems exhibiting perfect crystalline order. Comparison with the results of grand canonical Monte Carlo/molecular dynamics simulations evidence that the theory provides an accurate description for the three dimensional density distribution of the adsorbed fluid, both at the level of density profiles and bidimensional density maps across representative sections of the porous material. Interestingly, we will also see that the crude approximation implied by using the ROZ-HNC equation to describe the fluid adsorbed in an ordered network of pores, gives reasonable results for the average fluid-fluid correlations and for the saturation behavior of the adsorption isotherms.

Model description

We present here the solution of the 3DOZ-HNC equation for a simple fluid, argon modeled as a one-site LJ fluid, adsorbed into three zeolite models, namely, silicalite-1 (all silica analogue of the ZSM-5 zeolite, framework type MFI), silicalite-2 (all silica analogue of the ZSM-11 zeolite, framework type MEL) and an all silica model of faujasite (framework type FAU). Both MFI and MEL zeolites are composed of 4-, 5-, and 6-membered rings linked to form a system of channels with 10-membered ring openings [Bibby et al., 1979]. In MFI, there is a combination of linear and zig-zag channels, while in MEL-type zeolites, all the channels are linear. Their channels are typically in the range of 5.4- 5.6 Å wide. All the channels in faujasite are formed by 12-membered rings and are also linear, being considerably wider (7.4 Å) and intersecting to form a cavity of 12Å of diameter. In contrast to the application of 2DOZ-HNC in **Section 3.2**, the adsorbent material is now formed by a regular network of interconnected channels, i.e a regular and highly inhomogeneous confining medium. However, the system composed by the fluid and the adsorbent will still be thought as a partly quenched

mixture following the ideas of Ravikovitch and Neimark [2006].

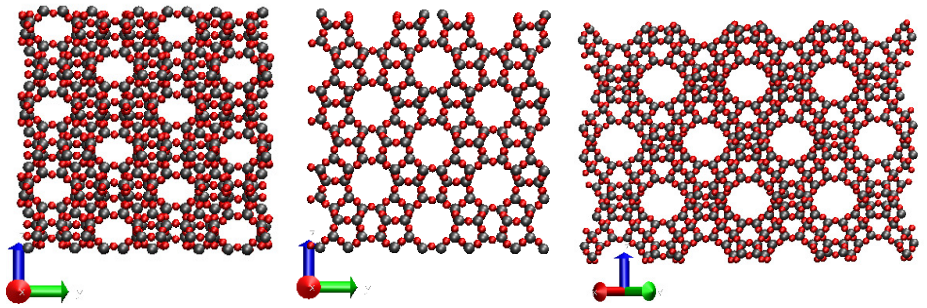

Figure 4.19: *MFI (left), MEL (center) and FAU (right) zeolites are shown. Note that the xy and xz projections of the MEL zeolites are identical, and the xz projection of the MFI zeolite is identical to that of the MEL zeolite. The projection of the FAU zeolite corresponds to the plane 110. Oxygen and silicon atoms are represented by red and grey circles respectively.*

The interactions between Ar atoms in our model are represented via a LJ potential of the form:

$$u_{ArAr(r)} = 4\epsilon_{ArAr}\left[\left(\frac{\sigma_{ArAr}}{r}\right)^{12} - \left(\frac{\sigma_{ArAr}}{r}\right)^{6}\right], \tag{4.2}$$

with $\epsilon_{ArAr}/k_B = 124.07$ K and $\sigma_{ArAr} = 3.38$Å [García-Pérez et al., 2008]. For our calculations, we have used a super-cell of $2 \times 2 \times 3$ unit cells for the MFI and MEL frameworks and one of $2 \times 2 \times 2$ unit cells for the FAU framework. The structure of the three zeolites in question is illustrated in Figure 4.19. Structural data for these zeolites are taken from [Terasaki et al., 1996; Olson et al., 1981; Baerlocher et al., 2007]. For the zeolite-Ar interaction, we will use the model of García-Pérez et al. [2008] that is, a Lennard-Jones interaction with $\epsilon_{OAr}/k_B = 107.69$ K and $\sigma_{OAr} = 3.15$Å. As it is customary when modeling adsorption in zeolites, if charges are not taken into account, the interaction between Ar and Si atoms is neglected,

being the latter completely embedded within the oxygen tetrahedra. In the case of the faujasite framework, one must take into account that in each unit cell there are eight inaccessible cavities, large enough to host an Ar atom. Obviously, these cavities will not participate in the adsorption process, and this must be borne in mind both when running grand canonical Monte Carlo (GCMC) simulations or when building the matrix-adsorbate potential for the solution of the 3DOZ equation. To that aim we have placed in the center of each cavity auxiliary sites which interact with the adsorbate molecules with a WCA-like interaction with ϵ and σ identical to those of the O-Ar potential. For computational efficiency, we have truncated and shifted the interactions at $R_c = 3\sigma_{ArAr}$.

Ar atoms adsorbed into MFI and MEL zeolites are under conditions of very tight confinement. In both instances, the channel width can only accommodate one atom, and the channel portion between intersections two atoms. Channel intersections have room for up to 4-6 atoms. As a whole, these rigid zeolite models can accommodate 30-40 atoms per unit cell. In contrast, FAU frameworks accept a loading of up to 150 Ar atoms per unit cell. These different levels of confinement will have a significant reflection in the performance of the theoretical approach. In order to assess the quality of our approximations, we have performed GCMC simulations for the adsorption isotherms of Ar in the three zeolite frameworks at 77 K for MEL and FAU and at 176 K for MFI. These simulations were 2×10^6 steps long, of which the first 500 000 were used for equilibration. Each step implies a displacement attempt of all the sample particles, one deletion attempt and one insertion attempt. The procedure uses a cavity bias algorithm to speed up the simulation [Snurr et al., 1993]. Three dimensional density maps of the adsorbed fluid were then generated for MEL at 77 K and a load of 30 Ar atoms/u.c., for MFI at 176 K and a load of 22 Ar/u.c., and for FAU for 104 Ar/u.c. at 77 K. For that purpose from the final GCMC configurations for a given load, canonical Molecular Dynamics (MD) simulations were run for 5×10^6 steps with a 1 fs timestep. Averages were calculated over 5000 configurations separated by 1000 steps with a time step of one fs. The loads were chosen such that in the case of MEL is close to the satu-

ration and above the adsorption step present in the experimental isotherm [Sánchez-Gil et al., 2016] and for MFI is just below the load corresponding to the adsorption step found at 77 K [García-Pérez et al., 2008]. In the case of FAU, the loading corresponds to two thirds of saturation, and its adsorption isotherm does not present any singular feature.

Solving ROZ-HNC equation

As a first step to solve the 3DOZ-HNC equation, we first have to solve the ROZ-HNC equations. This we have done on a 2048 point grid with a grid size of $0.02\sigma_{ArAr}$ using standard procedures [Lomba and Weis, 2010]. As input data our calculations require the knowledge of the structure factor. Instead of using matrix-matrix correlations obtained form the solution of a decoupled set of HNC equations as required by Eqs. 2.47 (which is not possible for a crystalline solid), here we will directly employ the exact structure factors for each zeolite structure. This is in stark contrast with the idea implicit in the ROZ equations of averaging over disorder. We might however interpret that the average is performed over the fluctuating positions of the lattice sites, which are not fixed due to thermal movement. This approximation will turn out to yield relatively good results. Additionaly, the zeolite structures are well-known and the structure factors can be accurately determined, due to their periodic nature, using direct q-sampling techniques. With these data at hand one can solve the ROZ equation, both using either a single component (O) matrix or a two component (Si/O) matrix. We will analyze the effect of the particular matrix model on the adsorption isotherms and on the pair correlation functions of the Ar-Ar and Ar-O in next Sections.

4.2.1 Adsorption isotherm

As we can see in Figure 4.20, the adsorption isotherms of the ROZ-HNC using the two component matrix are very poorly predicted. The problem

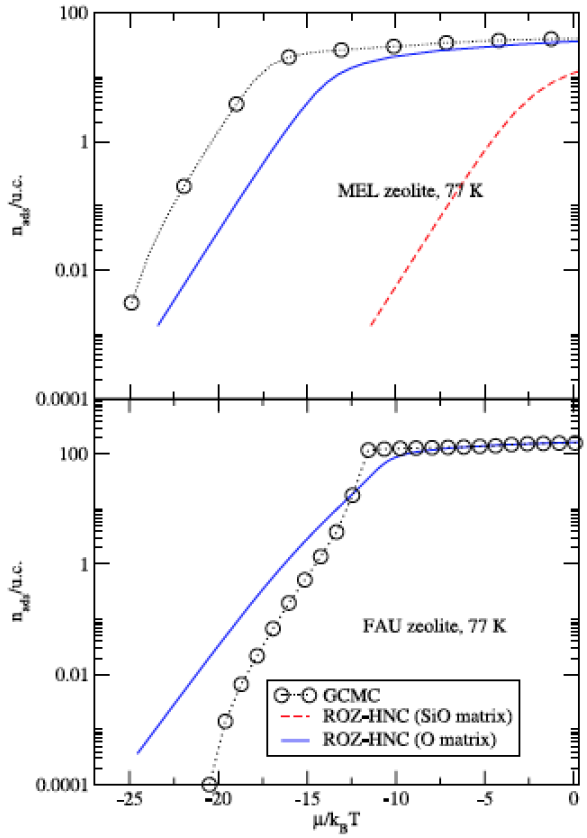

Figure 4.20: *Adsorption isotherms of Ar in MEL (upper graph) and FAU zeolites (lower graph) obtained from GCMC simulations and from the ROZ-HNC approximation*

clearly stems from the fact that including the Si atoms in the ROZ calculation increases the matrix density (i.e., lowers the porosity), and the atom-atom structure factors contain only partial information on the zeolite structure, namely information at the pair level which is clearly insufficient to describe the porosity of the system.

If we now focus on the adsorption results for the one component matrix, we observe that both in the case of MEL and FAU zeolites the saturation behavior is correctly reproduced. This is somehow telling us that the knowledge of the matrix density (that of the O atoms that form the channel structure) and the corresponding structure factors is sufficient to account for the volume available to the adsorbate. This is the quantity that determines the maximum load. Interestingly, the quality of the ROZ results deteriorates at low loads, where adsorption is mostly determined by energetic factors. Here, we observe that the adsorption in MEL zeolites is underestimated and in FAU is overestimated. This low adsorption load regime basically follows Henry's law, i.e., $n_{ads} = K_H \exp(\mu/k_B T)$. The theory predicts basically the same adsorption in MEL and in FAU at low chemical potentials ($K_H(MEL) = 0.0125$ atoms/u.c. vs $K_H(FAU) = 0.0114$ atoms/u.c.). This is not what happens in the simulation. When the number of adsorbate atoms is low, MEL adsorbs substantially more than FAU at the same chemical potential as a result of the stronger interactions between Ar atoms and the narrower channels of the MEL. In this case, an adsorbate molecule interacts directly with all the surrounding O atoms forming the channel, whereas in the case of FAU, the Ar-O interaction takes place mostly with part of channel surface, given the much larger size of the channels. Obviously in the case of low load, Ar-Ar contributions to the net interaction are negligible. It is clear that this difference is strongly dependent on the topology of the channel network, and as mentioned this is only partially incorporated into the ROZ equations via the structure factors. Since these are orientationally averaged pair functions that enter into a set of equations where all the functions are assumed to be homogeneous, one can hardly expect that such effects could be reproduced by the theory. In fact the latter behaves as if the pore network of its averaged "quenched" matrix would be somewhere in between that of MEL (narrow pores) and FAU (wide pores) zeolites.

4.2.2 Structural results

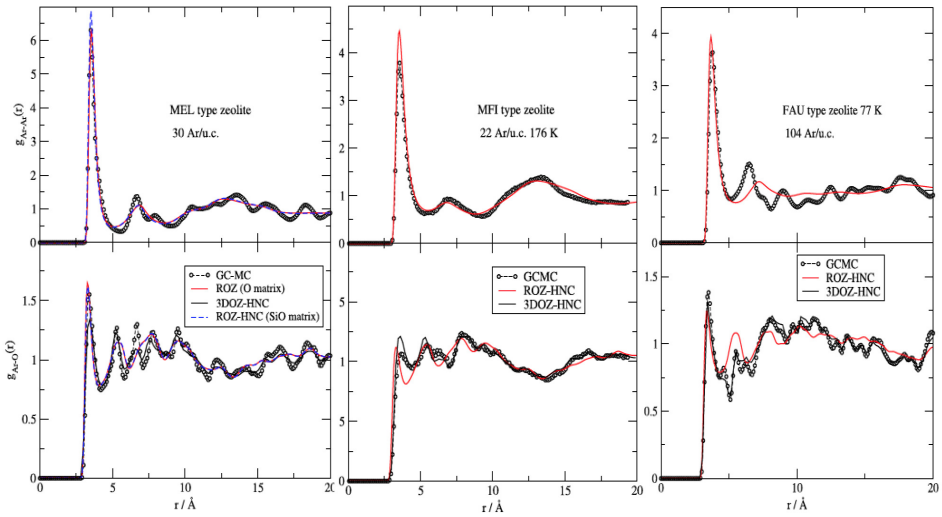

Figure 4.21: *Fluid-fluid (upper graphs) and zeolite-fluid (lower graphs) average pair distribution functions for Ar adsorbed into a MEL-zeolite at 77 K, MFI-zeolite at 176 K and FAU-zeolite at 77 K. Simulation results are denoted by circles, red curves represent results from the ROZ-HNC equations -in the case of MEL-zeolite (left) we have distinguished between the results with a one component matrix (red curves) and those of the two component matrix (dashed-dotted blue curves)- and solid black curve corresponds to results from the 3DOZ-HNC (at 94 K in the case of MEL and MFI-zeolites).*

We have found that the structural results when considering the two component matrix are practically indistinguishable from those of the single component matrix; this is shown in the left panel of Figure 4.21, where the theoretical Ar-Ar and Ar-O pair distribution functions for MEL zeolite are compared with simulation results.

In the central and right panels of Figure 4.21, we present the corresponding pair distribution functions for MFI and FAU zeolites at a some-

what lower relative loading. In these instances, only the single component matrix ROZ results are plotted. We note in passing that at the pair level structure, the ROZ results for the MEL and MFI are practically indistinguishable (and the simulation results for the pair distribution functions averaged over the inhomogeneity are also extremely close). In any case, when analyzing the results of Figure 4.21, it is rather obvious that the crude ROZ approximation we are using provides a qualitatively correct picture of the pair distribution functions averaged over the lattice inhomogeneities. Note however that the results for FAU (in particular for g_{ArAr}) are considerably worse than those for MFI or MEL. One might speculate that this can be related to the fact that Ar in the much larger cavities and channels of FAU is probably better represented by a fluid confined in a cylindrical cavity than in a disordered array of matrix particles. In the case of MEL/MFI, it may be that the higher degree of confinement can be somewhat better described from the structural point of view by our disordered matrix model.

With the fluid-fluid correlation provided by the ROZ-HNC approximation as indicated above, we solved the 3DOZ-HNC following the scheme summarized in Eqs. 2.52-2.61 using a cubic $256 \times 256 \times 256$ grid, by which the grid size is given by $\Delta x = L_x/256$, $\Delta y = L_y/256$ and $\Delta z = L_z/256$ where (L_x, L_y, L_z) are (40.12Å, 40.12Å, 40.209Å), (40.14Å, 39.84Å, 40.26Å) and (48.69Å, 48.69Å, 48.69Å) for MEL, MFI and FAU respectively. The equations typically converge in a couple of hundreds of iterations and take a few minutes to yield converged results.

Now, when solving the 3DOZ-HNC for MEL and MFI zeolites, we could not find convergence below 94 K (which is most likely associated with the extremely negative values of the zeolite-Ar interaction in the exponential). One may appreciate that the first peak in g_{ArO}, shown in left-lower panel of Figure 4.21, is underestimated as a consequence of the inability to reach the correct temperature. We insist on comparing theory and simulation in these conditions even when temperatures are rather different, since 77 K is one of the reference temperatures for adsorption experiments of noble gases.

4.2.3 Density maps and profiles

In Figures 4.22 and 4.23 we present bidimensional density profiles for the most unfavorable situation, MEL-zeolites in which the desired temperature (77K) could no be reached. In these figures, one can see the projection of the fluid density on some relevant planes of the zeolite structure that reflect the channel filling. Note that the MD results are averaged over a slab of 1.5 Å of thickness in order to collect sufficient statistics during the simulation run. Obviously, the theory can provide results with a resolution of approximately 0.2 Å (depending on the grid size) but we have performed a corresponding average over 1.5 Å to be able to compare with the simulation. One immediately appreciates that the theory reproduces qualitatively all the details of the spatial distribution within the channels. This can be seen from a more quantitative perspective in Figure 4.23, where the density profiles are plotted. One observes that both $\rho(x)$ and $\rho(y)$ are more structured in the theoretical results. This discrepancy is most likely due to the characteristic enhanced correlations of the HNC closure at contact, that in our case might as well be responsible for the breakdown of the equation when lowering the temperature.

In Figure 4.24, we present density maps for the MFI zeolite under less harsh conditions (a load of 22 Ar atoms/u.c. and 176 K). Results of the integral equation are now fully converged at the desired average adsorbate density and temperature. One observes that the agreement is now almost perfect. This is even more clearly seen in left panel of Figure 4.25 where the cumulative density profiles on the x and y axes are represented, and in the right panel of Figure 4.25 where we plot sections of the profiles for slabs around specific planes. In all cases, we observe here an excellent agreement between the theory and the simulation for all the details of the profiles.

Finally, we take now a look at the results for Ar adsorbed into faujasite for a load of 104 Ar atoms/u.c. and 77 K. In Figure 4.27, we plot the density maps corresponding to slabs centered on the relevant planes for this framework, which are now the 110 and $1\bar{1}0$, orthogonal and parallel to the

channels. The agreement is again fairly good, and one might even speculate that some discrepancies are due to the limited sampling of the MD run, e.g., some areas of the MD profile present a much starker contrast, which we have seen tends to become blurred as the sampling is increased. The corresponding cumulative density profile and the profile within a 1.5Å thick slab centered around the 110 plane are plotted in Figure 4.27. The overall performance of the theory is once more good with minor discrepancies in the heights of the peaks.

As an additional illustration of the structuring of the adsorbed fluid, we present in Figures 4.28 three dimensional representations of the fluid density, by means of isosurfaces using VMD software package [Humphrey et al., 1996]. A first isosurface represented in transparent glass corresponds to $\rho_1(x, y, z) = 0.005$ Å^{-3}, which is close to the average fluid density within the zeolite. In yellow (or red for FAU-zeolite), we indicate areas of high fluid concentration (close to liquid density) $\rho_1(x, y, z) = 0.058$ Å^{-3}. One can appreciate the presence of a high density region within the channels and two wide regions on the bottom and the top of the intersections together with 4 small regions in the middle of the intersection. These correspond to the locations where the 6 Ar atoms will be found at full loading [Sánchez-Gil et al., 2016]. In addition, one can also see that for the FAU framework (right panel in Figure 4.28), high adsorbate concentrations can be found equally scattered along the channels and intersections. This figure is a clear illustration of the information on the spatial disposition of the adsorbates that this type of approach can furnish.

In summary, we have seen that the 3DOZ-HNC provides an accurate description of the microscopic structure of simple fluids adsorbed into narrow channel zeolites, and in considerable shorter computer time that molecular simulation, opening an avenue for research in this type of system in parallel with the recent developments of the use of 3D-RISM in solvation problems of large molecules.

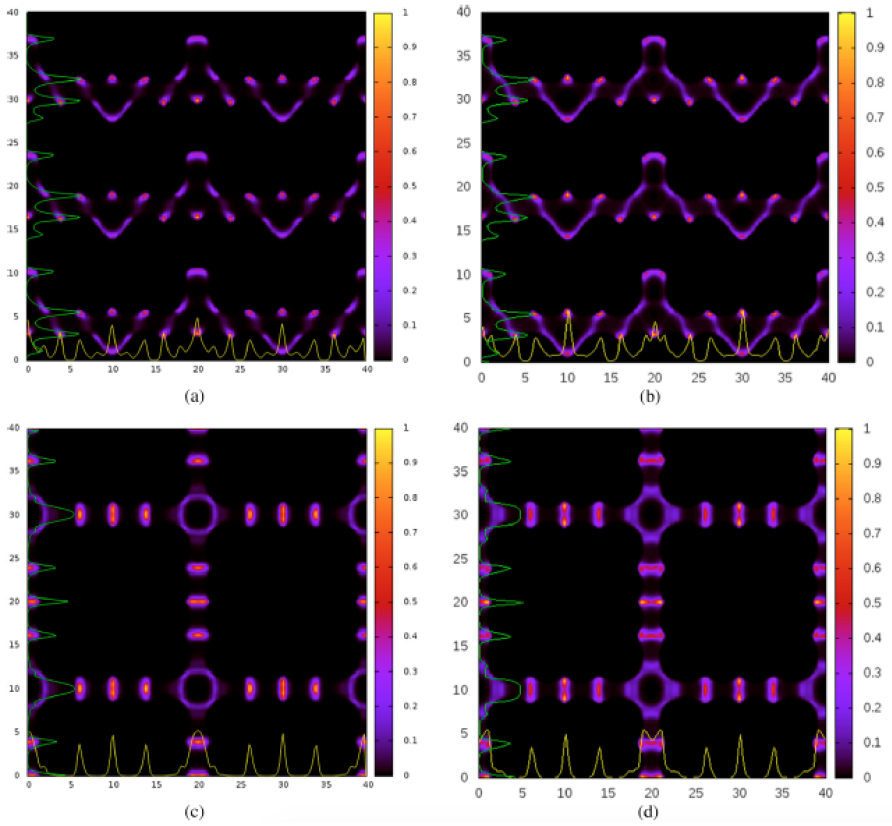

Figure 4.22: *Scaled fluid density distribution* $\rho_1(x,y,z)/\rho^{max}$ *of adsorbed Ar atoms into a MEL zeolite corresponding to a 1.5 Å thick slab centered at* $y_0 = 20.36$ *Å for the xz-plane and for the xy-plane at* $z_0 = 23.4$ *Å as computed from the 3DOZ-HNC equation for* $T = 94$ *K and 32 Ar/u.c. and simulation results for the same load and 77 K. Density profile projections on the y- and z-axis for a 1.5 Å thick slab are illustrated by green and yellow curves arbitrarily normalized to ease the visibility of the graphs. The plane positions are chosen to illustrate the channel structure.* ρ^{max} *is chosen as the maximum value of* $\rho_1(x,y,z)$ *-both in the 3DOZ and MD results- so as to normalize the color scale of the plot. (a) MD* $\rho_1(x,y_0,z)/\rho^{max}$*, (b) 3DOZ* $\rho_1(x,y_0,z)/\rho^{max}$*, (c) MD* $\rho_1(x,y,z_0)/\rho^{max}$*, (d) 3DOZ* $\rho_1(x,y,z_0)/\rho^{max}$

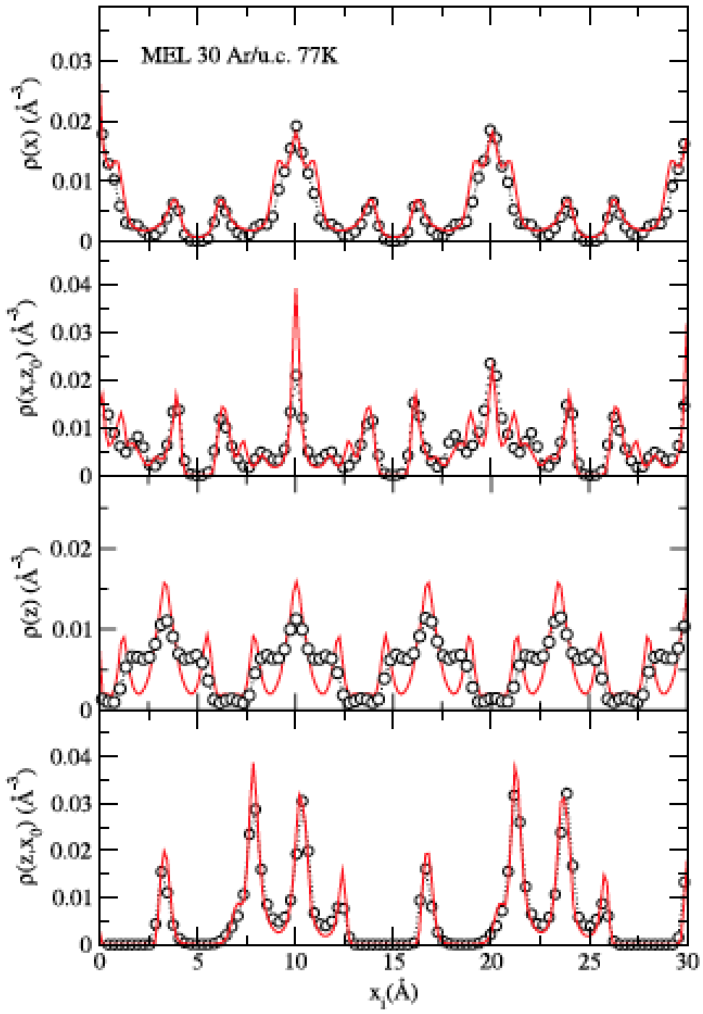

Figure 4.23: *Cumulative average density profiles of Ar atoms projected on the x axis, $\rho(x)$, and the z axis, $\rho(z)$, and sections $\rho(x, z_0)$ and $\rho(z, x_0)$ for slabs of 1.5 Å thickness around $x_0 = 20.36$ Å and $z_0 = 23.4$ Å for a load of 30 Ar atoms adsorbed into a MEL zeolite at 77 K, obtained from the 3DOZ-HNC approximation (solid curve) and computer simulation (circles). Note that the 3DOZ-HNC results correspond to the lowest converging temperature, 94 K. The axis label x_i denotes x or z depending on the graph under consideration.*

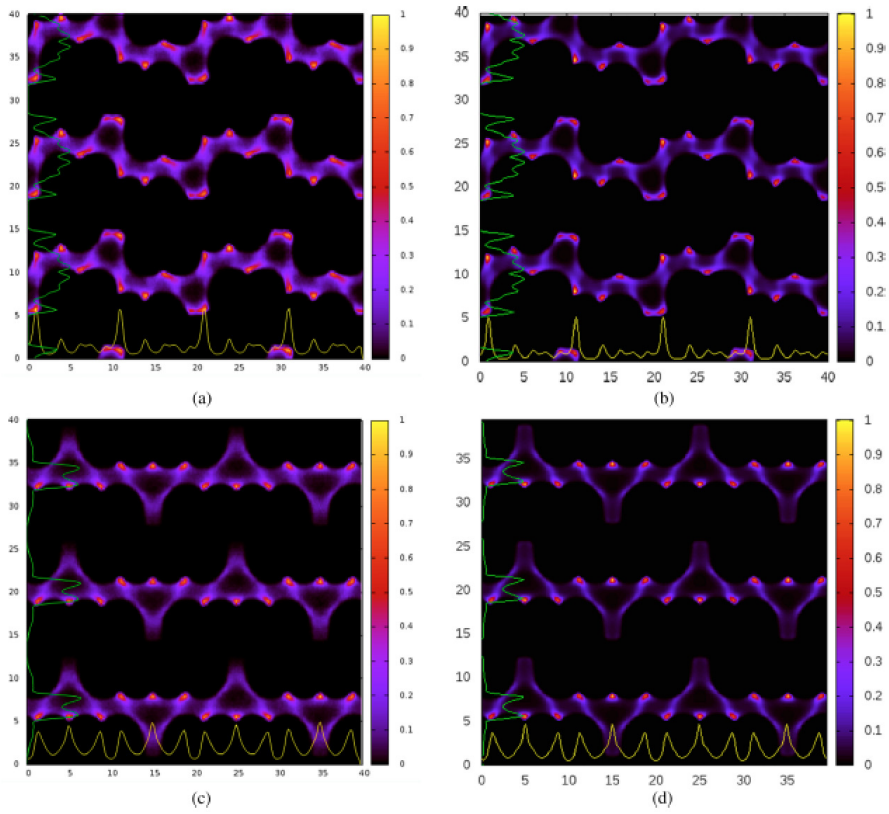

Figure 4.24: *Scaled fluid density distribution* $\rho_1(x,y,z)/\rho^{max}$ *of adsorbed Ar atoms into a MFI zeolite corresponding to a 1.5 Å thick slab placed at* $x_0 = 20.04$ *Å for the yz-plane and for the xz-plane at* $y_0 = 20.36$ *Å as computed from the 3DOZ-HNC equation and MD simulations for* $T = 176$ *K and 22 Ar/u.c. Density profile projections on the y- and z-axis for a 1.5 Å thick slab are illustrated by green and yellow curves arbitrarily normalized to ease the visibility of the graphs. The plane positions are chosen to illustrate the channel structure.* ρ^{max} *is chosen as the maximum value of* $\rho_1(x,y,z)$ *— both in the 3DOZ and MD results — so as to normalize the color scale of the plot. (a) MD* $\rho_1(x_0,y,z)/\rho^{max}$*, (b) 3DOZ* $\rho_1(x_0,y,z)/\rho^{max}$*, (c) MD* $\rho_1(x,y_0,z)/\rho^{max}$*, (d) 3DOZ* $\rho_1(x,y_0,z)/\rho^{max}$*.*

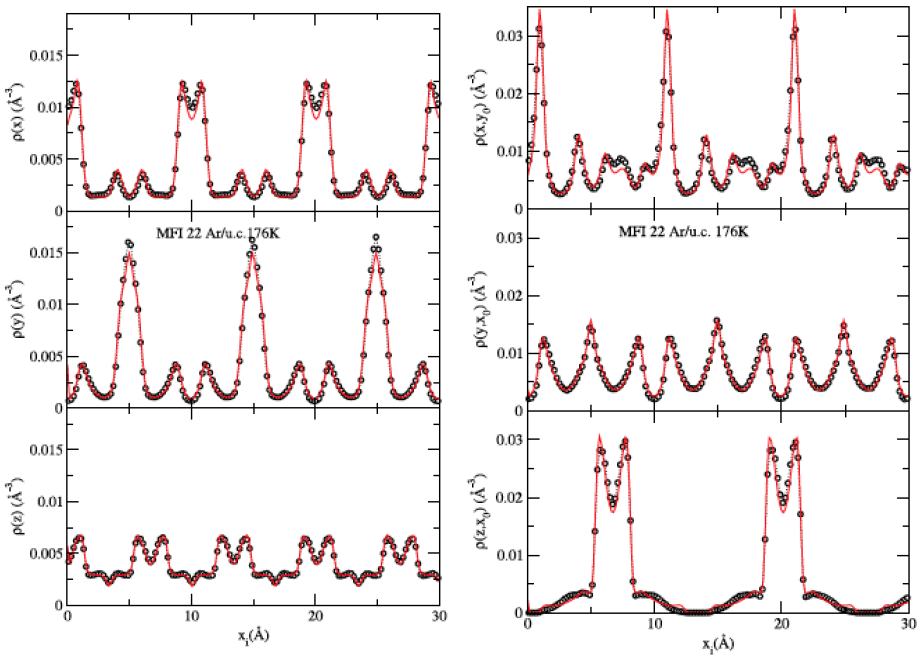

Figure 4.25: *Left graph: Cumulative average density profile of Ar atoms projected on the x axis, $\rho(x)$, y-axis, $\rho(y)$, and z axis, $\rho(z)$ for a load of 22 Ar atoms adsorbed into a MFI zeolite at 176 K obtained from the 3DOZ-HNC approximation (solid curve) and computer simulation (circles). Right graph: Sections of the density profiles of Ar atoms projected on the x axis, $\rho(x, y_0)$ for $y_0 = 24.90$ Å, y-axis, $\rho(y, x_0)$ for $x_0 = 20.04$ Å, and z-axis planes, $\rho(z, x_0)$ for $x_0 = 20.04$ Å for a slab of 1.5 Åthickness around the planes for a load of 22 Ar atoms adsorbed into a MFI zeolite at 176 K obtained from the 3DOZ-HNC approximation (solid curve) and computer simulation (circles). The axis label x_i denotes x, y, or z depending on the graph under consideration.*

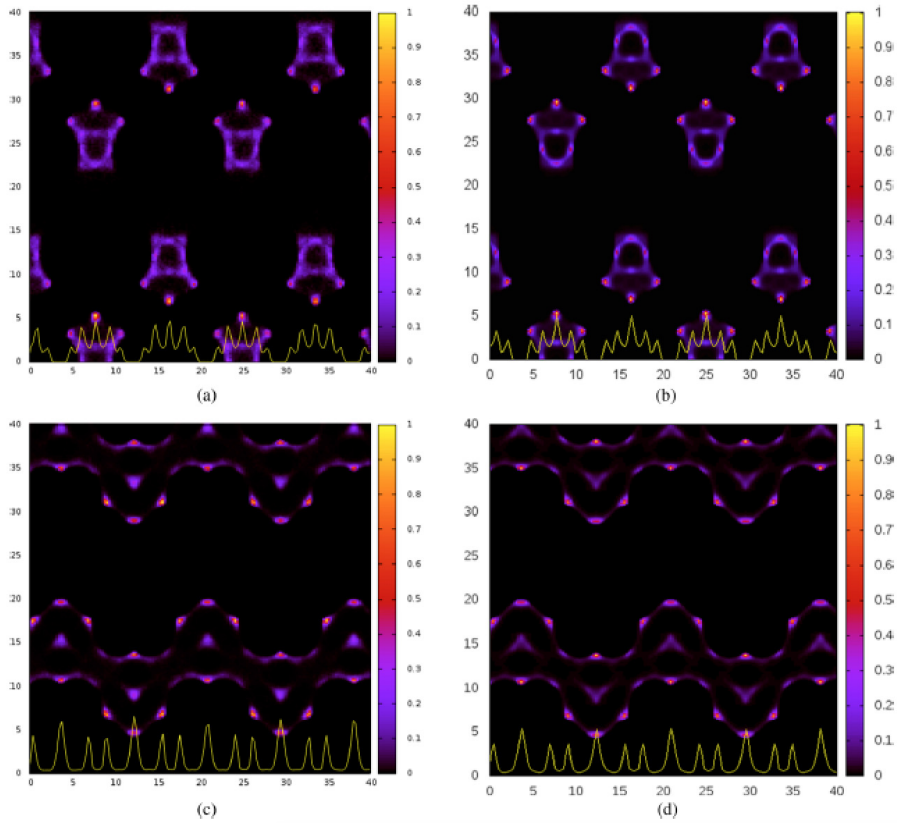

Figure 4.26: *Scaled fluid density distribution* $\rho_1(x,y,z)/\rho^{max}$ *of adsorbed Ar atoms into a FAU zeolite corresponding to a slab of 1.5 Å around the planes 110 (upper graphs) and* $1\bar{1}0$ *(lower graphs), as computed from the 3DOZ-HNC equation and MD simulations for* $T = 77$ *K and 104 Ar/u.c. Density profile projections on the diagonal axis of the xy plane defined by* $y = x$ *or* $y = L_x - x$ *for a slab of 1.5 Åthickness are illustrated by yellow curves and arbitrarily normalized to ease the visibility of the graphs.* ρ^{max} *is chosen as the maximum value of* $\rho_1(x,y,z)$ *- both in the 3DOZ and MD results - so as to normalize the color scale of the plot. (a) MD* $\rho_1(x,x,z)/\rho^{max}$*, (b) 3DOZ* $\rho_1(x,x,z)/\rho^{max}$*, (c) MD* $\rho_1(x,L_x-x,z)/\rho^{max}$*, (d) 3DOZ* $\rho_1(x,L_x-x,z)/\rho^{max}$*.*

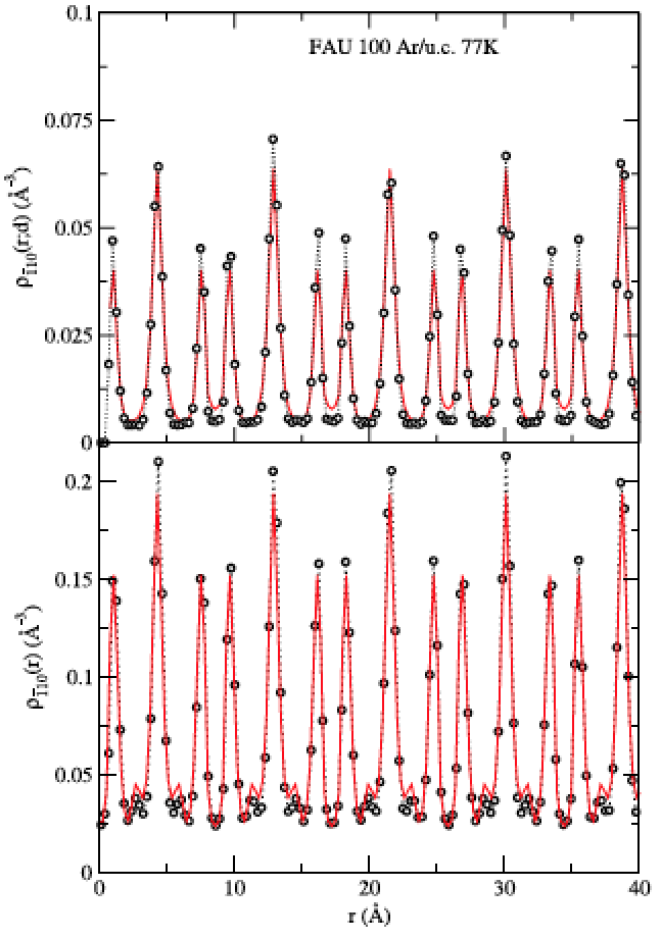

Figure 4.27: *Density profile of Ar atoms for a 1.5 Å thick slab around the* $\bar{h}110$ *plane,* $\rho_{\bar{h}110}(r;d)$*, and integrated over the xy plane in the 110-direction,* $\rho_{\bar{h}110}(r)$*, for a load of 104 Ar atoms adsorbed into a FAU zeolite at 77 K obtained from the 3DOZ-HNC approximation (solid curve) and computer simulation (circles). The r represents the distance to the origin across the diagonal of the xy-plane.*

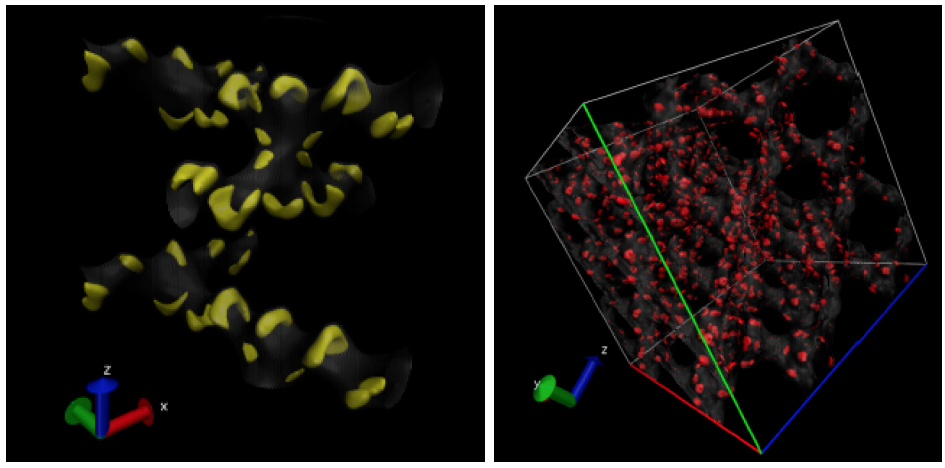

Figure 4.28: *Three-dimensional density distribution of Ar atoms for a load of 30 Ar atoms adsorbed into a MEL zeolite at 94 K (left panel) and for a load of 104 Ar atoms adsorbed into a FAU zeolite at 77 K (right panel) obtained from the 3DOZ-HNC approximation, plotted by means of isosurfaces defined by* $\rho_1(x, y, z) = 0.005$ *Å*$^{-3}$ *(glassy surface) and 0.058 Å*$^{-3}$ *(yellow for MEL and red for FAU).*

Conclusions

As mentioned in the **Preface**, along this thesis we have pursued three objectives: to reveal how does the confinement influence self-assembling fluids, to evaluate the capabilities of new nanostructured materials for adsorption applications, and to construct an integral equation based theory suitable to deal with adsorption and confinement processes. To this aim, simple and self-assembling fluids have been confined in a variety of porous media, and studied by means of both theoretical and simulation approaches. The result obtained from the analysis of these systems are described in **Chapter 3** and **Chapter 4**.

In what follows, we highlight the most relevant conclusions obtained in this thesis, underlying the connection with our goals.

1. To reveal *the effect of the confinement on the properties of self-assembling fluids* constitutes our first goal. To this aim, we have considered different models of fluids exhibiting spontaneous order emergence and their confinement into both regular (slit-pores) and disordered (porous glasses) media.

    - First, we have considered a simple mixture of dimers and monomers, with short range attractive and repulsive interactions. It turns out that this simple "toy model" gives rise to the presence of

nanostructural order in the form of micro-segregation in bicontinuous structures (which in turn translates into the characteristic presence of a prepeak in the site-site structure factors). The effective site-site potentials extracted from the pair distribution functions by means of an inverse MC and integral equation approach display the characteristic features of the SALR interactions, with the repulsive long range increasing as the total density (and hence the ordering) increases. Furthermore, the addition of charges to the model enhances the nanostructural order. This analysis presents a unified view of microsegregated bi-continuous domains, pre-peaks in structure factors, and SALR type interactions, which are common to many complex systems with self-assembling features, and explains how pattern formation at the nanoscale level can occur even without the presence of explicit long-range interactions. We find that confinement of this model mixture both in regular and disorder porous tends to enhance pattern to demixing. In the case of disordered media, finite structures are somewhat favored due to spatial constraint.

- We have also analyzed the confinement of a fluid described by means of an effective SALR potential into a model of porous glass, showing large and random disordered cavities. We have found that the adsorption process of the SALR fluid in our porous matrix strengthens the formation of droplets, i.e. it stabilizes the cluster phase and impedes the formation of percolating structures. Emerging stripe phases can still be found in large pores, whereas in small pores the cluster phase transforms into a bubble phase upon increasing fluid density. For the type of matrix we have considered, we find that the pores are wide enough to preserve the average intercluster separation in the confined fluid with values quite close to those obtained for the infinite fluid. Future work may focuse on the modulation of the fluid mesophases by tuning of the matrix-fluid interactions, possibly

including the presence of heterogeneities in the matrix composition.

- In the case of RTILs confined between graphene layers, we have found that our $[BMIM][PF_6]$ RTIL model does not wet the pore walls for low packing densities, which rules out the possibility of practical coating of the inner surface of carbon porous materials with this IL, in order to enhance the adsorption capabilities. It remains open the question of the effect of temperature and very specially the length of the non polar chain.

- In addition, we have also studied the dynamics of this SALR fluid both in bulk and confined in the disordered matrix. The cluster emergency is reflected in the dynamics of the fluid through the cage effect of the particles within each cluster that can be observed at gas-like densities and low temperatures. Comparing the dynamics of the SALR fluid in bulk and under confinement, we have found that the effect of this confining medium is relatively weak, because collisions with the matrix have a lower impact on the velocities correlations than those with other clusters, but correlations decay somewhat faster in bulk than under confinement.

Summarizing, we have found that the effect of the confinement over the structural order emerged in self-assembling fluids is the enhancement of finite non-percolating patterns, and the appearance of preferred positions in the confining media, which translates into a layered structure near the walls when they are confined in slit pores, and into permanent droplets placed in certain cavities when confined in a disorder matrix. Dynamics of the SALR fluid clearly reflects the emergence of particle aggregates, and it is weakly

affected by the confinement probably due to the specific nature of our confining medium.

2. Our second goal is to explore *the feasibility of the storage of small molecules storage in short capped nanotubes.* We have first studied the encapsulation of simple molecules such as CS_2 and H_2 into a single carbon based short-capped nanotube both in solvent and in vacuum; and afterwards we have studied the adsorption of H_2 into a molecular crystal formed by short-capped nanotubes.

   The results for the experimentally observed $CS_2@C_{50}H_{10}$ complex obtained using Molecular Dynamics simulations are in excellent agreement with those obtained by Dodziuk and Korona by means of the SAPT(DFT) theory. Both predict that the complex becomes unstable at temperatures larger than 340K at 1 atm. Furthermore, the simulations also indicate that the $CHCl_3$ solvent stabilizes the complex. This opens the possibility of using these nanocages for transport of other molecules, e.g. biologically active chemicals) and study their release in different environments. On the contrary, we have found that the $H_2@C_{50}H_{10}$ complex has a much lower stability, particularly in the presence of H_2 atmosphere.

   Furthermore, we have found from a porous distribution analysis of the crystal made up of short capped nanotubes, that only small cavities are present in the material, thus only He and H_2 molecules may be adsorbed... which is reflected in the stepped shape of the adsorption isotherms, the amount of H_2 adsorbed rules out its potential use for H_2 storage.

   To conclude, $C_{50}H_{10}$ nanocages might well have the potential use for encapsulation of molecules of biological/medical interest, but its use for H_2 storage is ruled out. However, this

study paves the way to scrutinize potential new longer short-capped nanotubes, and search for either molecular crystals of disordered structures with larger interstitial spaces, considerably enhancing the stability of the adsorbed and their capability as adsorbent.

3. Finally, we have constructed and tested a *new theoretical approach, in the framework of integral equation theory*, that provides an explicit and detailed description of the fluid distribution into the porous media.

   - We have first explored the ability of a full 2D solution of the HNC (and PY) equation for the description of the self-assembling fluid, described by means of the SALR potential, adsorbed into a disordered porous matrix with a large degree of porosity. The equation was complemented by the use of a ROZ-HNC equation to faithfully approximate the fluid-fluid correlations under confinement. We have shown that this approach reproduces in a satisfactory way the average fluid-fluid spatial correlations of different types of adsorbates and its combination with the 2DOZ-HNC equation also yields a fair approximation for the matrix-fluid correlations. Additionally, subject of future work will be the analysis of the correlation between porosity and cluster size distribution.

   - We have also applied this procedure to three dimensional model systems of Ar adsorbed into MEL, MFI, and FAU zeolites. Fluid-fluid direct correlation functions were approximated using the ROZ-HNC equations using as matrix-matrix correlations those calculated from the zeolite structure factors. The average fluid-fluid and fluid-zeolite structure provided by the ROZ-HNC using a one-component (oxygen atoms) matrix turned out to be quali-

tatively correct, particularly in the case of MFI and MEL (tight confinement). Interestingly, the adsorption isotherms obtained from the one component ROZ-HNC reproduce well the saturation limits of the zeolites and much better than those obtained using a two component matrix. Using the ROZ-HNC fluid-fluid correlations, the 3DOZ-HNC was solved for the three systems of interest. At higher temperatures/lower loads or for low temperature adsorption in faujasite, the theoretical results agree remarkably well with the simulation and provide an accurate three dimensional picture of the fluid distribution with a much higher resolution. Additionally, we have shown that the averaged fluid-adsorbate distribution function can also be accurately computed from the 3DOZ equation, outperforming the ROZ-HNC results for this structural quantity. The fact that the 3DOZ-HNC incorporates explicitly many body effects from the adsorbate-matrix interaction explains the better accuracy of this approach.

- A straightforward application of this 3DOZ-HNC approach, which is under performance at this moment, is to use it for describing the adsorption of H_2 in the molecular crystal of $C_{50}H_{10}$ nano cages, and its extension to mixtures of adsorbed fluids, including molecular liquids in the RISM approximation.

In conclusion, this work presents a very useful tool, in the framework of the Integral Equation Theory, for providing a detailed average density map of the adsorbed fluids in both two and three dimensional systems. We have applied this technique to study simple noble gasses and complex fluids with self-assembling properties confined in both random disordered (pore glasses) and regular (zeolites) porous media, finding in all cases a good agreement with simulation results at a substantially lower computational cost.

Conclusiones

En el **Prefacio** se han señalado los tres objetivos perseguidos a lo largo de esta tesis: analizar la influencia del confinamiento sobre el comportamiento de los fluidos con propiedades autoensamblantes, evaluar la capacidad de nuevos materiales nano-estructurados para aplicaciones de adsorción, y construir una teoría, en el marco de las Ecuaciones Integrales, adecuada para situaciones de adsorción y confinamiento. Para cumplir estos objetivos, se han analizado, mediante métodos teóricos y de simulación, fluidos simples y con propiedades auto-ensamblantes confinados en diferentes medios porosos. Los resultados obtenidos se han descrito en los **Capítulos 3** y **4**.

En los siguientes items se describen las conclusiones mas relevantes que se han encontrado a lo largo de esta tesis:

1. Se ha encontrado que en condiciones de confinamiento, el orden estructural que emerge en fluidos auto-ensamblantes se ve afectado de forma que se acentúa la formación de patrones finitos no percolantes. Además, aparecen posiciones preferenciales en determinados lugares de los medios porosos. Esto se traduce a una estructura ordenada en forma de láminas en los poros tipo "slit-pore" en las zonas cercanas a las paredes, y en agregados permanentes situados en determinadas cavidades cuando el medio poroso es desordenado. La dinámica de los fluidos tipo SALR refleja claramente la presencia de agregados de partículas, y está débilmente afectada por el confinamiento, probablemente debido a la naturaleza del medio de confinamiento específico

que hemos utilizado.

2. Las nanocajas ($C_{50}H_{10}$) pueden usarse para encapsular moléculas con interés biológico o médico, sin embargo este estudio concluye que su uso para almacenamiento de hidrógeno queda descartado. No obstante, queda abierta la posibilidad de considerar nuevas moleculas del mismo estilo pero un poco mas largas, y construir con ellas tanto cristales moleculares como estructuras desordenadas con espacios intersticiales mas grandes mejorando considerablemente la estabilidad del compuesto, y por tanto la capacidad del material como adsorbente.

3. Por último, este trabajo presenta una útil herramienta, en el marco de la teoría de Ecuaciones Integrales, que provee un detallado mapa de densidad del fluido adsorbido en sistemas de dos y tres dimensiones. Hemos aplicado esta técnica para estudiar tanto gases nobles como fluidos complejos por propiedades auto-ensamblantes confinados en medios porosos aleatoriamente desordenados (vidrios porosos) y también regulares (zeolitas). Se ha encontrado en ambos casos una buena concordancia con los resultados obtenidos mediante métodos de simulación y al mismo tiempo una disminución sustancial del coste computacional.

The main results of this thesis are collected in the following publications:

1. *A Carbon Nanotube Container: Complexes of $C_{50}H_{10}$ with small molecules.* H. Dodziuk, T. Korona, E. Lomba and C. Bores, *J. Chem. Theory Comput.* **8** 4546 (2012)

2. *Explicit spatial description of fluid inclusions in porous matrices in terms of an inhomogeneous integral equation.* E. Lomba, C. Bores, G. Kahl, *J. Chem Phys.* **141** 164704 (2014)

3. *Demixing and confiment of non-additive hard-sphere mixtures in slit pores.* N.G. Almarza, C. Martín, E. Lomba and C. Bores, *J. Chem. Phys.* **142** 014702 (2015)

4. *Pattern formation in binary fluid mixtures induced by short-range competing interactions.* C. Bores, E. Lomba, A. Perera and N.G. Almarza, *J. Chem. Phys.* **143** 084501 (2015)

5. *Adsorption of a two dimensional system with competing interactions in a disordered, porous matrix.* C. Bores, N.G. Almarza, E. Lomba, G. Kahl, *J.Phys: Condensed matter* **27** 194127 (2015)

6. *A three dimensional integral equation approach for fluids under confinement: Argon in zeolites.* E. Lomba, C. Bores, V. Sanchez-Gil, E.G. Noya, *J. Chem. Phys.* **143** 164703 (2015)

7. *Confinement effects on a simple self-assembling mixture model* C. Bores, E.Lomba, A.Perera and B. Kracic (2016). In preparation.

8. *Hydrogen adsorption in molecular crystals of short-capped nanotubes: simulation and integral equation studies* C. Bores, E.Lomba and R. Notario (2016). In preparation.

Appendix A

Generalization of the structure factor: from 1D to 3D

The 1d discrete Fourier Transform and its inverse are:

$$Y_k = \sum_{j=0}^{N-1} X_j e^{-i\frac{2\pi}{N}jk} \; ; \; X_j = \frac{1}{N}\sum_{k=0}^{N-1} Y_k e^{i\frac{2\pi}{N}jk}. \tag{A.1}$$

It is possible to generalize these one-dimensional expressions to the multi-dimensional case by multiplying the 1d transforms along each dimension [**?**]:

$$Y_{k_{1,\ldots,d}} = \sum_{j_1=0}^{N_1-1}\sum_{j_2=0}^{N_2-1}\ldots\sum_{j_d=0}^{N_d-1} X_{j_{1,\ldots,d}}\omega_1^{-j_1k_1}\omega_2^{-j_2k_2}\ldots\omega_d^{-j_dk_d}, \tag{A.2}$$

where $\omega_s = e^{i2\pi/N_s}$ for all $s \in 1, 2, ..., d$ being d the dimension. It can be shown how this multi-dimensional array made up of mono-dimensional functions preserves Fourier transforms properties like orthogonality.

Moreover, the Fourier transform of a discrete convolution of the form:

$$F_j = \frac{1}{N} \sum_{i=0}^{N-1} h_i g_{j-1}, \tag{A.3}$$

may be decomposed as:

$$\tilde{F}_k = \sum_{j'=-l}^{N-1-l} g_{j'} e^{i\frac{2\pi}{N}k_{j'}} \sum_{l=0}^{N-1} h_l e^{i\frac{2\pi}{N}k_l} = \frac{1}{N}\tilde{G}\tilde{H}. \tag{A.4}$$

Bibliography

Alexander, M., Rojas-Ochoa, L., Leser, M., and Schurtenberger, P. (2002). Structure, dynamics, and optical properties of concentrated milk suspensions: an analogy to hard-sphere fluids. *Journal of colloids and interface science*, 253:35–46.

Allen, M. and Tildesley, D. (1987). *Computer Simulation of Liquids*. Oxford University Press.

Almarza, N., Martín, C., and Lomba, E. (2009). Phase behavior of the hard-sphere maier-saupe fluid under spatial confinement. *Phys. Rev. E*, 80:031501.

Almarza, N., Martín, C., Lomba, E., and Bores, C. (2015). Demixing and confinement of non-additive hard-sphere mixtures in slit pores. *Journal of Chemical Physics*, 142:014702.

Almarza, N. G. and Lomba, E. (2003). Determination of the interaction potential from the pair distribution function: An inverse monte carlo technique. *Phys. Rev. E*, 68(1):011202.

Anderson, E., Bai, Z., Bischof, C., Blackford, S., Demmel, J., Dongarra, J., Croz, J. D., Greenbaum, A., Hammarling, S., McKenney, A., and Sorensen, D. (1999). *LAPACK Users' Guide*. Society for Industrial and Applied Mathematics, third edition.

Anta, J. (1997). *Teoria y simulacion de transiciones de fase en fluidos simples y moleculares*. PhD thesis, CSIC.

Archer, A. (2008). Two-dimensional fluid with competing interactions exhibiting micro phase separation:theory for bulk and interfacial properties. *Physical Review E*, 78:031402.

Attard, P. (1991). Lennard jones bridge functions and triplet correlation functions. *The Journal of Chemical Physics*, 95(6):4471.

Axilrod, B. M. and Teller, E. (1943). Interaction of the van der waals type between three atoms. *The Journal of Chemical Physics*, 11(6):299.

Baerlocher, C., McCusker, L., and Olson, D. (2007). *Atlas of Zeolite Framework Types*. Elsevier, Amsterdam, The Netherlands, 6th edition.

Balucani, U. and Zoppi, M. (1994). *Dynamics of the Liquid State*. Number 10 in Oxford Series on Neutron Scattering in Condensed Matter. Oxford University Press, 1 edition.

Barrat, J. and Hansen, J. (2003). *Basic Concepts for Simple and Complex Liquids*. Cambridge University press.

Barrat, J., Hansen, J., and Pastore, G. (1988). On the equilibrium structure of dense fluids. *Molecular Physics*, 63(5):747–767.

Bartlett, P., Ottewill, R. H., and Pusey, P. N. (1992). Superlattice formation in binary mixtures of hard-sphere colloids. *Phys. Rev. Lett.*, 68(32):3801.

Barton, T., Bull, L., Klemperer, W., Loy, D., McEnaney, B., Misono, M., Monson, P., Pez, G., Scherer, G., Vartuli, J., and Yaghi, M. (1999). Tailored porous materials. *Chem. Mater.*, 11:2633.

Bates, E., Mayton, R., Ntai, I., and Davis, J. (2002). Co_2 capture by a task-specific ionic liquid. *JACS*, 124:926.

Bathia, A. and Thornton, D. (1970). Structural aspects of the electrical resistivity of binary alloys. *Physical Review E*, 2(8):3004.

Beglov, D., , and Roux, B. (1997). An integral equation to describe the solvation of polar molecules in liquid water. *The Journal of Physical Chemistry B*, 101(39):7821–7826.

Beglov, D. and Roux, B. (1995). Numerical solution of the hypernetted chain equation for a solute of arbitrary geometry in three dimensions. *Journal of Chemical Physics*, 103:360.

Beglov, D. and Roux, B. (1996). Solvation of complex molecules in a polar liquid: An integral equation theory. *The Journal of Chemical Physics*, 104(21):8678–8689.

Behler, J. and Parrinello, M. (2007). Generalized neural-network representation of high-dimensional potential-energy surfaces. *American Physical Society*, 98(14):146401.

Benjamin, I. (1995). Photodissociation of icn in liquid chloroform: Molecular dynamics of ground and excited state recombination, cage escape, and hydrogen abstraction reaction. *The Journal of Chemical Physics*, 103(7):2459–2471.

Berendsen, H., van der Spoel, D., and van der Drunen, R. (1995). Gromacs: A message-passing parallel molecular dynamics implementation. *Computer Physics Communications*, 91:43.

Bhargava, B. and Balasubramanian (2007). Refined potential model for atomistic simulations of ionic liquid [bmim][pf6]. *J. of Chem. Phys.*, 127:114510.

Bhargava, B., Balasubramanian, S., and Klein, M. (2008). Modelling room temperature ionic liquids. *Chem. Comm.*, pages 3339–3351.

Bibby, D. M., Milestone, N. B., and Aldridge, L. P. (1979). Silicalite-2, a silica analogue of the aluminosilicate zeolite zsm-11. *Nature*, 280(5724):664–665.

Bomont, J., Bretonnet, J., Costa, D., and Hansen, J. (2012). Communication:thermodynamic signatures of cluster formation in fluids with competing interactions. *Journal of Chemical Physics*, 137:011101.

Bores, C., Almarza, N., Lomba, E., and Kahl, G. (2015a). Adsorption of a two dimensional system with competing interactions in a disordered, porous matrix. *J. Phys: Condensed Matter*, 27(19):194127.

Bores, C., Lomba, E., Perera, A., and Almarza, N. (2015b). Pattern formation in binary fluid mixtures induced by short-range competing interactions. *J. Chem. Phys.*, 143:084501.

Bratko, D., Blum, L., and Bhuiyan, L. (1990). The structure of a model ionic melt in a planar slit. *J. Chem. Phys.*, 94:586.

Brazhkin, V., Fomin, Y., Lyapin, A., Ryzhov, V., and Trachenko, K. (2012). Two liquids states of matter: A dynamic line on a phase diagram. *Physical Review E*, 85:031202.

Brenner, D., Harrison, J., White, C., and Colton, R. (1991). Molecular dynamics simulations of the nanometer-scale mechanical porperties of compressed buckminsterfullerene. *Thin Solid Films*, 206:220–223.

Brenner, D., Shenderova, O., Harrison, J., Stuart, S., and Sinnott, S. (2002). A second-generation reactive empirical bond order (rebo) potential enrgy expression for hydrocarbons. *J. Phys.: Condens. Matter*, 14:783–802.

Brown, M., Wang, P., Plimpton, S., and Tharrington, A. (2011). Implementing molecular dynamics on hybrid high performance computers - short range forces. *Computer Physics Communications*, 182:898–911.

Broyles, A. (1960). Radial distribution functions form the born-green integral equation. *J. Chem. Phys.*, 33:456.

Bunz, H. (1986). Identification of clusters in computer experiments with periodic boundary conditions. *Computer Physics Communications*, 42:435–439.

Callen, H. (1981). *Termondinámica*. Editorial AC.

Camp, P. (2003). Phase behavior of a two-dimensional system with core-softened and long-range repulsive interactions. *Phys. Rev. E*, 68:061506.

Canongia-Lopes, J., Deschamps, J., and Pádua, A. A. (2004). Modeling ionic liquids using a systematic all-atom force field. *Journal of Physical Chemistry B*, 108:2038.

Canongia Lopes, J. and Pádua, A. (2006). Nanostructural organization in ionic liquids. *Journal of Physical Chemistry B*, 110:3330.

Cerdà, J. J., Ballenegger, V., Lenz, O., and Holm, C. (2008). P3m algorithm for dipolar interactions. *The Journal of Chemical Physics*, 129(23).

Chai, Y., Guo, T. ad Jin, C., Haufler, R., Felipe Chibante, L., Fure, J., Wang, L., Alford, J., and Smalley, R. E. (1991). Fullerenes with metals inside. *J. Phys. Chem.*, 95:7564–7568.

Charbonneau, P. and Reichman, D. (2007). Phase behavior and far-from-equilibrium gelation in charged attractive colloids. *Physical Review E*, 75:050401.

Chen, S., Rouch, J., Sciortino, F., and Tartaglia, P. (1994). Static and dynamic properties of water-in-oil micro emulsions near the critical and percolation points. *J. Phys: Condensed Matter*, 6:10855–10883.

Chennamsetty, N., Bock, H., Lísal, M., and Brennan, J. K. (2011). *An Introduction to Coarse-Graining Approaches: Linking Atomistic and Mesoscales*, chapter 2, pages 43–84. Wiley VCH Verlag GmbH and Co. KGaA.

Chun, S., Dzyuba, S., and Bartsch, R. (2001). Influence of structural variation in room-temperature ionic liquids on the selectivity and efficiency of competitive alkali metal salt extraction by a crown ether. *Analytical Chemistry*, 73(15):3737–3741. PMID: 11510842.

Coasne, B., Viau, L., and Vioux, A. (2011). Loading-controlled stiffening in nanoconfined ionic liquids. *J. Phys. Chem. Letters*, 2:1150–1154.

Corma, A. (1997). From microporous to mesoporous molecular sieve materials and theris use in catalysis. *Chemical Reviews*, 97:2373.

Cortis, C. M., Rossky, P. J., and Friesner, R. A. (1997). A three-dimensional reduction of the ornstein–zernicke equation for molecular liquids. *The Journal of Chemical Physics*, 107(16):6400–6414.

Crocker, J. and Grieg, D. (1996). Methods of digital video microscopy for colloidal studies. *Journal of Colloid and Interface Science*, 179:298–310.

Cusack, N. (1987). *The physics of structurally disordered matter: An introduction*. Hilger, A., Bristol.

Darden, T., York, D., and Pedersen, L. (1993). Particle mesh ewald: an nlog(n(method for ewald sums in large systems. *J. Chem. Phys.*, 98:10089–10092.

Davis, H. T. (1996). *Statistical mechanics of phases, interfaces and thin films*. Wiley VCH, New York.

De Lorenzi-Venneri, G., Chisolm, E. D., and Wallace, D. C. (2008). Vibration-transit theory of self-dynamic response in a monatomic liquid. *Phys. Rev. E*, 78(4):041205.

Delaunay, B. (1934). Sur la sphère vide. a la mémoire de georges voronoï. *Bulletin de l'Académie des Sciences de l'URSS. Classe des sciences mathématiques et na.*, 6:793 – 800.

Derjaguin, B. and Landau, D. (1941). Theory of the stability of strongly charged lyophobic sols and of the adhesion of strongly charged particles in solution of electrolytes. *Acta Phys. Chim. USSR*, 14:633.

Diaz Peña, M. (1979). *Termodinámica estadística*. Ed Alhambra, 1 edition.

Dijkstra, M. (1998). Phase behavior of nonadditive hard-sphere mixtures. *Phys. Rev. E*, 58(6):7523.

Dodziuk, H. (2011). Endohedral fullerenes complexes and in-out isomerism in perhydrogenated fullerenes. In Cataldo, F., Graovac, A., and Ori, O., editors, *The Mathematics and Topology of Fullerenes*, volume 4, page 117. Springer.

Dodziuk, H. and Dolgonos, G. (2002). Molecular modeling study of hydrogen storage in carbon nanotubes. *Chemical Physics Letters*, 356(1–2):79–83.

Dodziuk, H., Korona, T., Lomba, E., and Bores, C. (2012). Carbon nanotube container: Complexes of c50h10 with small molecules. *Journal of Chemical Theory and Computation*, 8(11):4546–4555.

Du, Q., Beglov, D., , and Roux, B. (2000). Solvation free energy of polar and nonpolar molecules in water. an extended interaction site integral equation theory in three dimensions. *The Journal of Physical Chemistry B*, 104(4):796–805.

Edwards, S. F. and Anderson, P. W. (1975). Theory of spin glasses. *Journal of Physics F: Metal Physics*, 5(5):965.

Egelstaff, P. A. (1992). *An introduction to the liquid state*, volume 7 of *Oxford Series on Neutron Scattering in Condensed Matter*. Oxford University Press 1992, second edition.

Evrard, G. and Pusztai, L. (2005). Reverse monte carlo modeling of the structure of disordered materials with rmc++: a new implementation of the algorithm in c++. *Journal of Physics: Condensed Matter*, 17:S1–S13.

Fedorov, M. and Kornyshev, A. (2008). Ionic liquid near a charged wall: Structure and capacitance of electrical double layer. *J. Phys. Chem. B letters*, 112:11868–11872.

Feng, G., Zhang, J., and Giao, R. (2009). Microstructure and capacitance of the electrical double layers at the interface of ionic liquids and planar electrodes. *J. Phys. Chem. C*, 113:4549–4559.

Fernaud, M. J., Lomba, E., Martin, C., Levesque, D., and Weis, J.-J. (2003). Study of dipolar fluid inclusions in charged random matrices. *The Journal of Chemical Physics*, 119(1):364–372.

Fernaud, M. J., Lomba, E., and Weis, J. J. (2001). Adsorption of a diatomic molecular fluid into random porous media. *Phys. Rev. E*, 64(5):051501.

Ferreira, A. and Prodanescu, E. (2005). Fisher scaling in two dimensional ising magnetic lattice-gas. *Intern. Journal of Modern Physics C*, 16(1).

Fischer, H., Barnes, A., and Salmon, P. (2006). Neutron and x-ray diffraction studies of liquids and glasses. *Rep. Prog. Phys.*, 69:233–299.

Floquet, N., Coulomb, J., Bellat, J., Simon, J., Weber, G., and Andre, G. (2007). Heptane adsorption in silicalite-1: Neutron scattering investigation. *J. Phys. Chem. C*, 111:18182.

Fontana, F. (1777). *Mem. Mat. Fis. Soc. Ital. Sci.*, 1:679.

Frenkel, D. and Smit, B. (2002). *Understanding Molecular Simulation*. Academic Press, London.

Fulde, P. (1995). *Electron correlations in molecules and solids*, volume 100 of *Springer Series in Solid-State Sciences*. Springer.

Fyfe, C., Diaz, A., Grondey, H., Lewis, A., and Förster, H. (2005). Solid state nmr method for the determination of 3d zeolite framework/sorbate structures. *Journal of American Chemical Society*, 127:7543.

García-Pérez, E., Parra, J. B., Ania, C. O., Dubbeldam, D., Vlugt, T. J. H., Castillo, J. M., Merkling, P. J., and Calero, S. (2008). Unraveling the argon adsorption processes in mfi-type zeolite. *The Journal of Physical Chemistry C*, 112(27):9976–9979.

Gelb, L. and Gubbins, K. (1998). Characterization of porous glasses: Simulation models, adsorption isotherms, and the brunauer-emmett-teller analysis method. *Langmuir*, 14:2097–2111.

Gelb, L., Gubbins, K., Radhakrishnan, R., and Sliwinska-Bartkowiak, M. (1999). Phase separation in confined systems. *Rep. Prog. Phys.*, 62:1573.

Given, J. A. and Stell, G. (1992). Comment on: Fluid distributions in two phase random media: Arbitrary matrices. *The Journal of Chemical Physics*, 97(6):4573–4574.

Gobel, R., White, R., Titirici, M., and Taubert, A. (2012). Carbon-based ionogels:tuning the properties of the ionic liquid via carbon-ionic liquid interaction. *Phys. Chem. Chem. Phys.*, 14:5992–5997.

Godfrin, P., Casta'neda-Priego, R., Liu, Y., and Wagner, N. (2013). Intermediate rands order and structure in colloidal dispersions with competing interactions. *J. Chem. Phys.*, 139:154904.

Godfrin, P., Valadez-Pérez, N., Castañeda-Priego, R., Wagner, N., and Liu, Y. (2014). Generalized phase behaviour of cluster formation in colloidal dispersions with competing interactions. *Soft Matter*, 10:5061.

Gor, G. and Neimark, A. (2011). Adsorption-induced deformation of mesoporous solids: Macroscopic approach and density functional theory. *Langmuir*, 27:6926.

Gozdz, W. (2003). Critical-point and coexistence curve properties of a symmetric mixture of nonadditive hard spheres: A finite size scaling study. *Journal of Chemical Physics*, 119(6):2003.

Grahn, M., Holmgren, A., and Hedlund, J. (2008). Adsorption of n-hexane and p-xylene in thin silicalite-1 films studied by ftir/atr spectroscopy. *J. Phys. Chem. C*, 112:7717.

Gray, C., Gubbins, K., and Joslin, C. (2011). *Theory of Molecular Fluids*, volume 2. Applications of *International Series of Monographs on Chemistry*. Oxford Science Publications.

Groenewold, J. and Kegel, W. (2001). Anomalously large equilibrium clusters of colloids. *Journal of Physical Chemistry B*, 105:11702.

Hagen, M. H. J., Meijer, E. J., Mooij, G. C. A. M., Frenkel, D., and Lekkerkerker, H. N. W. (1993). Does c60 have a liquid phase? *Nature*, 365(6445):425–426.

Haines, R. and McIntosh, R. (1947). Length changes of activated carbon rods caused by adsorption of vapors. *J. Chem. Phys.*, 15(1):28.

Haller, W. (1965). Rearrangement kinetics of the liquid-liquid immiscible microphases in alkali borosilicate melts. *J. Chem. Phys.*, 42(2):686.

Hanke, C., Price, S., and Lynden-Bell, R. (2001). Intermolecular potentials for simulations of liquid imidazolium salts. *Mol. Phys.*, pages 801–809.

Hansen, J. (1986). *Theory of simple liquids*. ACADEMIC PRESS.

Hansen, J. P. (1991). An introduction to molecular dynamics, with applications to the glass transition. In Meyer, M. and Pontikis, V., editors, *Computer Simulations in Material Science: Interatomic Potentials, Simulation Techniques and Applications*, pages 3–21. Kluwer Academic Publishers.

Hansen, J. P. and McDonald, I. R. (1986). *Theory of simple liquids*. Academic Press.

Hansen, J.-P. and Verlet, L. (1969). Phase transitions of the lennard-jones system. *Phys. Rev.*, 184(1):151–161.

Harrison, J., Stuart, S., Robertson, D., and White, C. (1997). Properties of capped nanotubes when used as spm tips. *J. Phys. Chem. B*, 101(47):9682.

Henderson, D. (1992). *Integral Equation Theories for Inhomogeneous Fluids*, chapter 4, page 177. Marcel Dekker, Inc., New York.

Henderson, R. (1974). A uniqueness theorem for fluid pair correlation functions. *Physics Letters A*, 49(3):197 – 198.

Hoover, W. (1985). Canonical dynamics: Equilibrium phase-space distributions. *Physical Review A*, 31(3):1695.

Hoye, J. S., Lomba, E., and Stell, G. (1993). Analysis of the hypernetted chain equation for ionic fluids. *Molecular Physics*, 79(3):523–536.

Humphrey, W., Dalke, A., and Schulten, K. (1996). Vmd-visual molecular dynamics. *J.Molec. Graphics*, 14:33–38.

Iijima, S. (1991). Helical microtubules of graphitic carbon. *Nature*, 354(7):56.

Imperio, A., Pini, D., and Reatto, L. (2006). Fluctuations and pattern formation in fluids with competing interactions. In *International Workshop on Collective Phenomena in Macroscopic System*, Villa Olmo, Como, Italy.

Imperio, A. and Reatto, L. (2004). A bidimensional fluid system with competing interactions: spontaneous and induced pattern formation. *J. Phys.: Condens. Matter*, 16:S3769–S3789.

Imperio, A. and Reatto, L. (2006). Microphase separation in two-dimensional systems with competing interactions. *J. Chem. Phys.*, 124:164712.

Imperio, A. and Reatto, L. (2007). Microphase morphology in two-dimensional fluids under lateral confinement. *Phys. Rev. E*, 76:040402(R).

Ishizuka, R. and Yoshida, N. (2012). Application of efficient algorithm for solving six-dimensional molecular ornstein-zernike equation. *J. Chem. Phys.*, 136(11):114106.

Izvekov, S., Parrinello, M., Burnham, C. J., and Voth, G. A. (2004). Effective force fields for condensed phase systems from ab initio molecular dynamics simulation: A new method for force-matching. *The Journal of Chemical Physics*, 120(23):10896–10913.

Johnston, K., Maynard, J., Truskett, T., Borwankar, A., Miller, M., Wilson, B., Dinin, A., Khan, T., and Kaczorowski, K. (2012). Concentrated dispersions of equilibrium protein nanoclusters that reversibly dissociate into active monomers. *ACS nano*, 6(2):1357–1369.

Jorge, S., Lomba, E., and Abascal, J. L. F. (2001). An inhomogeneous integral equation for the triplet structure of binary liquids. *The Journal of Chemical Physics*, 114(8):3562–3569.

Jorgensen, W., Maxwell, D., and Tirado-Rives, J. (1996). Development and testing of the opls all-atom force field on conformational energetics and properties of organic liquids. *J. Am. Chem. Soc.*, 118(45):11225.

Kelley, C. and Montgomery Pettitt, B. (2004). A fast algorithm for the ornstein-zernike equations. *Journal of Computational Physics*, 197:491.

Kepler, G. and Fraden, S. (1994). Attractive potential between confined colloids at low ionic strength. *Physical Review Letters*, 73(2):356.

Kholmurodov, K., Aru, G., and Yasuoka, K. (2010). Molecular dynamics simulations of the interaction of carbon nanotube and a carbon disulfide solvent. *Natural Science*, 2(8):902–910.

Kiselev, A. V. (1965). Non-specific and specific interactions of molecules of different electronic structures with solid surfaces. *Discussion of the Faraday Society*, 40:205–218.

Kleinert, H. (2006). *Path integrals in Quantum Mechanics, Statistics, Polymer Physics, and Financial Markets*. Freie Universitaet Berlin, 4th edition.

Koningsveld, H. v. and Tuinstra, F. (1989). The location of p-xylen ein a single crystal of zeolite h-zsm-5 with a new, sorbate-induced, orthorhombic framework symmetry. *Acta Cryst.*, B45:423–431.

Kovalenko, A. and Hirata, F. (1998). Three-dimensional density profiles of water in contact with a solute of arbitrary shape: a rism approach. *Chemical Physics Letters*, 290:237–244.

Kovalenko, A. and Hirata, F. (1999). Self consistent description of a metal-water interface by the kohn-sham density functional theory and the three-dimensional reference interaction site model. *J. Chem. Phys.*, 110:10095.

Kowalczyk, P., Ciach, A., and Neimark, A. V. (2008). Adsorption-induced deformation of microporous carbons: Pore size distribution effect. *Langmuir*, 24(13):6603–6608. PMID: 18522449.

Kratschmer, W., Lamb, L., Fostiropoulos, K., and Huffman, D. (1990). Solid c60: a new form of carbon. *Nature*, 347:354.

Kroto, H. W. (2003). Symmetry, space, stars and c60. In Grenthe, I., editor, *Nobel Lectures, Chemistry 1996-2000*, page 44, Singapore. World Scientific Publishing Co.

Kroto, H. W., Heath, J., O'Brien, S., Curl, R., and Smalley, R. E. (1985). C60: Buckminsterfullerene. *Nature*, 318(14):162.

Kuhn, H. (2008). Origin of life - symmetry breaking in the universe: Emergence of homochirality. *Current Opinion in Colloid and Interface Science*, 13:3–11.

Lado, F., Foiles, S. M., and Ashcroft, N. W. (1983). Solutions of the reference-hypernetted-chain equation with minimized free energy. *Phys. Rev. A*, 28(4):2374.

Lado, F. and Lomba, E. (1998). Heisenberg spin fluid in an external magnetic field. *Phys. Rev. Lett.*, 80(16):3535.

Landau, D. and Binder, K. (2009). *A Guide to Monte Carlo Simulations in Statistical Physics*. Cambridge University press, 3 edition.

Levesque, D., Lamari, F., Weinberger, B., and Kunowsky, M. (2002). Monte carlo simulations of hydrogen storage in carbon nanotubes. *J. Phys.: Condens. Matter*, 14:9285–9293.

Levitz, P., Sinha, S., and Drake, J. (1991). Porous vycor glass: The microstructure as probed by electron microscopy, direct energy transfer, small angle scattering, and molecular adsorption. *J. Chem. Phys.*, 95(8):6151.

Lindahl, E., Hess, B., and van der Spoel, D. (2001). Gromacs 3.0: A package for molecular simulation and trajectory analysis. *J. Mol. Mod.*, 7:306.

Llewellyn, P. L., Coulomb, J., Grillet, Y., Patarin, J., Lauter, H., Reichert, H., and Rouquerol, J. (1993). Adsorption by mfi-type zeolites examined by isothermal microcalorimetry and neutron diffraction. 1. argon, krypton and methane. *Langmuir*, 9:1846.

Lomba, E. and Almarza, N. (1994). Rola of the interaction range in the shaping of phase diagrams in simple fluids. the hard sphere yukawa fluid as a case study. *J. Chem. Phys.*, 100(11):1.

Lomba, E., Alvarez, M., Lee, L., and Almarza, N. (1995). Phase stability of binary non-additive hard-sphere mixtures: A self-consistent integral equation study. *The Journal of Chemical Physics*, 104:4180–4188.

Lomba, E., Bores, C., and Kahl, G. (2014). Explicit spatial description of fluid inclusions in porous matrices in terms of an inhomogeneous integral equation. *J. Chem. Phys.*, 141:164704.

Lomba, E., Bores, C., Sanchez, V., and Noya, E. (2015). A three dimensional integral equation approach for fluids under confinement: Argon in zeolites. *J. Chem. Phys.*, 143:164703.

Lomba, E., Given, J., Stell, G., Weis, J., and Levesque, D. (1993). Ornstein-zernike equations and simulation results for hard-sphere fluids adsorbed in porous media. *Phys. Rev. E*, 48:233.

Lomba, E. and Weis, J. (2010). A computational study of electrolyte adsorption in a simple model for intercalated clays. *Journal of Chemical Physics*, 132:104705.

Madden, W. and Glandt, D. (1988). Distriution functions for fluids in random media. *J. Statistical Physics*, 51(3):537.

Magda, J. J., Tirrell, M., and Davis, H. T. (1985). Molecular dynamics of narrow, liquid filled pores. *The Journal of Chemical Physics*, 83(4):1888–1901.

Maginn, E. (2009). Molecular simulation of ionic liquids: current status and future opportunities. *J.Phys.:Condens. Matter*, 21:373101.

Mani, E., Lechner, W., Kegel, W., and Bolhuis, P. (2014). Equilibrium and non-equilibrium cluster phases in colloids with competing interactions. *Soft Matter*.

Mansoori, G. (2005). *Principles of Nanotechnology: Molecular based study of condensed matter in small systems*. World Scientific Publishing Co. Pte. Ltd.

Maolin, S., Fuchun, Z., Guozhong, W., Chunlei, W., Shimou, C., Yi, Z., and Jun, H. (2008). Ordering layers of [bmim][pf6] ionic liquid on graphite surfaces: Molecular dynamics simulation. *J. Chem. Phys.*, 128:134504.

Martín-Calvo, A., Gutierrez-Sevillano, J., Parra, J., Ania, C., and Calero, S. (2015). Transferable force fields for adsorption of samll gases in zeolites. *Phys. Chem. Chem. Phys.*

Mata, R. and Werner, H.-J. (2007). Local correlation methods with a natural localized molecular orbital basis. *Molecular Physics*, 105(19-22):2753.

Mendez-Morales, T., Carrete, J., Perez-Rodriguez, M., Cabeza, O., Gallego, L., Lyndel-Bell, R., and Varela, L. (2014). Molecular dynamics simulations of the structure of the graphene-ionic liquid/alkali salt mixtures interface. *Phys. Chem. Chem. Phys.*, 16:13271.

Merlet, C., Rotenberg, B., Madden, P., Taberna, P., Simon, P., Gogotsi, Y., and Salanne, M. (2012a). On the molecular origin of super capacitance in nano porous carbon electrodes. *Nature materials*.

Merlet, C., Salanne, M., and Rotenberg, B. (2012b). New coarse-grained models of imidazoliun ionic liquids for bulk and interfacial molecular simulations. *Journal of Physical Chemistry C*, 116:7687.

Metropolis, N. and Ulam, S. (1949). The monte carlo method. *Journal of American Statistical Association*, 44(247):335–341.

Meyra, A., Zarragoicoechea, G., and Kuz, V. (2012). Vegetation patterns in limited resource ecosystems: a statistical mechanics model and monte carlo simulations. *Molecular Physics*, 110(3):173.

Mezzenga, R., Schurtenberger, P., Burbidge, A., and Michel, M. (2005). Understanding foods as soft materials. *Nature materials*, 4:729.

Monk, J., Singh, R., and Hung, F. (2011). Effects of pore size and pore loading on the properties of ionic liquids confined inside nano porous cmk-3 carbon materials. *J. Phys. Chem. C*, 115:3034–3042.

Murthy, K. (2003). An introduction to monte carlo simulation of statistical physics problem.

Murthy, K. (2004). *Monte Carlo Methods in Statistical Physics*. Universities Press.

Myers, A. and Monson, P. (2014). Physical adsorption of gases: the case for absolute adsorption as the basis for thermodynamic analysis. *Journal of Interational Adsorption Society*.

Ng, K. (1974). Hypernetted chain solutions for the classical one-component plasma up to gamma=7000. *J. of Chem. Phys.*, 61:2680.

Nishihara, H., Yang, Q.-H., Hou, P.-X., Unno, M., Yamauchi, S., Saito, R., Paredes, J., Martínez-Alonso, A., Tascón, J. M., Sato, Y., Terauchi, M., and Kyotani, T. (2009). A possible buckybowl-like structure of zeolite templated carbon. *Carbon*, 47:1220–1230.

Nosé, S. (1984). A unified formulation of the constant temperature molecular dynamics methods. *The Journal of Chemical Physics*, 81(1):511–519.

NSTC (2000). National nanotechnology initiative: leading to the next industrial revolution. In Science, N. and Council, T., editors, *A report by the Interagency Working Group on Nanoscience, Engineering and Technology Committee on Technology*, Washington DC.

Nygard, K., Kjellander, R., Sarman, S., Chodankar, S., Perret, E., Buitenhuis, J., and van der Veen, J. F. (2012). Anisotropic pair correlations and structure factors of confined hard-sphere fluids: An experimental and theoretical study. *Phys. Rev. Lett.*, 108(3):037802.

Ohno, H., editor (2005). *Electrochemical Aspects of Ionic Liquids*. John Wiley and Sons, Inc.

Olson, D. H., Kokotailo, G. T., Lawton, S. L., and Meier, W. M. (1981). Crystal structure and structure-related properties of zsm-5. *The Journal of Physical Chemistry*, 85(15):2238–2243.

Parrinello, M. and Rahman, A. (1980). Crystal structure and pair potentials: A molecular-dynamics study. *Phys. Rev. Lett.*, 45(14):1196.

Parrinello, M. and Rahman, A. (1981). Polymorphic transitions in single crystals: A new molecular dynamics method. *Journal of Applied Physics*, 52:7182.

Percus, J. (1964). *The Equilibrium Theory of Classical Fluids*. W.A. Benjamin, New York.

Perdew, J., Burke, K., and Ernzerhof, M. (1996). Generalized gradient approximation made simple. *Phys. Rev. Letters*, 77(18):3865.

Perera, A. and Kezic, B. (2013). Fluctuations and micro-heterogeneity in mixtures of complex liquids. *Faraday Discuss.*, 167:145–158.

Perera, A. and Mazighi, R. (2015). Simple and complex forms of disorder in ionic liquids. *Journal of Molecular Liquids*, 210, Part B:243 – 251. Mesoscopic structure and dynamics in ionic liquids.

Perkyns, J. S., Lynch, G. C., Howard, J. J., and Pettitt, B. M. (2010). Protein solvation from theory and simulation: Exact treatment of coulomb interactions in three-dimensional theories. *The Journal of Chemical Physics*, 132(6).

Phillips, J. and Hammerbacher, M. (1984). Methane adsorbed on graphite. i. intermolecular potentials and lattice sums. *Physical Review B*, 29(10):5859.

Pinilla, C., Popolo, M., Kohanoff, J., and Lyndel-Bell, R. (2007). Polarization relaxation in an ionic liquid confined between electrified walls. *J. Phys. Chem. B*, 111:4877–4884.

Pizio, O., Duda, Y., Trokhymchuk, A., and Sokolowski, S. (1998). Associative replica ornstein-zernike equations and the structure of chemically associating fluids in disordered porous media. *Journal of Molecular Liquids*, 76:183–194.

Plimpton, S. (1995). Fast parallel algorithms for short-range molecular dynamics. *Journal of Computational Physics*, 117:1–19.

Plimpton, S. and Thompson, A. (2012). Computational aspects of many-body potentials. *MRS Bulletin*, 37:513–521.

Poon, W., Pirie, A., Haw, M., and Pusey, P. (1997). Non-equilibrium behaviour of colloid-polymer mixtures. *Physica A*, 235:110–119.

Popov, A., Yang, S., and Dunsch, L. (2013). Endohedral fullerenes. *Chemical Reviews*, 113:5989–6113.

Rajput, N., Monk, J., and Hung, F. (2012a). Structure and dynamics of an ionic liquid confined inside a charged slit graphitic nano pore. *J. Phys. Chem. C*, 116:14504–14513.

Rajput, N., Monk, J., and Hung, F. (2014). Ionic liquids confined in a realistic activated carbon model: a molecular simulation study. *J. Phys. Chem. C*, 118:1540–1553.

Rajput, N., Monk, J., Ramesh, S., and Hung, F. (2012b). On the influence of pore size and pore loading on structural and dynamical heterogeneities of an ionic liquid confined in a slit pore. *J. Phys. Chem. C*, 116:5169–5181.

Rapaport, D. (2004). *The Art of Molecular Dynamics Simulation*. Cambridge University press, 2 edition.

Ravikovitch, P. and Neimark, A. (2006). Density functional theory model of adsorption on amorphous and microporous silica materials. *Langmuir*, 22(26):11171–11179. PMID: 17154599.

Reed, A., Weinstock, R., and Weinhold, F. (1985). Natural population analysis. *J. Chem. Phys.*, 83:735.

Reed, S., Lanning, O., and Madden, P. (2007). Electrochemical interface between and ionic liquid and a model metallic electrode. *J. Chem. Phys.*, 126:084704.

Robens, E. (1994). Characterization of porous solids iii. some intringuin items in the history of adsorption. In Rouquerol, J., Rodríguez-Reinoso, F., Sing, K., and Unger, K., editors, *Studies in Surface Science and Catalysis*, volume 87, page 109. Academic Press, El Sevier.

Robertson, J. (1986). Amorphous carbon. *Advances in Physics*, 35(4):317–374.

Rouquerol, F., Rouquerol, J., Sing, K., Llewellyn, P., and Maurin, G. (2014a). *Adsorption by Powders and Porous Solids. Principles, Methodology and Applications*. Academic Press, 2 edition.

Rouquerol, J., Avnir, D., Everett, D., Fairbridge, C., Haynes, M., Pernicone, N., Ramsay, J., Sing, K., and Unger, K. (1994). Characterization of porous solids iii. guidelines for the characterization of porous solids. In Rouquerol, J., Rodríguez-Reinoso, F., Sing, K., and Unger, K., editors, *Studies in Surface Science and Catalysis*, volume 87, page 1. Academic Press, El Sevier.

Rouquerol, J., Rouquerol, F., Sing, K., LLewellyn, P., and Maurin, G. (2014b). *Adsorption by Powders and Porous Solids. Principles , Methodology and Applications*. ACADEMIC PRESS, second edition.

Royall, C. P., Poon, W. C. K., and Weeks, E. R. (2013). In search of colloidal hard spheres. *Soft Matter*, 9:17–27.

RSC (2014). Royal society of chemistry - periodic table - carbon.

Sánchez-Gil, V., Noya, E. G., Guil, J. M., Lomba, E., and Valencia, S. (2016). Adsorption of argon on pure silica mel. volumetric experiments and grand canonical monte carlo simulations. *Microporous and Mesoporous Materials*, 222:218 – 225.

Sarkisov, L. (2012). Accesible surface area of porous materials: Understanding theoretical limits. *Advanced Materials*, 24:3130–3133.

Sarkisov, L. and Harrison, A. (2011). Computational structure characterisation tools in application to ordered and disordered porous materials. *Molecular Simulation*, 37(15):1248–1257.

Scheele, C. (1777). *Chemische Abhandlungen von der Luft und dem Feuer*. Upsala; Leipzig.

Scherer, G. (1986). Dilatation of porous glass. *J. Am. Ceramic Society*, 69(6):473.

Schlitter, J. (1993). Targeted molecular dynamics simulation of conformational change-application to the t¡-¿r transition in insulin. *Molecular Simulation*, 10(2-6):291–308.

Schlitter, J., Swegat, W., and Mulders, T. (2001). Distance-type reaction coordinates for modelling activated processes. *Journal of Molecular Modeling*, 7:171–177.

Schöll-Paschinger, E., Levesque, D., Weis, J., and Kahl, G. (2001). Phase diagram of a symmetric binary fluid in a porous matrix. *Physical Review E*, 64:011502.

Schwanzer, D. and Kahl, G. (2011). Two-dimensional systems with competing interactions: microphase formation under the effect of a disordered porous matrix. *Condens. Matter Phys.*, 14(3):33801.

Schwanzer, D. F. and Kahl, G. (2010). Two-dimensional systems with competing interactions: microphase formation versus liquid¡e2¿¡80¿¡93¿vapour phase separation. *J. Phys. : Condens. Matter*, 22:415103.

Sciortino, F., Mossa, S., Zaccarelli, E., and Tartaglia, P. (2004). Equilibrium cluster phases and low-density arrested disordered states: the role of short-range attraction and long-range repulsion. *Physical Review Letters*, 93(5):055701.

Scott, L., Jackson, E., Zhang, Q., Steinberg, B., Bancu, M., and Li, B. (2011). A short, rigid, structurally pure carbon nanotube by stepwise chemical synthesis. *Journal of the American Chemical Society*, 134:107–110.

Sear, R. P., Chung, S.-W., Markovich, G., Gelbart, W. M., and Heath, J. R. (1999). Spontaneous patterning of quantum dots at the air-water interface. *Phys. Rev. E*, 56:R6255.

Segre, P., Prasad, V., Schofield, A., and Weitz, D. (2001). Glasslike kinetic arrest at the colloidal-gelation transition. *Physical Review Letters*, 86(26):6042.

Seul, M. and Andelman, D. (1995). Domain shapes and patterns: the phenomenology of modulated phases. *Science*, 267:476.

Sha, M., Dou, Q., and Wu, G. (2012). Molecular dynamics simulation of ionic liquids adsorbed onto a solid structure and confined in nano space. *Chem. Modell.*, 9:186–217.

Sha, M., Wu, G., Fang, H., Zhu, G., and Liu, Y. (2008). Liquid-to-solid phase transition of a 1,3.dimethylimidazolium chloride ionic liquid monolayer confined between graphite walls. *J. Phys. Chem. C*, 112:18584–18587.

Shinohara, H. (2014). The early days of metallofullerene research. In Yang, S. and Wang, C.-R., editors, *Endohedral fullerenes. From fundamentals to application*, volume Chapter 1. World Scientific Publishing Co. Pte. Ltd.

Siggia, E. (1979). Late stage of spinodal decomposition in binary mixtures. *Physical Review A*, 20:595.

Singh, M., Singh, R., and Chandra, S. (2014). Ionic liquids confined in porous matrices: physicochemical properties and applications. *Progress in Material Science*.

Singh, R., Monk, J., and Hung, F. (2010). A computational study of the behavior of the ionic liquid [bmim+][pf6-] confined inside a multi walled carbon nanotubes. *J. Phys. Chem. C*, 114:15478–15485.

Singh, R., Monk, J., and Hung, F. (2011a). Heterogeneity in the dynamics of the ionic liquid [bmim+][pf6-] confined in a slit nanopore. *J. Phys. Chem. C*, 115:16544.

Singh, R., Rajput, N., He, X., Monk, J., and Hung, F. (2011b). Molecular dynamics simulations of the ionic liquid [emim+][tfmsi]. *J. Phys. Chem. C*, 115:16544.

Sink'o, K., Torma, V., and Kov'acs, A. (2008). Saxs investigation of porous nanostructures. *Journal of Non-Crystalline Solids*, 354:5466.

Smit, B. and Maesen, L. (2008). Molecular simulations of zeolites: Adsorption, diffusion, and shape selectivity. *Chem. Rev.*, 108:4125–4184.

Snurr, R. Q., Bell, A. T., and Theodorou, D. N. (1993). Prediction of adsorption of aromatic hydrocarbons in silicalite from grand canonical monte carlo simulations with biased insertions. *The Journal of Physical Chemistry*, 97(51):13742–13752.

Stanley, H. (1971). *Introduction to Phase transitions and critical phenomena*. Clarendon Press-Oxford.

Stauffer, D. (1979). Scaling theory of percolation clusters. *Physics Reports*, 1:1–74.

Stillinger, F. (1963). Rigorous basis of the frenkel-band theory of association equilibrium. *Journal of Chemical Physics*, 38:1486.

Stillinger, F. and Weber, T. (1985). Computer simulation of local order in condensed phases of silicon. *Phys. Rev. B*, 31:5262.

Stoddard, S. D. (1978). Note. identifying clusters in computer experiments on systems of particles. *Journal of Computational Physics*, 27:291–293.

Stone, J. E., Phillips, J. C., Freddolino, P. L., Hardy, D. J., Trabuco, L. G., and Schulten, K. (2007). Accelerating molecular modeling applications with graphics processors. *Journal of Computational Chemistry*, 28(16):2618–2640.

Stradner, A., Sedgwick, H., Cardinaux, F., Poon, W., Edelhaaf, S., and Schurtenberger, P. (2004). Equilibrium cluster formation in concentrated protein solutions and colloids. *Nature*, 432:492.

Stuart, S., Tutein, A., and Harrison, J. (2000). A reactive potential for hydrocarbons with intermolecular interactions. *J. Chem. Phys.*, 112(14):6472.

Swendsen, R. H. and Wang, J.-S. (1987). Nonuniversal critical dynamics in monte carlo simulations. *Phys. Rev. Lett.*, 58(2):86–88.

Tazi, S., Salanne, M., Simon, C., and Turq, P. (2010). Potential-induced ordering transition of the adsorbed layer at the ionic liquid/ electrified metal interface. *J. Phys. Chem. B*, 114:8453–8459.

Terasaki, O., Ohsuna, T., Sakuma, H., Watanabe, D., Nakagawa, Y., , and Medrud, R. (1996). Direct observation of "pure mel type" zeolite. *Chemistry of Materials*, 8(2):463–468.

Thess, A., Lee, R., Nikolaev, P., Scuseria, G., Tománek, D., Fischer, J., and Smalley, R. E. (1996). Crystalline ropes of metallic carbon nanotubes. *Science*, 273:483.

Thijssen, J. (1999). *Computational physics*. Cambridge University press.

Thommes, M. and Cychosz, K. (2014). Physical adsorption characterization of nanoporous materials: progress and challenge. *Journal of Interational Adsorption Society*.

Tildesley, D. and Madden, P. (1981). An effective pair potential for liquid carbon disulphide. *Molecular Physics*, 42(5):1137–1156.

Torquato, S. (2001). *Random Heterogeneous Materials*. Springer-Verlag, New York.

Vatamanu, J., Borodin, O., and Smith, G. (2010). Molecular insights into the potential and temperature dependences of the differential capacitance of a room-temperature ionic liquid at graphite electrodes. *JACS*, 132:14825–14833.

Verwey, E. and Overbeek, J. (1948). *Theory of the Stability of Lyophobic Colloids*. Elsevier, Amsterdam.

Wang, F. and Landau, D. P. (2001). Efficient, multiple-range random walk algorithm to calculate the density of states. *Phys. Rev. Lett.*, 86(10):2050.

Weeks, J., Chandler, D., and Andersen, H. (1971). Role of repulsive forces in determining the equilibrium structure of simple liquids. *Journal of Chemical Physics*, 54:5237.

Welton, T. (1999). Room-temperature ionic liquids. solvents for synthesis and catalysis. *Chem. Rev.*, 99:2071–2083.

Wilkes, J. (2002). A short history of ionic liquids-from molten salts to neoteric solvents. *Green Cemistry*, 4:73–80.

Wood, B., Bhide, S., Kandagal, V., Pathak, A., Punnathanam, S., Ayappa, K., and Narasimhan, S. (2012). Methane and carbon dioxide adsorption on edge-functionalized graphene: A comparative dft study. *J. Chem. Phys.*, 137:054702.

Yadav, S., Laue, T., Kalonia, D., Singh, S., and Shire, S. (2012). The influence of charge distribution on self-association and viscosity behavior of monoclonal antibody solutions. *Molecular Pharmaceutics*, 9:791–802.

Yamazaki, T. and Kovalenko, A. (2011). Spatial decomposition of solvation free energy based on the 3d integral equation theory of molecular liquid: Application to miniproteins. *The Journal of Physical Chemistry B*, 115(2):310–318. PMID: 21166382.

Yearley, E., Zarraga, I., Shire, S., Scherer, T., Gokam, Y., Wagner, N., and Y., L. (2013). Small-angle neutron scattering characterization of monoclonal antibody conformations and interactions at high concentrations. *Biophysical Journal*, 105:720–731.

Zerah, G. and Hansen, J. (1986). Self consistent integral equations for fluid pair distribution functions: Another attempt. *The Journal of Chemical Physics*, 84(4):2336–2343.

Zhang, L. and Tassel, R. (2000). Theory and simulation of adsorption in a templated porous material: Hard sphere systems. *Journal of Chemical Physics*, 112:3006.

Zhang, L. and Van Tassel, P. (1999). Theroy and simulation of adsorption in a templated porous material: Hard sphere systems. *Journal of Chemical Physics*, 112(6):3006.

Zhao, X., Chen, B., Karaborni, S., and Siepmann, I. (2005). Vapor-liquid and vapor-solid phase equilibria for united-atom benzene models near their triple points: The importance of quadrupolar interactions. *J. Phys. Chem. B*, 209:5386–5374.

Zhu, B., Lee, R., and Robinson, G. (1988). Molecular dynamics simulation of liquid carbon disulphide with a harmonic intramolecular potential. *Molecular Physics*, 65(1):65.